

# Journal of Energy

ISSN 1849-0751 (On-line)  
ISSN 0013-7448 (Print)  
UDK 621.31

**VOLUME 61 Number 1–4 | 2012 Special Issue**

- 03** R. P. Marek  
Dielectric comparisons of different types of aramid insulation
- 13** P. Gabrić, M. Glavinić, A. Mikulecky, V. Podobnik  
Research of transformer main insulation design rules
- 20** T. Judendorfer, R. Woschitz, M. Muhr, W. Exner, S. Jaufer  
Electrical conductivity of pressboard and the influence of moisture content
- 28** A. Hadži-Skerlev, V. Haramija, D. Vrsaljko, B. Musulin  
Carbon monoxide and carbon dioxide in closed-type power transformers
- 35** A. Orešković, Z. Godec, M. Poljak, R. Gardijan  
On-site accuracy comparison of capacitor and inductive voltage transformers
- 46** M. Ertl, S. Voss  
Load noise increase of transformers by load harmonics
- 63** C.J.G. Spoorenberg  
Statistical analysis of temperature rise test for increased accuracy on x- and y- exponents
- 73** Z. Cheng, N. Takahashi, B. Forghani, X. Wang  
Engineering-oriented benchmarking and application-based magnetic material modeling in transformer research
- 87** O. Bíró, U. Baumgartner, G. Koczka, G. Leber, B. Wagner  
Finite element method for nonlinear eddy current problems in power transformers
- 97** R. Sitar, Ž. Janić  
Impact of electromagnetic shields on local overheating in transformer tank
- 107** F. Kelemen, K. Capuder, L. Štrac  
Skin – effect losses in different loading conditions of a power transformer
- 113** F. Kelemen, G. Plišić, S. Berberović  
Estimation of stray losses in power transformers using 3D FEM and statistics
- 119** B. Čučić  
Magnetic field computation of a loaded transformer
- 129** R. Wittmaack  
CFD simulations of oil immersed and dry type transformers
- 139** W. Calil, V. Rubio, J. Inhasz  
Development of a program for the determination of the temperature at transformers copper bus bars by calculating their dimensionless numbers
- 149** R. Gardijan, A. Keller  
Transformer bushing – a part of measurement system
- 160** S. K. Joshi, H. O. Gupta, P. Agarwal, G. Kumbhar  
Field investigations into harmonics pollution affecting transformers
- 170** A. Mikulecky  
Transformer bushings – failure case studies

# Journal of Energy

Scientific Professional Journal Of Energy, Electricity, Power Systems

Online ISSN 1849-0751, Print ISSN 0013-7448, VOL 61

## Published by

HEP d.d., Ulica grada Vukovara 37, HR-10000 Zagreb

HRO CIGRÉ, Berislavićeva 6, HR-10000 Zagreb

## Publishing Board

**Robert Krklec**, (president) HEP, Croatia,

**Božidar Filipović-Grčić**, (vicepresident), HRO CIGRÉ, Croatia

## Editor-in-Chief

**Goran Slipac**, HEP, Croatia

## Associate Editors

**Helena Božić** HEP, Croatia

**Stjepan Car** Končar-Electrical Engineering Institute, Croatia

**Tomislav Gelo** University of Zagreb, Croatia

**Davor Grgić** University of Zagreb, Croatia

**Mičo Klepo** Croatian Energy Regulatory Agency, Croatia

**Stevo Kolundžić** Croatia

**Vitomir Komen** HEP, Croatia

**Marija Šiško Kuliš** HEP, Croatia

**Dražen Lončar** University of Zagreb, Croatia

**Goran Majstrovic** Energy Institute Hrvoje Požar, Croatia

**Tomislav Plavšić** Croatian Transmission system Operator, Croatia

**Dubravko Sabolić** Croatian Transmission system Operator, Croatia

**Mladen Zeljko** Energy Institute Hrvoje Požar, Croatia

## International Editorial Council

**Franco Barbir** University of Split, Croatia

**Tomislav Barić** J.J. Strossmayer University of Osijek, Croatia

**Anastasios Bakirtzis** University of Thessaloniki, Greece

**Frank Bezzina** University of Malta

**Tomislav Capuder** University of Zagreb, Croatia

**Ante Elez** Končar-Generators and Motors, Croatia

**Dubravko Franković** University of Rijeka, Croatia

**Hrvoje Glavaš** J.J. Strossmayer University of Osijek, Croatia

**Mevludin Glavić** University of Liege, Belgium

**Božidar Filipović Grčić** University of Zagreb, Croatia

**Dalibor Filipović Grčić** Končar-Electrical Engineering Institute, Croatia

**Josep M. Guerrero** Aalborg Universitet, Aalborg East, Denmark

**Dirk Van Hertem** KU Leuven, Faculty of Engineering, Belgium

**Žarko Janić** Siemens-Končar-Power Transformers, Croatia

**Igor Kuzle** University of Zagreb, Croatia

**Niko Malbaša** Ekoneg, Croatia

**Matislav Majstrovic** University of Split, Croatia

**Zlatko Maljković** University of Zagreb, Croatia

**Predrag Marić** J.J. Strossmayer University of Osijek, Croatia

**Viktor Milardić** University of Zagreb, Croatia

**Srete Nikolovski** J.J. Strossmayer University of Osijek, Croatia

**Damir Novosel** Quanta Technology, Raleigh, USA

**Hrvoje Pandžić** University of Zagreb, Croatia

**Robert Sitar** Končar-Electrical Engineering Institute, Croatia

**Damir Sumina** University of Zagreb, Croatia

**Elis Sutlović** University of Split, Croatia

**Damir Šljivac** J.J. Strossmayer University of Osijek Croatia

**Darko Tipurić** University of Zagreb, Croatia

**Bojan Trkulja** University of Zagreb, Croatia

**Nela Vlahinić Lenz** University of Split, Croatia

**Mario Vražić** University of Zagreb, Croatia

## INTRODUCTION

Journal of Energy special issue: Papers from 2<sup>nd</sup> International Colloquium "Transformer Research and Asset Management"

Welcome to this special issue, which is based on selected papers presented at the 2<sup>nd</sup> International Colloquium "Transformer Research and Asset Management", held in Dubrovnik, Croatia, on May 16<sup>th</sup>-18<sup>th</sup>, 2012.

The International Colloquium was organized by the Croatian CIGRÉ National Committee in cooperation with the Faculty of Electrical Engineering and Computing in Zagreb and the Centre of Excellence for Transformers in Zagreb with support from CIGRÉ A2 Study committee (Transformers). The goal of the Colloquium was to share latest research in the in the areas of distribution, power and instrument transformers.

The Colloquium extended over three days. Two CIGRÉ tutorials were offered to all participants. In total there were 148 participants from 26 countries. All of the 47 accepted papers were presented in oral sessions, out of that there were three invited lectures. Participants from manufacturers, utilities and universities took part in discussions.

All the papers were divided into three sessions

### Numerical Modeling

- Electromagnetic field
- Coupled fields
- Transients
- Numerical modeling in design, etc.

### Materials, Components and New Technologies

- Insulating material
- Magnetic material
- Transformer components
- Transformer new technologies, etc.

### Transformer Life Management

- Monitoring
- Diagnostics
- Failures
- Asset management, etc.

From the 47 papers presented at the Colloquium, 18 papers were accepted for publication in Journal of Energy after having undergone the peer-review process. We would like to thank the authors for their contributions and the reviewers who dedicated their valuable time in selecting and reviewing these papers. We hope this special issue will provide you a valuable source of newest achievements in transformer technology.

### Guest Editors

*asst. prof. dr. sc. Žarko Janić*

Končar Power Transformers

A joint Venture of Siemens AG and Končar d.d.

*asst. prof. dr. sc. Bojan Trkulja*

University of Zagreb, Croatia

Faculty of Electrical Engineering and Computing

Richard P. Marek  
DuPont, Energy Solutions  
[Richard.p.marek@usa.dupont.com](mailto:Richard.p.marek@usa.dupont.com)

## DIELECTRIC COMPARISONS OF DIFFERENT TYPES OF ARAMID INSULATION

### SUMMARY

This paper summarizes the results of a number of very different test programs designed to characterize the dielectric performance of three families of aramid paper products. The first part of the testing includes a range of papers that seem well suited to layer type liquid-immersed transformer winding applications. The rapid rise breakdown testing includes multiple thicknesses of the three aramid families that vary in density and surface texture. Wire wrap insulation is the focus of the second part of the testing examined. The results include several different types of test programs, ranging from single flat sheet to multiple flat sheets to actual wire wrapped with multiple thicknesses of the sample insulation. In this series, both rapid rise and impulse breakdown testing is reported. Where possible, statistical analysis was used to make comparisons.

**Key words:** aramid, dielectric strength, insulation testing, liquid-immersed transformer, breakdown testing

### 1. INTRODUCTION

High-temperature aramid insulation has been used for many years in liquid-immersed transformer applications. A number of papers have presented some of the supporting dielectric test data for both paper and board. However, most of this information was developed for wire wrap and pressboard insulation for applications in power transformers, such as high-temperature mobile substations and for on-board traction applications in high-speed trains. Very little has been published on test results in liquid for other aramid paper types. Although most of these other products were originally designed for dry-type applications in motors and transformers, they are beginning to see widespread use in liquid-immersed transformer applications as well.

IEC and IEEE standards that address high-temperature liquid-immersed transformers are currently under development, signaling an increased global interest in applications, such as wind turbine step-up and lightweight pole mounted and platform mounted transformers. These units and new designs in traction on-board transformers, which use layer-type windings, are better suited to these alternate paper types. Accordingly, the dielectric performance in liquids has become increasingly more important for optimized usage. This paper presents the results of several recent research studies that will help to fill in many of the dielectric information gaps and will begin characterizing a more complete dielectric picture of aramid products in various dielectric liquids, under different test configurations. For reference purposes, a comparison will also be made to a limited range of conventional kraft insulation types.

## 2. TEST DESCRIPTION AND ANALYSIS

### 2.1. Layer Insulation

Aramid paper is available in a range of thicknesses for several different product families that vary in density and surface texture. These products were designed for transformer, motor slot liner and other dry-type layer winding applications, but are suitable for layer type liquid-immersed coil winding applications as well. In this test series, high-density and medium-density aramid paper families were tested to determine dielectric capability in mineral oil. The high-density products were further divided into smooth surface and textured surface families. In most cases, the samples were also selected from three different rolls in order to account for some of the inherent manufacturing variability in the paper making process. Five samples were tested from each roll, for a total of fifteen samples for each thickness. Note that multiple rolls were not available for the samples of the kraft paper and the 0,18 mm medium density aramid paper (marked with an asterisk in the tables). Samples for these papers were all taken from the same roll.

Logically, the data set should be divided into groups. Each group is defined by density, surface texture and thickness. Papers measuring less than about 0,10 mm typically target the wire wrap insulation application. These will be addressed later. The medium thickness papers range from about 0,10 mm to less than 1,0 mm. Since pressboard thicknesses begin at about 0,50 mm, there is some overlap for the two products that are made very differently. Pressboard, however is not part of this investigation.

#### 2.1.1. Test Protocol

The flat sheet samples were dried, impregnated with mineral oil and then tested between two 25 mm diameter flat electrodes, according to IEC 60243-1[1]. During the rapid rise test, the 50 Hz voltage was raised linearly with time. The rise time was chosen in such a way that the breakdown occurred within 10 to 20 seconds after the start of the test. Each sample was cut to the same dimension of 100 mm x 100 mm, with one test per sheet.

During the tests, the mineral oil quality was monitored by periodically testing the dielectric strength and when necessary, the mineral oil was filtered and dried. For additional comparison purposes, the density of each sample is shown in Tables I, II, III and IV along with the permittivity calculated for mineral oil. The permittivity is also calculated with synthetic ester liquid, since both natural and synthetic esters have seen increasing interest. The permittivity is calculated according to the formula described in the book, Transformerboard II[2].

#### 2.1.2. Test Data

Table I - High-Density Aramid - Smooth Surface (HDS)

Thickness (mm)	0,13	0,18	0,25	0,38	0,51	0,76
Measured Mean Thickness (mm)	0,130	0,182	0,260	0,385	0,511	0,762
Density (g/cm <sup>3</sup> )	0,87	0,95	0,96	1,03	1,06	1,10
Permittivity – Mineral Oil	3,24	3,34	3,36	3,45	3,49	3,55
Permittivity – Ester Liquid	3,69	3,73	3,74	3,78	3,80	3,82
Mean Breakdown Stress (kV/mm)	84,2	79,7	75,5	72,7	68,6	66,7
Breakdown Stress Std Deviation (kV/mm)	4,42	3,85	2,95	2,86	2,35	2,66
Minimum Breakdown Stress (kV/mm)	74,6	74,5	71,0	69,0	64,9	60,1

Table II - High-Density Aramid - Textured Surface (HDT)

Thickness (mm)	0,18	0,25	0,38
Measured Mean Thickness (mm)	0,193	0,262	0,408
Density (g/cm <sup>3</sup> )	0,94	0,95	0,98
Permittivity – Mineral Oil	3,33	3,34	3,38
Permittivity – Ester Liquid	3,73	3,73	3,75
Mean Breakdown Stress (kV/mm)	87,5	86,5	77,4
Breakdown Stress Std Deviation (kV/mm)	2,91	4,14	1,72
Minimum Breakdown Stress (kV/mm)	83,1	80,1	74,8

Table III - Medium-Density Aramid (MD)

Thickness (mm)	0,18 *	0,25	0,38	0,51
Measured Mean Thickness (mm)	0,167	0,245	0,367	0,489
Density (g/cm <sup>3</sup> )	0,68	0,67	0,67	0,67
Permittivity – Mineral Oil	3,00	2,98	2,98	2,98
Permittivity – Ester Liquid	3,58	3,57	3,57	3,57
Mean Breakdown Stress (kV/mm)	90,5	79,4	70,4	69,9
Breakdown Stress Std Deviation (kV/mm)	4,59	5,47	4,21	2,24
Minimum Breakdown Stress (kV/mm)	80,8	67,1	62,5	66,3

Table IV – Kraft Paper (K)

Thickness (mm)	0, 50
Measured Mean Thickness (mm)	0,464
Density (g/cm <sup>3</sup> )	1,15
Permittivity – Mineral Oil	4,35
Permittivity – Ester Liquid	4,66
Mean Breakdown Stress (kV/mm)	59,0
Breakdown Stress Std Deviation (kV/mm)	1,95
Minimum Breakdown Stress (kV/mm)	54,7

### 2.1.3. Layer Insulation Data Analysis

The usual statistics of mean breakdown stress, standard deviation and lowest breakdown stress provide a means of comparing different materials. Figure 1 compares the breakdown stress for the three different aramid families versus the product mean measured thickness. The single kraft test point is also shown for reference. As is typical for solid insulation, the breakdown stress for aramid products declines as the product thickness increases. Comparing the densities, it is interesting to note that the breakdown stress for the medium density product (MD) is not significantly different from the high-density product with the smooth surface (HDS). However, the high-density aramid family with the textured surface (HDT) does show an apparent improvement compared to both the medium density family and the high-density family with smooth surface.

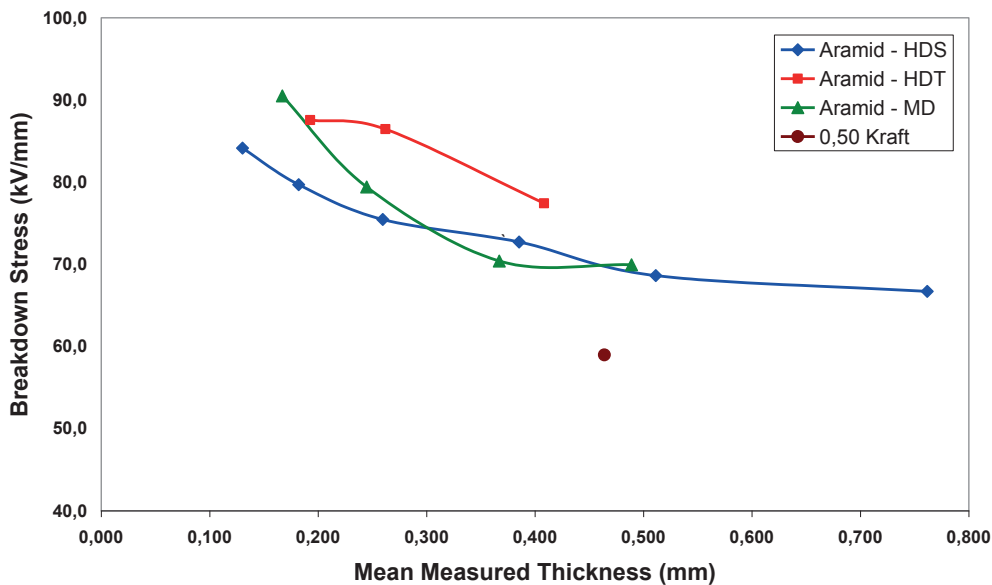


Figure 1 – Layer Insulation Breakdown Stress vs. Thickness

The density also greatly affects the permittivity of all paper insulation. Compared to kraft paper, the aramid products have permittivity closer to that of the dielectric medium, especially the esters where a 3,2 is typical. However, the medium density family with permittivity of 3,0 for mineral oil and 3,6 for ester is even closer due to the lower density, while the dielectric strength is maintained.

## 2.2. Wire Wrap Insulation

Aramid sheet insulation designed for wire wrap insulation applications typically differs from thicker paper structures and from kraft paper, with lower density and lower permittivity. This section compares the breakdown stress of a new aramid wire wrap insulation, specifically designed for use in liquid-immersed transformer applications, with the original aramid wire wrap and with kraft paper. Both the new aramid and the original aramid papers belong to the high-density smooth surfaced product family. Three separate test programs will be reviewed in characterizing the new wire wrap insulation and different techniques will be used for comparison.

### 2.2.1. First Test Series

The first series was part of the layer insulation test series and included the new aramid paper and a kraft paper of similar thickness. The test conditions were the same as previously described and the results are shown in Table V along with reference data for the original aramid paper, which was not part of the test series. The table also includes key parameters of density and permittivity.

In analyzing insulation breakdown test data, IEC 62539[3] considers a data set of less than fifteen to twenty breakdowns to be a small set. Consequently this data set of 14/15 breakdowns is marginal for statistical analysis, but should provide a good indication. The guide also states the following: "Distributions for electrical breakdown include Weibull, Gumbel and lognormal. The most common for solid insulation is the Weibull and is the main distribution described in this guide. It is found to have wide applicability and is a type of extreme value distribution in which the system fails when the weakest link fails."

A typical Weibull plot is shown in Figure 2 and provides a good visual indication of the quality of fit, based on how closely the data points fit the curve. The curve is useful in characterizing a test series and especially in comparing two insulation materials. In this case the new aramid paper is plotted as an example. The basic parameters of the curve are the scale and the shape, where the scale parameter is analogous to the mean value in the more familiar normal distribution model and is designated by the reference line drawn through the 63,2 probability percentile on the curve. The shape parameter is analogous to the inverse of the standard deviation and is a measure of the range or spread of the breakdown values. These parameters are also shown in Table V.

Table V – Aramid and Kraft Wire Wrap

	<b>Kraft Paper</b>	<b>Aramid - New</b>	<b>Aramid - Original</b>
<b>Actual Mean Thickness (mm)</b>	1,97	2,07	2,33
<b>Density (g/cm<sup>3</sup>)</b>	0,96	0,71	0,72
<b>Permittivity – Mineral Oil</b>	3,94	3,03	3,05
<b>Permittivity – Ester Liquid</b>	4,39	3,59	3,60
<b>Mean Breakdown Stress (kV/mm)</b>	72,3	83,5	N/A
<b>Breakdown Stress Std Deviation (kV/mm)</b>	6,68	6,47	N/A
<b>Minimum Breakdown Stress (kV/mm)</b>	58,6	72,6	N/A
<b>Weibull Distribution Shape</b>	15,0	15,23	N/A
<b>Weibull Distribution Scale</b>	75,0	86,4	N/A

### Probability Plot of 0,05 mm Aramid - New

Weibull - 90% CI

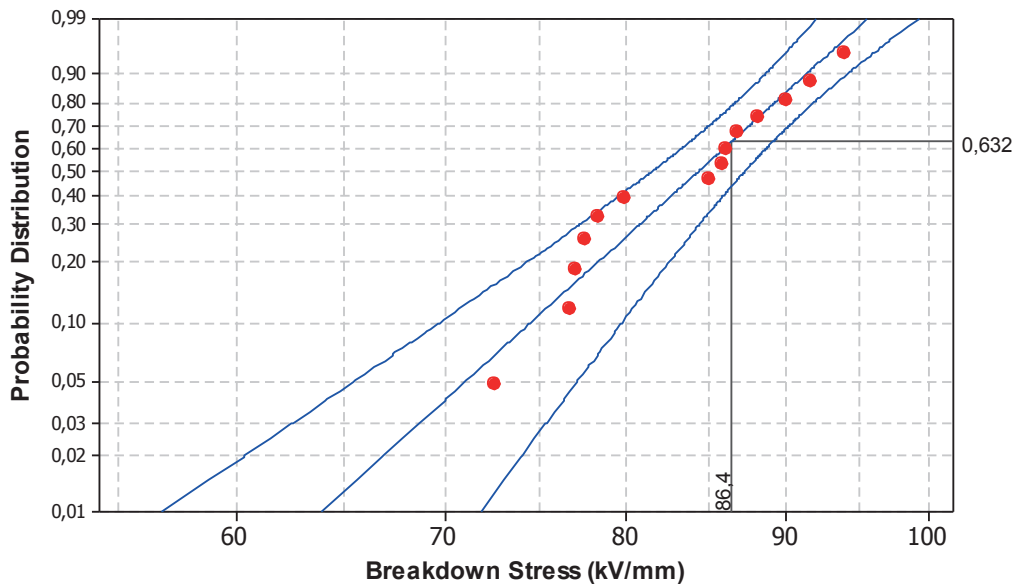


Figure 2 – Weibull Probability Plot of New Aramid Breakdown Stress

#### 2.2.2. Second Test Series – Rapid Rise

The second series was also a flat sheet test program but included impulse breakdown as well as rapid rise breakdown. Multiple sheets were tested in a medium of both mineral oil and ester liquid, which should be a better representation of actual application, since an insulated wire would always have multiple thicknesses. The flat sheet samples were dried, impregnated with the test medium and then tested between unequal diameter electrodes of 25 mm and 75 mm, according to IEC 60243-1. During the rapid rise test, the 60 Hz voltage was raised linearly with time. The rise time was chosen in such a way that the breakdown occurred within 10 to 20 seconds after the start of the test. Each sample was cut to the same dimension of 300 mm x 300 mm, with five tests per sheet and a total of ten tests for each condition.

Table VI – Rapid Rise Breakdown in Mineral Oil

Number of Insulation Sheets Tested		1	3	4	5	10	Mean
Aramid New	Mean Breakdown Stress (kV/mm)	68,4	76,0	68,8	68,6	67,5	69,8
	Minimum Breakdown Stress (kV/mm)	48,0	70,9	66,1	64,9	62,4	
	Breakdown Stress Std Deviation (kV/mm)	9,2	3,1	2,5	2,7	2,9	4,0
	Number of Tests	10	10	10	10	10	
Aramid Original	Mean Breakdown Stress (kV/mm)	49,3	72,4	67,8	64,1	52,0	61,1
	Minimum Breakdown Stress (kV/mm)	39,7	69,6	64,7	60,3	48,9	
	Breakdown Stress Std Deviation (kV/mm)	5,6	1,7	1,6	3,1	1,7	2,7
	Number of Tests	10	10	10	10	10	

Table VII – Rapid Rise Breakdown in Synthetic Ester

Number of Insulation Sheets Tested		1	3	4	5	10	Mean
Aramid New	Mean Breakdown Stress (kV/mm)	64,3	77,8	72,8	70,7	76,4	72,4
	Minimum Breakdown Stress (kV/mm)	53,9	70,8	68,6	62,1	67,6	
	Breakdown Stress Std Deviation (kV/mm)	6,5	4,0	2,8	3,9	3,3	4,1
	Number of Tests	10	10	10	10	10	
Aramid Original	Mean Breakdown Stress (kV/mm)	63,1	75,0	69,2	66,8	69,7	68,8
	Minimum Breakdown Stress (kV/mm)	46,4	65,0	60,7	63,8	65,0	
	Breakdown Stress Std Deviation (kV/mm)	11,6	5,2	5,5	2,1	3,1	5,5
	Number of Tests	10	10	10	10	10	

### 2.2.3. Second Test Series – Impulse

For the impulse voltage tests, the flat sheet samples were dried, impregnated with the test medium and then tested between two 50 mm diameter flat electrodes. The voltage of successive sets is increased in magnitude until breakdown of the test specimen occurs, according to IEC 60243-3[4]. The standard wave shape is a 1,2 by 50  $\mu$ s wave, reaching peak voltage in approximately 1,2  $\mu$ s and decaying to 50% of peak voltage in approximately 50  $\mu$ s after the beginning of the wave. This wave is intended to simulate a lightning stroke that may strike a system without causing failure on the system. During these two test series, the test medium quality was monitored by periodically testing the dielectric strength and when necessary, the dielectric liquid was filtered and dried.

Table VIII – Impulse Breakdown in Mineral Oil

Number of Insulation Sheets Tested		1	3	4	5	10	Mean
Aramid New	Mean Breakdown Stress (kV/mm)	128,0	137,2	175,3	171,6	157,3	153,9
	Minimum Breakdown Stress (kV/mm)	115,9	130,0	157,1	160,4	148,5	
	Breakdown Stress Std Deviation (kV/mm)	8,3	5,4	9,8	7,8	6,7	7,6
	Number of Tests	9	6	10	10	10	
	Impulse Ratio	1,87	1,81	2,55	2,50	2,33	2,21
Aramid Original	Mean Breakdown Stress (kV/mm)	111,3	118,5	146,4	155,3	145,7	135,4
	Minimum Breakdown Stress (kV/mm)	82,1	102,5	124,6	140,0	132,7	
	Breakdown Stress Std Deviation (kV/mm)	20,7	8,4	12,2	10,8	7,5	11,9
	Number of Tests	9	10	8	10	10	
	Impulse Ratio	2,26	1,64	2,16	2,42	2,80	2,26

Table IX – Impulse Breakdown in Synthetic Ester

Number of Insulation Sheets Tested		1	3	4	5	10	Mean
Aramid New	Mean Breakdown Stress (kV/mm)	125,0	137,4	184,4	176,6	145,7	153,8
	Minimum Breakdown Stress (kV/mm)	103,9	126,0	168,0	168,2	137,8	
	Breakdown Stress Std Deviation (kV/mm)	12,7	5,6	10,8	6,6	4,5	8,1
	Number of Tests	10	9	10	10	10	
	Impulse Ratio	1,83	1,81	2,68	2,57	2,16	2,21
Aramid Original	Mean Breakdown Stress (kV/mm)	105,5	125,6	142,6	158,1	135,4	133,4
	Minimum Breakdown Stress (kV/mm)	84,6	99,9	115,0	140,4	123,5	
	Breakdown Stress Std Deviation (kV/mm)	13,6	11,1	14,6	9,5	6,2	11,0
	Number of Tests	10	10	10	10	10	
	Impulse Ratio	2,14	1,74	2,10	2,47	2,60	2,21

### 2.2.4. Third Test Series

The third series uses a special test setup first published by Prevost and Franchek[5]. The test series is designed to more closely simulate the wire-to-wire stresses of a power transformer winding and is the best representation of the three test series presented. The wire-to-wire tests were performed on wire wrapped with the new aramid wire insulation. The samples included wire wrapped with four different insulation builds. For the test, two straight sections of wire are cut to length and each end is formed to the shape of a Rogowski curve. The wires are then tested back-to-back. The specially shaped ends force the stress to the flat central region of the wire contact, reducing false breakdown in the oil wedge at each end. This test method is much more representative of actual transformer application than flat electrode testing and includes the mechanical stresses applied to the insulation during the wrapping process. The fixture is then submerged in a plastic container filled with the dielectric liquid. Figures 3 and 4 show photos of the test fixture.

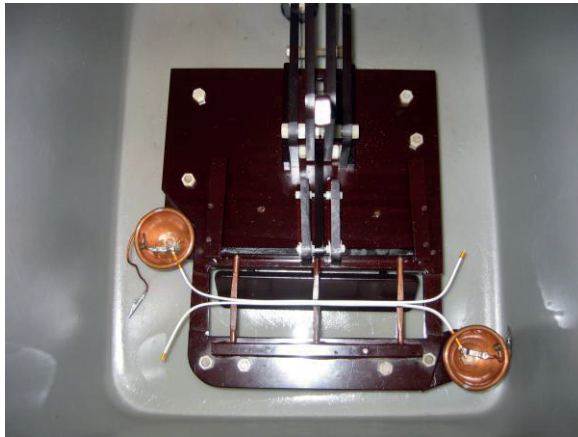


Figure 3 – Wire-to-Wire Test fixture

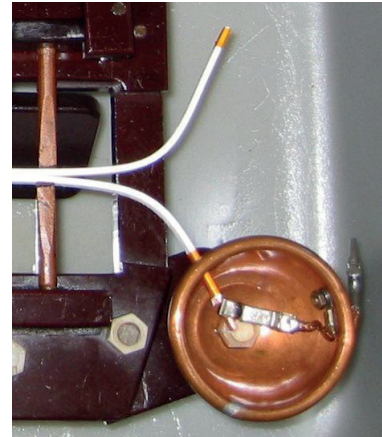


Figure 4 – Detail of Wire Shape

For this series, mineral oil was the dielectric liquid. The quality of the oil was monitored by periodically testing the dielectric strength and when necessary, the oil was filtered and dried. This type of test has been used over many years and the results of this test series are shown in Tables X and XI.

Table X – Rapid Rise Wire-to-Wire

Insulation Thickness (mm)	0,31	0,41	0,81	1,22	Mean
Mean Breakdown Stress (kV/mm)	62,3	59,0	47,5	42,3	52,8
Minimum Breakdown Stress (kV/mm)	53,5	56,1	43,2	39,8	
Breakdown Stress Std Deviation (kV/mm)	5,6	2,0	2,0	1,8	2,9
Number of Tests	17	14	14	15	

Table XI – Impulse Wire-to-Wire

Insulation Thickness (mm)	0,31	0,41	0,81	1,22	Mean
Mean Breakdown Stress (kV/mm)	145,0	142,4	122,7	110,4	130,1
Minimum Breakdown Stress (kV/mm)	131,0	124,2	114,7	103,0	
Breakdown Stress Std Deviation (kV/mm)	8,2	9,5	4,6	3,7	6,5
Number of Tests	13	14	14	15	
Impulse Ratio	2,33	2,41	2,58	2,61	2,48

### 2.2.5. Wire Wrap Insulation Data Analysis

In the first test series, the breakdown stress data in Table V suggests a clear improvement of the aramid over the kraft in dielectric strength, although several factors must be considered. Most importantly, this is only one of many readily available kraft papers and these products do vary in performance. The data set is also quite small and only marginally adequate. However, a comparison by Weibull plot is possible, since the test conditions were the same, which is one of the considerations for

using this comparison technique. The other main condition is to determine whether the data is a good fit to the Weibull distribution.

To test the adequacy of using the Weibull distribution model, IEC 62539 suggests determining the correlation coefficient for the data set and then checking to make sure this value is greater than the critical correlation coefficient taken from the graph in the document on goodness-of-fit for a two-parameter Weibull distribution. This correlation is a function of the number of specimens broken down.

The correlation coefficient,  $R^2$  equals 0,930 for the aramid paper and 0,964 for the kraft paper. This compares to a critical correlation coefficient value of 0,929 based on 14 samples. Accordingly, the fit is adequate, although only marginal for the aramid paper. The test then for comparison, as advocated in IEC 62539 is taken from Weibull who suggested that: “a useful hypothesis test is to examine whether there is overlap in the confidence limits at a given percentile and he suggested the 10th percentile for this purpose”.

The result is shown in Figure 5 with the region of interest circled in red. Note that while there is no overlap, the results are certainly not conclusive. Based on this test set, the two products are statistically different at the 10th percentile, but not by much. However, at the lower percentiles the performance of the two products is statistically not different, since the confidence limits overlap in this region. Although a comparison is generally made at the mean value, or in the case of a Weibull distribution, the scale at a probability percentile of 63,2, it is the lower percentiles well below 10 that define the working voltage stress capability of a material.

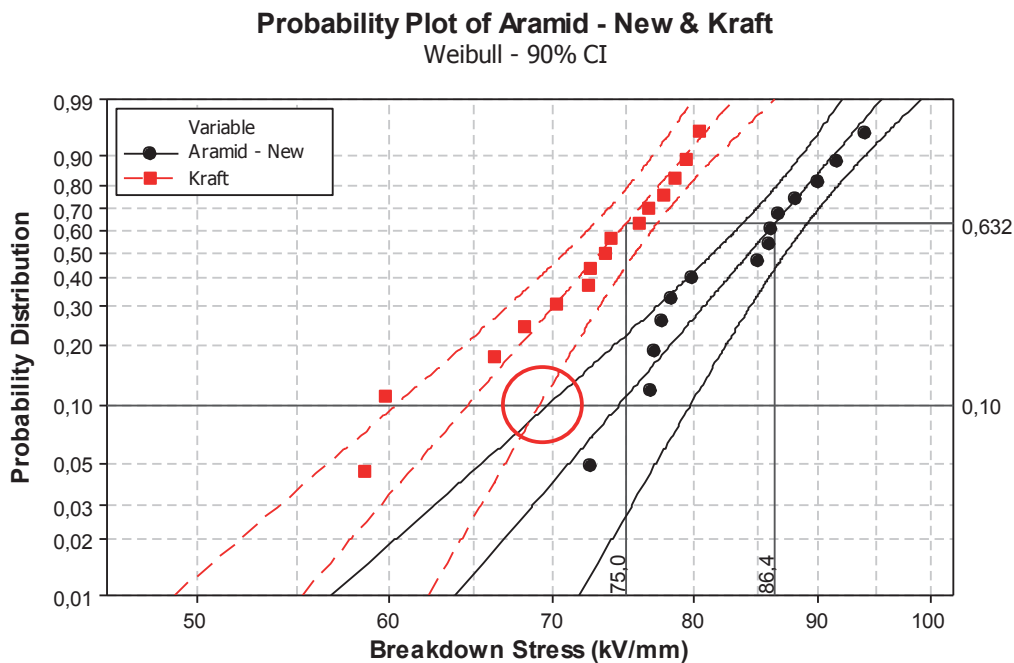


Figure 5 – Weibull Probability Plot Comparison

In the second test series, the mean value of the breakdown stress for all of the rapid rise tests is calculated for a given liquid and then the results for the new and original aramid papers are compared. The data does not fit the Weibull distribution model, but considering the standard deviation for the synthetic ester test, the results indicate the two products are not statistically different. For the mineral oil test, there is a difference, but it is small. The test series also indicates the difference in the liquid medium has no affect on the dielectric properties of the two products for the rapid rise test.

The same comparison is made for the impulse test results, except that the results are more conclusive than for the rapid rise test. While again, there is no difference in the dielectric strength due to the liquid test medium, there is a significant difference between the impulse breakdown stresses for the two products suggesting about a 15% improvement for the new aramid paper compared to the original paper. From this test series, the impulse ratio is determined by dividing the impulse test results by the rapid rise test results. The approximate 2,2 value is not very different from that of typical kraft paper and the commonly assumed value of 2,4.

Table XII compares the breakdown test results of the third test series to historical test results for the original aramid, the high-density textured aramid and the mean values of test results for kraft products from five different manufacturers. Again, the data sets do not adequately fit the Weibull distribution model, but a comparison of the mean rapid rise breakdown stress values with the standard deviation shows there is no statistical difference between the aramid products. However, the comparison indicates that all three aramid products show an improvement over the mean values of the five kraft products. This can be seen visually in Figure 6.

Table XII – Comparison of Historical Breakdown Test Data

	Rapid Rise		Impulse		Impulse Ratio
	Breakdown (kV/mm)	Std Dev (kV/mm)	Breakdown (kV/mm)	Std Dev (kV/mm)	
<b>Kraft</b>	40,1	2,3	89,3	8,4	2,25
<b>Aramid – Original (HDS)</b>	47,0	2,2	111	5,5	2,42
<b>Aramid (HDT)</b>	52,0	2,8	135	7,5	2,63
<b>Aramid - New</b>	52,8	2,9	130	6,5	2,48

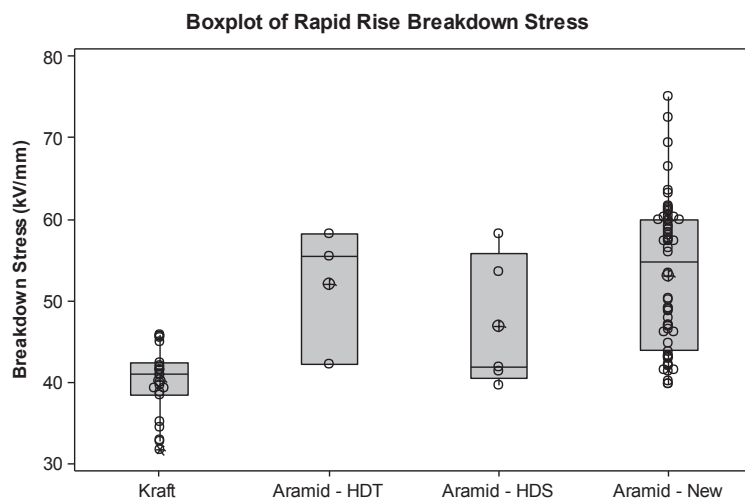


Figure 6 – Box Plot Comparing Rapid Rise Breakdown

Comparing the impulse breakdown stress of these same four products from Table XII indicates the new aramid paper is essentially equivalent to the high-density textured aramid. Both of these products are slightly better than the high-density smooth surfaced aramid paper. While all three aramid products show an improvement over the averaged five kraft products. The comparison is shown in Figure 7. In this series, the impulse ratio of the aramid papers is a bit higher than that of the kraft by about ten percent, but closer to the generally assumed value of 2,4.

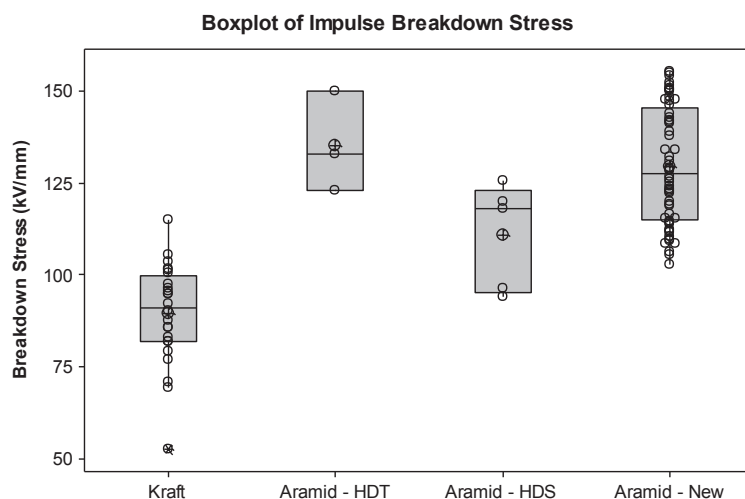


Figure 7 – Box Plot Comparing Impulse Breakdown

### 3. CONCLUSION

A number of conclusions may be drawn from this test program. For the layer type insulation, the three aramid families, differentiated by density and surface texture show a clear permittivity advantage, with values closer to the dielectric mediums of mineral oil or synthetic ester, compared to kraft paper. This advantage carries through to the wire insulation as well, again due partially to the lower density compared to the kraft paper. Contrary to conventional expectation, the medium density aramid papers compared very favorably in breakdown stress to the more widely used smooth surfaced, high-density products. However, the textured surfaced high-density aramid performed better than both of the other two aramid products.

The wire wrap insulation breakdown stress comparisons included impulse testing as well as rapid rise tests and the results were similar to the layer insulation comparisons. While there was little difference in the rapid rise test results, there was a noticeable improvement of the aramid papers compared to the kraft papers for impulse breakdown stress. Again, under impulse conditions, the textured surfaced aramid paper performed better than the other tested aramid and kraft papers. This testing also confirmed that the impulse ratio for the aramid products is similar to that of the kraft papers.

### REFERENCES

- [1] IEC 60243-1 Electric strength of insulating materials – Test methods – Part 1: Tests at power frequencies, January 1998
- [2] H. Moser, V. Dahinden, “Transformerboard II: Properties and Application of Transformerboard of Different Fibres”, second edition, EHV Weidmann, 1999
- [3] IEC 62539 Guide for the statistical analysis of electrical insulation breakdown data, July 2007
- [4] IEC 60243-3 Electric strength of insulating materials – Test methods – Part 3: Additional requirements for 1,2/50  $\mu$ s impulse tests, July 2001
- [5] T. Prevost, M. Franchek, “Conductor insulation tests in oil aramid vs. kraft”, IEEE Insulation Magazine, July/August 1989, page 10

Petar Gabrić  
Končar - Electrical Engineering Institute  
[pgabric@koncar-institut.hr](mailto:pgabric@koncar-institut.hr)

Antun Mikulecky  
Končar - Electrical Engineering Institute  
[amikul@koncar-institut.hr](mailto:amikul@koncar-institut.hr)

Maja Glavinić  
Končar - Electrical Engineering Institute  
[mglavinic@koncar-institut.hr](mailto:mglavinic@koncar-institut.hr)

Vladimir Podobnik  
Končar Power Transformers,  
A joint venture of Siemens and Končar  
[vladimir.podobnik@siemens.com](mailto:vladimir.podobnik@siemens.com)

## RESEARCH OF TRANSFORMER MAIN INSULATION DESIGN RULES

### SUMMARY

Kappeler research performed more than 50 years ago is widely used for HV transformers insulation design. Even though the original experiment was done for oil ducts width from 0.5 to 6 mm, the results have been extrapolated to ducts up to 100 and more mm without detailed publication that would confirm the validity of this extrapolation.

This paper presents the experiment that aims to expand Kappeler research to oil duct width up to 30 mm. Model setup also allows creepage and barriers effect testing up to 30 mm.

**Key words:** power transformer, insulation, electric field, partial discharges, insulation design

### 1. INTRODUCTION

Power transformer insulation consists of two main materials: paper and oil. These two materials have proven their reliability for HV transformer insulation for many decades. They can be used in transformer in various forms – from oil impregnated paper between electrodes (usually between winding turns) to oil impregnated paper in combination with oil gap (usually used for leads and many other application). A special combination of the least is a so called oil barrier insulation and it is used for insulation between windings and between windings and earthed parts in all oil immersed HV power transformers.

The essential fact for oil barrier insulation is that oil channels are divided with paper barriers with the aim of increasing their withstand voltage. Insulation should be designed in such manner that the ratio of permissible stress and obtained (calculated) stress in all channels is greater than a certain value. This ratio is well known as the safety factor or margin.

In spite of a very long and successful usage of oil and paper in oil-immersed transformers, the design of transformer insulation is still sort of an art because a well-proven and a widely accepted breakdown theory has not yet been found. Permissible dielectric strength of oil ducts is increased when oil duct width decreases. The following formula for permissible electric field is widely used:

$$E_p = Ax^{-b} \quad (1)$$

where:

$A$  and  $b$  are factors obtained by experiments  
 $x$  is the oil duct width along electric field line.

One of the widely used researches regarding the above-mentioned is [1], in transformer society well known as Kappeler research. This research was performed more than 50 years ago, and published in 1958. It deals with observation of gas bubbles in an oil gap between paper insulated electrodes that form nearly homogeneous AC electric field. Voltage exposure time was 3 min and the experiment was performed for degassed and gas (air) saturated oil. Oil distance range between electrodes was from 0.5 to 6 mm (Figure 1).

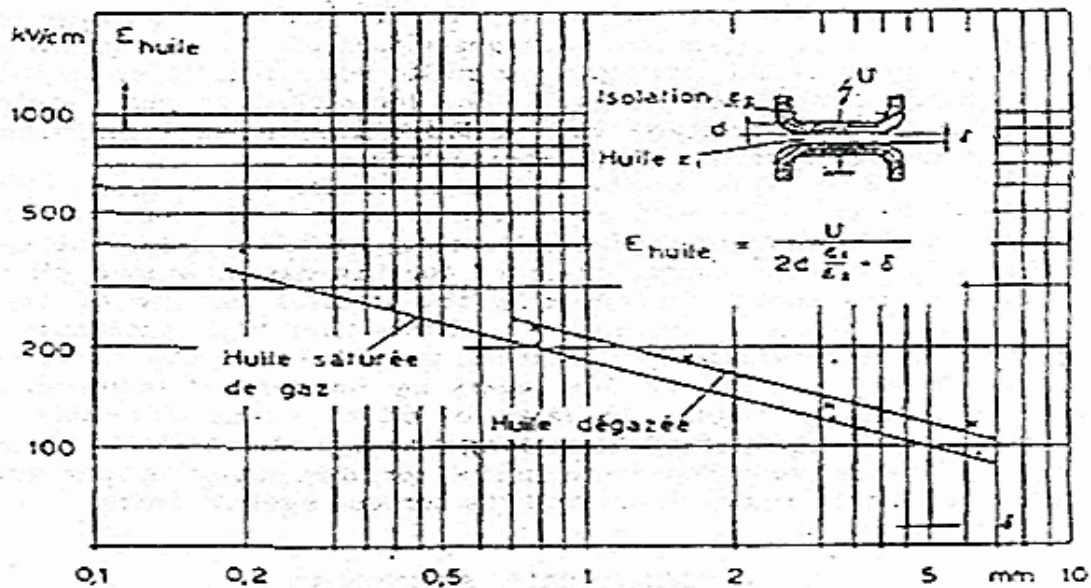


Figure 1. Kappeler research results

It is important to note that Kappeler research is extrapolated up to 100 and more mm and is used for oil ducts design in HV transformers. According to the authors' knowledge, validity of that extrapolation was not well published in literature. Also, Kappeler (or similar) results are used for paper - oil creepage design and some other very specific purposes in HV power transformer insulation [2].

Regarding the above mentioned, it has been decided to perform one of the most intriguing research in oil immersed transformer insulation design: estimation of oil ducts dielectric strength. This paper presents the experiment that will test Kappeler research but with enlarged oil ducts width up to 30 mm. Such oil distances need pretty complicated and large model setup arrangement that is PD free up to approx. 325 kV. Because of that electric field around electrodes is extensively studied.

Configuration of electrodes used in this research differs from the configuration that Kappeler used in his investigations. Voltage shape and PD measurement method are also not the same since Kappeler observed gas bubble appearance as a PD indication and in this research electric and acoustic methods are used. All the mentioned differences may result in certain discrepancies between the results of these two experiments. Besides testing Kappeler results the aim is to research barrier effect and spacers creepage strength as well. For this purpose several dozen of models will be manufactured in 16 different arrangements. Possible variations of models are:

- models without barrier and spacers
- models with spacers (without barrier)
- models with barrier and spacers (one and two barriers per model)

## 2. MODEL CONCEPT

Specially designed static end rings (similar to that widely used on HV transformer windings) are used as electrodes and placed in an insulating frame that allows changing of oil gap width using insulating screws. Inner diameter of electrodes used in model is about 450 mm and outer about 700 mm. Figure 2 shows the arrangement of electrodes in the model and Figure 3 shows the cross section of the model. Static rings were chosen for model electrodes because of various reasons: they are easy to produce in transformer factory, it is not difficult to obtain low tolerances, it is relatively easy to obtain near

homogeneous el. field and what is perhaps the most important they are used in the area of a transformer exposed to the highest electric stresses. Because of their simple cylindrical geometry it is easy to calculate el. field and to solve possible creepage stresses problems.

Model consists of two identical pair of electrodes, upper and lower static end rings. Each static end ring is split in two parts with a small gap between them. Such arrangement is used because it is easier to achieve better tolerances. This gap is also used for fastening of the rings to other insulating parts. Each static end ring is connected in two points with paper insulated copper rope which is used for grounding or voltage appliance (not shown on fig 2 and 3). Ring electrode is produced in a similar way as for transformer end rings with an exception – electrode overlap is not used.

Three groups of models will be produced as stated in the introduction. In models with barriers, spacers are used to assure the distance between both electrodes and between one or two barriers. Barriers will be placed horizontally between electrodes in the middle of oil gap, so tangential el field on the barrier will be negligible.

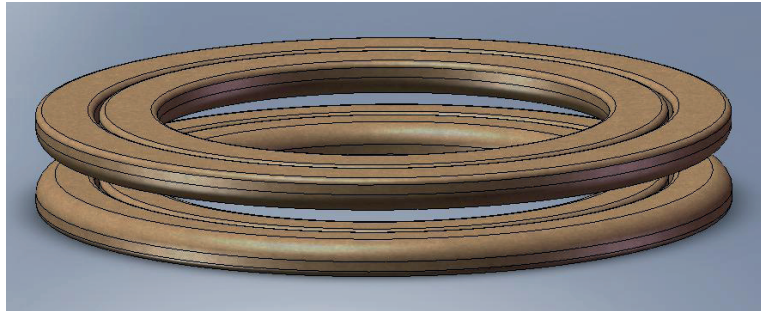


Figure 2. Arrangement of electrodes in the model

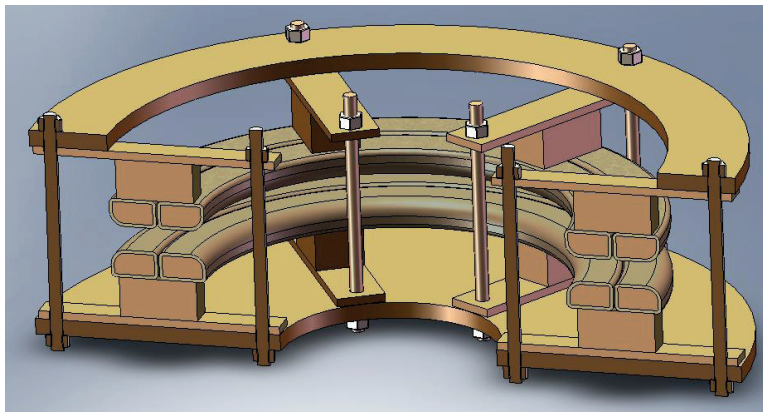


Figure 3. Model cross section

### 3. ELECTRIC FIELD CALCULATION

In order to achieve the lowest possible inhomogeneity factor, several electrode parameters have been analysed - paper insulation ( $d_{paper}$ ), radius of the ring body ( $r_2$ ) and the gap between the rings ( $d_{gap}$ ). Cross section of electrodes configuration is given in Figure 4.

Electric field inhomogeneity factor is calculated according to expression:

$$f_{in} = \frac{E_{max}}{E_{hom}} \quad (2)$$

where:

$E_{max}$  is maximal electric field in oil on oil-paper bound,

$E_{hom}$  is average magnitude of electric field in oil on oil- paper bound in the area where field is homogenous.

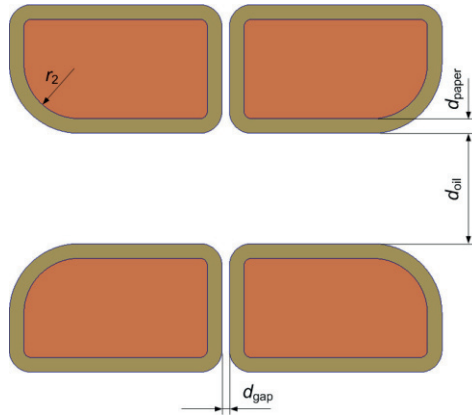


Figure 4. Cross section of electrodes configuration

Size of electrodes and paper thickness which result in the lowest inhomogeneity factor have been chosen. Procedure was based on several calculations of electric field (using FEM based software) for different electrode parameters and analysis of field inhomogeneity in oil. Obtained inhomogeneity is about 1,1 for oil distance of 30 mm. It decreases to 1 rapidly with the decrease of oil distance, so that for 15 mm inhomogeneity is about 1,02. Chosen insulation thickness, ring radiuses and the gap between the inner and outer ring remain the same for all the models. Models mutually differ in the gap between the upper and the lower rings, barriers and spacers (weather they have them or not). Electrical field has been calculated as cylindrical.

Field distribution for model without barriers and with a 30 mm gap between the rings is given in Figure 5. Shaded plot displays field magnitude and contour plot equipotential lines.

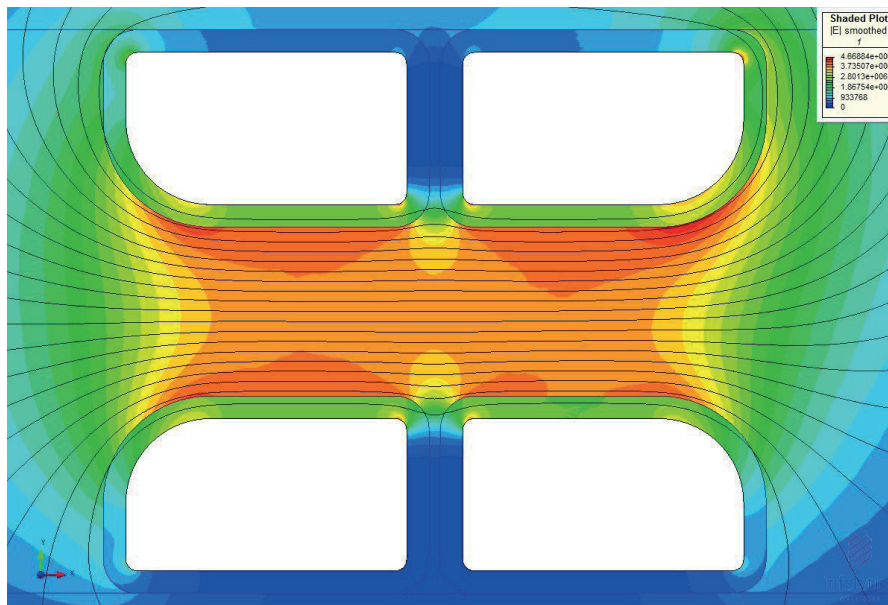


Figure 5. Electric field distribution

Figure 6 shows field lines in the gap between two outer rings along which safety margins have been calculated. Although they were calculated along 17 field lines, only few of them are shown in the figure. Safety margins have been obtained using cumulative method, [2], which means that they are defined as a ratio of permissible stress  $E_p(x)$  and actual average field  $\bar{E}(x)$  along the same field line.  $E_p(x)$  has been calculated according to (1). Minimum safety margin  $\sigma_{min}$  is the minimum value of the function  $\sigma(x)$ .

$$\sigma(x) = \frac{E_p(x)}{\bar{E}(x)} \quad (3)$$

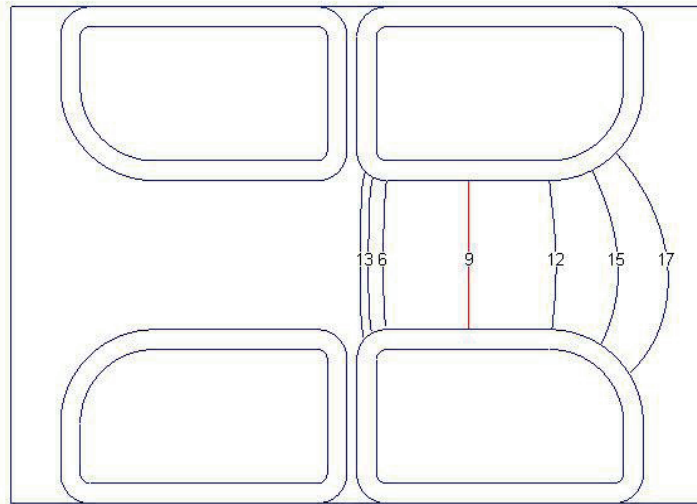


Figure 6. Field lines along which safety margins were calculated

Calculated safety margins for  $U = 213\ 216\ \text{kV}$  are given in Figure 7. Permissible stress is according to Kappeler research for degassed oil. Minimum safety margin has been obtained for field line no.9 and it's equal to minimum allowable value  $\sigma_{\min} = 1$ . It is worth while to notice that minimum safety margin does not lie on the field line which starts at the point of maximum el. field ( $E_{\max}$ ). This is a consequence of the applied cumulative method for safety factor calculation and it happens often in complex el. fields.

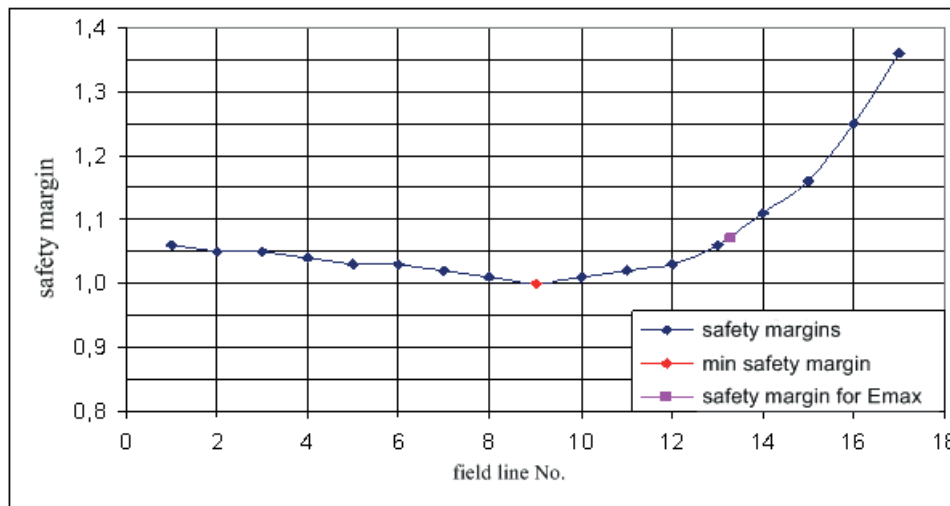


Figure 7. Safety margins along field lines 1-17 (Figure 6), calculated for  $U = 216\ \text{kV}$

#### 4. MODEL TESTING ARRANGEMENT AND PROCEDURE

Assembled models are vacuum dried in a drying oven at the temperature of about  $110\ ^\circ\text{C}$  for seven days. Duration of drying process depends on moisture content and is usually seven days. After the completion of the drying process, pressure in the oven should be below approx.  $0,5\ \text{mbar}$ . Dried models are finally checked, tightened, assembled with leads and placed in a testing vessel (volume cca  $2\ \text{m}^3$ ), and assembled with appropriate bushing, figure 8. In the next step, models are vacuum treated and impregnated with processed mineral oil. The final value of vacuum in a testing vessel after impregnation should be less than approx.  $0,2\ \text{mbar}$ . After impregnation, oil is processed once again with an oil processing plant to decrease the particle content. Before testing starts oil samples are taken for DGA, air content, humidity content, particle content measurements and BDV.



Figure 8. Model in a testing vessel, side view

Model is connected to AC voltage source using insulated leads and 245 kV bushing (Figure 9). Test voltage shape is a ramp in steps as shown in a Figure 10. Expected test voltages of all models are lower than 325 kV. The first voltage step should be approx. 60% of calculated withstand voltage. The increase of voltage per step should be about 3% of calculated withstand voltage. Each voltage step (T1) should last for 1 min.



Figure 9. Test arrangement

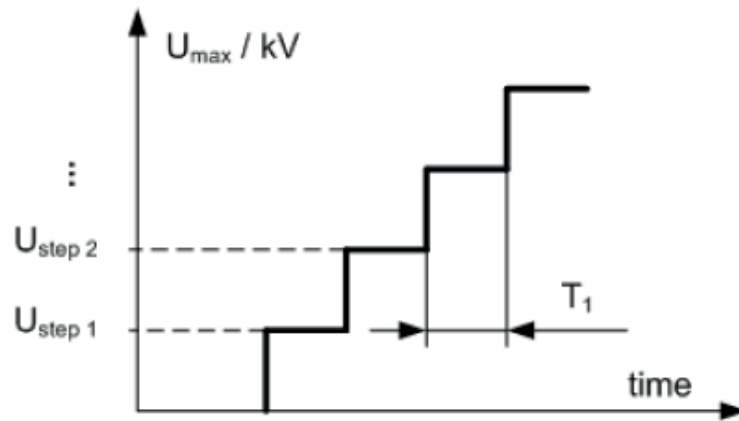


Figure 10. Test voltage shape

Voltage will be applied until PD starts and after that the model will be deenergized. Voltage must be decreased and switched off at the moment PDs are detected. If possible, each model should be tested 10 times. Time between subsequent tests of the same model should be at least 1 hour. PDs are measured using standard electric method and acoustic method. Sensitivity of the acoustic method might be a problem. In case of PD level which is too low, this method cannot be used. A serious problem could be in case of breakdown without PD inception. If this happens the number of models will be increased.

## 5. CONCLUSION

Paper explains some basic principles of HV transformer insulation design. Those principles originate from Kappeler research performed more than 50 years ago. Kappeler's results have been extrapolated and widely used in transformer society all over the world even though the validity of that extrapolation has not been properly published in literature. This paper presents the research that is meant to test the validity of Kappeler results and the validity of the extrapolation to larger oil ducts. Besides Kappeler results testing, the aim is to research barrier effect and crepage strength as well. The paper describes model arrangement and construction, electric field calculation as well as laboratory testing procedure.

## REFERENCES

- [1] H. Kappeler: Recent Forms of execution of 380 kV Transformer Bushing, CIGRE session in Paris, 4-14 June 1958.
- [2] W. Dahinden, K Shultz, A. K uchler: Function of Solid Insulation in Transformers, Transform 98, 20.-21. April 1998, Forum der Technik, M unchen

T. Judendorfer, R. Woschitz, M. Muhr  
Graz University of Technology  
Inffeldgasse 18, 8010 Graz  
Austria  
[thomas.judendorfer@tugraz.at](mailto:thomas.judendorfer@tugraz.at)

W. Exner, S. Jaufer  
WEIDMANN Electrical Technology AG  
Neue Jonastraße 60, 8640 Rapperswil  
Switzerland

## ELECTRICAL CONDUCTIVITY OF PRESSBOARD AND THE INFLUENCE OF MOISTURE CONTENT

### SUMMARY

The electrical conductivity  $\sigma$  is an important parameter for material condition evaluation at AC applications and is responsible for electrical field distribution in DC equipment. With a focus on HVDC equipment design, the influence of moisture content in oil-impregnated pressboard is determined in this preliminary investigation. The electrical conductivity of pressboard samples, which have been wetted artificially in the laboratory, is investigated within this work. Moisture contents between <0,3% and 5,5% could be achieved artificially through increasing pressboard moisture content levels in a climate chamber. The electrical conductivity was determined by voltage-current measurements at 20°C in the style of IEC 60093 with measurement times up to and longer than 24 hours. For these investigations, the pressboard samples with a thickness of 1 mm have been placed in an (mineral) oil-filled test vessel and stressed by a DC field with  $E = 3 \text{ kV/mm}$ .

It could be demonstrated that the moisture content of pressboard has a strong influence onto the electrical conductivity: An increase of electrical conductivity by a factor of around 10 for each percentage point of moisture increase up to moisture levels of around 3,5% was observed. At higher moisture contents (>5%), other mechanisms seem to govern the electrical current and the conductivity respectively, which is also discussed within the work.

**Key words:** Electrical conductivity, pressboard, moisture content, artificial moistening, HVDC equipment

### 1. INTRODUCTION

Electrical conductivity is an important parameter for insulating materials, especially at HVDC applications. At (steady-state) DC stress, the electrical field within an insulation system distributes according to the geometry and the different electrical conductivities of the materials used. Therefore, the electrical conductivities play an important role in terms of dielectric behavior of an insulation system.

At oil-cellulose insulation systems, which are commonly used at HVDC converter transformers, the electrical conductivities of oil and board can vary strongly. For example, at 20°C the electrical conductivity of pressboard can be around 10 to 100 times lower than the conductivity of typical mineral oils. During HVDC network operation, the insulation system of e.g. a converter transformer is severely stressed by AC and also through superimposed DC stress. In case of such a mixed electrical stress, the electrical field distribution is different from the one at pure AC stress, which is governed by the (relative)

permittivities only. Several factors are influencing the electrical conductivity. For example, there is a strong effect of temperature as well as moisture content, which is investigated here.

## 2. ELECTRICAL CONDUCTIVITY

The determination of electrical stress in HVDC equipment is more complex than at AC stress, as the electrical conductivity is the governing parameter in terms of field stress. The conductivity of typical high-voltage insulation materials can differ easily by one or even several orders of magnitude. Further, electrical conductivity depends on temperature, moisture content and field strength, as indicated by Figure 1 and 2. Currently, in measurement and simulation processes, electrical conductivity is often considered as a single value only; at best a field and temperature dependence will be considered. This could lead to the misjudgment of the real situation in an insulation system, which is also discussed in [1, 2] in detail. The main influencing parameters of the electrical conductivity of oil-impregnated paper (OIP) are described for example in [3].

Due to polarization and charging processes, Ohm's law cannot be applied directly at insulation oils and pressboard, as the resistivity varies with (measurement) time. In detail, knowledge about charge carrier density and mobility is needed for a theoretical approach [4].

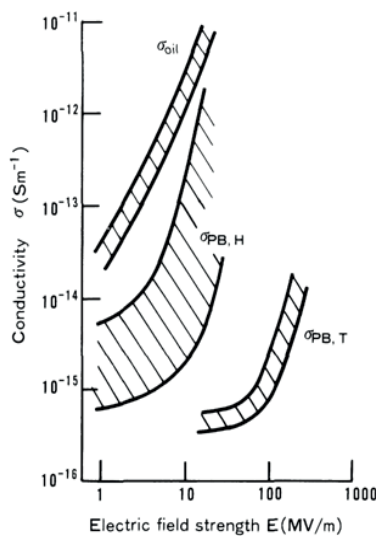


Figure 1 - Electrical conductivity of oil and pressboard (Index  $\tau$  – Conductivity through and  $H$  – Conductivity along laminated layers) [5]

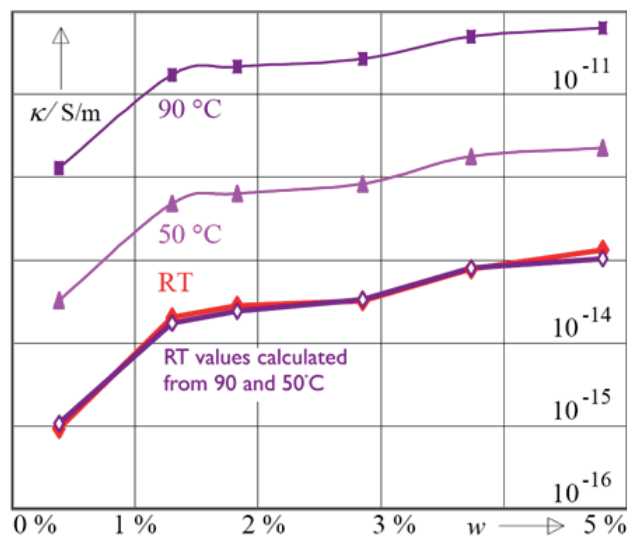


Figure 2 - Electrical conductivity of oil-impregnated paper (OIP) in variation of temperature and moisture content at  $E = 0,1$  kV/mm (from [6])

### 2.1. Determination of the electrical conductivity of solids

Guidelines for the determination of electrical conductivity determination of solid insulating materials can be found in the standard IEC 60093 [7]. A typical set-up consisting of three electrodes is pictured in Figure 3. A guard electrode is used for the elimination of surface currents. However, standards like this one are criticized (see exemplary [2, 8]) when it comes to HVDC applications. Basically, this is due to two reasons: First, present standards only determine a single conductivity value without considering polarisation and charging processes. Furthermore, this single value is determined already 1 minute after voltage application. Secondly, the field strength used for measurement purposes is generally much less than the actual operational field strength. Both drawbacks may lead to strong discrepancy between material measurement data and actual behaviour. Possible remedies are the determination of the time trend at higher field strengths and even the usage of a different method, e.g. charge-difference method (CDM) [8].

When using the voltage-current method, the specific resistivity can be determined from measuring the time trend of the current when applying a (constant) direct voltage:

$$\rho = R_x \cdot \frac{A}{h} \quad (1)$$

where:

$\rho$	Specific Resistivity [ $\Omega\text{m}$ ]
$R_x$	Measured Resistivity [ $\Omega$ ]
$A$	Area of measurement electrode [ $\text{m}^2$ ]
$h$	(averaged) Sample thickness [m]

For the determination of the (effective) measurement electrode surface area, the method described in [7] is used. In literature, different approaches are documented, which take e.g. flux fringing into account [9]. However, at comparable thin samples (in reference to the diameter), the influence of such methods and processes respectively is low [10]. Resistivity was determined for every data sample (sampling rate of around 1 Hz) through voltage-current measurements. The electrical conductivity  $\sigma$  is then determined as the inverse of the specific resistivity  $\rho$ .

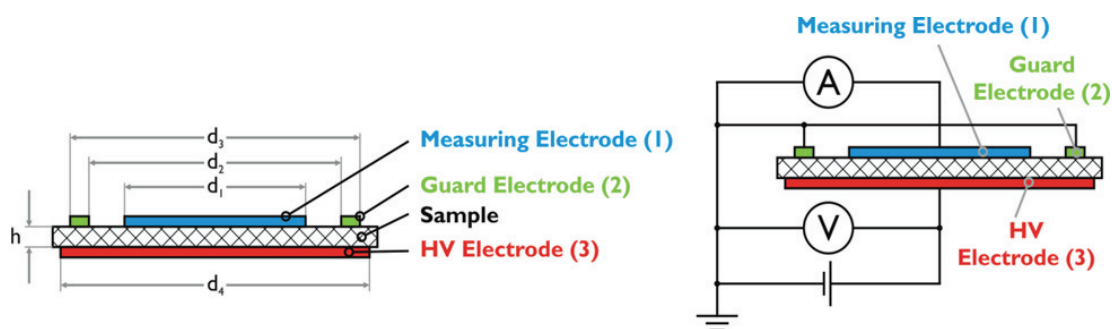


Figure 3 - Schematic set-up for the determination of electrical conductivity according to IEC 60093

### 3. PARAMETERS INFLUENCING THE ELECTRICAL CONDUCTIVITY OF PRESSBOARD

Selected parameters (besides moisture content) for pressboard are discussed briefly below. More details can be found, for example, in [10].

#### 3.1. Temperature

Temperature constitutes one of the strongest influences onto the electrical conductivity. With rising temperature, conductivity increases and time constants decrease. A conversion of measurement data to temperatures, which differ from the temperature during measurements, is possible with the Arrhenius equation. In [6] this is conducted exemplary for steady-state conductivity values of 50 and 90°C to estimate the conductivity values at 20°C (see also Figure 2).

#### 3.2. Electrical field strength

As indicated in Figure 1, there is a strong nonlinear behavior of the electrical conductivity of pressboard at higher field strengths somewhere in the region of  $E = 100 \text{ MV/m}$  (when measured through the bulk of the material). At lower field strengths, the influence is negligible (e.g. see [10]). However, if the conductivity along laminated layers is studied, a nonlinear behavior can be observed also at much lower field strengths [5]. There, interfacial effects dominate the conduction process which leads to an increased conductivity when compared to bulk conductivity, as seen in Figure 1. For thin samples, the electrical conductivity through the bulk is quite independent of electrical field strength [8, 10].

#### 3.3. Other parameters

Other parameters, like material ageing, acid content or impregnation oil type may also influence the electrical conductivity. An increase of electrical conductivity with ageing is very plausible, as with

progressive ageing the moisture content of both oil and cellulose rises due to degradation processes. Furthermore, ageing by-products like acids might be generated, which also influence (rise) the electrical conductivity respectively. The influence of ageing and impregnation oil type for pressboard is discussed in [10] and for OIP in [3].

#### 4. MEASUREMENT SET-UP AND PROCEDURE

High density pressboard samples (Type B3.1 [11], with sieve structure) with a diameter of 190 mm and a thickness of 1 mm have been used for this investigation.

##### 4.1. Sample preparation and artificial moistening

Pressboard samples have been dried and impregnated with a mineral oil ( $\sigma_{oil}$  around  $10^{-14}$  S/m at  $20^{\circ}\text{C}$ ,  $E = 1$  kV/mm) prior usage. The pressboard discs have been dried in a thermal oven at  $105^{\circ}\text{C}$  for more than 48 hours. Afterwards, they have been transferred into a vacuum oven. There they have been dried further (at a pressure  $<1$  mbar) at  $105^{\circ}\text{C}$  for at least 24 hours. Then the temperature was reduced to  $90^{\circ}\text{C}$  for the following impregnation process (in the style of [12]). Samples have been kept oil-immersed under vacuum for another 24 hours. This leads to good impregnated and dried samples with moisture contents of  $<0,3\%$  and a degree of polymerization (DP) of around 1.200 [10].

Samples prepared in such a manner have been artificially wetted in a climate chamber subsequently. They were kept in a controlled environment with  $40^{\circ}\text{C}$  and at 70% relative humidity. A residence time of around 1 hour was necessary for each percentage point increase of moisture content. This was controlled regularly with Karl-Fischer-Titration (oven method) through the whole process.

However, most of the moisture is assumed to be at or very near the pressboard surface. This can be observed also visually, as pictured in Figure 4: The left picture shows a new and processed sample series (with a moisture content  $<0,3\%$ ) directly after removing them from aluminum compound foil. After around 1 h residence time within the climate chamber, a thin moisture film and a slight change in color was noticed, as seen in the figure below.



Figure 4 - Samples before insertion into climate chamber and after wetting process right before removal

##### 4.2. Test set-up

Within this work, a customized set-up in the style of IEC 60093 [7] (see Figure 3 and Figure 5) was utilized to determine the electrical conductivity of pressboard. A stabilized voltage source with a very low ripple was used to supply a constant voltage of  $U = 3$  kV. At the investigated samples ( $h = 1$  mm), this leads to a field strength of  $E = 3$  kV/mm. Stainless steel electrodes ( $\varnothing_{HV} = 170$  mm,  $\varnothing_{Meas.} = 147$  mm,

gap of 1,5 mm) have been used, as well as an additional weight (stainless steel, 1,4 kg). This totals with the electrodes and the spacer in a weight of 7,8 kg and a pressure on the sample of  $>0,2 \text{ N/cm}^2$ , which is recommended in [13].

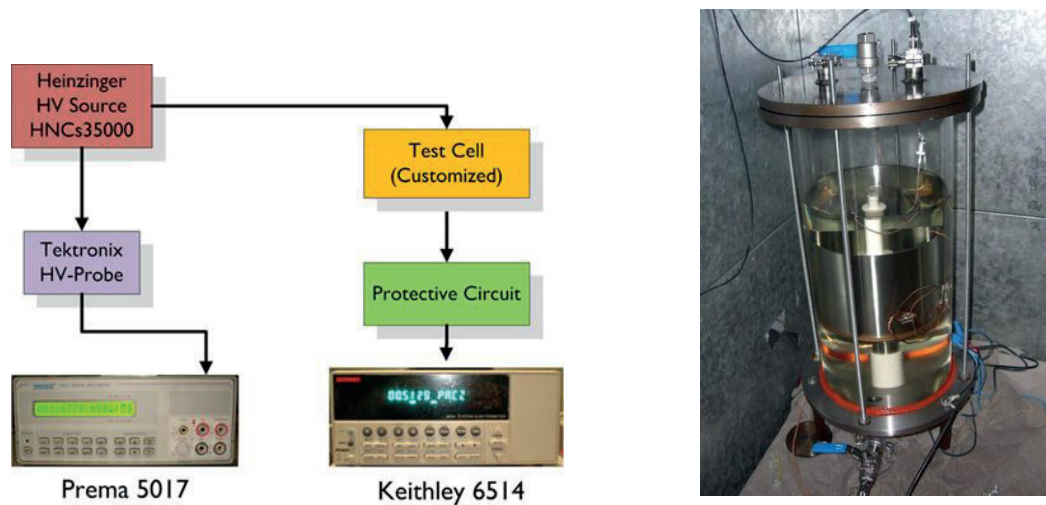


Figure 5 - Measurement schematic and actual set-up

### 4.3. Data processing

The determination of electrical conductivity of artificially wetted samples was conducted - with one exception (only one sample at 2,3%) – for at least 3 independent samples. The herein presented results are averaged values of these single measurements. The raw current (and voltage) measurement data has been checked for outliers, e.g. due to measurement range changes of the electrometer or caused by external disturbances, before applying a moving average filter. Especially due to long measurement times and when operating at such low currents (pA range), averaging is an elegant possibility to reconstruct the (average) time trend.

## 5. RESULTS

The influence of moisture content onto electrical conductivity of pressboard is clearly shown in Figure 6. With the exception of the very wet samples (5,5%), the electrical conductivity decreases steadily during the measurement time interval. The slope of the current ( $di/dt$ ) and conductivity ( $d\sigma/dt$ ) respectively is decreasing with increasing moisture content. This implicates that polarization processes proceed faster and the steady state value is reached sooner.

The results are summarized in Table I. There, the values in the column “n” denote the number of single measurements made on individual samples to determine electrical conductivity. It can be seen, that the increase of electrical conductivity during the measurement time range is between a factor of 3,7 and around 13 for each increase in moisture content by 1 percentage point. Basically, these results are in good agreement with results reported in literature, for example in [3], which have been gained at OIP and pressboard samples.

An unexpected behavior was observed at the samples with very high moisture content (5,5%): The current and the electrical conductivity actually increased after voltage application. This indicates that no charge carrier depletion is taking place but instead conductive paths in the bulk (or more probably near the surface) are formed. Dielectric heating as the source for the increase of current and conductivity respectively can be ruled out, as the converted power is very low (around 1 mW, [10]).

Generally, the reproducibility of the conductivity measurements is good, as Figure 7 indicates. The differences in electrical conductivity between the investigated moisture contents are large enough to allow the secure determination at each level.

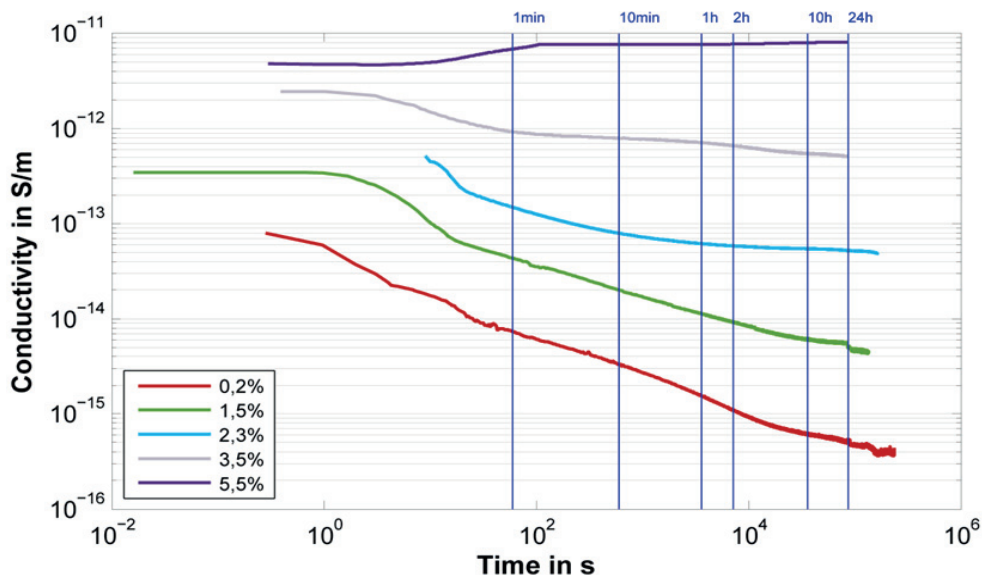


Figure 6 - Electrical conductivity of investigated pressboard samples with varied moisture content (artificially wetted), determined in the style of IEC 60093 with  $E = 3 \text{ kV/mm}$

Table I - Average electrical conductivity  $\sigma$  of  $n$  pressboard samples with varied moisture content in S/m

Moisture	n	1 min	10 min	1 h	2 h	10 h	24 h
0,2%	3	7,31E-15	3,33E-15	1,53E-15	1,10E-15	6,04E-16	5,23E-16
1,5%	7	4,37E-14	2,01E-14	1,14E-14	9,22E-15	6,12E-15	4,96E-15
2,3%	1	1,49E-13	7,90E-14	6,19E-14	5,84E-14	5,45E-14	5,20E-14
3,5%	3	9,31E-13	7,92E-13	7,11E-13	6,57E-13	5,45E-13	5,09E-13
5,5%	3	6,85E-12	7,69E-12	7,67E-12	7,71E-12	7,98E-12	8,08E-12

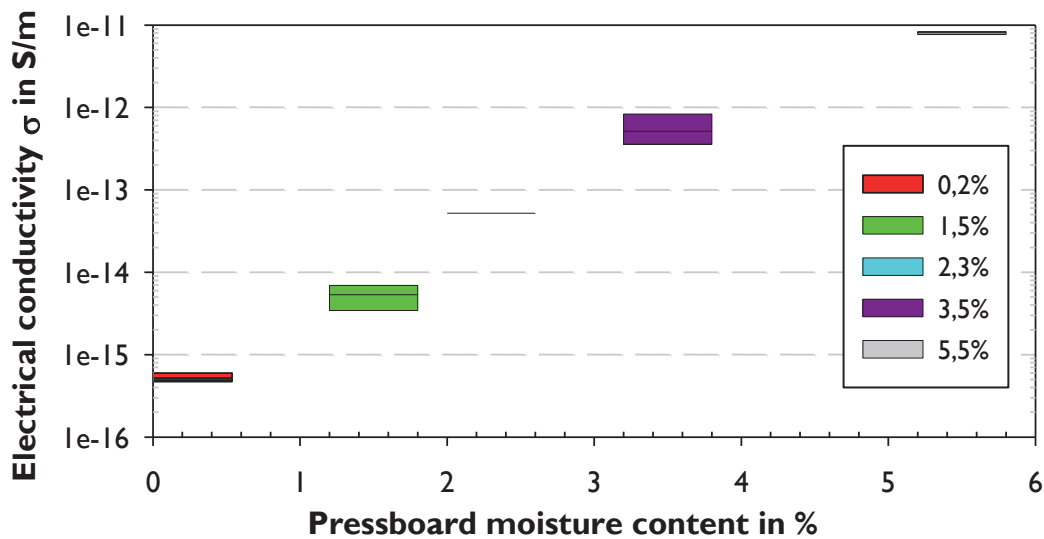


Figure 7 - End values of determined electrical conductivity of pressboard with varied moisture content

## 6. CONCLUSION

Moisture content of pressboard has significant influence on the electrical conductivity as demonstrated at the investigated samples. However, these results may only serve as a basis for further research: Due to the comparable short residence times of the pressboard samples within the climate chamber, most of the moisture is concentrated onto or near the surfaces. Diffusion processes have much larger time constants - therefore it is very likely that a moisture gradient inside the samples existed with reduced local moisture content with increasing sample thickness/depth. A different procedure with an improved set-up with a stabilized supply of air, which has a defined moisture content, over several hours or even days is necessary to achieve a homogeneous moisture penetration.

For moisture determination however no difference is expected, as the Karl-Fischer-Titration (oven method) is always an integrative method and therefore an averaged moisture content of a volume is determined. In terms of electrical conductivity an inhomogeneous moisture distribution might have an influence though.

The large spread of electrical conductivity of oil and pressboard and insulation paper respectively is troublesome in terms of electrical field distribution at HVDC equipment. With typical ratios of around 10 to 100 between pressboard and oil, the former gets stressed much more severe by the same factor. Now, if the moisture content of pressboard is slightly increased, say in the range between 1 to <2% and when using a very low conducting oil, the electrical field distribution is homogenized between oil and board/paper. In that sense, some kind of field grading is possible if moisture levels can be controlled. However, the long-term stability of such a distribution is questionable, as it might change with ageing processes.

## REFERENCES

- [1] M. Liebschner, "Interaktion von Ölspalten und fester Isolation in HVDC-Barriersystemen," Dissertation, TU Ilmenau, 139 pages, 2009.
- [2] U. Piovan and G. Schenk, "Effects of variability of mineral oil electrical conductivity on reliability of HVDC converter transformers," *Trafotech, 8th International Conference*, 2010.
- [3] A. Küchler, F. Hüllmandel, K. Böhm, M. Liebschner, C. Krause and B. Heinrich, "Parameters determining the dielectric properties of oil impregnated pressboard and presspaper in AC and DC power transformer applications," *ISH 07 International Symposium on High Voltage Engineering*, 2007.
- [4] K. C. Kao, *Dielectric Phenomena in Solids: With Emphasis on Physical Concepts of Electronic Processes*. San Diego, California: Elsevier Academic Press, 2004.
- [5] A. Kurita, E. Takahasi, J. Ozawa, M. Watanabe and K. Okuyana, "DC Flashover Voltage Characteristics and Their Calculation Method for Oil-Immersed Insulation Systems in HVDC Transformers," *Power Delivery, IEEE Transactions on*, vol. 1, pp. 184-190, 1986.
- [6] A. Küchler, F. Hüllmandel, K. Böhm, N. Koch, P. Brupbacher and C. Krause, "Das dielektrische Verhalten von Öl-Papier-Isolationen unter der Wirkung von Grenzflächen-, Material- und Prüfparametern," *ETG-Fachtagung „Grenzflächen in elektrischen Isoliertsystemen“*, 2005.
- [7] International Electrotechnical Commission, *IEC 60093: Methods of Test for Volume Resistivity and Surface Resistivity of Solid Electrical Insulating Materials*. Geneva: 1980.
- [8] A. Küchler, M. Liebschner, A. Reumann, C. Krause, U. Piovan, B. Heinrich, R. Fritsche, J. Hoppe, A. Langens and J. Titze, "Evaluation of Conductivities and Dielectric Properties for Highly Stressed HVDC Insulating Materials," *CIGRÉ Session 2010, Paper D1-106-2010*, 2010.
- [9] R. Bartnikas, Ed., *Engineering Dielectrics Volume IIB: Electrical Properties of Solid Insulating Materials: Measurement Techniques*. Philadelphia: ASTM, 1987.
- [10] T. Judendorfer, "Oil-cellulose insulation systems for HVDC application," Dissertation, TU Graz, unpublished.
- [11] Verband der Elektrotechnik, Elektronik und Informationstechnik, *VDE 0315-3-1: Tafel- Und Rollenpressspan Für Elektrotechnische Anwendungen - Teil 3: Bestimmungen Für Einzelne Werkstoffe - Blatt 1: Anforderungen Für Tafelpressspan, Typen B.0.1, B.0.3, B.2.1, B.2.3, B.3.1, B.4.1, B.4.3, B.5.1, B.5.3 Und B.6.1*. Berlin: 2009.

- [12] Verband der Elektrotechnik, Elektronik und Informationstechnik, *VDE 0315-2: Tafel- Und Rollenpressspan Für Elektrotechnische Anwendungen - Teil 2: Prüfverfahren (IEC 60641-2:2004)*. Berlin: 2005.
- [13] Verband der Elektrotechnik, Elektronik und Informationstechnik, *VDE 0303-3/05-83: Prüfung Von Werkstoffen Für Die Elektrotechnik: Messung des elektrischen Widerstandes von nichtmetalenen Werkstoffen (Zurückgezogen 1993-12)*. Berlin: 1983.

**Acknowledgements:** The authors would like to express their thanks to C. Bonini for his contribution to this work.

Anđela Hadži-Skerlev  
Končar- Electrical Engineering Institute  
[andjela@koncar-institut.hr](mailto:andjela@koncar-institut.hr)

Dijana Vrsaljko  
Končar- Electrical Engineering Institute  
[dvsaljko@koncar-institut.hr](mailto:dvsaljko@koncar-institut.hr)

Veronika Haramija  
Končar- Electrical Engineering Institute  
[veronika@koncar-institut.hr](mailto:veronika@koncar-institut.hr)

Božena Musulin  
Končar- Electrical Engineering Institute  
[bmusulin@koncar-institut.hr](mailto:bmusulin@koncar-institut.hr)

## CARBON MONOXIDE AND CARBON DIOXIDE IN CLOSED-TYPE POWER TRANSFORMERS

### SUMMARY

Gases carbon monoxide (CO) and carbon dioxide (CO<sub>2</sub>) are formed in transformers in larger quantities as a product of degradation of cellulose, than by oxidation of oil.

In transformers with closed-type breathing system, without any indication of failure or fault, it was observed that the concentrations of CO are higher than the typical values according to IEC 60599 and CO<sub>2</sub>/CO ratios lower than 3 frequently have been found.

This paper presents results of laboratory investigation of some influence parameters on formation gases CO and CO<sub>2</sub>.

The typical values for CO as well scheme concerning their ratios need to be revised in standard IEC 60599. The criteria need to be established separately for closed type transformers.

**Key words:** carbon monoxide, carbon dioxide, cellulose, mineral oil

### 1. INTRODUCTION

Thermal and electrical overstresses in power transformers decompose insulating materials oil and paper and generate gases, which dissolve in the oil. Characteristic gases are: hydrogen, methane, ethane, ethylene, acetylene, carbon monoxide (CO), carbon dioxide (CO<sub>2</sub>). They are determined by the standardized laboratory method, gas chromatography analysis of the gases dissolved in oil [1]. Based on their quantity and ratio, the condition of transformer insulation system is estimated.

The gases carbon monoxide (CO) and carbon dioxide (CO<sub>2</sub>) are formed in large amounts as a product of cellulose degradation processes, depending strongly on temperature, water and oxygen contents. The polymeric chains of cellulosic (paper) insulation are thermally less stable than the hydrocarbon bonds in oil, and are therefore decomposed at lower temperature.

Apart from that, carbon gases are formed in a transformer in lesser amounts as a product of oil degradation. In some cases carbon gases can be formed as a degradation product of some other organic materials (paints, rubber, plastic materials, glues etc.).

In transformers with closed-type breathing system oxygen content in oil is lower than in air saturated oil. It means that at the same temperature more carbon monoxide will be produced and

concentration will grow faster than in oil in open-breathing system transformers, because the membrane does not allow the release of produced gases to air.

According to IEC interpretation [2] of DGA, the assumed initial transformer failure is diagnosed primarily on the basis of the given hydrogen to hydrocarbon ratios. CO and CO<sub>2</sub> are auxiliary indicators for the condition of cellulose insulation, and the CO<sub>2</sub>/CO ratios between 3 and 10 are considered to be typical for normal cellulose degradation.

IEC 60599, Table A2 specifies the range of 90% typical CO and CO<sub>2</sub> concentration values observed in power transformers, from about 25 electrical networks worldwide and including more than 20000 transformers. Typical values apply to both open-breathing and hermetically sealed (close-type) transformers. Typical concentrations should be primarily considered as initial guidelines for diagnosis of transformer condition when no other experience is available.

It is recommended that the 90% typical values should be used only for orientation, in the case if there are no data of one's own.

Permanently increased concentrations of CO and CO<sub>2</sub>, although not accompanied by increased contents of other gaseous products of oil degradation, can cause concern to transformer users, because they interpret such data solely as a result of accelerated cellulose degradation – what means a shortening of transformer life.

The condition of 26 closed-type power transformers installed in Croatia, with 1-10 years of service without any registered stress or fault inception (“healthy transformers”) was investigated.

Laboratory tests were carried out to determine the impact of materials (oil and paper) as well content of residual air on the development of CO and CO<sub>2</sub> gases in closed-type power transformers.

## 2. FORMATION OF CO AND CO<sub>2</sub>

Gases are the first products of the insulating oil and paper materials (cellulose) degradation in normal aging of insulating system as well as in rapid degradation due to increased electrical and thermal stresses.

Mineral insulating oils are made of a blend of different hydrocarbon molecules containing CH<sub>3</sub>, CH<sub>2</sub> and CH chemical groups linked together by carbon-carbon molecular bonds. Scission of some of the C-H and C-C bonds may occur as a result of electrical and thermal faults, with the formation of small unstable fragments, in radical or ionic forms which recombine, through complex reactions, into gas molecules such as hydrogen (H<sub>2</sub>), methane (CH<sub>4</sub>), ethane (C<sub>2</sub>H<sub>6</sub>), ethylene (C<sub>2</sub>H<sub>4</sub>), acetylene (C<sub>2</sub>H<sub>2</sub>), carbon monoxide (CO) and carbon dioxide (CO<sub>2</sub>). Formed gases dissolve in oil and distribute throughout the oil volume by circulation and diffusion.

Solid insulation in electrical equipment is largely made of cellulose in the form of electrotechnical paper (Kraft paper) and pressboard. The polymeric chains of solid cellulosic insulation contains a large number of anhydroglucose rings, and weak C-O molecular bonds and glycosidic bonds which are thermally less stable than the hydrocarbon bonds in mineral oil, and which decompose at lower temperatures. Significant polymer chain scission occurs at temperatures higher than 105 °C, with complete decomposition and carbonization above 300 °C. Carbon monoxide and dioxide as well as water are the final products of cellulose degradation. Furanic compounds are intermediary products of cellulose degradation, they can be analysed according to IEC 61198 [3] and used to confirm cellulose degradation.

In individual power transformers, CO and CO<sub>2</sub> concentrations can be permanently or temporarily increased depending on various possible parameters:

- influence of design (air- breathing or closed–type transformers, mass ratio oil/cellulose, winding design, cooling system),
- influence of mineral oil and solid insulation quality,
- influence of processing (bad removal of moisture and oxygen in factory, moisture ingress at surface of oil immersed cellulose during assembling of bushings, absorption of air during shipment and bad removal during evacuation in the field due to “oil corks” which do not dissolve at low temperatures),
- influence of transformer loading (operating temperatures)

It is important to take into account all these variables when determining the origin and cause of content increase of these gases.

The rate of CO and CO<sub>2</sub> generation is exponentially dependent on temperature, and directly on volume of the material.

### 3. CLOSED-TYPE POWER TRANSFORMERS INSTALLED IN CROATIA

Analysis of the condition of 26 closed-type power transformers installed in Croatia was made and presented separately for 5 closed-type generator transformers and 21 closed-type transmission transformers.

#### 3.1. Generator transformers

These 5 generator transformers are located in Hydro Plants, in service from 5 to 10 years, and normally run at 100 % load except when the power station is shut down. The results of the latest dissolved gas analysis for closed-type generator transformers are shown in the table I.

Table I - Gas values,  $\mu\text{L/L}$  (ppm) and ratio CO<sub>2</sub>/CO for generator transformers

GAS, $\mu\text{L/L}$ (ppm)	Rate of transformer / Type of cooling / Year of service				
	1. 245 kV OFAF 2007.	2. 123 kV ONAF 2006.	3. 123 kV ONAF 2004.	4. 123 kV ONAF 2004.	5. 123 kV ONAF 2000.
Hydrogen, H <sub>2</sub>	6	6	3	3	3
Methane, CH <sub>4</sub>	15	11	10	10	10
Acetylene, C <sub>2</sub> H <sub>2</sub>	0	0	0	0	0
Ethylene, C <sub>2</sub> H <sub>4</sub>	1	0	0	0	0
Ethane, C <sub>2</sub> H <sub>6</sub>	2	0	0	0	0
CO	824	1307	716	1046	871
CO <sub>2</sub>	1637	2942	3462	3422	3878
Ratio CO <sub>2</sub> /CO	2.0	2.2	4.8	3.2	4.4
Oxygen	9592	12581	5808	6497	5359
Nitrogen	45365	69544	28573	35817	25427

Graphical presentation of the CO gas formation in closed-type generator transformers during their normal operation is given in figure 1.

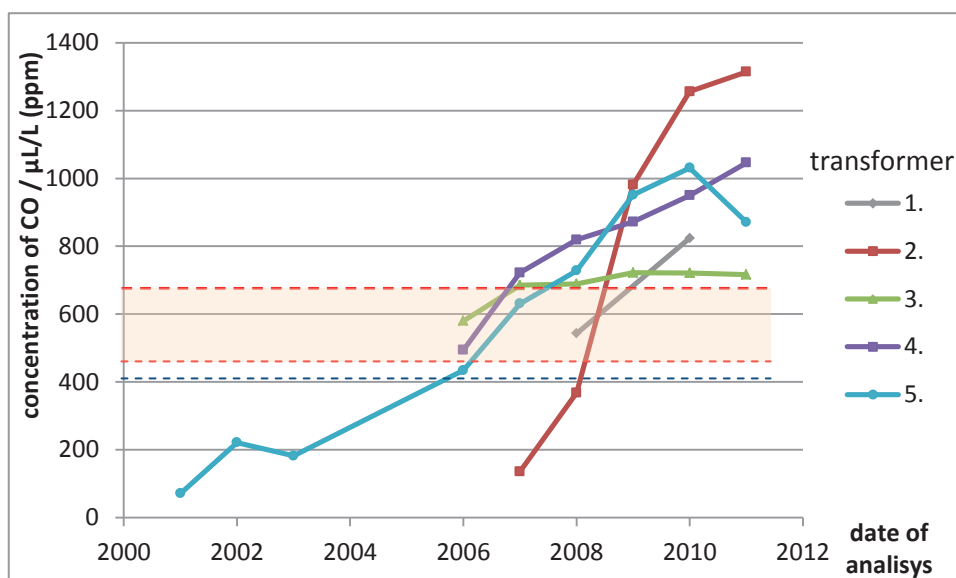


Figure 1 - Formation of CO in closed-type generator transformers

In all five generator transformers, already after 1-4 years of operation, CO gas concentration is significantly higher than the range of normal values given in IEC 60599 Tbl. A2 (400 - 600  $\mu\text{L/L}$ ) and the normal values according to the IEEE Std C57.104 Tbl. 1 (350  $\mu\text{L/L}$ ).

Graphical presentation of the CO<sub>2</sub> gas formation in closed-type generator transformers during their normal operation is given in figure 2.

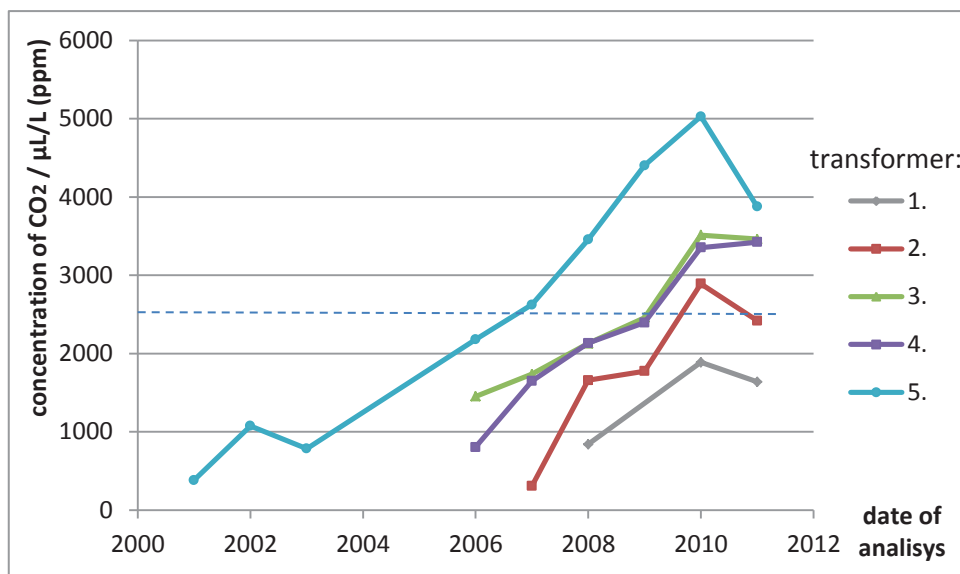


Figure 2 - Formation of CO<sub>2</sub> in closed-type generator transformers

At all generator transformers the value of CO<sub>2</sub> concentration is within the normal range according to IEC 60599 Tbl. A2 (3800 -14 000  $\mu\text{L/L}$ ), while the normal value of CO<sub>2</sub> by the IEEE Std C57.104 Tbl. 1 (2500  $\mu\text{L/L}$ ) is exceeded after approximately 5 years of normal operation.

The measured water content in the oil for all generator transformers is lower than 10 mg/kg.

### 3.2. Closed-type transmission transformers

These 21 closed-type transmission transformers are in operation from 1-10 years and normally loaded. The range of characteristic gas values,  $\mu\text{L/L}$  (ppm) and ratio CO<sub>2</sub>/CO for transmission power transformers are shown in the table II.

Table II - Range of gas values,  $\mu\text{L/L}$  (ppm) and ratio CO<sub>2</sub>/CO for transmission power transformers

GAS, $\mu\text{L/L}$ (ppm)	Rate of transformer/ Type of cooling / number of units				
	20 MVA 110 kV ONAN/ONAF 7 units	40 MVA 110 kV ONAF, ONAN 6 units	63 MVA 110 kV ONAF 2 units	100 MVA 110 kV ONAF 1 unit	$\geq 300$ MVA 420 kV OFAF 5 units
Hydrogen, H <sub>2</sub>	5-20	11-18	12-17	16	2-31
Methane, CH <sub>4</sub>	2-8	7-12	11-14	22	10-18
Acetylene, C <sub>2</sub> H <sub>2</sub>	0	0	0	0	0
Ethylene, C <sub>2</sub> H <sub>4</sub>	0	0	0	1	0-1
Ethane, C <sub>2</sub> H <sub>6</sub>	0	0	0	3	0-3
CO	148-1197	761-1457	1135-1157	1208	468-825
CO <sub>2</sub>	337-2853	1274-4652	2270-2521	2817	1945-2892
Ratio CO <sub>2</sub> /CO	1,0-11,2	1,7-3,6	2,0-2,2	2,3	2,5-4,9
Oxygen	7117-19444	5532-10794	9706-10582	7857	5642-11384
Nitrogen	31850-63613	27110-55101	52276-60703	50629	24404-58148

The measured water content in the oil for all transmission transformers is lower than 10 mg/kg.

According to IEC 60599, the ratio  $CO_2/CO < 3$  indicates a possible accelerated degradation of cellulose. In closed-type transformers, due to lack of oxygen, the thermodynamic balance is shifted towards generation of CO, so a lower ratio  $CO_2/CO$  is frequently found.

For 15 closed-type transmission power transformers (with OLTC) the ratio  $CO_2/CO$  is lower than 3, and 1 of the 21 transformers has ratio higher than 10. Only at 5 of them typical  $CO_2/CO$  ratios are between 3 and 10 which corresponds to normal degradation of cellulose.

Accelerated degradation of cellulose can be confirmed by increase of furan content in oil. Furan content in oil was analysed in the all closed-type transmission transformers. It was found to be low, what means that there are no indications of accelerated cellulose degradation.

#### 4. LABORATORY TESTINGS

Laboratory tests were carried out to investigate the impact of the main isolation materials oil and paper, as well as the residual air in oil, on formation of CO and  $CO_2$  gases.

##### 4.1. Influence of oil and paper on CO and $CO_2$ formation

Kraft paper and pressboard were subjected to thermal degradation testing in an oven at 115 °C. All samples were tested separately, in degassed inhibited mineral oil (total gas content between 1.5% and 2.0%). Residual oxygen content was 4000-4500  $\mu\text{L/L}$ ,  $CO < 5 \mu\text{L/L}$  and  $CO_2 65 - 75 \mu\text{L/L}$ . Kraft paper and pressboard to mineral oil ratio was 1 g in 50 mL of oil. Tests were performed in gas tight syringes.

As expected, thermal degradation of mineral oil and Kraft paper resulted in significant increase of CO concentration.

Gassing of mineral oil at higher temperatures is well known and it has been shown that different mineral oils can generate different amounts of CO and  $CO_2$  [5].

CO generation from mineral oil and Kraft paper was linear through the testing period and it was more intensive from Kraft paper.

CO generation from pressboard was significant after 48 hours of testing, but it did not increase during testing period. After 360 hours, the pressboard had minor influence on CO generation. Influence of mineral oil, Kraft paper and pressboard on CO generation is presented in figure 3.

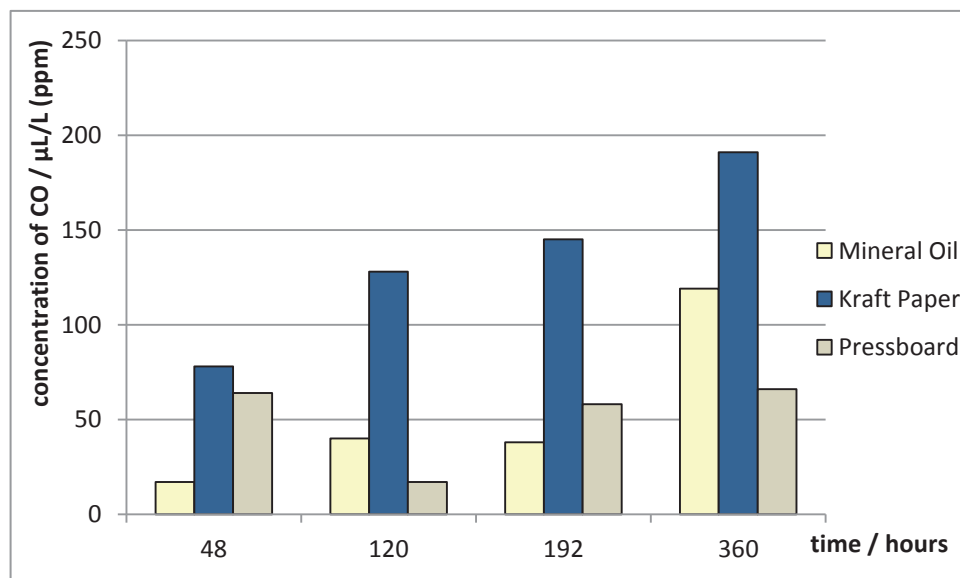


Figure 3 - CO generation from mineral oil, Kraft paper and pressboard at 115 °C

Kraft paper, as well as pressboard, had the similar impact on the generation of  $CO_2$ . The impact of mineral oil is insignificant, as shown in figure 4. The  $CO_2$  gas amount generated from Pressboard decreased after 360 hours of testing (possible gas leaking from syringes).

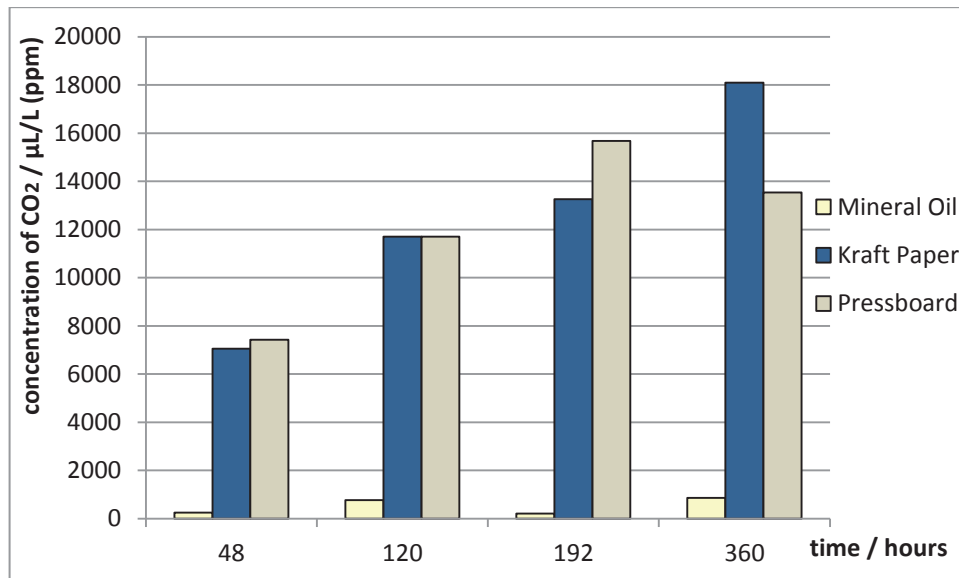


Figure 4 - CO<sub>2</sub> generation from mineral oil, Kraft paper and pressboard at 115 °C

#### 4.2. Influence of residual air on CO and CO<sub>2</sub> formation

The impact of oil degassing on CO and CO<sub>2</sub> formation was investigated. New degassed mineral oils with different total content of residual air in the oil (0.5%, 1.5% and 2.0%), were subjected to thermal degradation testing in a oven at 70°C. The development of emissions of CO and CO<sub>2</sub>, after 168 and 336 hours of test, was monitored.

As presented in figure 5. oil with more residual air (2.0% TGC) had higher impact on concentrations of CO and CO<sub>2</sub> than oil with less residual air (0.5% TGC).

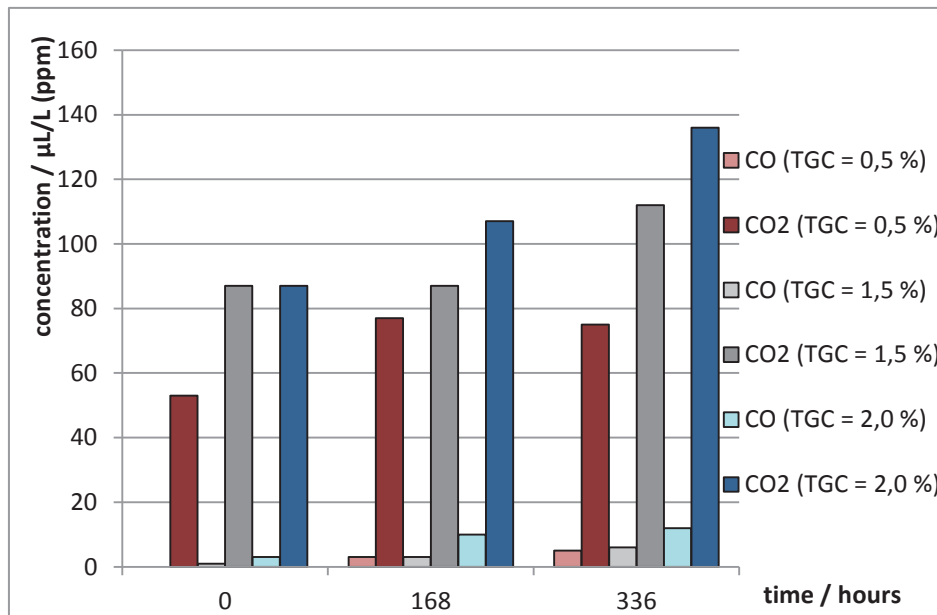


Figure 5 - Influence of total gas content (TGC) on formation of CO and CO<sub>2</sub> at 70 °C

It is important to degas the oil and transformer during the manufacturing process of transformer to the lowest possible amount of residual gas. The total content of gas in oil in closed-type transformers should be kept low during the operation, and if it is higher than 5% it is necessary to degas the oil, to prevent the increased development of CO.

## 5. CONCLUSION

Carbon monoxide and dioxide as well as water are the final products of cellulose degradation. Except cellulose, and in lesser extent mineral oil, the auxiliary materials (paints, rubber, plastic materials, glues etc.) also have the impact on CO and CO<sub>2</sub> generation.

Laboratory testing show the influence of residual air (total gas content) in oil on formation of CO and CO<sub>2</sub>. Better degassing assures lower concentrations of these two gases. In transformers with closed-type breathing system oxygen content in oil is lower than in air saturated oil, so the equilibrium is shifted towards CO production. Besides that, the membrane does not allow the release of produced gases to air, so increase of the gases during operation is higher.

Because of presented facts it can be concluded that in normal operating closed-type transformers, CO can be present in greater concentration and CO<sub>2</sub> in some lower concentration than in transformers with open breathing system (lower ratio CO<sub>2</sub>/CO).

It is important to distinguish the normal values for CO and CO<sub>2</sub> concentration for closed-type and open breathing system transformers. The typical values for CO as well scheme concerning their ratios need to be revised in standard IEC 60599. The criteria need to be established separately for closed type transformers as particular category of equipment.

## REFERENCES

- [1] IEC 60567 (1992): Guide for sampling of gases and oil from oil-filled electrical equipment and for the analysis of free and dissolved gases.
- [2] IEC 60599 (2007): Interpretation of the analysis of gases in transformers and other filled electrical equipment in service
- [3] IEC 61198 (1993): Ed.1-Mineral insulating oils - Methods for the determination of 2-furfural and related compounds
- [4] IEEE Std C57.104 (2008): IEEE Guide for the Interpretation of Gases Generated in Oil-Immersed Transformers
- [5] Schmidt J., Eitner R., Hartwing R., Gassing Behaviour of Transformer Oils at Temperatures Above 60°C, 7<sup>th</sup> International Symposium on High Voltage Engineering, August 26-30, 1991
- [6] Atanasova-Hohlein I., Frotcher R., Relevance and Importance of the Carbon Oxide and their Ratio for the Interpretation of dissolved Gas Analysis in Transformers and Tap Changers; Cigre Session, Paris

Ana Orešković  
Končar - Electrical Engineering Institute  
[aoreskovic@koncar-institut.hr](mailto:aoreskovic@koncar-institut.hr)

Miroslav Poljak  
Končar - Electrical Industry Inc.  
[poljak.dd@koncar.hr](mailto:poljak.dd@koncar.hr)

Zdenko Godec  
Končar - Electrical Engineering Institute  
[zgodec@koncar-institut.hr](mailto:zgodec@koncar-institut.hr)

Rajko Gardijan  
Končar - Electrical Engineering Institute  
[rgard@koncar-institut.hr](mailto:rgard@koncar-institut.hr)

## ON-SITE ACCURACY COMPARISON OF CAPACITOR AND INDUCTIVE VOLTAGE TRANSFORMERS

### SUMMARY

In this paper an on-site accuracy comparison of capacitor and inductive voltage transformers is presented. A 400/110 kV transformer substation in Croatia has been chosen as an appropriate location for the comparison as both types of transformers (capacitor and inductive) operate there simultaneously. Each transformer type is a part of one of the two existing measuring chains for measurement of electrical energy. Their accuracy comparison is, therefore, carried out indirectly, by actually comparing the energies measured by the first and the second measuring chain and then estimating the measurement uncertainty of their difference. Without measurement uncertainty, a parameter that shows the quality of any measurement result, it is generally not possible to conclude about the accuracy of measurement or to compare measurement results mutually. In this measurement uncertainty estimation real on-site conditions in transformer substation, especially those which effect voltage transformer accuracy, have been taken into account (voltage, transformer load, frequency, temperature, etc.)

**Key words:** Capacitor voltage transformer, inductive voltage transformer, measurement accuracy, measurement uncertainty, measurement of electrical energy

### 1. INTRODUCTION

Capacitor voltage transformer (hereinafter referred to as CVT) is a special type of voltage transformer. It consists of a capacitor divider and an electromagnetic (inductive) unit. In steady state the error of a CVT depends on operating conditions and changes with voltage, burden, frequency and temperature. Relatively large number of influence quantities that affect the error is an important drawback of this type of transformers. In both the new (from 2012) IEC 61869-5 standard and the old IEC 60044-5 standard (which was official at the time this research was done) for capacitor voltage transformers it is stated that present day service experiences show that CVTs may be satisfactorily used only in the accuracy class 0.5. However, the standards do not list any articles, researches or studies that would support this statement. For inductive voltage transformers there are no such statements and they are generally considered to be sufficiently accurate in service even in higher accuracy classes (like 0,2). These transformers are sensitive to changes in load and burden with some minor influence of temperature on winding resistance variation.

On high voltage revenue metering points (indirect electrical energy measurement) both types of transformers can be found as a part of an electrical energy measuring chain.

A 400/110 kV transformer substation in Croatia is a high voltage revenue metering point and it has two electrical energy measuring chains. In a 400 kV line bay three capacitor (420 kV CVT, accuracy class 0.2), three inductive (420 kV inductive voltage transformers, accuracy class 0,2) and three current transformers (accuracy class 0,2) are installed. Two electrical energy meters of the same type are used. One meter's voltage circuit consists of capacitor and other meter's voltage circuit of inductive voltage transformers. Current circuits (current transformers) are the same for both meters. Measuring chains, therefore, differ only in the type of voltage transformer used.

Simultaneous work of capacitor and inductive voltage transformers in a 400/110 kV substation, shown in figure 1, makes this substation an appropriate location for their on-site accuracy comparison. The conclusion about the accuracy of the transformers is reached indirectly, by comparing the energies (active and reactive) acquired by the meter using capacitor and by the meter using inductive voltage transformers and then estimating the measurement uncertainty of their difference.

The accuracy of measurement is related to and estimated by the uncertainty of measurement. Measurement uncertainty is a parameter, associated with the result of measurement, that characterizes the dispersion of the values that could be reasonably attributed to the measurand [1]. It is an indication of the quality of the result and without measurement uncertainty results cannot be compared, either among themselves or with reference values given in a specification or a standard. Measurement uncertainty has many components that are categorized according to the method used to evaluate them. Generally two types of uncertainty are recognized: type A uncertainty (evaluation of uncertainty by the statistical analysis of series of observations) and type B uncertainty (methods other than the statistical analysis, a priori probability distributions). Measurement uncertainty, like its components, is expressed by standard deviation. Expanded uncertainty is obtained by multiplying the standard uncertainty with a coverage factor  $k$ , which is typically in the range 2 to 3. The choice of factor  $k$  is based on the chosen probability (approx. 95% for  $k=2$  and approx. 99% for  $k=3$ ) that the interval of values covered with expanded uncertainty includes the real value of the measurand [2].

On-site accuracy comparison of capacitor and inductive voltage transformers is done by comparing the energies measured by the two measuring chains these transformers are a part of and by estimating the measurement uncertainty of their difference. Here, one hour values of active and reactive energies over a one year period (from October 2009 to October 2010) have been compared. In order to estimate the uncertainty of a difference, measurement uncertainty of each measuring chain needs to be estimated individually.

## 2. ESTIMATION OF MEASUREMENT UNCERTAINTY OF ELECTRICAL ENERGY MEASUREMENT

### 2.1. Mathematical model

Estimation of measurement uncertainty starts with the establishment of a mathematical model of the measurement. A mathematical expression is needed to describe the relationship between the output quantity – the measurand (measurement result) and the input quantities on which the measurand depends. Input quantities can also be observed as results of some other measurement and can themselves depend on other variables [1]. Here, the input quantities are active ( $W_p$ ) and reactive ( $W_Q$ ) energy and are given by the following expressions:

$$W_p = (U \cdot I \cdot \cos \phi) \cdot t \quad (1)$$

$$W_Q = (U \cdot I \cdot \sin \phi) \cdot t \quad (2)$$

Input quantities are the voltage ( $U$ ), current ( $I$ ), phase angle between voltage and current ( $\phi$ ) and time ( $t$ ).

In the substation there are two electrical energy measuring chains. Chains consist of voltage transformers (capacitor in one and inductive in the other chain), current transformers, electricity meters and secondary lines connecting transformers low voltage terminals to the meter input terminals. Uncertainty of each of the input quantity ( $U$ ,  $I$ ,  $\phi$ ,  $t$ ) is linked to one or more of the mentioned measuring chain components.

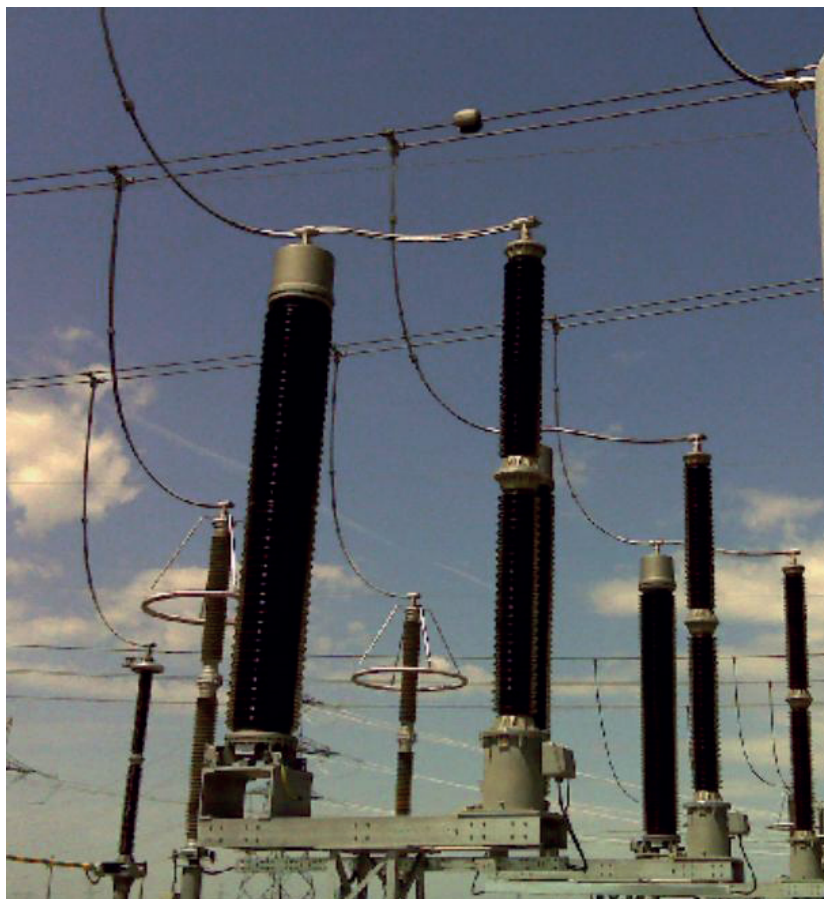


Figure 1 – Simultaneous work of capacitor and inductive voltage transformers in a 400/110 kV substation

Voltage, current and phase angle are the input signals of the electricity meter. In expressions (1) and (2) they actually define active and reactive power brought to the meter at any time. Uncertainties of voltage, current and phase angle are linked to voltage and current transformers and secondary lines. These are then the sources of uncertainties for active and reactive power as well. Active and reactive energies are read directly from the meter. The meter, therefore, directly contributes to the uncertainty of energy measurement. The uncertainty of time is a part of the overall uncertainty of the meter. The total uncertainty of active and reactive energy consist of the uncertainty of the meter and the uncertainty of the input signal, active or reactive power, brought to the meter.

Generally, if the measurand  $y$  is determined from  $N$  other, mutually independent, quantities  $x_1, \dots, x_N$  through a functional relationship  $F$ , than the standard measurement uncertainty  $u(y)$  of the measurand  $y$  is given, according to [1], by:

$$u(y) = \sqrt{\sum_{i=1}^N \left( \frac{\partial F}{\partial x_i} \right)^2 \cdot u^2(x_i)} \quad (3)$$

where:  $u(x_i)$  are standard uncertainties of input quantities from which  $y$  is determined.

Measurement uncertainty of active power is according to (3):

$$u(P)_{\%} = \frac{u(P)}{P} \cdot 100\% = \sqrt{u^2(U)_{\%} + u^2(I)_{\%} + (100\% \cdot \tan \phi \cdot u(\phi))^2} \quad (4)$$

Measurement uncertainty of reactive power is according to (3):

$$u(Q)_{\%} = \frac{u(Q)}{Q} \cdot 100\% = \sqrt{u^2(U)_{\%} + u^2(I)_{\%} + \left( 100\% \cdot \frac{u(\phi)}{\tan \phi} \right)^2} \quad (5)$$

Expressions (4) and (5) define the uncertainty of active and reactive power per one phase. In a three phase system the total power is the sum of the amount of power in each phase. With the assumption of a symmetrical three phase system (which is in most cases true for high voltage lines) expressions for the uncertainty of total active and reactive power are:

$$u(P_{\text{tot}})_{\%} = \frac{1}{3} \cdot \sqrt{u^2(P_1)_{\%} + u^2(P_2)_{\%} + u^2(P_3)_{\%}} \quad (6)$$

$$u(Q_{\text{tot}})_{\%} = \frac{1}{3} \cdot \sqrt{u^2(Q_1)_{\%} + u^2(Q_2)_{\%} + u^2(Q_3)_{\%}} \quad (7)$$

As already stated, total measurement uncertainty of electrical energy (active or reactive) consists of the uncertainty of electrical power (active or reactive, expressions (6) and (7)) and the uncertainty of the meter:

$$u(W_P)_{\%} = \sqrt{u^2(P_{\text{tot}})_{\%} + u_{\text{mt}}^2(P)_{\%}} \quad (8)$$

$$u(W_Q)_{\%} = \sqrt{u^2(Q_{\text{tot}})_{\%} + u_{\text{mt}}^2(Q)_{\%}} \quad (9)$$

$u_{\text{mt}}(P)_{\%}$  and  $u_{\text{mt}}(Q)_{\%}$  are percentage uncertainties of active and reactive energy meter

According to expressions (4) to (9) for the estimation of uncertainty of electrical energy it is necessary to know the uncertainties of voltage  $u(U)_{\%}$ , current  $u(I)_{\%}$ , phase angle  $u(\varphi)$  and the meter  $u_{\text{mt}}(P)_{\%}$  and  $u_{\text{mt}}(Q)_{\%}$ .

## 2.2. Measurement uncertainty of voltage

Capacitor and inductive voltage transformers are the sources of uncertainty of voltage measurement. The uncertainty is a consequence of the ratio error which a voltage transformer introduces into the measurement. The actual transformation ratio is not equal to the rated transformation ratio. That is why the voltage brought to the meter multiplied by the rated transformation ratio does not equal the actual voltage on the primary side. Additional error occurs because of the voltage drop on the connection wires in the secondary circuit due to the load current.

IEC standards 61869-5 [3] and 61869-3 [4] for capacitor and inductive voltage transformers define the limits of voltage errors for different accuracy classes under prescribed conditions of use. By using the upper (or lower) error limit  $G_{\%}$  according to [3] and [4] and by assuming a symmetric rectangular a priori probability distribution uncertainty of voltage can be calculated as  $G_{\%}/\sqrt{3}$ . In most cases, however, this leads to overestimation of measurement uncertainty. Actual voltage errors of transformers are smaller than the maximum allowable errors defined in standards. This can be confirmed by inspecting transformers calibration reports. Measurement uncertainty of voltage can be calculated using maximum errors obtained during last calibration  $G_{\text{MAX}\%}$  with the uncertainty of calibration  $u_{\text{CAL}}(U)_{\%}$  also taken into account [5].

$$u(U)_{\%} = \sqrt{\left(\frac{G_{\text{MAX}\%}}{\sqrt{3}}\right)^2 + \left(u_{\text{CAL}}(U)_{\%}\right)^2} \quad (10)$$

Real working conditions in the substations differ from calibration conditions (transformers were last calibrated in transformers' factory in October 2008 at the temperature of  $(20 \pm 5)^{\circ}\text{C}$  and frequency of  $(50 \pm 0,1)$  Hz and with burdens of 100% and 0% of rated value). The real maximum error is therefore larger or even smaller than the maximum error from the calibration report. Because of that, additional corrections are required. Real working conditions that affect the error are burden, burden power factor, ambient temperature and frequency (only for CVT). The effect of real working conditions is taken account by using transformers equivalent circuits and the corresponding expressions.

The information about real operating conditions is collected by appropriate measurements. Voltage transformers' real burden, impedance of secondary circuit lines, electrical energy quality parameters and the temperature in the vicinity of the transformers have been measured. The device for measurement of quality of electrical energy registers voltages and currents of all phases, frequency, rapid voltage changes and total harmonic distortion factor of all voltages and currents. For the sake of ambient

temperature measurement two overhead transmission line monitoring devices have been used. The devices have been mounted on a 400 kV high voltage line in two phases, on approx. 1,5 meters distance from the top of CVT insulators. They measure ambient temperature every two minutes.

Results of measurement of the total impedance connected to the secondary transformer terminals show that transformers have low secondary burdens. Such results are to be expected because their secondary circuit devices are electronic devices with high input impedance. Regarding actual burden, capacitor and inductive voltage transformers are treated as transformers operating under no load. Because calibration reports include transformer errors for no load operation (0% of rated burden), error correction because of real burden is not necessary.

The device for energy quality measurement has recorded maximum and minimum frequency in the period from October 2009 to October 2010 and they are 50,1 Hz and 49,9 Hz (deviation of  $\pm 0,2\% f_n$ ).

Maximum and minimum temperature in the period from October 2009 to October 2010 have been recorded by overhead transmission monitoring devices and they are  $+40^\circ\text{C}$  (June, July and August 2010) and  $-16^\circ\text{C}$  (December 2009.g.).

Equivalent circuit of a 420 kV CVT from the substation is shown in figure 2. In calculating the error and error correction, parameters provided by the manufacturer are used. By using these parameters it is not possible to fully reconstruct the measured errors from calibration reports for transformers in the substation. This is because every individual transformer has some extra turns (as a part of a primary winding) for fine tuning of voltage error and these are not taken into account in equivalent circuit. Calculated error from the equivalent circuit approximately matches the one from the calibration report. Using expressions (11) to (14) [6] it is possible to calculate how the error changes with temperature and frequency and what is the maximum possible error (absolute value) regarding the actual substation frequency and temperature range. It is assumed that the errors for the transformers in the substation (real errors from calibration reports) change in the same manner and amount with frequency and temperature as calculated ones. The error correction obtained by using the equivalent circuit is applied on calibration errors and with these corrected errors uncertainty of voltage is calculated using expression (10).

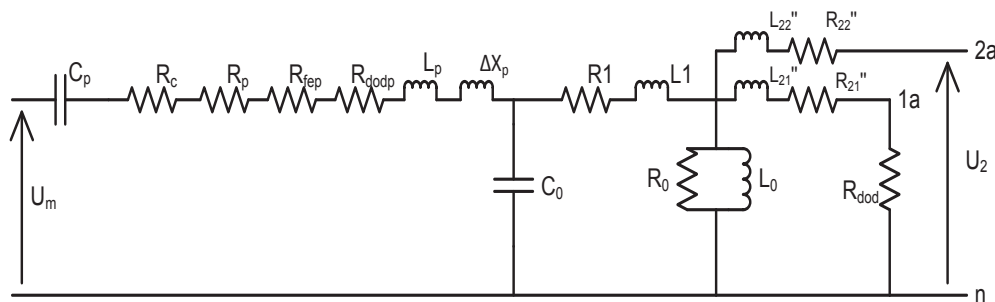


Figure 2 – Equivalent circuit of a 420 kV capacitor voltage transformer

Voltage (ratio) error of a CVT under no load  $p_0$  is calculated using the following expressions:

$$p_0 = \left( -A \cdot \frac{S_{dod}}{U_m^2} + C \right) \cdot 100\% + 0,2\% \quad (11)$$

$$A = 0,8 \cdot (R_c + R_p + R_{fep} + R_{dodp} + R_1 + R_{21}'') + 0,6 \cdot (X_1 + X_{21}'' + X_p + \Delta X_p - X_c) \quad (12)$$

$$C = \frac{X_p + \Delta X_p - X_c}{X_{C_0}} - \frac{R_c + R_p + R_{fep} + R_{dodp} + R_1}{R_0} - \frac{X_1 + X_p + \Delta X_p - X_c}{X_0} \quad (13)$$

$$S_{dod} = \frac{U_2^2}{R_{dod}} \quad (14)$$

where  $U_m$  is the intermediate voltage of transformer (voltage on intermediate voltage capacitor),  $U_2$  secondary voltage,  $C_p$  substitute capacitance of a capacitor divider,  $R_c$  substitute resistance of a capacitor divider (resistance due to dielectric loss),  $R_p$  substitute resistance of compensating reactor winding,  $R_{fep}$  substitute resistance of compensating reactor core,  $R_{dodp}$  extra resistance of compensating reactor due to air gap,  $R_1$  primary winding resistance,  $L_1$  primary winding leakage inductance,  $R_0$  and  $L_0$  ohmic and inductive core resistance,  $C_0$  substitute primary winding capacitance,  $L_{21}$ ,  $L_{22}$ ,  $R_{21}$ ,  $R_{22}$  first and secondary winding leakage inductance and resistance reduced to the primary side,  $R_{dod}$  feroresonant filter resistance and  $\Delta X\rho$  extra reactance for error correction.

The change of frequency effects all reactances and the change of temperature has the effect on:  $C_p$ ,  $R_c$ ,  $R_p$ ,  $R_1$ ,  $R_{22}$  and  $R_{21}$ .

Inductive voltage transformers errors do not depend on frequency (for such small frequency deviations) so the errors from calibration reports are corrected only regarding temperature deviation from reference value (20°C). Inductive voltage transformers in the substation are open magnetic core transformers. Temperature effects their voltage error through primary winding resistance  $R_1$ . In the expression for voltage error for this type of transformers according to [7], resistance  $R_1$  appears as a part of a ratio  $R_1/R_0$ , where  $R_0$  is the substitute resistance representing core loss. This ratio is in the order of  $10^{-5}$  and its change has a negligible effect on the error. That is why the errors of inductive voltage transformers are not corrected.

It has already been mentioned that an additional error occurs because of the voltage drop on the connection wires in the secondary circuit. In the substation the impedances of these wires have been measured. The extra error is about 100 times smaller than the errors of voltage transformers and is also considered to be negligible.

### 2.3. Measurement uncertainty of current

Because of the current transformer ratio error the current of an electricity meter is different than the 400 kV line current multiplied by the rated transformation ratio. The ideal transformation is never achieved so the current transformers represent the source of uncertainty for measurement of current.

The uncertainty of current is determined in the same way as for voltage, using calibration reports (maximum errors  $G_{MAX\%}$  measured in the range of 5% to 110% of nominal current) and measurement uncertainty of calibration  $u_{CAL}(I)\%$  according to expression (15) [5].

$$u(I)\% = \sqrt{\left(\frac{G_{MAX\%}}{\sqrt{3}}\right)^2 + \left(u_{CAL}(I)\%\right)^2} \quad (15)$$

Current transformers in the substations were calibrated on-site. The errors were measured with real burdens and real burden power factors over a range of primary currents. It is, therefore, not necessary to additionally correct these errors.

### 2.4. Measurement uncertainty of phase angle

The phase relationship  $\varphi$  between voltage and current in the secondary circuit ( $\varphi = \varphi_U - \varphi_I$ ) is changed compared to their relationship in the primary circuit. This is due to phase angle error of voltage ( $\delta_U$ ) and current transformer ( $\delta_I$ ). The uncertainty of phase angle  $u(\varphi)$  equals the uncertainty of the difference of voltage and current transformers phase angle errors  $u(\varphi_S) = u(\delta)$ ,  $\delta = \delta_U - \delta_I$  and it is:

$$u(\varphi) = u(\delta) = \sqrt{u^2(\delta_U) + u^2(\delta_I)} \quad (16)$$

By inspecting calibration reports it is possible to make a more realistic uncertainty estimation by calculating with maximum phase angle errors of pair of voltage and current transformers in each phase:

$$\delta_{MAX} = \max\left(|\delta_{VTmin} - \delta_{CTmax}|, |\delta_{VTmax} - \delta_{CTmin}|\right) \quad (17)$$

where:  $\delta_{VTmin}$  and  $\delta_{VTmax}$  are the minimum and maximum phase angle errors of voltage transformers from the last calibration report additionally corrected regarding real working conditions. Minimum

and maximum current transformers phase angle errors  $\delta_{CTmin}$  and  $\delta_{CTmax}$  from the last calibration report do not need to be additionally corrected (on-site calibration).

Additional correction for phase angle error of CVTs is done in a similar way as for ratio error, using the equivalent circuit from figure 2 and expressions (18) to (20) [6]. All the values in the expressions have been explained in chapter 2.2.

$$\delta_0 = \left( -D \frac{S_{dod}}{U_m^2} + F \right) \cdot 3440 \text{ min} \quad (18)$$

$$D = 0,8 \cdot (X_1 + X_{21}'' + X_p + \Delta X_p - X_c) - 0,6 \cdot (R_c + R_p + R_{fep} + R_{dodp} + R_1 + R_{21}'') \quad (19)$$

$$F = \frac{R_c + R_p + R_{fep} + R_{dodp} + R_1}{X_0} - \frac{X_1 + X_p + \Delta X_p - X_c}{R_0} - \frac{R_c + R_p + R_{fep} + R_{dodp}}{X_{C0}} \quad (20)$$

Phase angle errors of inductive voltage transformers are corrected only regarding ambient temperature deviation from reference value (20°C).

Open core inductive transformer no load phase angle error  $\delta_0$  is according to [7]:

$$\delta_0 = 3440 \cdot (R_1 / X_0) [\text{min}] \quad (21)$$

$R_1$  is primary winding resistance and  $X_0$  reactance representing core losses.

$R_1$  changes with temperature according to the expression:

$$R_1' = R_{1_{20^\circ\text{C}}} \cdot (1 + k \cdot \Delta T) \quad (22)$$

$k$  is copper temperature coefficient and it's value is 0,00392 [1/K].

At some other temperature than 20°C,  $\delta_0$  is:

$$\delta_0' = \delta_0 \cdot (R_1' / R_{1_{20^\circ\text{C}}}) = \delta_0 \cdot (1 + k \cdot \Delta T) \quad (23)$$

Expression (23) is used for inductive voltage transformer phase angle correction.

Finally, measurement uncertainty of phase angle  $u(\phi)$  is calculated as:

$$u(\phi) = u(\delta) = \sqrt{\frac{(\delta_{MAX})^2}{3} + u_{CALVT}^2(\delta) + u_{CALCT}^2(\delta)} \quad (24)$$

$u_{CALVT}(\delta)$  and  $u_{CALCT}(\delta)$  are uncertainties of voltage and current phase angle calibration.

## 2.5. Measurement uncertainty of active and reactive energy meter

Energy meters in the substation are electronic meters connected to the measuring point via current and voltage transformers. Their nominal current is 1 A and maximum current 1,2 A. They measure active and reactive energy in both energy flow in all quadrants with maximum errors defined by accuracy class 0,2 according to IEC 62053-22 [8] standard for active and accuracy class 2 according to IEC 62053-23 [9] standard for reactive energy. Instead of using maximum errors defined in standards it is possible to estimate meters' uncertainty by combining maximum errors from calibration reports  $G_{MAXmt\%}$  (if such reports are available) and the uncertainty of calibration  $u_{CALmt}$ . Extra notice should be taken regarding reference conditions defined in standards (reference ambient temperature, voltage, frequency, THD factor, foreign electromagnetic fields, etc.) and the additional percentage error  $G_{ad}$  due to deviation of real working conditions from reference ones. In the substation reference conditions have been checked using the data collected by the device for measurement of quality of electrical energy and by performing additional measurements of electrical and magnetic fields in the vicinity of the meters.

The uncertainty of active  $u_{mt}(P)$  and reactive energy  $u_{mt}(Q)$  meter is:

$$u_{mt\%} = \sqrt{\left(\frac{G_{MAXmt}}{\sqrt{3}}\right)^2 + (u_{CALmt})^2 + \sum_{i=1}^n \left(\frac{G_{adi}}{\sqrt{3}}\right)^2} \quad (25)$$

## 2.6. Expanded measurement uncertainty of active and reactive energy

The expanded measurement uncertainty of active and reactive energy is obtained by multiplying the expressions (8) and (9) with a coverage factor  $k=2$ .

$$U(W_p)_{\%} = 2 \cdot \sqrt{u^2(P)_{\%} + u_{mt}^2(P)_{\%}} \quad (26)$$

$$U(W_Q)_{\%} = 2 \cdot \sqrt{u^2(Q)_{\%} + u_{mt}^2(Q)_{\%}} \quad (27)$$

Expanded measurement uncertainties for the measuring chain containing capacitor and the chain containing inductive voltage transformers in the 400/110 kV substation in Croatia for the period from October 2009 to October 2010 are given in table I.

Table I: Expanded measurement uncertainty in a 400/110 kV substation in Croatia for the period from October 2009 to October 2010

	Expanded measurement uncertainty , $k=2$	
	Active energy	Reactive energy
capacitor transformers	0,162 %	3,40 %
inductive transformers	0,159 %	3,41 %

## 3. ESTIMATION OF MEASUREMENT UNCERTAINTY OF THE DIFFERENCE IN ACTIVE AND REACTIVE ENERGY MEASUREMENT USING CAPACITOR AND INDUCTIVE VOLTAGE TRANSFORMERS

### 3.1. Mathematical model

Simultaneous measurements of electrical energy with two different measuring chains, one with capacitor and other with inductive voltage transformers, are done in order to establish whether there is a difference between results of the two chains and if that difference is statistically significant.

The average one hour active energy measured with the first chain (CVT transformers) for the period from October 2009 to October 2010 is 200790,6 kWh and with the second chain (inductive voltage transformers) 200535,6 kWh. The average one hour difference in energies measured with the two chains for the same period (8040 pairs of measurement) is 254,69 kWh (0,127%) with a standard deviation of the arithmetic mean of 4,25 kWh.

The average one hour reactive energy measured with the first chain (CVT transformers) for the period from October 2009 to October 2010 is -48288,1 kvarh and with the second chain (inductive voltage transformers) -48336,1 kvarh. The average one hour difference in energies measured with the two chains for the same period (8040 pairs of measurement) is 48 kvarh (0,099%) with a standard deviation of the arithmetic mean of 4,31 kvarh.

Energies measured with the two chains are not mutually independent. Current transformers in all phases are shared by both chains. All three currents and all three current phase angles are variables on which both energies depend. The energies are, therefore, correlated and this correlation needs to be taken into account while defining the mathematical model for the uncertainty of their difference.

Generally, if the measurand  $y$  is determined from  $N$  other input correlated quantities  $x_1, \dots, x_N$  through a functional relationship  $F$ , then the measurement uncertainty of  $y$  is given by [1]:

$$u(y) = \sqrt{\sum_{i=1}^N \left( \frac{\partial f}{\partial x_i} \right)^2 u^2(x_i) + 2 \cdot \sum_{i=1}^{N-1} \sum_{j=i+1}^N \frac{\partial f}{\partial x_i} \frac{\partial f}{\partial x_j} u(x_i, x_j)} \quad (28)$$

$u(x_i, x_j)$  are covariances associated with  $x_i$  and  $x_j$

If two input quantities  $x_1$  and  $x_2$  depend on a set of uncorrelated variables  $q_1, q_2, \dots, q_L$  so that  $x_1 = F(q_1, q_2, \dots, q_L)$  i  $x_2 = G(q_1, q_2, \dots, q_L)$ , although some of these variables may actually appear only in one function and not the other, than the covariance associated with  $x_1$  and  $x_2$  is:

$$u(x_1, x_2) = \sum_{i=1}^L \frac{\partial F}{\partial q_i} \frac{\partial G}{\partial q_i} u^2(q_i) \quad (29)$$

Measurement uncertainty of difference in measured active energy using capacitor (CVT) and inductive (IVT) transformers  $W_{PD} = W_{PCVT} - W_{PIVT}$  is calculated according to (28) and (29):

$$\begin{aligned} u^2(W_{PD}) = & \left( \frac{u(W_{PCVT})_{\%}}{100\%} \cdot W_{PCVT} \right)^2 + \left( \frac{u(W_{PIVT})_{\%}}{100\%} \cdot W_{PIVT} \right)^2 + u^2(\overline{W_{PD}}) - \\ & 2 \cdot \left( \frac{u(W_{PCVT1}, W_{PIVT1})_{\%}}{100\%} \cdot W_{PCVT1} \cdot W_{PIVT1} + \frac{u(W_{PCVT2}, W_{PIVT2})_{\%}}{100\%} \cdot W_{PCVT2} \cdot W_{PIVT2} \right. \\ & \left. + \frac{u(W_{PCVT3}, W_{PIVT3})_{\%}}{100\%} \cdot W_{PCVT3} \cdot W_{PIVT3} \right) \end{aligned} \quad (30)$$

where:

$$\begin{aligned} u(W_{PCVTi}, W_{PIVTi})_{\%} &= \frac{u(W_{PCVTi}, W_{PIVTi})}{W_{PCVTi} \cdot W_{PIVTi}} \cdot 100\% \\ &= \frac{u^2(I_i)_{\%}}{100\%} + \tan(\phi_{CVTi} - \phi_{li}) \cdot \tan(\phi_{IVTi} - \phi_{li}) \cdot u^2(\phi_{li}) \cdot 100\% \end{aligned} \quad (31)$$

$i = 1, 2, 3$

Measurement uncertainty of difference in measured reactive energy using capacitor (CVT) and inductive (IVT) transformers  $W_{QD} = W_{QCVT} - W_{QIVT}$  is calculated according to (28) and (29):

$$\begin{aligned} u^2(W_{QD}) = & \left( \frac{u(W_{QCVT})_{\%}}{100\%} \cdot W_{QCVT} \right)^2 + \left( \frac{u(W_{QIVT})_{\%}}{100\%} \cdot W_{QIVT} \right)^2 + u^2(\overline{W_{QD}}) - \\ & 2 \cdot \left( \frac{u(W_{QCVT1}, W_{QIVT1})_{\%}}{100\%} \cdot W_{QCVT1} \cdot W_{QIVT1} + \frac{u(W_{QCVT2}, W_{QIVT2})_{\%}}{100\%} \cdot W_{QCVT2} \cdot W_{QIVT2} \right. \\ & \left. + \frac{u(W_{QCVT3}, W_{QIVT3})_{\%}}{100\%} \cdot W_{QCVT3} \cdot W_{QIVT3} \right) \end{aligned} \quad (32)$$

where:

$$u(W_{QCVTi}, W_{QIVTi})_{\%} = \frac{u(W_{QCVTi}, W_{QIVTi})}{W_{QCVTi} \cdot W_{QIVTi}} \cdot 100\% \\ = \frac{u^2(I_i)_{\%}}{100\%} + ctg(\phi_{CVTi} - \phi_i) \cdot ctg(\phi_{IVTi} - \phi_i) \cdot u^2(\phi_i) \cdot 100\% \quad (33)$$

$$i = 1, 2, 3$$

$u(\overline{W_{PD}})$  and  $u(\overline{W_{QD}})$ , are A types of uncertainty, statistically estimated standard deviations of arithmetic means of series of observed differences in measured energies. Tangents and cotangents of phase angles per phases are average values for the period from October 2009 to October 2010.

### 3.2. Standard measurement uncertainty of the difference in active and reactive energy measurement when using capacitor and inductive voltage transformers

Standard measurement uncertainty of the difference in active and reactive energy measurement when using capacitor and inductive voltage transformers according to expressions from (30) to (33) is given in table II.

Table II: Standard measurement uncertainty of the difference in active and reactive energy measurement using capacitor and inductive transformers for the period from October 2009 to October 2010

	Standard measurement uncertainty of difference
Active energy $u(W_{PD})$	192 kWh
Reactive energy $u(W_{QD})$	1153 kvarh

### 3.3. Statistical difference test

In statistics, a result is called statistically significant if it is unlikely to have occurred by chance. Statistical significance of the determined average differences in active (254,69 kWh) and reactive (48 kvarh) energies measured is concluded on by conducting a statistical test of difference, by stating and then checking the hypothesis (so called null hypothesis) about the differences.

For the null hypothesis a claim is chosen that there is no difference between the energies measured using capacitor and inductive transformers, that the difference is zero. In the process of testing, a probability of rejecting the true hypothesis is defined in advance. This is actually the probability of test error and it is called the significance level –  $\alpha$ . The value of  $\alpha$  is in most cases 0,05 or 5%. In order to check null hypothesis, a so called z value is calculated as:

$$z = \Delta W / u(\Delta W) \quad (34)$$

where:  $\Delta W$  is the average difference of the measured energies (active and reactive) and  $u(\Delta W)$  measurement uncertainty of that difference ( $u(\Delta W) = u(W_{PD})$  for active and  $u(\Delta W) = u(W_{QD})$  for reactive energy according to table II). Null hypothesis is accepted in the case  $|z|$  is smaller than the critical z value ( $z_{cr}$ ), that is if  $\Delta W$  lies inside the interval  $0 \pm z_{cr} \cdot u(\Delta W)$  (95% confidence interval if  $\alpha=0,05$ ). Assuming a normal distribution,  $z_{cr}$  is 1,96.

In a 400/110 kV substation in Croatia z value for active energy, according to (34), is 1,33 and for reactive energy 0,04 (absolute values) and in both cases is less than the critical value. Null hypothesis is accepted for both the differences, in active and reactive energy. The differences in energies measured using capacitor and inductive transformers are not statistically significant at 95% level of confidence.

#### 4. CONCLUSION

Measurement of electrical energy with the help of capacitor voltage transformers in the 400/110 kV substation in Croatia is just as accurate as electrical energy measurement with the help of inductive voltage transformers. The same accuracy is achieved under operating conditions that include the operation of voltage transformers with low burden (no load operation), frequency deviation range of  $\pm 0,2\% f_n$ , voltage variation range of  $\pm 10\% U_n$  and ambient temperature change from  $-16^\circ\text{C}$  to  $+40^\circ\text{C}$  in a period of one year. The expanded measurement uncertainty ( $k=2$ ) of active energy measurement is in both cases 0,16% in relation to the measured active energy. Measurement uncertainties are the same for reactive energy measurement as well (3,4% in both cases).

By comparing measurements of energies over a period of one year (October 2009 to October 2010) very small differences between the measurement with the help of the capacitor and with the help of the inductive voltage transformer have been determined (0,127% or 255 kWh and 0,099% or 48 kvarh). The differences are neither statistically nor technically significant. Differences occur at random and cannot be associated with different types of voltage transformers used in electrical energy measuring chains.

Type of capacitor voltage transformer investigated in this article, can be, providing the same or similar operating conditions as indicated, satisfactorily used as a voltage measuring instrument of accuracy class 0,2 in the measuring chain for electrical energy measurement.

#### REFERENCES

- [1] Guide to the expression of uncertainty in measurement, ISO, 1993., ISBN 92-67-10188-9, International Organization of standardization, 1993.
- [2] Z. Godec: Expressing the result of measurement (in Croatian), Graphis Zagreb, 1995
- [3] IEC 61869-5: 2012, Instrument transformers – Part 5: Specific requirements for capacitor voltage transformers
- [4] IEC 61869-3: 2012, Instrument transformers – Part 3: Specific requirements for inductive voltage transformers
- [5] Z.Godec, S.Gazivoda, J.Šimić, M. Lasić, N.Knez: Experimental research, localization of some non technical electrical energy losses and establishing their causes in specific points in distribution network, Annex P6: Measurement uncertainty of electrical energy. Ordered by: HEP d.d., Development sector, 2006 (in Croatian)
- [6] I.Paić: Software for voltage and phase error calculation of capacitor voltage transformer, thesis, FER, Zagreb, 2003.g. (in Croatian)
- [7] V.Bego: Instrument transformers, Školska knjiga, Zagreb, 1977 (in Croatian)
- [8] IEC 62053-22, Electricity metering equipment (a.c.) – Particular requirements, Static meters for active energy (classes 0,2S and 0,5S)
- [9] IEC 62053-23:2003, Electricity metering equipment (a.c.) – Particular requirements, Static meters for reactive energy (classes 2 and 3)

Michael Ertl  
SIEMENS Transformers, Nuremberg  
[michael.ertl@siemens.com](mailto:michael.ertl@siemens.com)

Stephan Voss  
SIEMENS Transformers, Nuremberg  
[stephan.voss@siemens.com](mailto:stephan.voss@siemens.com)

## LOAD NOISE INCREASE OF TRANSFORMERS BY LOAD HARMONICS

### SUMMARY

Harmonic components in the load-current have a larger impact to the increase of the load noise level of transformers than might be expected from their amplitude. The reasons are (a) the interaction of the harmonics with the large load-current at power frequency, (b) the rising sound radiation efficiency with frequency and (c) the A-weighting filter curve which suppresses sound components at lower frequencies. This paper presents a calculation scheme able to estimate the noise increase and the noise spectrum of electrical transformers for non-sinusoidal load conditions. The proposed calculation scheme is applied to three practical examples.

### 1. INTRODUCTION

Electrical power and distribution transformers in field operation regularly show significant deviation in the load noise level in comparison to the sound measurements in the test field of the manufacturer where controlled and standardised measurement conditions apply. The main reason therefore are (a) the changed acoustical ambient conditions on-site caused by sound reflection and diffraction effects of nearby obstacles; (b) changed structural and acoustical resonances, and (c) the different principal operation conditions on-site. Whereas at the factory tests a pure sinusoidal current with short-circuited secondary winding is applied for load noise determination, transformers on-site operate at changed load power factors (phase angle between voltage and load-current), loading beyond the rated power (overload, partial load) as well as harmonics in the load-current.

Harmonic components in the power grid are caused primarily by nonlinear loads and by the nonlinear transfer characteristic of the power grid. Any electrical device which shows a nonlinear consumption of active power or a nonlinear change of the source impedance draws a distorted current waveform even if the supply voltage is sinusoidal. With the growing use of electrical and electronic devices, distorted waveforms in power supply grid by harmonics have been largely increased within the past years. Devices like variable speed drives, six-pulse bridge rectifiers used in power electronics, and discharge lamps draw a non-sinusoidal but pulsating current. Whereas most electric devices generate solely odd harmonics, some devices with fluctuating power consumption generate odd, even and also interharmonic currents [1].

Load noise is generated by electromagnetic forces acting on transformer windings. The forces are proportional to the square of the load-current (Section 2.2). This quadratic response behaviour generates winding vibrations at frequencies beyond the power frequency. In case of harmonics in the load-current, the resulting magnetic force and noise components have harmonics as well- with a more complex frequency spectrum. The related increase of the load noise level must be considered in the estimation of the total noise level of transformers under real load conditions. The question arise how to

predict the resulting noise level at these loading conditions to guarantee the maximum allowed sound level at the transformer site as requested by legislative regulations or the owners specification.

Starting from basic principles, we describe and quantify the generation of harmonics in winding forces, winding vibrations and load noise of electrical transformers caused by load harmonics. A calculation scheme for a fast and practically accurate estimation of the increase in the load noise level for a given load spectrum presented. The effects of A-weighting and frequency-dependent sound radiation efficiency of transformers to the total noise level are discussed. Finally, three practical examples are given.

## 2. LOAD NOISE GENERATION WITH RESPECT TO LOAD HARMONICS

### 2.1. Description of harmonics in the load-current

Consider a transformer in operation with power supply at the operating frequency  $f_1$ , with load-current amplitude  $\hat{I}_1$ , and phase  $\varphi_1$ . In case of superimposed harmonics, the transient load-current has the general form

$$I(t) = \sum_{i=1}^N \hat{I}_i \sin(\omega_i t + \varphi_i). \quad (1)$$

In equation (1),  $N$  denotes the total number of harmonics, whereby a harmonic component of order  $n_i$  is completely described by its angular frequency  $\omega_i = 2\pi f_i$ , amplitude  $\hat{I}_i$ , and phase angle  $\varphi_i$ .

### 2.2. Generation of magnetic forces on windings

In a real transformer the magnetic coupling of the windings is imperfect so that a magnetic leakage flux field arise between the concentric windings if the transformer is at load. According to Ampere's law in the quasistatic case, the load-current  $I$  in the transformer windings generates a magnetic field which is proportional to the current density

$$\nabla \times \mathbf{H} = \mathbf{J}. \quad (2)$$

Hereby,  $\mathbf{H}$  denotes the vector of the magnetic field strength and  $\mathbf{J}$  the current density vector. Since the windings of liquid-immersed transformers are located in an oil-filled tank, the constant magnetic permeabilities  $\mu$  in this non-ferromagnetic material dominate the magnetic field properties in any closed contour of magnetic flux crossing the windings. Thus, the magnetic flux density  $B$  is proportional to the magnetic field strength

$$\mathbf{B} = \mu \mathbf{H}. \quad (3)$$

The magnitude of the leakage flux next to a winding can be estimated by

$$B \approx \mu_0 \frac{NI}{l}, \quad (4)$$

whereby  $\mu_0 = 4\pi \times 10^{-7} \text{ VsAm}$  denotes the magnetic constant,  $N$  the number of winding turns and  $l$  the winding length. It is an appropriate to assume this linear transfer function between  $B$  and  $I$  and consider the spatial field distribution of the leakage flux to be identical for all load harmonics. This assumption is valid for standard transformers with vector groups without phase-angle differences - but not valid for double-tier-transformer with a vector group where the phasing of harmonics is changing (e.g. at wye and delta connection). In the later case, the magnetic field and magnetic force distribution differ with changing harmonic components [2, 3].

The interaction of the magnetic leakage flux field generated by one current carrying winding with the currents in the conductors of other windings gives rise to magnetic volume forces

$$\mathbf{f}_m = \mathbf{J} \times \mathbf{B} \quad (5)$$

which act on the conductors of the windings. Hereby,  $\mathbf{f}_m$  denotes the magnetic force density vector. Equation (5) corresponds to the force relation defined by Lorentz in case that eddy currents in the windings are neglected. A winding section with volume  $V$  therefore experience the magnetic force

$$\mathbf{F}_m = \int \mathbf{f}_m dV. \quad (6)$$

The force density is proportional to the magnetic flux density and the electrical current density, both which are actually present in a certain winding section. It is a good approximation to assume that the magnetic flux and the load-current are there always in phase - even in a 3-phase transformer. Thus, the magnitude of the resulting winding forces are proportional to the square of the load-current and we can write

$$\begin{aligned} F_m(t) &\propto I(t)^2 \\ &= \left( \sum_{i=1}^N \hat{I}_i \sin(\omega_i t + \varphi_i) \right)^2 \\ &= \sum_{i=1}^N \sum_{j=1}^N \hat{I}_i \sin(\omega_i t + \varphi_i) \hat{I}_j \sin(\omega_j t + \varphi_j). \end{aligned} \quad (7)$$

This quadratic response behaviour gets obvious if we remind that for any load-current component at frequency  $f_i$ , the direction of the magnetic field vector alternates simultaneously with the direction of the current density vector. Thus, for each half-wave the vector product of the magnetic volume force (5) is oriented in the same direction (Fig. 1).

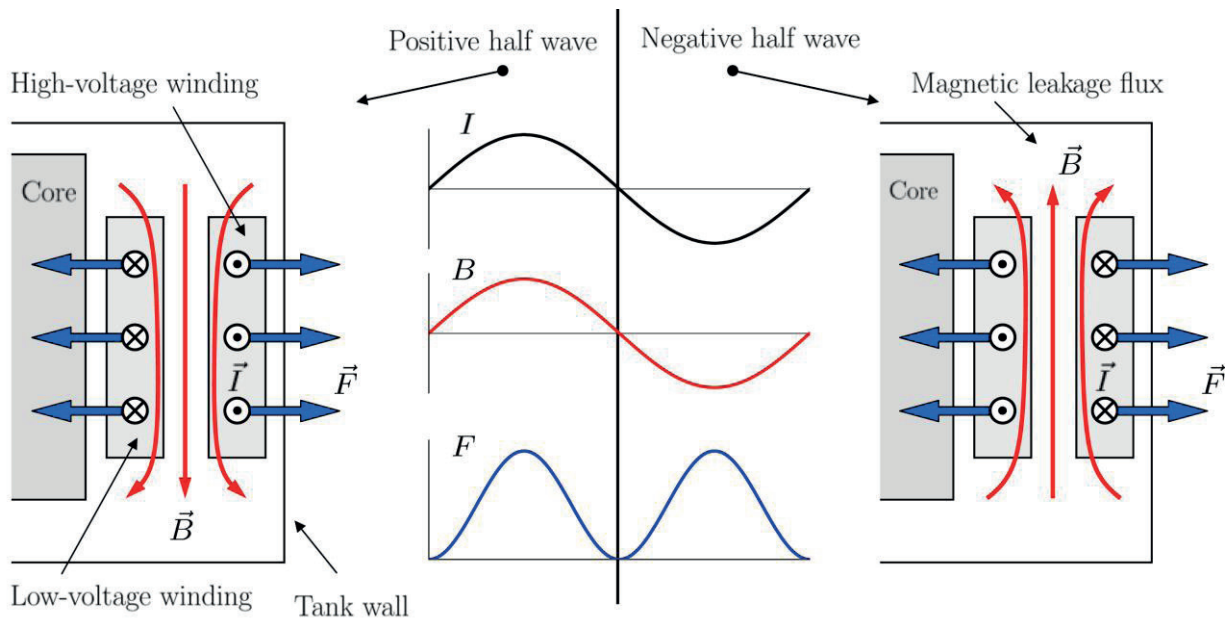


Figure 1: Quadratic response of the magnetic forces acting on the concentric windings of a transformer with respect to load-current.

The double sum in equation (7) can be split up into a sum of quadratic terms ( $i = j$ ) and a sum of product terms ( $i \neq j$ )

$$F_m(t) \propto \underbrace{\sum_{i=1}^N \hat{I}_i^2 \sin^2(\omega_i t + \varphi_i)}_{\text{quadratic terms}} + 2 \underbrace{\sum_{i=1}^{N-1} \sum_{j=i+1}^N \hat{I}_i \sin(\omega_i t + \varphi_i) \hat{I}_j \sin(\omega_j t + \varphi_j)}_{\text{product terms}} \quad (8)$$

Applying trigonometric identities, the two terms of equation (8) can be rewritten to

$$F_m(t) \propto \frac{1}{2} \sum_{i=1}^N \hat{I}_i^2 + \frac{1}{2} \sum_{i=1}^N \hat{I}_i^2 \sin \left[ 2\omega_i t + 2\varphi_i - \frac{\pi}{2} \right] + \sum_{i=1}^{N-1} \sum_{j=i+1}^N \hat{I}_i \hat{I}_j \sin \left[ (\omega_i - \omega_j)t + \varphi_i - \varphi_j + \frac{\pi}{2} \right] + \sum_{i=1}^{N-1} \sum_{j=i+1}^N \hat{I}_i \hat{I}_j \sin \left[ (\omega_i + \omega_j)t + \varphi_i + \varphi_j - \frac{\pi}{2} \right]. \quad (9)$$

Now, for each line in (9) we can deduce frequency components of the magnetic force:

#### Line 1: Constant component generation

Each of the  $N$  load-current harmonics contributes a force component at  $f = 0\text{Hz}$ . The resulting constant force component cause a static deformation of the winding and will add no dynamic vibrations. Therefore no sound pressure fluctuations are generated and the constant force component does not contribute to load noise generation (Fig. 2).

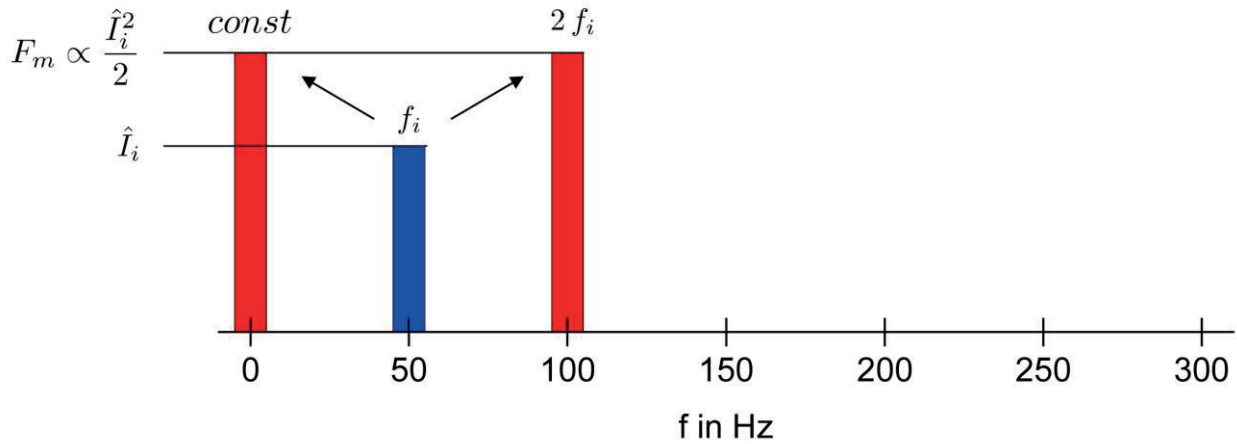


Figure 2: Generation of second harmonic and constant force component by quadratic terms

#### Line 2: Second harmonic generation

Each of the  $N$  load-current components generates further a force component at doubled frequency  $2f_i$ , in total again  $N$  magnetic force components. The amplitude of each component is proportional to the square of the load-current amplitude  $I_i$  and the phase  $2\varphi_i - \pi/2$  (Fig. 2).

### Line 3: Difference frequency generation

For each pair of load-current components  $n_i \neq n_j$ , the product terms in line 3 give rise to a magnetic force component at difference frequency  $|f_i - f_j|$  and phase  $\varphi_i - \varphi_j + \pi/2$  (Fig. 3). The amplitude of the magnetic force components is proportional to the product of the corresponding load-current harmonics  $I_i I_j$ . The product terms deliver  $N(N-1)/2$  force components at difference frequency.

### Line 4: Sum frequency generation

As in line 3, each pair of load-current components  $n_i \neq n_j$  generates further a magnetic force component at sum frequency  $f_i + f_j$  with same amplitude but differing phase  $\varphi_i + \varphi_j - \pi/2$  (Fig. 3). Again,  $N(N-1)/2$  magnetic force components are generated.

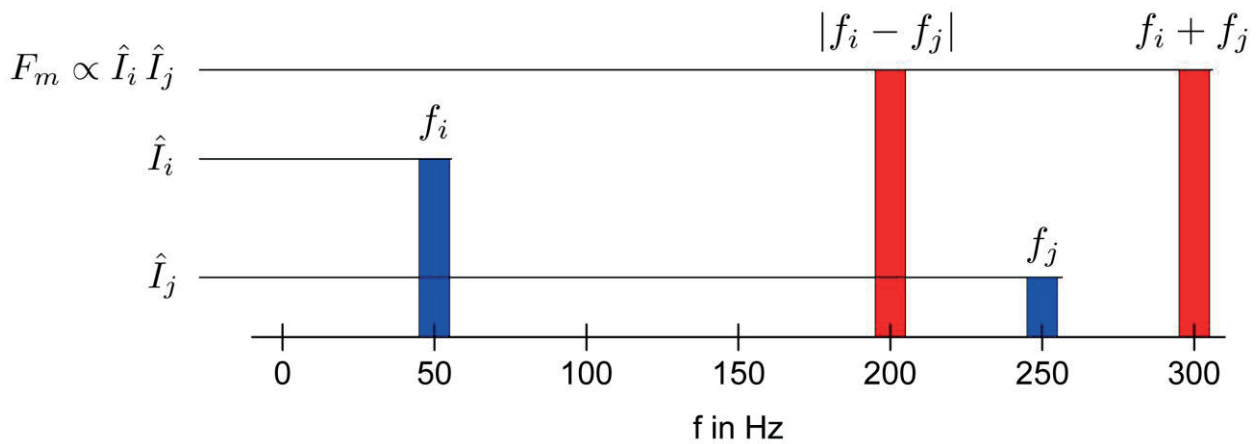


Figure 3: Generation of force components at sum and difference frequencies by product terms

In summary, for a load-current having  $N$  frequency components, the quadratic response behaviour results in a magnetic force having  $N^2$  frequency components at maximum (including the constant component at  $f = 0\text{Hz}$ ). Hereby, the quadratic terms in (8) are responsible for the generation of static force components and force components at doubled frequencies, whereas the product terms in (8) contribute force components at difference frequencies  $f_i - f_j$  and sum frequencies  $f_i + f_j$ . Since the arising force terms can have identical frequencies, the total number of arising magnetic force harmonics is at real conditions much smaller than the theoretical maximal number of force harmonics ( $N^2$ ) and typically in the range of  $2N$ . In case that force components have identical frequencies, vectorial addition of mono-frequent forces is performed to achieve the total magnetic force amplitude and phase angle at the corresponding frequency. Hereby the amplitude of the resulting magnetic force is determined by the phase angle relations of the involved force components. Since the superpositions can be constructive or destructive, the resulting total force component can show large variations in amplitude and phase.

### 2.3. Determination of the winding vibrations

A transformer winding typically consists of isolated conductors, spacers and pre-compressed boards which can be considered as a passive system of distributed mass, stiffness and damping. Thus, the winding assembly is a linear and lightly damped mechanical system able to vibrate which undergoes a forced vibration by distributed magnetic forces. For dynamic analyses, we start from the equation of motion

$$M\{\ddot{d}\} + C\{\dot{d}\} + K\{d\} = \{F_m\}, \quad (10)$$

whereby the mechanical multi-degree-of-freedom system is described by the mass matrix  $M$ , the damping matrix  $C$  and the stiffness matrix  $K$ . The vectors of acceleration, velocity, displacement, and magnetic force are denoted by  $\{\ddot{d}\}$ ,  $\{\dot{d}\}$ ,  $\{d\}$  and  $\{F_m\}$  respectively. The displacements are with respect to a rest position at which no dynamic forces act on the windings. For a single-degree-of-freedom subsystem of (10) with mass  $m$ , damping  $c$ , and stiffness  $k$ , the steady-state solution for forced vibration with a harmonic magnetic force  $F_m = \hat{F}_m \sin(\omega t)$  is (see, e.g. [4])

$$d = R \frac{\hat{F}_m}{k} \sin(\omega t - \theta). \quad (11)$$

The winding displacement is at the forcing frequency  $\omega$  and for a non-zero damping coefficient  $c$ , the phase  $\theta$  in equation (11) between the applied force and the resulting displacement is different than zero and given by

$$\theta = \tan^{-1} \left( \frac{2\xi\omega / \omega_n}{1 - \omega^2 / \omega_n^2} \right) \quad (12)$$

$$\text{with natural frequency } \omega_n = \sqrt{\frac{k}{m}}$$

$$\text{and fraction of critical damping } \xi = \frac{c}{2m\omega_n}.$$

In equation (11), the resulting winding displacement in radial or in axial direction is a linear function of the applied magnetic force and the effective stiffness in the considered force direction (radial or axial). This corresponds to Hooke's law in the linear-elastic range for a statically applied force. The dimensionless response factor  $R$  in (11) writes

$$R = \frac{1}{\sqrt{(1 - \omega^2 / \omega_n^2)^2 + (2\xi\omega / \omega_n)^2}} \quad (13)$$

and represents the amplitude ratio of the dynamic displacement to the displacement in case the force  $F_m$  were applied statically. In the stiffness-controlled frequency range at low frequencies ( $\omega \ll \omega_n$ ), the response factor  $R$  is about 1. It rises with higher frequencies and has its maximum in the damping-controlled range near the natural frequency ( $\omega = \omega_n$ ), and approaches zero in the mass-controlled range for high frequencies ( $\omega \gg \omega_n$ ), see Figure 4. The first natural frequency of a transformer winding assembly is typically below the first mechanical excitation frequency (100Hz/120Hz). Thus, the winding vibration can be considered as mass-controlled the steady-state solution of the equation of motion can be rewritten to

$$d \simeq \frac{\hat{F}_m}{k} \left( \frac{\omega_n}{\omega} \right)^2 \sin \omega t = \frac{F_m}{m\omega^2} \sin \omega t. \quad (14)$$

The homogeneous composition of the transformer windings (i.e. with periodic repeated substructures like conductor loops) allows us to assume an uniform viscous damping [4]. In this case, each mode in a damped multi-degree-of-freedom system responds as a simple damped oscillator as in equation (11).

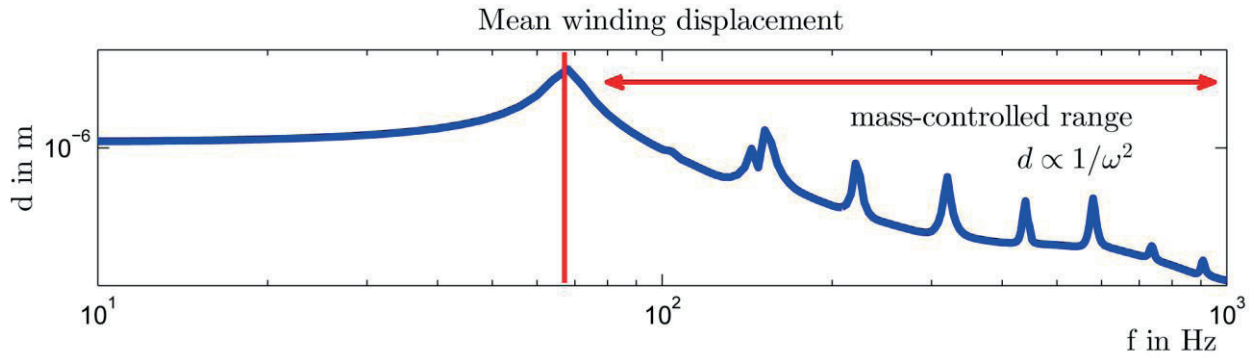


Figure 4: Frequency response characteristics of the mean displacement of a typical oil-immersed transformer winding representing a mechanical multi-degree-of-freedom system.

At nominal operation conditions of the transformer, the dynamic magnetic forces acting on the windings result in a linear-elastic stress-strain response within all materials of transformer winding assembly. Therefore we assume a mechanical linear system and apply a linear superposition of all frequency components of magnetic forces arising from load-current harmonics.

#### 2.4. Calculation of the radiated sound

The vibrating solid surfaces of the windings are in contact with the surrounding fluid (transformer oil) and displace the fluid volume at the structure-fluid-interface. As the fluid which completely surrounding the vibrational sources is essentially incompressible and there is no significant sound absorption in the fluid, the sound power transmitted through the fluid is conserved. In the low frequency range, where the distances of the windings to the tank are relatively small compared to an acoustic wavelength in the fluid, the net volume velocity of the windings will be translated to a net volume velocity of the tank. Interestingly, in this configuration the transmitted sound power is very insensitive to any details of the spatial distribution of the normal surface velocity [5].

For arbitrary shaped vibrating surfaces of finite size, the sound power  $P$  that is radiated into free field at a certain frequency can be estimated by the fundamental equation of vibroacoustics (see, e.g. [6]),

$$P = \sigma \rho c S \langle \overline{v^2} \rangle. \quad (15)$$

Hereby,  $\sigma$  denotes the frequency-dependent radiation factor (see below),  $\rho$  the density of air,  $c$  the speed of sound in air,  $S$  the total surface area of the vibrating body (here: the tank), and  $\langle \overline{v^2} \rangle$  the time-and-space-mean of the square normal surface velocity. Applying the mentioned net volume velocity balance between winding and tank wall surfaces, the mean square velocity of the tank can be calculated from the volume velocity of the windings. Hereby, the surface velocity at any winding location can be derived from the surface vibration amplitude  $d$  in (14). Using  $v = \dot{d} = \omega d$ , the time-mean square surface velocity at a location writes in the harmonic case

$$\overline{v^2} = \frac{1}{T} \int_0^T v^2(t) dt = \frac{\omega^2 \hat{d}^2}{2}. \quad (16)$$

The most uncertain parameter in the estimation of the radiated sound power is the radiation factor  $\sigma$ , which is a function of the frequency, geometry dimensions, material properties, and of the presence of any structural discontinuities (e.g. tank stiffeners, attached structures to the tank). The radiation factor is a measure for the sound radiation effectiveness of a vibrating structure. The transformation of structure-borne-sound (normal tank surface vibration) into air-borne sound changes with frequency due to the dispersive character of bending waves in the thin-walled tank. This leads to a frequency-dependent ratio of the structural bending wavelength and the wavelength of the radiated sound [5, 6].

Maximal conversion of sound energy occurs at and above the coincidence frequency  $f_c$ . At this frequency, the bending wavelength of the structure is identical to the wavelength of the sound wave in the surrounding fluid (total sound radiation). Below the coincidence frequency, the sound radiation efficiency decreases with frequency. In this frequency range, acoustic near field effects have to be considered. These are mainly the local compensation of sound pressure variation (acoustic short-circuit) and evanescent wave components that don't propagate to the far-field [5].

#### 2.4.1. The radiation factor of transformer tanks

All dominating sound components of transformer load noise are below the coincidence frequency of the transformer tank. Therefore we need a sufficient accurate determination of the frequency response curve of the radiation factor to estimate the contribution of each frequency component to the total load noise level. The radiation factor  $\sigma$  can be determined by measurements or by numerical calculations. In an analytical approach, the sides of a transformer tank can be considered as rib-stiffened, flat plates with a added mass by the one-sided heavy fluid load of the oil [5]. The radiation factor of this configuration shows the typical frequency-response characteristics of Fig. 5. The radiation factor approaches unity at the coincidence frequency  $f_c$  within the frequency band of transformer noise. Larger transformer tanks have a coincidence frequency  $f_c$  at lower frequencies, so that they show a better radiation efficiency for higher load noise harmonics. In case that no measurement or numerical data are available, it is a good starting point for a typical power transformer to set  $f_c \approx 600\text{Hz}$  and set the rise of the radiation factor to be 7dB per octave for frequencies below  $f_c$ .

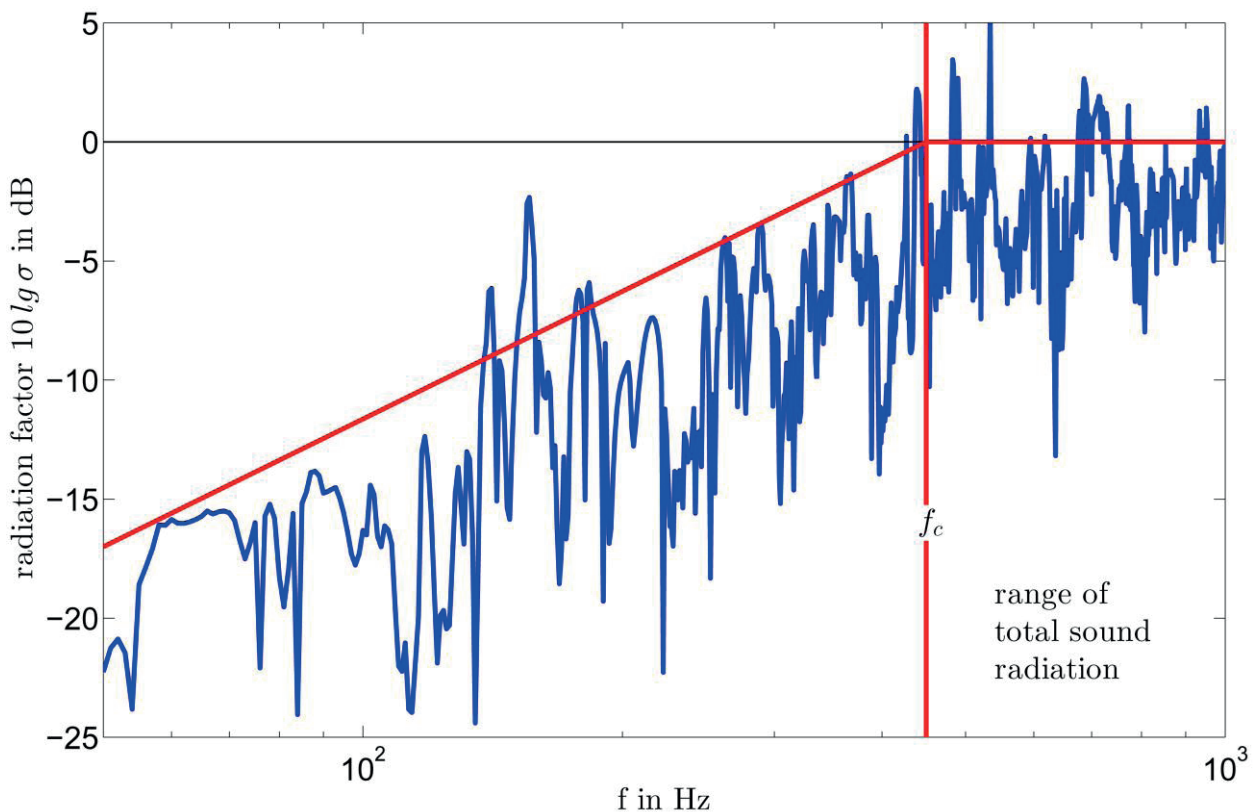


Figure 5: Typical sound radiation factors of a oil-filled 150MVA transformer. Data based on Finite-Element analyses including the fluid-structure-coupling at the surfaces oil-tank-air.

For a first approximation of the radiated sound power, any further changes of the sound radiation characteristics arising from the modal response of the tank or internal fluid-structure-interactions like acousto-structural mode coupling or cavity modes are not considered in this investigations. Hence the modal averaged radiation factor of a transformer tank as shown by the red line in Fig. 5 is used in equation (15).

### 2.4.2. The determination of a load noise component

By using the magneto-mechanical coupling term (9), the solution of the equation of motion (14), the fluid-structure-coupling term (15) and equation (16), the sound power generated by a magnetic force component at any frequency can be written to

$$P(f) = C \sigma \hat{F}_m(f)^2 . \quad (17)$$

The added constant  $C$  unites all non-frequency-dependent parameters which arise in the underlying equations mentioned above. As we will see later, the actual value of the constant  $C$  is of no interest for the calculation of sound level differences due to load harmonics.

The related sound power level generated by a magnetic force component acting on the windings can be finally written as

$$\begin{aligned} L_w &= 10 \lg \frac{P}{P_0} \text{ dB} \\ &= 10 \lg (C \hat{F}_m^2) + L_\sigma \quad \text{with} \quad L_\sigma = 10 \lg \sigma , \end{aligned} \quad (18)$$

whereby  $P_0 = 2 \times 10^{-12} \text{ W}$  denotes the reference sound power at the auditory threshold and  $L_\sigma$  the level of radiation efficiency.

### 2.5. Total load noise and A-weighting of noise harmonics

The international standard for the determination of the sound levels of transformers [7] specifies the use of the A-weighting filter for transformer sound measurements (Fig. 6). This is to suppress sound signals at low and high frequencies and thus account for the lower sensitivity of the human ear in this frequency regions.

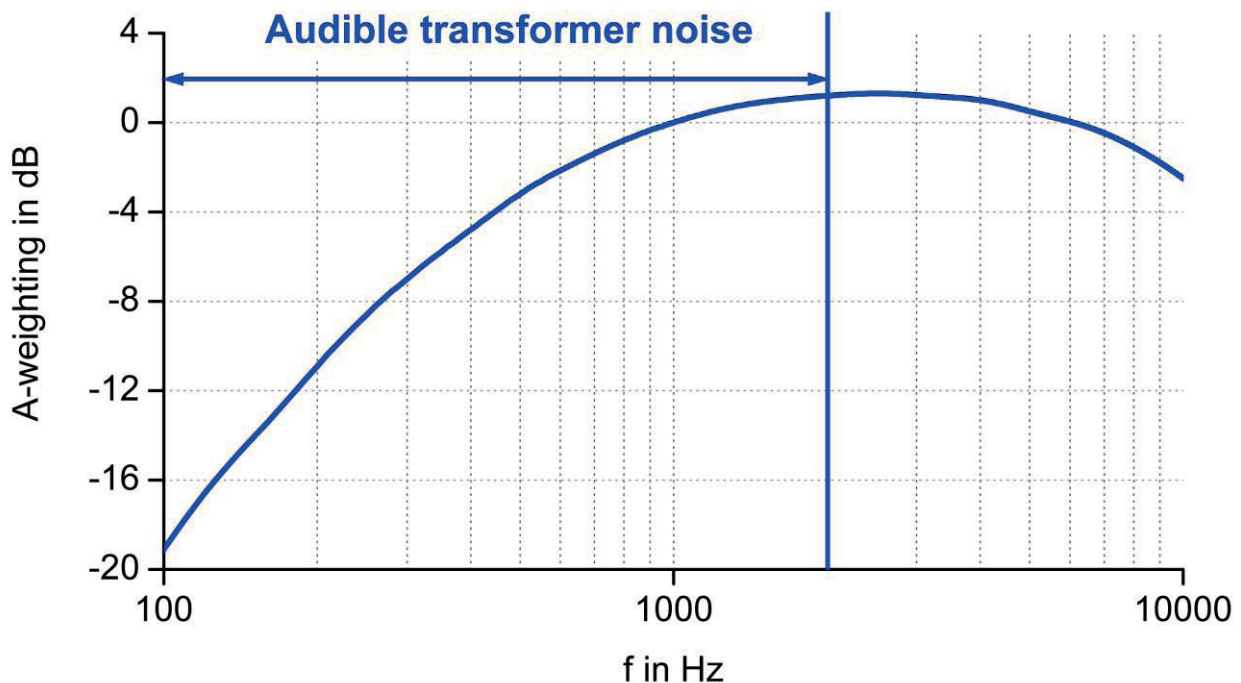


Figure 6: The A-weighting curve suppresses the lower frequency components of audible transformer noise.

The A-weighted sound power level of a sound frequency components reads

$$L_{WA} = (L_W + A) dB(A) \quad (19)$$

whereby  $A$  denotes the correction term due to the frequency-dependent A-weighting filter. The total A-weighted load noise sound power level of a transformer having load-current harmonics  $L_h$  can be achieved by logarithmic addition of all sound components whose levels  $L_i$  are calculated according to equation (19):

$$L_h = 10 \lg \left( \sum_i^N 10^{L_i/10} \right) dB(A) \quad (20)$$

In absence of higher harmonics in the load-current, the load noise of a transformer has solely one fundamental sound component

$$L_n = \left( 10 \lg \left( C \hat{F}_n^2 \right) + R_1 + A_1 \right) dB(A) \quad (21)$$

Hereby  $A_1$  denotes the A-weighting of the fundamental sound component which is generated by the fundamental magnetic force component at twice the line frequency

$$F_n(t) \propto \frac{\hat{I}_1^2}{2} \cos 2(\omega_1 t + \varphi_1). \quad (22)$$

Note that the sound level of the fundamental sound component  $L_n(f_1)$  in the absence of harmonics can differ from the corresponding sound level  $L_1(f_1)$  in the presence of harmonics. This change originates in additional magnetic force components which are superposed to the fundamental force component in the presence of harmonics by the difference frequency generation according to line 3 of equation (9).

Eventually, the load noise increase due to harmonics in the load-current corresponds to the level difference

$$\begin{aligned} \Delta L &= L_h - L_n \\ &= 10 \lg \left( \frac{\sum_i^N \left( \hat{F}_i^2 10^{(R_i + A_i)/10} \right)}{\hat{F}_n^2 10^{(R_1 + A_1)/10}} \right) dB(A). \end{aligned} \quad (23)$$

By taking the difference of logarithms, the (unknown) non-frequency dependent parameter  $C$  cancels out.

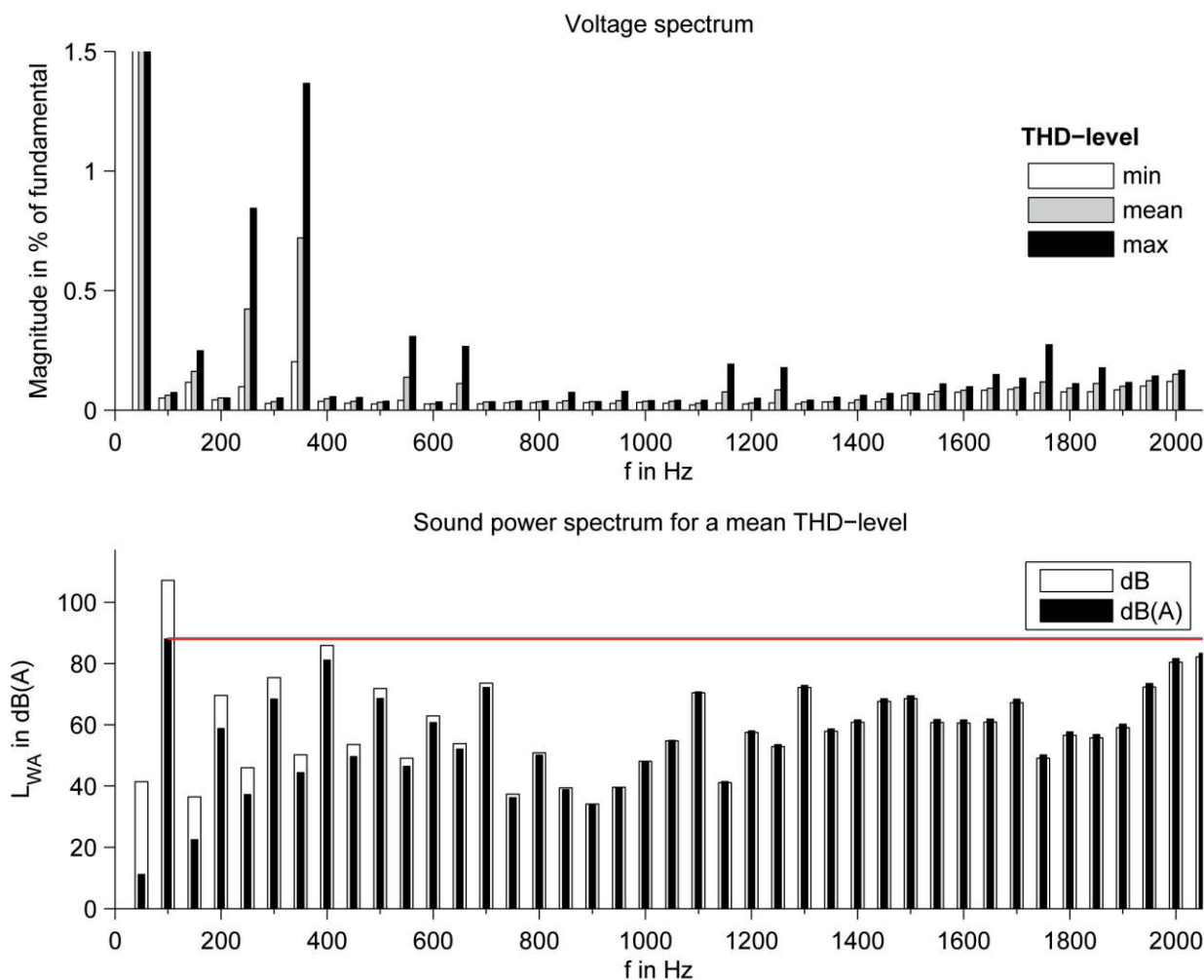


Figure 7: Example 1: Sound spectra for voltage harmonics in a 400kV power line at different harmonic distortion levels

### 3. PRACTICAL EXAMPLES OF LOAD NOISE INCREASE AT LOAD HARMONICS

The presented calculation scheme for load noise increase at power grid harmonics is applied to two practical examples for further analyses of the generation process of load noise harmonics.

#### 3.1. Example 1: Voltage harmonics in a 400kV power line

The first example is related to a step-down oil-immersed power transformer with a rated power of 300MVA and a nominal load noise level of  $L_{WA} = 88\text{dB(A)}$ . To estimate the increase in load noise due to load harmonics, we consider the voltage spectra in a German 50Hz/400kV power grid for three different total-harmonic-distortion levels (THD) as shown in Figure 7.

The THD is defined as the amplitude ratio

$$THD = \frac{\sqrt{\sum_{i=2}^N \hat{I}_i^2}}{\hat{I}_1} \quad (24)$$

The standard EN 50160 [8] defines the voltage characteristic of electricity supplied by public supply networks and limits the THD of the supply voltage including all harmonics up to the order 40 to a

maximum of 8%. The related load noise increase due to load-current harmonics in this example is summarised in Table I. Already at a mean total-harmonic-distortion-level of 1% - which is far below the allowed tolerance level of EN 50160 - the psycho-acoustical relevant A-weighted sound power level increases by about 3dB. This sound level increase is clearly noticeable by the human perception of noise and corresponds formally to a doubling of the sound energy (twice the number of transformers).

Table I: Load noise increase by power grid harmonics without and with A-weighting

Distortion level	THD in %	$\Delta L$ in dB	$\Delta L(A)$ in dB
min	0.4	0.0	1.6
mean	1.0	0.0	2.9
max	1.8	0.0	5.8

### 3.2. Example 2: Load harmonics at distribution transformers in a computer centre

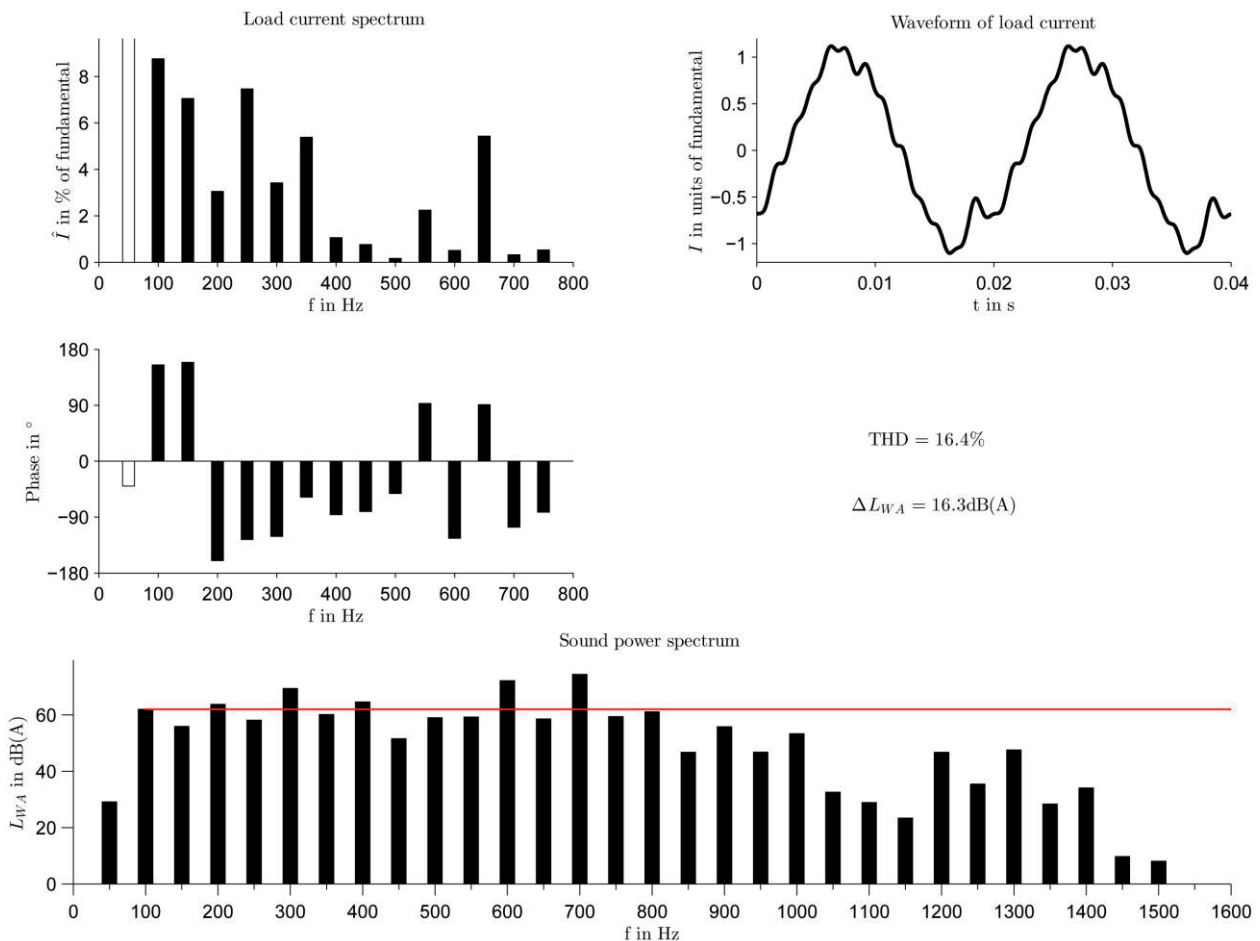


Figure 8: Example 2: Load noise sound spectrum of a distribution transformer with extraordinary high harmonic distortion

The second example is related to a 150kVA distribution transformer in a computer centre which was reported to be extraordinarily noisy. The transformer operates at a load factor of about 0.7 and the distinctive non-linear power consumption of converters in electronic equipment draws high distortion in the current waveform. The phase relations of the load-current components were also measured (Figure 8).

The presented calculation scheme shows magnetic force components with amplitudes up to 20% of the fundamental force component (Table II). The increasing sound radiation efficiency and A-weighting with rising frequency results in sound harmonics that largely exceed the fundamental sound component at frequencies below 700Hz. The corresponding increase of the total load noise level is 16.3dB(A) for a harmonic distortion of THD=16.4%.

Table II: Parameter related to the generation of load noise harmonics in Example 2. Magnetic force components and the resulting sound level differences are relative to the fundamental component at 100Hz.

Harmonic component $f$ in Hz	Magnetic force $F / F_0$ in %	Radiation factor $L_\sigma$ in dB	Sound level difference $\Delta L$ in dB
50	14.7	-22.1	-32.9
100	100.5	-17.0	0.0
150	19.5	-14.0	-6.0
200	26.2	-11.9	1.8
250	8.8	-10.3	-3.9
300	23.0	-8.9	7.4
350	6.0	-7.8	-1.8
400	8.0	-6.8	2.6
450	1.5	-5.9	-10.5
500	2.9	-5.2	-2.9
550	2.6	-4.5	-2.7
600	10.0	-3.8	10.2
650	1.9	-3.2	-3.4
700	10.4	-2.7	12.5

### 3.3. Example 3: Load harmonics at a HVDC-transformer

The interconnecting of a high-voltage, direct current (HVDC) electric power transmission line within an AC system requires the conversion from AC to DC and inversion from DC to AC. In both cases, the converter operation in HVDC substations results in AC current harmonics. By the half wave symmetry of pulse rectifiers, no even harmonics and no triplen (multiples of 3rd) harmonics are generated [9]. The stepwise change in load-current during the commutation from one valve to another results in the characteristic distribution of mainly odd harmonics from the 5th upwards (Fig. 9). This results in a very high harmonic distortion of THD=29% .

The sound power of a transformer in a HVDC substation was measured on-site using the sound pressure method according to the international standard [7]. The measured total sound increase of the transformer was  $\Delta L_{WA} = 21.9$  dB(A) compared with the nominal sound level of the transformer at the acceptance test without load harmonics. Beside the load noise, the emitted noise comprises also the no-load noise caused by magnetostriction and magnetic forces in the transformer core. The valve operation will give rise to a DC-magnetisation in the core, which can be identified by the existence of odd harmonics in the sound spectrum. Unfortunately, the sound signals of both sound sources can not be separated in the operation of a HVDC transformer. Thus, the calculated sound increase of 16.8dB(A) due to load-current harmonics is smaller than the measured total sound increase due to load harmonics and DC-magnetisation.

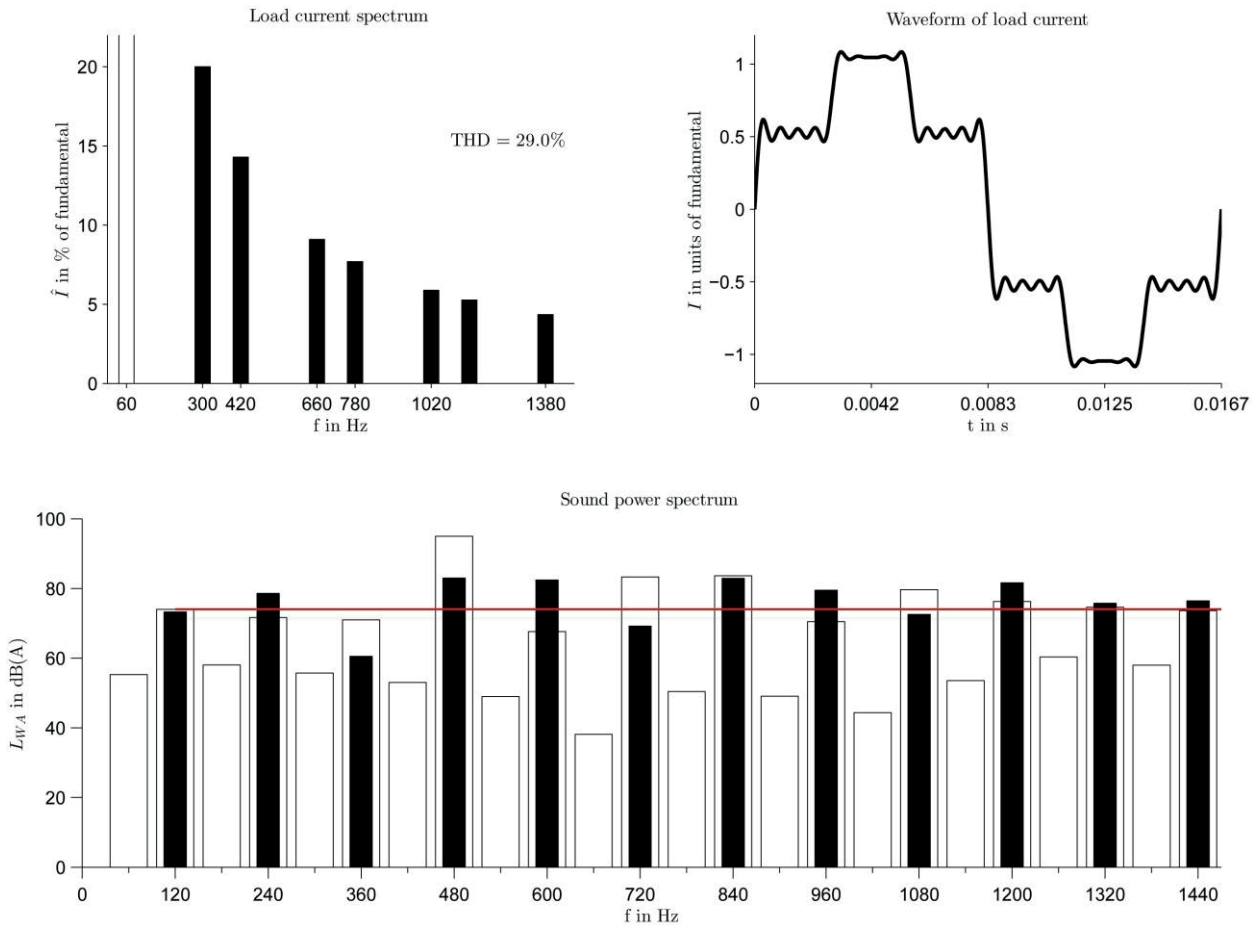


Figure 9: Example 3: Comparison of the calculated load noise spectrum and measured total sound spectrum (load noise and no-load noise) for a HVDC-transformer in operation. The measured odd harmonics are due to DC-magnetisation of the core.

In this example, we can study further the generation of sound component by the pronounced odd harmonics of the load-current. By the quadratic response of magnetic forces to load-current, the arising sound components are dominated by even harmonics as a result of the second harmonic, difference and sum frequency generation as described in equation (9).

#### 4. DISCUSSION AND RESULTS

##### 4.1. Effect of the A-weighting to the increase of the load noise level

Higher harmonics in the load-current have a disproportionately high impact to the total load noise level of the transformer. The main reason for the increase of the total noise level is the large rise of harmonic sound components by the A-weighting filter relative to the A-weighted fundamental sound component (Table III).

Table III: Rise of higher sound harmonics by the A-weighting filter.

f in Hz	200	300	400	500	600	700	800
$\Delta L$ in dB(A) re 100Hz	8.3	12.1	14.4	15.9	17	17.8	18.4

The A-weighting-effect can be clearly seen in the sound power spectrum of example 1 (see Fig. 7 and Table 1). Here, the load noise increase without A-weighting is negligible whereas the increase of the relevant A-weighted sound level is of practical interest.

## 4.2. Effect of the phase relation of load-current harmonics

Next, the effect of the phase relations in load-current components to the total load noise level is investigated. The load-current amplitude spectrum of example 2 is taken and a total variation of the phase relations of all load-current components is performed in the range  $\varphi = [0; 2\pi]$ . For each phase relation, the sound spectrum and the total load noise level are calculated.

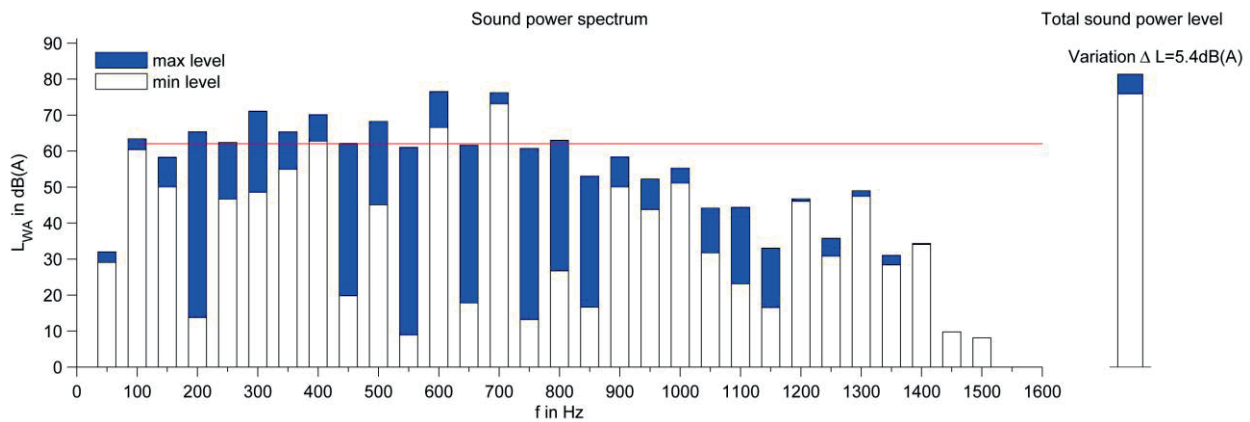


Figure 10: Maximal variation of load-noise components and the total load noise level by variation of the phase relations

Figure 10 shows the maximal variation of each individual sound component and the total load noise level caused by variations in the phasing of load-current harmonics. Depending if magnetic force components are added constructively or destructively, sound components vary up to 50dB by changed phase relations. The variation of the total noise level of 5.4dB due to changed phase relation is typical for transformers operating at a high harmonic distortion level. Thus we conclude, that for a useful estimation of the load noise increase due to load harmonics, the knowledge of the phase relations is required - at least for the dominant harmonic components.

## 4.3. Evaluation of the impact of a single harmonic load component

A graphical representation of the load noise increase due to a single harmonic load component is given in Figure 11 for the first 22 load-current harmonics at a fundamental frequency of 50Hz. Hereby the amplitudes of all other load-current harmonics are set to be zero. Further, the phase angle between the investigated single harmonic component and the fundamental component is also set to be zero.

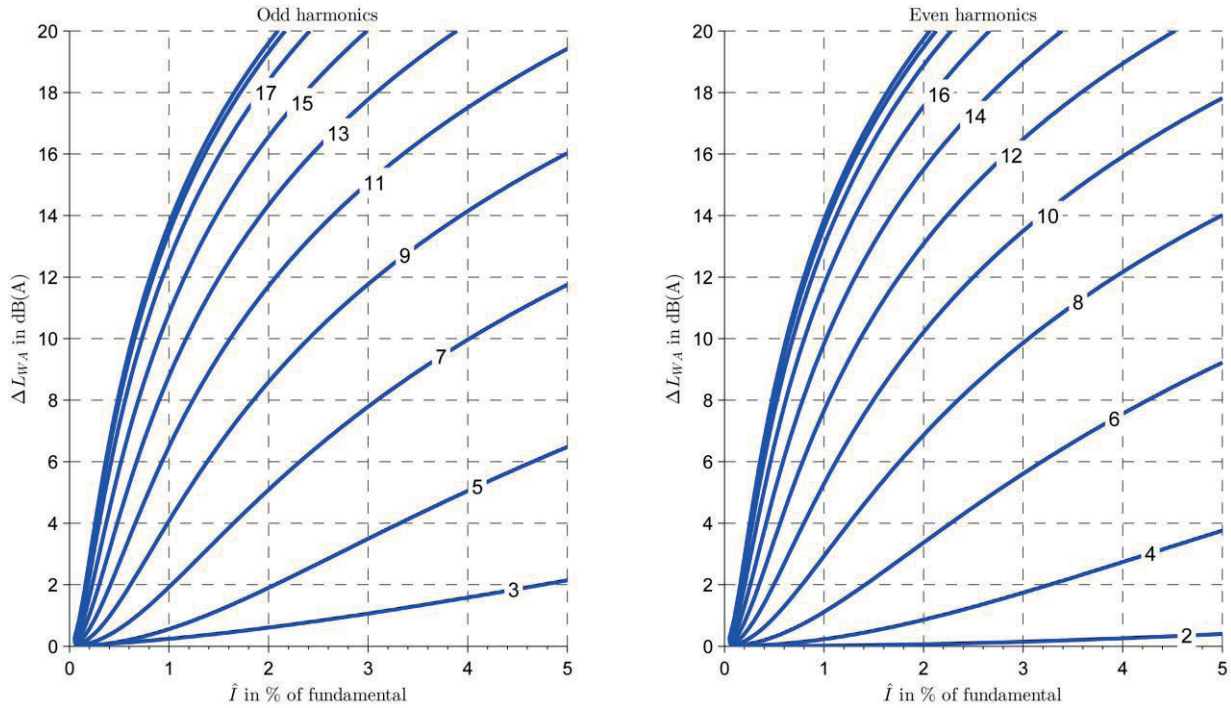


Figure 11: Load noise increase by a single harmonic component of the load-current for a typical 300 MVA power transformer.

Now we compare the increase in the load noise level by the existence of a single load-current component at a constant relative amplitude (vertical line in Fig. 11). Whereas the impact of low order harmonics is negligible due to the suppressing effect of the A-weighting, the higher harmonics will dominate the increase of the total load noise. Thus, the graph reflects again the dominating effect of the A-weighting.

Figure 11 can be used also for a rough graphical determination of the load noise increase by load harmonics. Hereby, the load noise increase  $\Delta L_i$  due to a single harmonic component is taken for each significant component in the load-current spectrum. The increase in the total load noise level  $\Delta L_h$  can be calculated then by logarithmic addition of all  $N$  components of  $\Delta L_i$  according to <sup>1</sup>

$$\Delta L_h = 10 \lg \left( 1 - N + \sum_i^N 10^{\Delta L_i / 10} \right) \text{dB(A)}. \quad (25)$$

## 5. CONCLUSIONS

The presented calculation scheme describes the change of the acoustic source strength of transformers at load due to load harmonics and offers a fast and sufficiently precise prediction of the increase in the load noise level. The disproportionately high impact of load harmonics to the total load noise level is attributed to the rising sound radiation efficiency of the transformer tank with frequency as well as the higher rating of harmonic sound components by the A-weighting filter.

By the analysis of the generation process of load noise harmonics we can further conclude:

- 1) To estimate the total load noise increase, it is sufficient to consider only force components where the fundamental load-current component is involved.
- 2) For a given current amplitude, high order load harmonics have the largest impact to the load noise increase.
- 3) Information of the phasing of load-current harmonics is required for a reliable estimation of load noise components and the total load noise level.

<sup>1</sup>The term  $1 - N$  originates in the fact that each sound level increase  $\Delta L_i$  due to a single harmonic component includes also the fundamental sound component.

The presented calculation scheme represents the minimum level in load noise increase we can expect. In measurements, the increase in the load noise levels by load-current harmonics tends to be higher. The main reason therefore is that the higher number of magnetic force components increases the probability of excitation of resonant vibrations in structural parts of the transformer (core, windings, tank) and the excitation of acoustical resonances (cavity modes inside the transformer tanks).

## REFERENCES

- [1] J. Lundquist, On harmonic distortion in power systems, Master thesis, Chalmers University of Technology, Gothenborg, Sweden (2001).
- [2] A. A. Elmoudi, Evaluation of power system harmonic effects on transformers: Hot spot calculation and loss of life estimation, Ph.D. thesis, Helsinki University of Technology (2006).
- [3] S. Kulkarni, S. Khaparde, Transformer Engineering: Design and Practice, 1st Edition, CRC Press, 2004.
- [4] C. Harris, A. Piersol, Harris' Shock and Vibration Handbook, 5th Edition, McGraw-Hill, 2002.
- [5] F. J. Fahy, P. Gardonio, Sound and Structural Vibration. Radiation, Transmission and Response, 2nd Edition, Academic Press, 2006.
- [6] P. Norton, G. Karczub, Fundamentals of Noise and Vibration Analysis for Engineers, 2nd Edition, Cambridge University Press, 2003.
- [7] IEC 60076-10 Power transformers - Part 10: Determination of sound levels (2001).
- [8] EN 50160 Voltage characteristics of electricity supplied by public distribution networks (2010).
- [9] The Energy Networks Association, Managing Harmonics - A Guide to ENA Engineering Recommendation G5/4-1, Third Edition, 2005.

C.J.G. Spoorenberg  
SGB - Smit Transformers Nijmegen  
[c.spoorenberg@smit-trafo.nl](mailto:c.spoorenberg@smit-trafo.nl)

## STATISTICAL ANALYSIS OF TEMPERATURE RISE TEST FOR INCREASED ACCURACY ON X- AND Y- EXPONENTS

### SUMMARY

On a large number ( $> 50$ ) of identical large power single-phase autotransformers ONAF temperature rise test have been performed as part of the customer specification. Part of the 24 hour test is a 125% overload for 8 hours. Based on this data one can statistically evaluate aspects as average value, standard deviation and correlation on many parameters.

Measurement tolerances have a large influence on the top oil exponent  $x$  and the winding exponent  $y$ . The calculation of  $x$  and  $y$  is determined by the ratio of two temperature differences due to a load difference, which can result in larger errors than expected.

In two transformers fibre optic (FO) sensors were installed in the common winding to measure the hot-spot, not only during steady state, but also during transient conditions. For ONAF cooling, a step increase of load takes a relatively long time before the oil flow reaches a steady state, as is described in the loading guide. The overshoot in the gradient between the hot-spot temperature and the top oil temperature is demonstrated and can influence the hot-spot gradient exponent  $z$ .

Based on the test results and a statistical simulation one can conclude that the normal tolerances in the temperature- and resistance measurements, result in a large standard deviation in the exponents  $x$  and  $y$ . Use of the exponents  $x$  and  $y$ , based on a heat run of one single transformer, should be handled with extreme care. In case of doubt, the use of the exponents given in the loading guide result in a safe margin when determining the overload capabilities of a transformer.

### 1. INTRODUCTION

The top oil exponent  $x$  ( $n$  in the IEEE standard [6]), the winding gradient exponent  $y$  ( $2.m$  in the IEEE standard [6]) and the hot-spot gradient exponent  $z$  determine the overloading capabilities of transformers as described in the standards ([1], [2] and [3]). Several published papers ([4] and [5]) present test data on these exponents for some large power transformers based on temperature rise tests. In this paper these exponents are determined for more than 50 large power transformers, all of the same identical design. Each transformer was subject to a 24 hour temperature rise test, consisting of a start with all coolers closed, then stabilizing at 100% load at ONAF which was followed with a 125% overload for 8 hours. Based on the large amount of test data, one can determine average value and standard deviation for the exponents and relate those to the standards. Based on a statistical theoretical simulation, taking into account all the tolerances on resistance and temperature measurement, the standard deviation on the factors  $x$ ,  $y$  (and  $z$ ) can already be explained.

## 2. DATA ANALYSIS OF A LARGE NUMBER OF TEMPERATURE RISE TESTS OF TRANSFORMERS OF IDENTICAL DESIGN

In the time frame of about 5 years, between the end of 2005 and the beginning of 2011, temperature rise tests were performed on about 50 transformers of the same identical design. The test environment remained essentially the same within this time frame, although investments in air cushion transportation and repositioning the capacitorbank took place in 2008. Investments in new test equipment in 2007 for the resistance measurements increased the accuracy on the cooling down curve. From a statistical point of view the ambient and the test equipment did not change in this timeframe.

## 3. DESCRIPTION OF TRANSFORMER DESIGN WITH MAIN CHARACTERISTICS

The transformers are a 280 MVA - ONAF cooled single-phase autotransformers 500 / 230 kV with +/- 5% DETC on the HV side. The transformer is a two-leg design and the common- and the series windings are Smit disk windings with axial cooling channels.



Picture 1 Active part in lifting crane before putting into tank



Picture 2 Smit disk winding on vertical winding machine

### 3.1. Presentation of data and results.

The gradients are determined as the difference between average winding temperature and average oil temperature ([3] – 11 but also [1] – 7.7 ) and by the cooling down curve when cooling down to a constant value ( [1] appendix C - Figure C3 with  $A_0$  is constant ). The results of all test values, as an average value and the standard deviation as according the Gauss distribution, are summarized in a table 1. The design values are also presented for comparison reasons.

The influence of the losses of the transformers on the temperatures can be neglected. The no-load loss has an average value of 56.8 kW with a standard deviation of 2.8 kW. The values for the load losses in tap 1 are 405 kW and 3.4 kW respectively. The resulting standard deviation on the total losses, might only contribute for a standard deviation of < 0.5 K on top oil rise and average winding rise.

Due to the two different loads ( 280 MVA and 350 MVA ) during the temperature rise test, one is able to determine the value of the exponents  $x$  and  $y$  on each transformer ( table 2 ). The  $x$  - exponent is calculated based on the top-oil rise and on the average oil rise . ( see table 2 ) The average value of  $x$  is 0.78 ( standard deviation 0.12 ) respectively 0.85 (standard deviation 0.1) and this corresponds well with the value of 0.8 according to the present standards.

There is a large difference in standard deviation between the  $y$  - exponent based on average winding – average oil and on the cooling down curve. The values of  $y$  between 1.4 to 1.5, based on cooling down curve, do not fully correspond with the value of 1.3 ([2] -table 5) in spite of the small standard deviation of 0.12 to 0.14.

The value of the  $y$ -exponent based on the average winding – average oil is much higher than 1.3 but the standard deviation is also very high ( 0.35 or 0.39). One may conclude that the value of the  $y$ -exponent, as determined by the tests, is not within the bandwidth of the IEC standard and [4] (see table 2).

Remark : Based on the Gauss curve, 68% of all test values are within a bandwidth defined by average minus standard deviation and average plus standard deviation. Also 95 % of all test values are within a bandwidth defined by average minus 2 x standard deviation and average plus 2 x standard deviation.

Table 1		Test data of more than 50 temperature rise tests.					
		280 MVA			350 MVA		
		Design values	average value	Standard deviation	Design values	average value	Standard deviation
HV	Twinding shutdown		75.8	5.39		102.5	5.85
	Time constant		9.3	0.58		8.2	0.39
	Delta T winding-oil (curve)	15.0	14.7	0.53	20.9	20.7	0.63
	Delta T oil (curve)	35.7	38.5	2.25	53.3	55.9	2.43
	Delta T winding-oil		10.6	2.09		16.6	2.51
	Delta T oil		42.2	2.26		59.6	2.82
	Delta T-winding	50.7	52.8	2.34	74.3	76.2	2.69
	LV	Twinding shutdown		78.3	5.00		105.3
Time constant			9.2	0.76		8.0	0.54
Delta T winding-oil (curve)		16.2	16.5	0.75	22.1	22.7	0.97
Delta T oil (curve)		37.3	38.8	2.20	55.1	56.2	2.36
Delta T winding-oil			13.0	2.19		19.3	2.68
Delta T oil			42.2	2.21		59.6	2.79
Delta T-winding		53.5	55.2	2.17	77.2	78.9	2.50
Top oil rise		48.6	52.9	2.20	67.3	72.4	2.6

Table 2		exponents x and y of test data compared with IEC and ref [4]			
	IEC 60076 7	Average value	Standard deviation	Average value [4]	Standard deviation [4]
x - component average oil		0.85	0.12		
x - component top oil	0.80	0.78	0.10	0.71	0.05
y - HV	1.30	2.04	0.40	1.12	0.36
y - HV (curve)		1.52	0.14		
y - LV	1.30	1.79	0.35	1.12	0.36
y - LV curve		1.43	0.12		

The temperature rise test was performed according to IEEE standards [3]. The cooling down curve is measured after stabilization of the top-oil rise, but not necessarily immediately after that point in time. During switch off and resistance measurement one needs extra personnel and one wants to organize the temperature rise test in such a way that it fits convenient within the time schedule of the test department. This results in a large variation in time of the first switch-off after start of the temperature rise test and consequently explains a part of the large standard deviation in the top oil exponent x. (see figure 1). It is clear that there is a relation between the value of x and the time after switch off. Due to the relative large standard deviation, one can only make an estimate of this relationship. This is expressed in figure 1, including an estimated bandwidth of +/- 0.1, which complies with the standard deviation as according table 1.

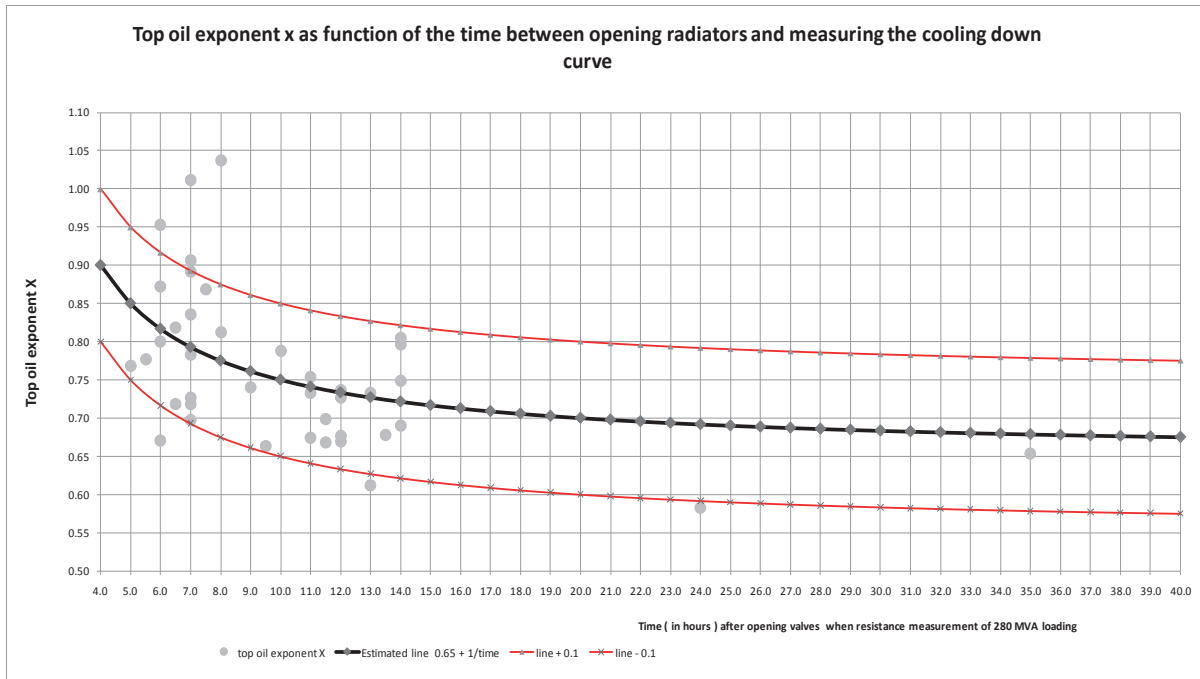


Figure 1 Top oil exponent x as function of time of switch off after opening cooler valves

As part of this investigation, the cooling down curve was measured twice for two transformers at 280 MVA. One time after stabilization, so about 8 hours after the start of the temperature rise test ( 280 MVA – first ) and for the second time at the end of the 24 hour test ( 280 MVA – at end ). In the latter case the 280 MVA load at the end lasted also about 8 hours after the shutdown of the 125% overload. The x exponents decrease of about 0.2 on average( see also figure 1 ). This is due the fact that at first shut down the temperatures are not fully stabilized starting from no load, although the it is according to the standards. At the shut down at the end, the temperature might also not be fully stabilized starting from a previous overload.

### 3.2. Temperature test with FO sensors.

In the loading guide ( [ 2 ] – table 5 ) the exponents x and y are defined, but also the dynamics of the hot-spot over top oil, by the factors k11, k21 and k22. As part of this investigation, two transformers are equipped with some FO sensors. One transformer ( serial number 3230146 ) had the normal temperature rise test and the sensors were placed in both LV and HV winding [8]. For the second transformer ( serial number 3230204 ) the temperature rise test started with nominal current and all cooling in operation.

The two major aspects of investigation are:

- The hot-spot gradient exponent z, which determines the increase in hot-spot gradient to top-oil in the steady state situation, can be calculated out of the gradients at the different loads.
- The dynamic behavior of the hot-spot gradient to top-oil in the case of change of load, when there is no change in cooling. This overshoot in the gradient is described in figure 9 of reference [2] by the function  $f_2(t)$  .

The temperature rise test started with nominal current and all coolers and fans in operation and the FO sensors were only assembled in the LV windings, but also sensors were mounted at the outlet of the LV windings to measure the oil exit temperature. The temperature rise test started with 100% current and all cooling in operation, to measure the overshoot in the case a cold transformer is put in service at nominal load. Also in this case one is able to estimate the value for sensor 1 of about  $( 34.5K - 0.0K ) / ( 20.0K - 0.0K ) = 1.7$ . The value for sensor 3 is  $35.3K / 19K = 1.85$

This overshoot is related to the gradient of the sensor minus the average top oil temperature as measured at the cover of the tank by the sensors immersed in the oil.

The FO sensors measuring the temperature gradient between top oil that exits the winding and the average top oil temperature have quite a similar behavior although positioned in different phases, but have a difference of several degrees. This also complies with figure 6 in reference [4].

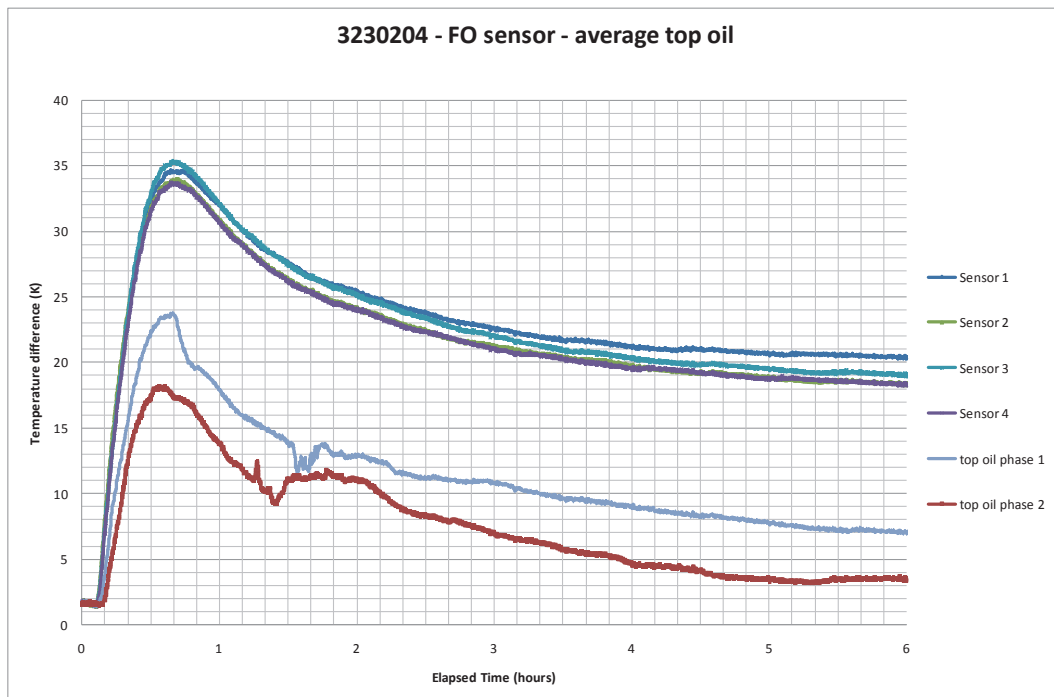


Figure 2 Temperature difference of FO sensors and averaged top oil.

#### 4. INFLUENCE OF TOLERANCES ON THE EXPONENTS X AND Y DETERMINED BY STATISTICAL SIMULATION.

As a starting point one has the parameters to be measured and the tolerances on each parameter.

Tolerances are not only related to the accuracy of the test equipment, but also related to the test set up such as (accurate) location of the sensors for the ambient temperature, the bottom oil temperature and the top oil temperature. Some tolerances are also related to the test environment such as the positioning of the large power transformer within the test department laboratory and the steady state temperature condition of the transformer when the transformer is positioned, due to the “outside” ambient temperature. Some of these tolerances are more or less exact, but others have to be estimated. The combination of all these tolerances can be simulated by the using the statistical features of Excel.

##### 4.1. Definition of parameters and their tolerances

For each parameter as defined in the IEC one can determine the measurement tolerance (table 3: column 2 until 17) and by using these tolerances and taking the average test values as input (table 1), one can simulate all the test values. The input parameters, which are measured data, are marked with a yellow colour.

The reference resistance has to be determined and is usually done in the factory with an tolerance in ambient temperature of  $\pm 0,5\text{ }^{\circ}\text{C}$  (column 2 with reference =  $13\text{ }^{\circ}\text{C}$ ). This cold resistance measurement has a tolerance of  $\pm 0,15\%$  (column 3 with reference =  $0.07183\ \Omega$  ([1] – 7.1.1.))

Warm resistance measurement after switch off has the same tolerance (resistance  $\pm 0,15\%$  (column 4 with reference =  $0.09074\ \Omega$ )).

The tolerance due to the extrapolation of in the cooldown curve for determining the winding temperature is estimated to be  $\pm 0.5\text{ }^{\circ}\text{C}$ . (column 5 - [1] – 7.5.)

To determine the winding temperature rise (column 7 - [1] – 7.6) one has to subtract the ambient temperature, as measured by sensors at the half height of the coolers and the ambient air temperature at the inlet of the fans. ([1] – 7.1.1) The ambient air temperature has a tolerance of  $\pm 1\text{ }^{\circ}\text{C}$ .

Remarks regarding the ambient temperature and the test method

- One of the main starting points is that the ambient temperature is a constant value, but during a temperature rise test on a large power transformer the ambient temperature changes also. The amount of change is influenced by such factors as the power(loss) input, the relative size of the transformer to the size of the laboratory and whether the laboratory has forced air ventilation in operation or not. The change in ambient temperature will have some time delay on a change of the average oil, which will affect the results with respect to the temperature rises.
- Temperature rise tests are sometimes performed in winter time and sometimes in the summer, so when comparing results one has to realize that the ambient temperatures are not the same for the tested transformers.
- The test has to last until the steady state is reached, as being when the variation of the top oil temperature rise is below 1 K during a consecutive period of 3 hours. ([3])
- The short circuit test method for the temperature rise test ([1] - 7.2.2.) in a test department of a transformer factory can only be a simulation of the operation conditions at site.

For practical reasons the bottom oil temperature is defined as the temperature of the oil returning from the cooling equipment. ( see [1] – 7.3.2 ). The bottom oil temperature ( column 8 [1] – 7.3.2 ) is measured by a thermocouple placed at the return headers of the coolers, the thermocouple must be thermally insulated from the ambient temperature. The tolerance of measurement is +/- 1°C but one also has to introduce an assembly tolerance, because the sensors are not assembled in the exact same way on every transformer. This assembly tolerance is taken as +/- 2°C at 280 MVA load. This relative tolerance in the oil temperatures due to location and assembly of the sensors does not change when this transformer is tested at a different load. ( marked orange in table 5 )

Remark : The same applies for the oil that enters the cooling equipment, which is not prescribed in [1]. but required for calculation of average oil as defined in [3]. ( coolin ( column 9 ) )

Top oil temperature ( column 13 – [1] – 7.3.1 ) is measured by one or more sensors immersed in the insulating liquid at the top of the tank , or in pockets in the cover and the same tolerances apply for the top oil sensor as the bottom oil thermocouples. To determine the temperature rises, one has to subtract the ambient temperature, as in the case of average oil rise ( column 11 – [1] – 7.4 ) and top oil rise ( column 14– [1] – 7.4 )

The hot-spot temperature is set with a reference of 93.7 °C at 280 MVA and the error is +/- 1°C. The hot-spot temperature ( column 15 – [1] – 7.8.2) and hot-spot temperature rise ( column 16 – [1] – 7.8.2 ) can be determined. The maximum reading shall be taken as the hot-spot winding temperature. In the case of several fibre optic sensors that are assembled close together, one can correct for the offset of the individual sensors. Before the start of the test the temperatures should all be the same and one may calibrate each sensor to that average value. In that way one compensates for the different tolerances among the sensors and the corresponding channels in the measurement equipment. The maximum difference between sensors before start of the test was about 1.5 °C

Remark : The average oil in the simulation is defined as top oil minus 0,5 \* temperature drop over the cooler [3] and the basic starting point is that the average oil temperature in the cooler is the same as the average oil temperature in each winding.

#### 4.2. Simulation results according [ 3 ].

In this section the IEEE definition of gradient winding – oil is according reference [3] – 11 ), while in the next section ( 4.3 ) the definition is according to reference [ 1 ] - annex C. By using Excel one can simulate the tolerance by using the function ASELECT(), as in following line.

$$T_{cold} = T_{cold}(\text{reference}) + 2 * T_{cold}(\text{tolerance}) * (\text{ASELECT}() * (0-1) + 1) - T_{cold}(\text{tolerance}).$$

For each parameter, if applicable, one can apply this function and each row in a spreadsheet simulates one transformer temperature rise test. In this way one can calculate in each row the hot-spot factor. At the end of the 50 rows the average value and the standard deviation of each parameter are calculated by Excel ( as a check of input for some parameters).

Table 3 Statistical simulation based on gradient winding - average oil ( IEEE )

280 MVA		Measurement tol. of resistance in %		Tolerance due to assembly of sensor										Input parameters												
		0.15	0.15																							
Tolerances in degrees and Ohms ( calculated on basis of % tolerance )				2.0	2.0											2.0										
Reference values of temperature and resistance				0.5	0.000108	0.0001361	0.50	2.5	1.0	1.0											1.0	2.0				
Reference values of temperature and resistance				13	0.07183	0.09074			23.0			53.1	73.7											75.7	93.7	1.35
1	2	3	4	5	6	7	8	9	10	11	12	13	14	15	16	17	Columnnumber									
Nr	T <sub>coild</sub>	R <sub>coild</sub>	R <sub>warm</sub>	T <sub>winding</sub>	T <sub>ambient</sub>	Winding rise	Bottom oil	Coolin	Average oil	Average oil rise	Gradient winding to oil	Topoil	Topoil rise	Thotspot	Hotspot rise	Hotspot factor										
	θ <sub>1</sub>	R <sub>1</sub>	R <sub>2</sub>	θ <sub>2</sub>	θ <sub>a</sub>	θ <sub>w</sub> = θ <sub>2</sub>	θ <sub>b</sub>	θ <sub>c</sub>	θ <sub>om</sub>	Δθ <sub>om</sub>	g	θ <sub>o</sub>	Δθ <sub>o</sub>	θ <sub>h</sub>	Δθ <sub>h</sub>	H										
	°C	Ω	Ω	°C	°C	°C	°C	°C	°C	°C	°C	°C	°C	°C	°C	°C										
1	13.5	0.07187	0.09081	79.7	22.8	56.9	50.6	74.8	64.3	41.4	15.5	76.4	53.5	95.5	72.7	1.24										
2	12.7	0.07176	0.09074	79.3	24.6	54.7	51.8	75.6	63.6	39.0	15.7	75.5	50.9	91.9	67.3	1.05										
49	12.5	0.07176	0.09063	78.6	23.5	55.0	52.1	75.8	64.2	40.6	14.4	76.0	52.4	92.6	69.0	1.15										
50	13.1	0.07190	0.09084	79.4	20.6	58.9	53.0	74.7	65.9	45.4	13.5	76.8	56.2	94.4	73.8	1.30										
Average	13.06	0.07	0.09	78.92	22.70	56.23	52.94	73.70	65.57	42.88	13.35	75.95	53.26	93.64	70.95	1.34										
St. Dev.	0.30	0.00	0.00	1.47	1.48	1.38	1.39	1.40	2.02	1.45	1.08	1.70	1.13	2.06	0.15											
%	2.27	0.09	0.08	0.57	6.46	2.64	2.60	1.88	2.13	4.72	10.83	1.42	3.19	1.21	2.91	11.04										
350 MVA																										
Tolerances in degrees and Ohms ( calculated on basis of % tolerance )				0.5	0.000108	0.0001478	0.50	2.5	2.23	2.32											2.73	2.0				
Reference values of temperature and resistance				13	0.07183	0.09855			27			60.6	85.9											99	124	1.29
Nr	T <sub>coild</sub>	R <sub>coild</sub>	R <sub>warm</sub>	T <sub>winding</sub>	T <sub>ambient</sub>	Winding rise	Bottom oil	Coolin	Average oil	Average oil rise	Gradient winding to oil	Topoil	Topoil rise	Thotspot	Hotspot rise	Hotspot factor	x	y	z							
	θ <sub>1</sub>	R <sub>1</sub>	R <sub>2</sub>	θ <sub>2</sub>	θ <sub>a</sub>	θ <sub>w</sub> = θ <sub>2</sub>	θ <sub>b</sub>	θ <sub>c</sub>	θ <sub>om</sub>	Δθ <sub>om</sub>	g	θ <sub>o</sub>	Δθ <sub>o</sub>	θ <sub>h</sub>	Δθ <sub>h</sub>	H										
	°C	Ω	Ω	°C	°C	°C	°C	°C	°C	°C	°C	°C	°C	°C	°C	°C										
1	13.5	0.07187	0.09842	105.5	28.8	76.7	57.1	87.4	85.4	56.6	20.1	100.6	71.8	124.3	95.4	1.18	0.72	1.17	0.95							
2	12.7	0.07176	0.09850	105.5	28.0	77.5	58.5	87.3	84.0	56.0	21.5	98.4	70.4	122.6	94.6	1.13	0.80	1.39	1.73							
49	12.5	0.07176	0.09858	106.0	29.2	76.8	59.3	87.8	85.2	56.0	20.8	99.5	70.2	124.9	95.6	1.22	0.72	1.66	1.91							
50	13.1	0.07190	0.09850	105.9	28.0	77.8	59.5	86.0	87.8	59.7	18.1	101.0	73.0	123.3	95.3	1.23	0.64	1.31	1.07							
Average	13.1	0.07184	0.09855	106.0	26.9	79.2	60.4	85.8	86.6	59.8	19.4	99.4	72.5	124.0	97.1	1.28	0.76	1.68	1.49							
St. Dev.	0.30	0.00006	0.00008	0.47	1.52	1.52	1.56	1.52	1.55	2.22	1.58	1.05	1.71	1.13	1.78	0.10	0.09	0.29	0.36							
%	2.27	0.09	0.08	0.45	5.67	1.92	2.59	1.77	1.78	3.72	8.18	1.06	2.36	0.91	1.84	7.53	11.81	17.43	23.98							

Remark :If one makes a second statistical simulation, the results vary a little. A population of 50 might be considered large in the power transformer business, but is not a large number for a population in the world of statistics

### 4.3. Comparison of statistical simulation and test results.

The main comparison is on the standard deviation of the exponents x and y and it is focused on the two different methods to determine the winding – oil gradient ( see table 4 )

Table 4 Comparison of exponents based on test data and statistical simulation

	IEEE definition with gradient winding - average oil				Cooling down curve to constant value			
	Simulation		Testresults		Simulation		Testresults	
	x	y	x	y ( LV+HV)	x	y	x	y ( LV+HV)
Average	0.76	1.66	0.78	1.86	0.82	1.57	0.78	1.46
St. Dev	0.08	0.29	0.10	0.37	0.11	0.14	0.10	0.13

The starting point of the simulation are the average values of the tests, so it is logical that test results and simulation comply very well, but the large standard deviation in the simulation is the outcome of all the tolerances.

## 5. EFFECT OF UNCERTAINTY ON X AND Y EXPONENT ON THE HOT SPOT TEMPERATURE RISE IN CASE OF OVERLOAD

The consequences of the uncertainty in values of the exponents  $x$  and  $y$  on the overload capability of a transformer needs to be determined. As a first step one has to determine if the  $x$  and  $y$  exponent, as based on the test results, are correlated or can be treated as independent variables. By using the function CORRELATIE in Excel one can determine the correlation (Table 5)

Table 5 Correlation between exponents and correlation with opening of coolers				
	x - exponent top oil	y - HV	y - LV	Time after opening coolers
Top oil rise 280 MVA	NA	NA	NA	0.44
Top oil rise 350 MVA	NA	NA	NA	-0.04
x - exponent top oil	1.00	0.05	0.05	-0.47
y - HV		1.00	0.85	-0.18
y - LV			1.00	0.07

Based on the previous results, these correlation coefficients are not that surprising. There is a correlation between the top oil rise at 280 MVA and the  $x$ -exponent with the time after opening the coolers, but is also clear from Figure 1. There is no correlation with the top oil rise at 350 MVA and the time after opening of the coolers, which is expected because the overload is always fixed at 8 hours and this measurement is made a long time after start of the heat run test.

There is also no correlation between the  $x$ -exponent and the  $y$ -exponents of LV and HV, so they can be treated as independent parameters for determining the overload capability. There is a large correlation between the  $y$  exponents of LV and HV.

Based on the value of the  $x$ - and  $y$  - exponent, one can determine the hot spot temperature rise as a function of the load factor  $K$  ( Figure 3 ). To compare the different results, the average values at 100% load are used as a starting point for comparison.

The overload curve based on the loading guide [2] IEC (  $x=0.8$  and  $y = 1.3$  ) can be compared with the final values of the temperature rise tests (  $x = 0.65$  as based on figure 1 and  $y = 1.9$  as average values of LV and HV in Table 2 ) and the difference between both curves is very limited.

In the case one would test only one transformer, one has to take into account the uncertainty in these exponents. Two overload curves are calculated, one based on the average values **minus** the standard deviation ( see Table 2 ) and one on the average values **plus** the standard deviation.

The overload curve of this single transformer would be between the two dashed lines. Based on that one may conclude that by using values as determined during a temperature rise test, the overloading will most likely more limited as based on IEC, which means that during operation the hot spot temperature rise will not be exceeded, but there is a possible risk that this is not the case.

Remark : As a reminder, one has to consider that a temperature rise test is performed in the tap position with the highest losses, but the tap position is not taken into account in the loading guide. In the case of plus/minus regulation this will have a large impact. The hot spot factor is considered as a constant but it depends on the tap position and can be different for the main windings.

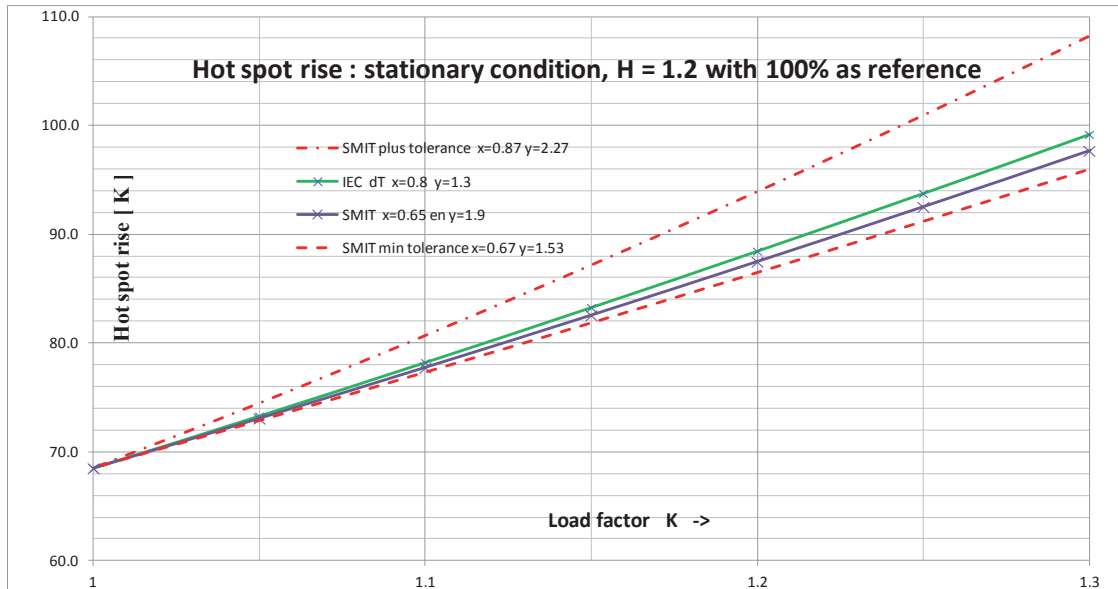


Figure 3 Comparison of hot spot temperature rise based on IEC and test results

There is always a lot of discussion on the values of the x- and y-exponent to be used. The variation on the value of the x-exponent is limited. There is a large variation on the value of y-exponent, but one has to consider that this is only related to the gradient of the winding to the oil. By making a numerical example, one can see quite clear the consequences on variation of the exponents.

#### Example

Starting point at 100% load

Top oil rise : 53 K

Gradient hot spot to top oil : 16 K

Difference in top oil rise at 130% load (neglecting no-load losses) in the case of x=0.65 compared to 0.8

$$53 * ((1.3^2)^{0.65} - (1.3^2)^{0.8}) \approx -6 \text{ K}$$

Difference in gradient hot spot to top oil at 130% in the case of x=1.9 compared to 1.3

$$16 * (1.3^{1.9} - 1.3^{1.3}) \approx 4 \text{ K}$$

## 6. CONCLUSIONS

The exponents x, y and z as determined by temperature rise test have as basic requirement that a steady state thermal situation has to be achieved before one makes the measurement. In the case of large power transformers with ONAF cooling, this will require a temperature rise test at nominal load taking at least 12 hours after ending the restriction by opening of the valves and in addition more than 6 hours in the case of the overload.

The exponents x, y and z are based on the difference of two temperature rise measurements. Also is each temperature difference based on two measured values with each it's own tolerance. This results in a large inaccuracy.

By performing a lot of temperature rise tests on "identical" transformers, one can statistically determine the average value and standard deviation of the oil-exponent x and winding exponent y. This will create a solid base to determine the exponents so that transformers can be loaded according the specification.

Simulation of the temperature rise test ( by Excel) with all their tolerances regarding:

- test environment,
- test setup,
- test sequence
- test equipment

explain the large standard deviation in the x- and y-exponent as determined by the temperature rise tests.

Based on the current practice, regarding

- the length of temperature test,
- the available, highly accurate, test equipment
- available test environments at transformer factories, an improvement by a smaller value for the standard deviation on the x- and y-exponent will not be expected.

The exponents  $x$ ,  $y$  and  $z$  can be determined during a temperature rise test of one single transformer. Due to the large inaccuracy, there is a possible risk that the use of these exponents will result in unacceptably high temperatures during overload. It is therefore recommended to use only the values according to the standard in that case.

## REFERENCES

- [1] IEC 60076-2 2011 - 02 Power Transformers – Part 2:Temperature rise for liquid immersed transformers
- [2] IEC 60076 – 7, 2005-12 Power Transformers – Part 7 : Loading guide for oil-immersed power transformers
- [3] IEEE C57.12.90 – 2006 Test Code for Liquid Immersed Distribution, Power and Regulating Transformers
- [4] H. Nordman, O. Takala: Transformer Loadability Based on Directly Measured Hot-Spot Temperature and Loss and Load Current Exponents.Cigre 2010 A2\_307\_2010
- [5] Norman, H; Hiironneieme, E; Pesonen, A.J.: Determination of hot-spot temperature rise at rated load and overload.Cigre 12-103 , 1990
- [6] IEEE Standard C57.91:1995, IEEE Guide for loading mineral-oil-immersed transformers.
- [7] J. Jaspár; C. Spoorenberg: Practical aspects of determining the hot-spot factor TJH2b conference Warwick UK 2011
- [8] C. Spoorenberg: The statistical analysis of temperature rise test for increased accuracy on x- and y-exponents TJH2b conference Chicago USA 2012

Zhiguang Cheng  
R & D Center, Tianwei Group Co., LTD, CHINA,  
[emlab@btw.cn](mailto:emlab@btw.cn)

Behzad Forghani  
Infolytica Corporation, CANADA,  
[forghani@infolytica.com](mailto:forghani@infolytica.com)

Norio Takahashi  
Dept. of E.E., Okayama University, JAPAN  
[norio@elec.okayama-u.ac.jp](mailto:norio@elec.okayama-u.ac.jp)

Xiaoyan Wang  
R & D Center, Tianwei Group Co., LTD, CHINA,  
[wangxiaoyan@btw.cn](mailto:wangxiaoyan@btw.cn)

## ENGINEERING-ORIENTED BENCHMARKING AND APPLICATION-BASED MAGNETIC MATERIAL MODELING IN TRANSFORMER RESEARCH

### SUMMARY

The paper highlights the engineering-oriented benchmarking and application-based magnetic material modeling, as two important events in transformer research, reviews the newly extended progress in TEAM (Testing Electromagnetic Analysis Methods) Problem 21 Family, and presents the related benchmarking results.

**Key words:** Application-based magnetic material modeling, engineering-oriented benchmarking, finite element, industrial application, Iron loss, magnetic flux.

### 1. INTRODUCTION

The effectiveness of the numerical modeling is essentially dependent on the analysis method, software being used, and the sufficient material property data. Consequently, the validation of both the numerical computation and the material property modeling becomes two important events.

In order to validate the numerical modeling, since 1985, the international COMPUMAG (biennial conference on the computation of the electromagnetic fields) society has paid great attention to organize the TEAM activities worldwide to test and compare the electromagnetic analysis methods, and established a series of benchmark problems widely used in the computational electromagnetics community [1]. Meanwhile, the IEEE Standard for validation of computational electromagnetics computer modeling and simulations has been issued [2]. The authors have made efforts to the engineering-oriented TEAM activities for years [3-13], also proposed a benchmark family, Problem 21[1], and updated it for three times since 1993, many scientists and engineers are interested in it up to now.

On the other hand, the more advanced material modeling techniques have been investigating systematically [14]. As a result, there has been significant progress in the efficient design of electromagnetic devices [15-18]. However, so far, what being widely used in industrial application is the standard one-dimensional B-H curves, obtained from either the Epstein frame or the single sheet tester (SST), and B-H properties change according to the working conditions, e.g. they could vary with the frequency, the temperature, and the stress action. Therefore, it is necessary to validate the availability of the B-H property data when modeling a device under working conditions.

In very large electromagnetic devices, for example a large power transformer, the reduction of stray-field loss, produced by the leakage flux from the transformer winding and heavy current leads, and

the protection against unallowable loss concentrations and then local over heating have become more and more significant[19-25]. Various types of power frequency shields are widely utilized to effectively save energy and ensure a reliable operation. In addition, the various shields can change and control the global distribution of the 3-D electromagnetic field within a large device. It is important to accurately model the multi-shielding effects and optimize shielding configurations at the electromagnetic design stage, but not use rough estimates [20-21].

The purpose of this paper is to focus on the engineering-oriented benchmarking and the application-based magnetic material modeling in power transformers, examine the effect of the variation in the different B-H representations used in different solvers on iron loss and flux in GO(grain-oriented) silicon steel sheets, and investigate the power frequency multi-shielding effect based on shield models. In addition, an improved method for measuring stray-field loss is proposed, and validated based on a newly designed benchmarking set up, making use of two leakage flux complementary coils.

## 2. ENGINEERING-ORIENTED BENCHMARKING

The electromagnetic and thermal field problems in large power transformers are usually very complicated, which involve multi-physic field coupling, multi-scale (very thin layer and very large bulk) components, and multi-materials varying with the working conditions. In order to obtain an effective solution, the strict validation of the analysis method and software used for solving such complex field problems are certainly necessary. However, it is impossible to do that via a large real product. Therefore, the verification based on the engineering-oriented benchmark models becomes a best way.

To investigate the stray-field loss problems in power transformers, a benchmark family, TEAM Problem 21 of 16 benchmark models, has been well established (the definition of Problem 21, v.2009, can be found at [www.compumag.org/TEAM](http://www.compumag.org/TEAM))[1], and a number of benchmarking results have been presented by the authors and the researchers worldwide[4]. All the benchmark models come from the typical structures of power transformers, presenting different electromagnetic behavior, and the engineering-oriented benchmarking activities have the following characteristics:

a) **Test electromagnetic analysis methods**

The original motivation of benchmarking (TEAM) is to test the analysis method and computation software, including the commercial software being in use, and is a regular topic of the international COMPUMAG conference.

b) **Verify computation models**

It is important to build up a correct numerical computation model, such as, taking the nonlinearity, electric and magnetic anisotropy of material, skin effect and loss concentration in components into account, and involving the reasonable simplification treatment for reducing the computation cost.

c) **Detail the field behavior of typical product structure**

Problem 21 is transformer-oriented, including transformer tank, core-plate, and shielding models. The detailed modeling of the stray field loss generated in different components and the electromagnetic field distributions will be helpful to improve product design.

d) **Benefit to large-scale numerical modeling**

Benchmark model is different from a large product, but the benchmarking results will be useful to solve large-scale field problems in the simplification of practical problem, the treatment of material properties, and the choice of the solvers.

Table 1 shows the benchmarking notes concerning with TEAM Problem 21, which is expected to be helpful for the numerical modeling in power transformers.

## 3. APPLICATION-BASED MAGNETIC MATERIAL PROPERTY MODELING

From the point of view of industrial application, both keeping track of advanced material modeling technologies and promoting the large-scale application using the existing material property data are really important and challenging.

Table 1 Benchmarking notes

P21 <sup>o</sup>	In the iron-loss calculation, the hysteresis loss component and the nonlinearity of the magnetic steel must be accounted (P21 <sup>o</sup> includes Model A and Model B of Problem 21).
P21 <sup>a</sup>	The satisfied results of eddy current losses in non-magnetic steel can be achieved using different 3-D analysis methods based on different potential sets, even with coarse mesh in non-magnetic components, but 2-D results is not available.
P21 <sup>b</sup>	The detailed examination and comparison of both the total loss and the loss concentration in the hybrid steel plate structure are of importance to improve the product design.
P21 <sup>c</sup>	The evaluations of the power loss and magnetic flux inside both electromagnetic and magnetic shields, as well as that of the separation-type shields, are given.
P21 <sup>d</sup>	Both the iron loss and magnetic field inside the GO silicon steel lamination with different excitation patterns, and the additional iron loss induced by normal magnetic flux are detailed.

a) **A bottleneck problem of industrial application**

The material property modeling is one of the key topics of this Colloquium, also is another regular topic of COMPUMAG. In author's opinion, it still is a bottleneck-problem of industrial application. This is because that, the measurement conditions of the material properties were standard, using the standard equipments, such as, Epstein frame, SST, or other equipments to be applied for getting vector magnetic properties, however, the working conditions of the components and device are not standard.

Up to now, the material property data provided by the material providers are one-dimensional, but the field problems in the real products are three-dimensional. So another problem is that how to use the existing property data to solve the practical problems?

b) **Combination of material modeling and numerical computation**

Most of the current electromagnetic-thermal analysis software can access the one-dimensional or the so-called orthogonal-anisotropic property data. A natural problem is that the software must be upgraded if the vector property data of the material is to be used.

c) **Improvement of magnetic property modeling technology**

Since many years ago, the standard testing equipments used for the magnetic material property modeling are commonly used. The extension of the measurement function and the updates of the setting value with the tester are necessary. For example, using Epstein frame to measure the different type of B-H curves ( $B_m$ - $H_m$  and  $B_m$ - $H_b$ ), the mean path length of the Epstein is varied with many factors but not a constant values [14,26].

4. **MAGNETIC PROPERTY MODELING OF GO SILICON STEEL SHEETS**

4.1. **Different B-H curves**

Two kinds of B-H curves, namely  $B_m$ - $H_m$  and  $B_m$ - $H_b$ , are currently used in electromagnetic field computation[11]. The  $B_m$ - $H_m$  curve takes the maximum values of both the flux density ( $B_m$ ) and the magnetic field strength ( $H_m$ ) within a cycle. Generally,  $B_m$  and  $H_m$  cannot achieve the maximum value at the same time inside the magnetic steel due to the eddy current, especially at low flux density, as shown in Fig.1. Thus there is another magnetic field strength  $H_b$  corresponding to the maximum value of the flux density  $B_m$ , i.e.  $B_m$ - $H_b$  curve, see Fig.1. The eddy current becomes zero at the instant when the flux becomes the maximum, therefore,  $B_m$ - $H_b$  curve can be referred to as a dc B-H curve.

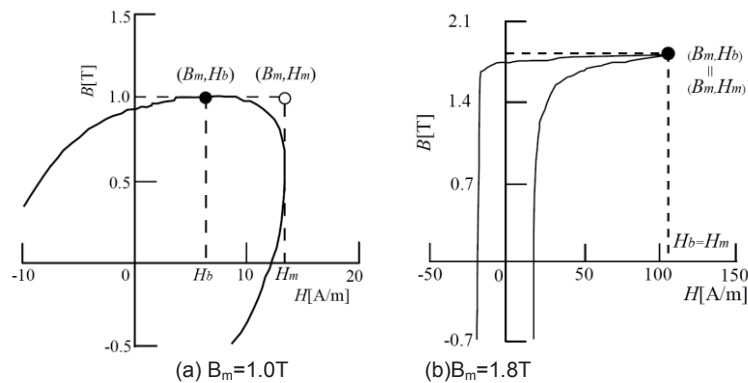


Fig.1. Definition of  $B_m$ ,  $H_m$  and  $H_b$ (30P105,  $f=50\text{Hz}$ ).

Fig.2 shows the examples of forming  $B_m-H_m$  and  $B_m-H_b$  curves based on hysteresis loops (30P105), and Fig.3 demonstrates the measured B-H curve family (SST with H coil) at different frequencies. Both Fig.2 and Fig.3 indicate that the  $B_m-H_b$  curves at around a commercial frequency (e.g., 50Hz) are similar to the dc B-H curve at low frequency (0.01Hz), but  $B_m-H_m$  curves are different from the quasi dc B-H curve.

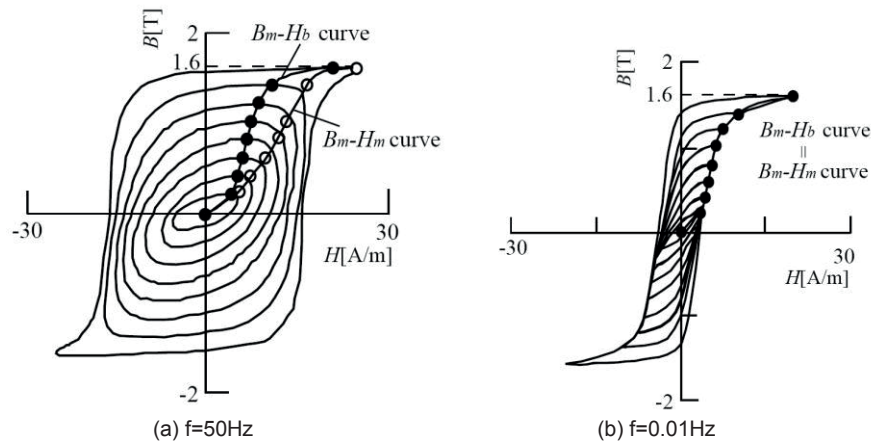


Fig. 2. Hysteresis loops at different frequencies (30P105).

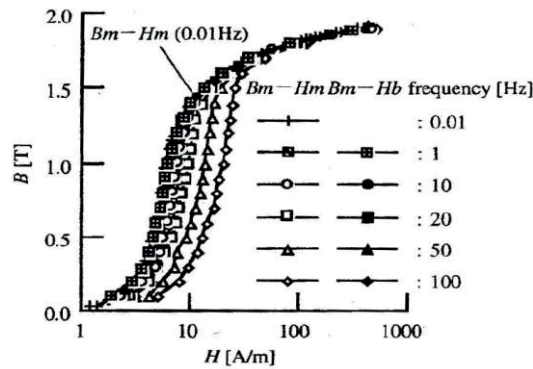


Fig.3. Comparison of B-H curves (30P105).

#### 4.2. Different sampling of GO silicon steel sheets

The magnetic property data of the GO silicon steel sheets 30P120 (made in Korea) are measured using Epstein frame, at the different sampling angles to the rolling direction and the different excitation frequency, as shown in Fig.4 [11].

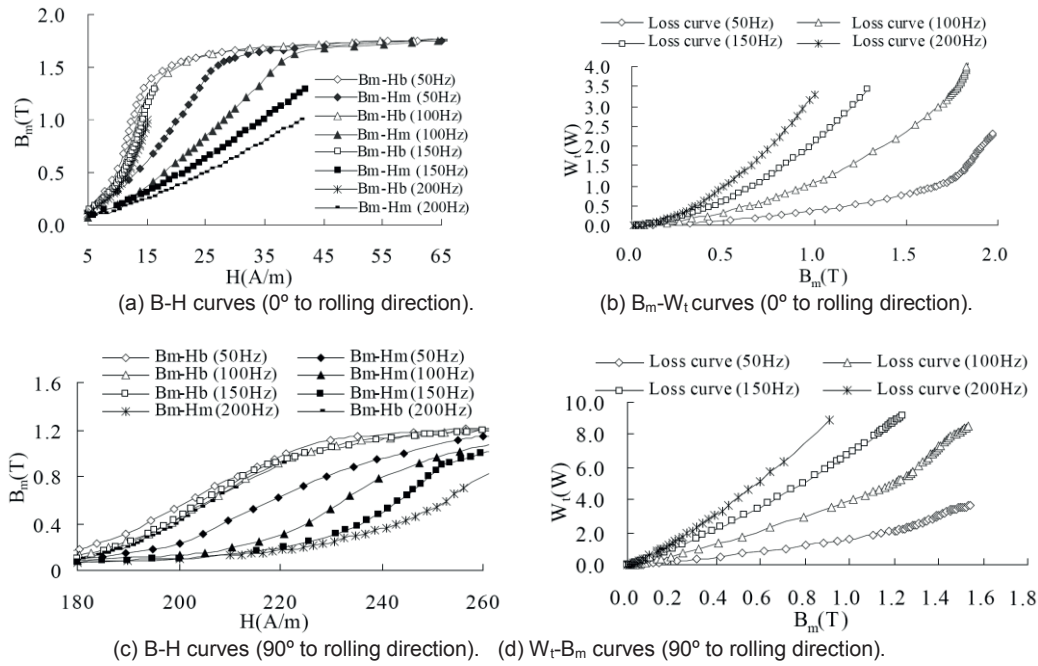


Fig.4. B-H and  $B_m$ - $W$  curves of 30P120.

A comparison between the B-H curves, i.e.,  $B_m$ - $H_m$  and  $B_m$ - $H_b$ , measured by using Epstein frame and SST respectively, is given. See Fig.5.

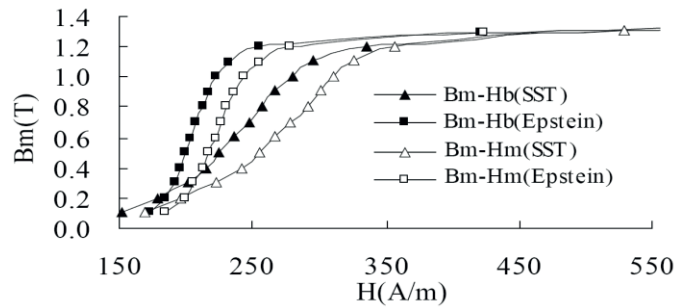


Fig.5. B-H curves (90° to rolling direction) measured using SST and Epstein frame (30P120).

#### 4.3. On the mean path length of Epstein frame

The mean path length of the Epstein frame (25 cm) is constant, 0.94m, in the IEC standard [26], it has found that the mean path length is dependent on many factors, and is not always equal to 0.94m. This paper shows the further experimental study, using two Epstein frames (i.e., standard 25cm and revised 17.5cm Epstein frame) regarding it. The field and loss distributions at the corner areas of the two Epstein frames are kept identical, and only the difference between two frames is in length of the Epstein limb, is a basic assumption.

The mean path length of the Epstein frame can be determined based on the specific total loss produced in the middle portions of the Epstein limb [26], denoted by  $l_{m1}$ , i.e., eliminating the effect of the Epstein corners on the specific total loss obtained based on two Epstein frames. However, the specific total losses at the limbs ( $P_{loss1}$ ) and the corner areas ( $P_{loss2}$ ) of the whole Epstein limb are different.

In order to define an actual mean path length of the Epstein frame (denoted by  $l_e$ ), both the contributions from the middle portion of the limbs and the rest of the whole frame, including the 4 corner laps, should be taken into account. For this reason, two things done by the authors are as follows:

- 1) The mean path lengths are defined by two methods, i.e., two kinds of the mean path lengths,  $l_{m1}$  and  $l_{m2}$  were determined by the specific loss of the middle part of the limbs and that of the rest of the whole frame, respectively.

- 2) A weighted processing method for the above mean path lengths is proposed, i.e., the resulting mean path length  $l_e$  is treated as a weighted sum of  $l_{m1}$  and  $l_{m2}$ , incorporating the weight factors  $\alpha$  and  $\beta$  respectively, as shown in (1),

$$l_e = \alpha \cdot l_{m1} + \beta \cdot l_{m2} \quad (1)$$

where

$$\alpha = \frac{P_x}{P_x + P_y}; \beta = \frac{P_y}{P_x + P_y}; P_x = \frac{1}{P_{limb}}; P_y = \frac{1}{P_{corner}}$$

The weighted mean path lengths of Epstein frame (25 cm), according to (1), have been determined under different sampling angle to the rolling direction, as shown in Figs.6-8.

It can be seen that,  $l_{m1}$  and  $l_{m2}$  are quite different and varying with the flux densities, however the weighted mean path length  $l_e$  is in between  $l_{m1}$  and  $l_{m2}$ , and  $l_e$  is close to 0.94m, 0.92m and 0.93m at the sampling angle  $0^\circ$ ,  $55^\circ$ , and  $90^\circ$ , respectively.

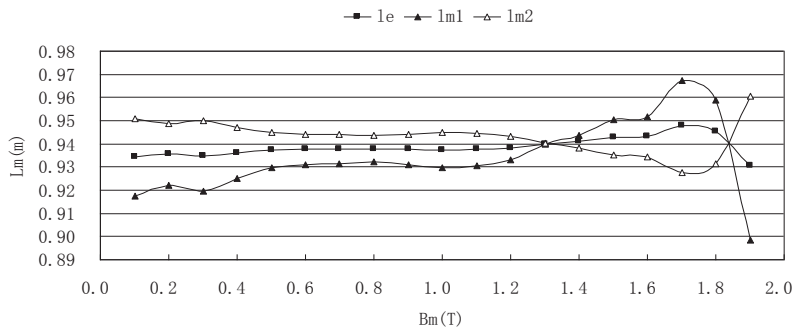


Fig.6 The mean path length determined by different methods(1)  
(30P120,  $0^\circ$  to the rolling direction, 50Hz)

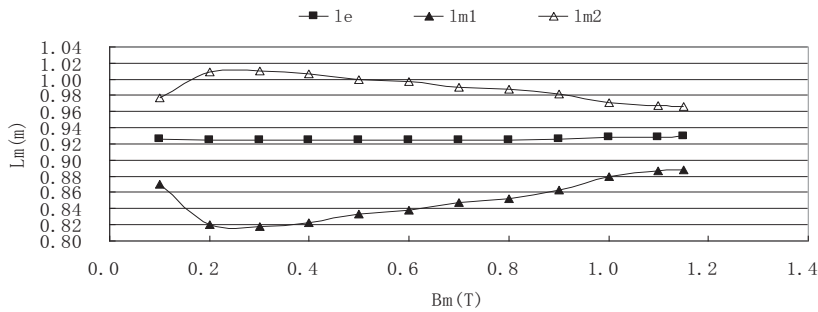


Fig.7 The mean path length determined by different methods(2)  
(30P120,  $55^\circ$  to the rolling direction, 50Hz)

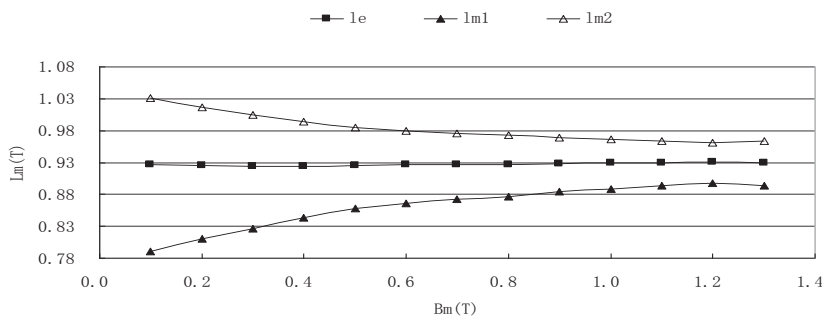


Fig.8 The mean path length determined by different methods(3)  
(30P120,  $90^\circ$  to the rolling direction, 50Hz)

Notes for Figs.6-8:

$l_e$ : weighted length based on specific total loss at both limb and corner;

$l_{m1}$ : length based on specific total loss at limb;

$l_{m2}$ : length based on specific total loss at corner area.

## 5. FE MODEL FOR LAMINATION CONFIGURATION

In order to reduce the computation costs and obtain the efficient solutions, many homogenization treatment methods of the lamination structures, such as, transformer core and magnetic shields, have been proposed [27-32]. The following benchmarking issue aims to deal with the standard iron loss and additional iron loss based on the simple model [10].

### 5.1. Finite element model

The simplified finite element model of the laminated GO silicon sheets has the following characteristics:

1) Treatment of electric anisotropy

Pattern 1: Modeling the first few laminations individually and modeling the rest as bulk; 3-D eddy currents flow in the individual laminations and 2-D eddy currents limited in each lamination in the bulk region where the anisotropic conductivity is used, see Fig. 9(a).

Pattern 2: Fine meshing within a thin surface layer, and coarse meshing inside the bulk. In the entire conducting domain the anisotropic conductivity is assumed. See Fig.9 (b).

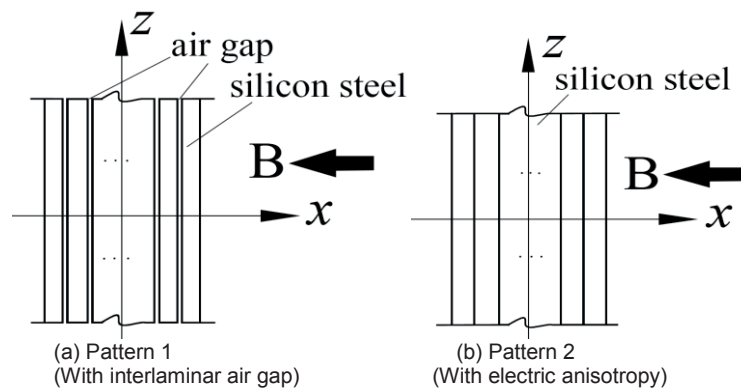


Fig.9. Simplification of laminated sheets.

2) Treatment of magnetic anisotropy

The resulting magnetic field inside the laminated sheet models is almost in one direction (along z-axis), making it a weak magnetic anisotropy problem, and the orthogonal anisotropic permeability is assigned in all the laminations.

### 5.2. Eddy current analysis

The well-established eddy current solvers based on various potential sets have been developed and applied in the computational electromagnetics and industry [33-37]. The  $\mathbf{T}$ - $\Omega$  potential set-based method is used in this paper, in which the magnetic field represents as the sum of two parts, i.e., the gradient of a scalar potential  $\Omega$  and  $\mathbf{T}$ , in the conductors, an additional vector field represented with vector-edge elements. As a result, the solution vector consists of the magnetic scalar potential at the nodes plus edge-degrees of freedom associated with the current flow in solid conductors. The  $\mathbf{T}$ - $\Omega$  based solver does not run into the convergence and instability issues associated with other formulations [36]. The governing equation in the eddy current region, in which involving anisotropic and nonlinear materials, is given by (2),

$$\nabla \times ([\sigma]^{-1} \nabla \times \mathbf{T}) + [\mu] \frac{\partial (\mathbf{T} - \nabla \Omega)}{\partial t} = 0 \quad (2)$$

The anisotropic and nonlinear permeability  $[\mu]$  of (2) can be represented by (3)

$$[\mu] = \begin{bmatrix} \mu_0 / (1 - c_p) & & \\ & C_p \mu_y & \\ & & C_p \mu_z \end{bmatrix} \quad (3)$$

where:  $C_p$  is the packing factor.

The anisotropic conductivity  $[\sigma]$  of the sheets can be dealt with as

$$[\sigma] = \begin{bmatrix} c_p \sigma_x & & \\ & c_p \sigma_y & \\ & & c_p \sigma_z \end{bmatrix} \quad (4)$$

where:  $\sigma_y = \sigma_z = \sigma_{yz}$  in sheets, while  $\sigma_x$  is expressed as

$$\sigma_x = \begin{cases} \approx 0 (2D \text{ eddy current region}) \\ \text{assigned} (3D \text{ eddy current region}) \end{cases} \quad (5)$$

The iron loss and flux generated in the GO laminations are computed based on the field analysis results of the eddy current field as part of the post processing. The additional iron loss  $P_a$  caused by the flux normally entering the laminated sheets can not be neglected. As a practical solution, the total iron loss  $P_t$  can be divided into two parts, i.e.,

$$P_t = P_a + P_s \quad (6)$$

where:  $P_s$  can be determined based on the measured loss curve Bm-Wt, and  $P_a$  can be calculated based on the field results of 2-D eddy current  $J_{yz}$  flowing in the plane of the lamination by (7),

$$P_a = \int \frac{\overline{J_{yz}}_{rms}^2}{\sigma_{yz}} dV \quad (7)$$

**Note that the standard specific iron loss  $P_s$  includes all the loss components, i.e. the classical eddy current loss  $P_e^{classic}$  and the anomalous eddy current loss  $P_e^{anomal}$  and the hysteresis loss  $P_h$ ,**

$$P_s = P_e^{classic} + P_e^{anomal} + P_h \quad (8)$$

The magnetic flux inside GO silicon sheets can be determined by integrating the calculated flux densities over the specified cross-sectional areas or based on the measurements using the search coils.

## 6. EFFECT OF B-H PROPERTIES ON IRON LOSS AND FLUX

### 6.1. Test models

To examine the effects of the different B-H representations on the iron loss and flux inside the lamination, two test models have been proposed, i.e. Model T1 and Model T2, which are derived from the benchmark Model P21<sup>c</sup>-M1 and P21<sup>c</sup>-M2 of Problem 21 Family, respectively. The brief comparisons among the benchmark models and the newly proposed Problem 21-based test models are shown in Table 2.

In Model T1, only six silicon steel sheets of 500×500mm (30P120) are driven by a twin AC source (50 to 200Hz), a 3-D excitation, see Fig.10(a). The purpose of Model T2 is to show the effect of the division of the wide sheets on the reduction of iron loss, see Fig.10(b).

Table 2 Specification of test model and benchmark model

Models	Magnetic plate of 10 mm thick	GO silicon sheets	Sheet-coil distance (mm)	Sheet size (mm)
T1	Without	30P120	15.0	500×500
T2	Without	30P120	12.0	80×458 (3 sets)
P21 <sup>c</sup> -M1	With	30RGH120	12.0	270×458
P21 <sup>c</sup> -M2	With	30RGH120	12.0	80×458 (3 sets)

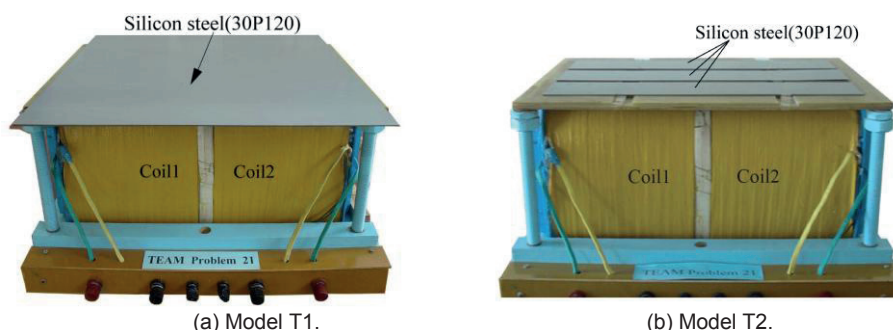


Fig.10. Models T1 and T2.

The B-H curves ( $B_m$ - $H_m$  and  $B_m$ - $H_b$ ) and the specific loss curve ( $W_t$ - $B_m$ ), measured at different sampling angles to the rolling direction of the GO steel sheet (30P120) and at different frequencies using the Epstein frame, are shown in Fig.4 [11].

## 6.2. Results and discussion

According to the pre-measurement results obtained by the authors, the saturation level of the laminated sheets is not so high, especially at lower excitations. Both the time harmonic (TH) and the time stepping (TS) solvers of the  $T$ - $\Omega$ -based MagNet, Infolytica, are used to solve the 3-D eddy current problem. Table 3 shows the calculated and measured results of total iron loss  $P_t$  of Model T1.

All the calculated results, using different B-H curves and different solvers, indicate that the use of TH solver and  $B_m$ - $H_m$  curve can offer the better results when compared to measurement. This is, because the element-permeability is dependent on the quasi-maximum values of B and H within a cycle in the TH solver. On the contrary, in the case of the TS solver,  $B_m$ - $H_b$  curve can offer the better results. This is, because in the TS solver the element-permeability is determined according to the instantaneous values of B and H at an instant. As a result, a more precise analysis is possible by the time stepping method using the  $B_m$ - $H_b$  curve, which is almost the same as the dc B-H curve.

Table 3 Total iron loss results (Model T1)

Current (A, rms, 50Hz)	Calc. (W)				Meas. (W)
	TH solver/Pattern 1		TS solver/Pattern 2		
	$B_m$ - $H_b$	$B_m$ - $H_m$	$B_m$ - $H_b$	$B_m$ - $H_m$	
10	2.61	2.74	2.54	2.35	2.52
15	7.26	7.89	6.66	6.24	7.12
20	12.74	14.14	13.37	12.65	13.7
25	20.31	22.47	23.68	24.01	23.8

Table 4 shows the contributions of additional iron loss  $P_a$  and standard specific iron loss  $P_s$  to the total iron loss  $P_t$ , using different solver and/or different kinds of B-H curves. Table 4 also indicates that  $P_s$  calculated using  $B_m$ - $H_b$  curve is larger than that using  $B_m$ - $H_m$  curve. This is, because the permeability taken from  $B_m$ - $H_b$  curve is higher than that taken from  $B_m$ - $H_m$  curve. See Fig.4.

However, from the calculated results,  $P_a$  has a different tendency, using different B-H curve and/or different (TH or TS) solver.

Table 4 Components of iron loss (Model T1)

Current (A, rms, 50Hz)	TH solver (W)				TS solver (W)			
	B <sub>m</sub> -H <sub>b</sub>		B <sub>m</sub> -H <sub>m</sub>		B <sub>m</sub> -H <sub>b</sub>		B <sub>m</sub> -H <sub>m</sub>	
	P <sub>a</sub>	P <sub>s</sub>						
10	1.53	1.08	1.81	0.93	1.73	0.81	1.72	0.63
15	5.50	1.76	6.35	1.54	5.20	1.46	5.12	1.12
20	10.44	2.31	12.07	2.07	11.15	2.22	10.95	1.70
25	17.19	3.12	19.89	2.58	21.22	2.46	21.59	2.42

The calculated results by both the TH and TS solvers show that the iron loss is mainly concentrated in a few layers on the side facing the exciting source, and goes down with the increase of layer-number going from 1 to 6, at 20A(50Hz) for Model T1, as shown in Fig.11.

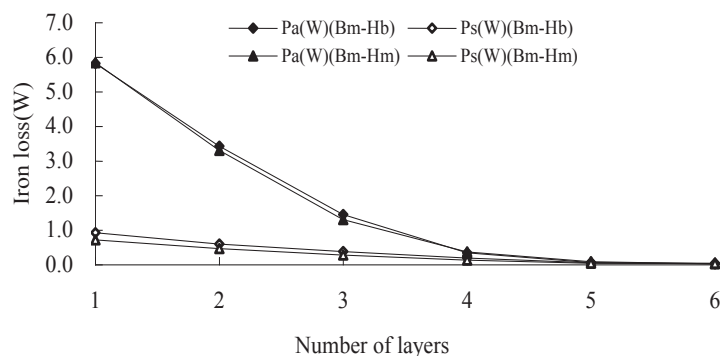


Fig.11. Iron loss distribution in layers (calculated by TS solver, Model T1, at 50Hz).

To determine the magnetic flux inside the laminated sheets, the search coils are set up in Model T1, see Fig.12(a). The magnetic fluxes, at the prescribed positions of the laminations under the different exciting currents, are calculated. Either TH solver and B<sub>m</sub>-H<sub>m</sub> curve or TS solver and B<sub>m</sub>-H<sub>b</sub> curve are applied. The calculated results agree well with the measured ones. See Fig.12(b).

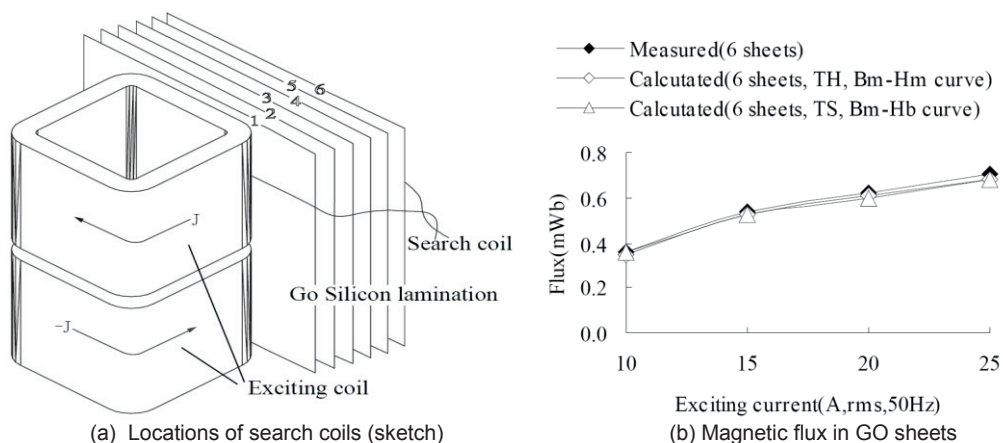


Fig.12. Magnetic flux inside GO laminated sheets (Model T1, 50Hz).

In Model T2, the iron loss produced in the three sets of the narrow GO silicon steel sheets of 80×458mm, which are placed in parallel, is considerably lower compared to that of Model T1 for the same exciting currents.

Fig.13 shows the calculated and the measured results of iron loss of Model T2 at 10A, under a frequency range from 50 to 200Hz. The results also denote that the iron loss increases with the exciting frequency.

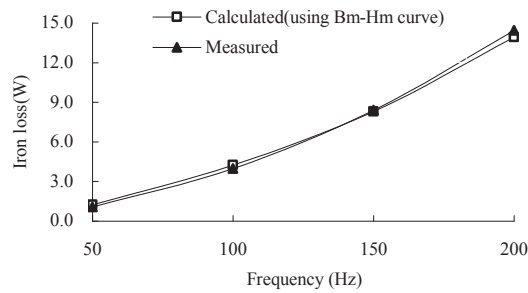


Fig.13. Iron loss varying with frequency (calculated by TH solver using  $B_m$ - $H_m$  curve, Model T2).

A very briefly summary is as follows:

- 1) The examination of the effect of the different B-H curves (obtained by different means and data access modes and at different frequencies) on iron loss and flux in GO silicon steel laminations is carried out. The numerical modeling results of the iron loss and flux based on the test models are practically in agreement with measured ones.
- 2) All the numerical modeling results suggest that the  $B_m$ - $H_b$  curve is desirable for the use in the transient solver, but the combination of the  $B_m$ - $H_m$  curve and the time harmonic solver is also available for the problem with lower saturation level.
- 3) The additional iron loss ( $P_a$ ) due to the normal flux exponentially drops from the surface facing the exciting source to the opposite side of the laminated sheets. On the other hand, the specific iron loss ( $P_s$ ) generated by the parallel flux drops slowly compared to  $P_a$ .

## 7. IRON LOSS EXPERIMENT WITH MAGNETIC FLUX COMPENSATION

The electromagnetic (EM) barrier, the magnetic (M) shunt and a combination of both are widely used in electrical devices in order to control stray fields and effectively reduce the power loss that may lead to hazardous local overheating. The hybrid (M+EM) shielding behavior of the current magnetic shunt configuration is numerically and experimentally examined, and compared to other types. The leakage flux complementary-based measurement method of stray-field loss is also proposed and verified based on the benchmark shielding models.

### 7.1. New generator and compensator of leakage flux

The authors have upgraded the original leakage flux generator (E-coils 1 and 2) specified in TEAM Problem 21 to product-level M- and MEM-type shields. The main change is the increase of the number of turns in the exciting coil (from 300 to 400) and the dimension of the copper wire (from 6.7mm×2mm to 9mm×3mm).

The leakage flux of the exciting coils changes when the magnetic components are removed (as in the no-load case) from the assembly shield models, especially, in the case of the elevated excitation. To keep the leakage magnetic field (reflecting the M- and EM shielding effects) of the exciting coils from changing under the “no-load” condition, two complementary coils (called the C-coils) are utilized, which have completely the same specification as the generator coils (E-coils), and are movable in parallel rails, as shown in Fig.14.

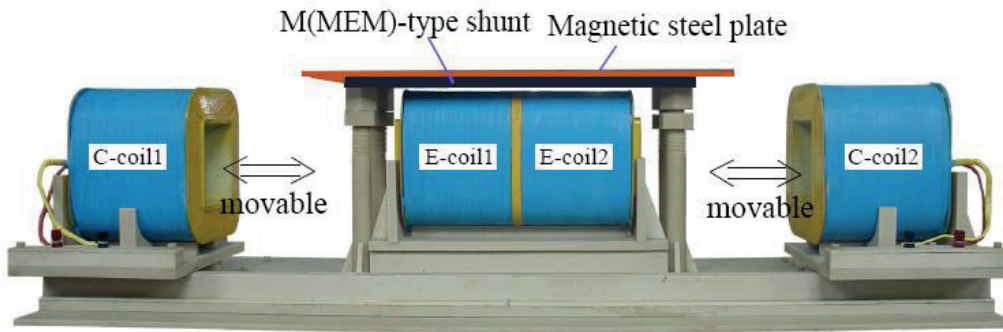


Fig.14. Shield loss measurement with C-coil (photo).

Accordingly, in the no-load (i.e., the magnetic components are removed) case, two C-coils are attached in the main assembly and are located in a symmetric position with respect to the twin exciting coils. However, in the load (i.e., the magnetic components are attached) case, the two C-coils are separated off. See Fig.14.

## 7.2. Transformer-based shielding models

Fig.15 shows two kinds of magnetic shunt components. The dimensions of the steel plate (A3) are 500×1000×10(mm) and the property data are available in the definition of TEAM Problem 21. In the M- and MEM-type shields, the GO silicon steel, 30P120, is used. The external dimensions of both the M- and MEM-type shunt are 200×860×20(mm).

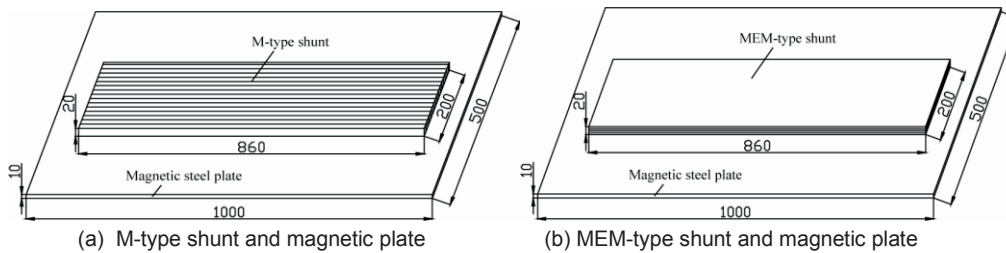


Fig.15. M- and MEM-type shields.

Table 5 shows the calculated and measured results of iron loss, generated in the magnetic component of MEM-type shield. The agreement between the calculated and measured results for total iron loss is satisfied when the C-coils are used. However, the measured results without the C-coils are not acceptable for the proposed shielding models.

Table 5 Iron loss in components of M-type shield

Currents (A,rms)	Calculated iron loss(W)			Measured iron loss(W)	
	Loss in shunt	Loss in plate	Total Loss	With C-coil	Without C-coil
5	0.032	0.370	0.402	0.40	1.24
10	0.13	1.33	1.46	1.45	4.79
15	0.29	3.10	3.39	3.45	10.52

Note that the differences between the iron-loss results of M- and MEM-type shields caused mainly by the loss produced in the magnetic shunt, and the losses in the magnetic plate are almost the same, based on the present results shown in Tables 5 and 6.

Table 6 Iron loss in components of MEM-type shield

Currents (A,rms)	Calculated iron loss(W)			Measured iron loss(W)	
	Loss in shunt	Loss in plate	Total loss	With C-coil	Without C-coil
5	0.37	0.35	0.72	0.70	1.52
10	1.49	1.43	2.92	2.95	6.25
15	3.91	3.05	6.96	7.06	14.81

## 8. CONCLUSION

The engineering-oriented benchmarking and the application-based magnetic material modeling, which are two important events in transformers research and industrial application, are highlighted in this paper, including some Problem 21-based new benchmarking results and some new material modeling results of magnetic properties.

The effect of the variation in the different B-H representations used in different solvers on iron loss and flux in GO silicon steel sheets are examined in detail, and the power frequency multi-shielding effect based on shield models are investigated. The measurement method of stray-field loss is improved and validated based on a newly designed benchmarking set up.

## ACKNOWLEDGMENT

The authors would like to thank the heads of the R & D Center, BTW, Q.Ding, C.Jiang, C.Fan, and X.Zhang, thank the colleagues, L.Liu, Y.Fan, T.Liu, Q.Hu, J.Zhang, J.Wang, J.Li and Q.Kong for their support and help in the long-term experiment and numerical modeling. The project was supported in part by the Natural Science Foundation of China under Grant No.50777042, and the China Postdoctoral Science Foundation under grant No. 2011M500534.

## REFERENCES

- [1] TEAM Benchmark Problems. [Online]. available: [www.compumag.org/TEAM](http://www.compumag.org/TEAM).
- [2] IEEE Std 1597.1<sup>TM</sup>-2008: IEEE Standard for validation of computational electromagnetics computer modeling and simulations.
- [3] Z.Cheng, Q.Hu, S.Gao, Z.Liu, C.Ye, M.Wu, J.Wang, and Z.Hu, "An engineering-oriented loss model (Problem 21)," Proc. of the international TEAM Workshop, Miami, pp.137-143, 1993.
- [4] Z.Cheng, Q.Hu, N.Takahashi, and B.Forghani, "Stray-field loss modeling in transformers," *International Colloquium Transformer Research and Asset Management*, Cavtat, Croatia, Nov.12-14, 2009.
- [5] N.Takahashi, T. Sakura and Z. Cheng, "Nonlinear analysis of eddy current and hysteresis losses of 3-D stray field loss model (Problem 21)," *IEEE Trans. on Magn.*, vol.37, no.5, pp.3672-3675, 2001.
- [6] Z.Cheng, R. Hao, N. Takahashi, Q. Hu, and C. Fan, "Engineering-oriented benchmarking of Problem 21 family and experimental verification," *IEEE Trans. on Magn.*, vol. 40, no.2, pp.1394-1397, 2004.
- [7] Z.Cheng, N. Takahashi, S. Yang, T. Asano, Q. Hu, S. Gao, X. Ren, H. Yang, L. Liu, and L. Gou, "Loss spectrum and electromagnetic behavior of Problem 21 family", *IEEE Trans. on Magn.*, vol.42, no.4, pp.1467-1470, 2006.
- [8] Z.Cheng, N. Takahashi, S. Yang, C. Fan, M. Guo, L. Liu, J. Zhang, and S. Gao, "Eddy current and loss analysis of multi-steel configuration and validation," *IEEE Trans. on Magn.*, vol.43, no.4, pp.1737-1740, 2007.
- [9] Z.Cheng, N. Takahashi, B. Forghani, G. Gilbert, J. Zhang, L. Liu, Y. Fan, X. Zhang, Y. Du, J. Wang, and C. Jiao, "Analysis and measurements of iron loss and flux inside silicon steel laminations," *IEEE Trans. on Magn.*, vol.45, no.3, pp.1222-1225, 2009.
- [10] Z.Cheng, N.Takahashi, B.Forghani, et al, "Effect of excitation patterns on both iron loss and flux in solid and laminated steel configurations," *IEEE Trans. on Magn.*, vol.46, no.8, pp.3185-3188, 2010
- [11] Z.Cheng, N.Takahashi, B.Forghani, et al, "Effect of variation of B-H properties on loss and flux inside silicon steel lamination," *IEEE Trans. on Magn.*, vol.47, no.5, pp.1346-1349, 2011.
- [12] Z.Cheng, N.Takahashi, B.Forghani, L.Liu, Y.Fan, T.Liu, J.Zhang, and X.Wang, "3-D finite element modeling and validation of power frequency multi-shielding effect," *IEEE Trans. on Magn.*, vol.48, no.2, pp.243-246, 2012.
- [13] Z.Cheng, N.Takahashi, B.Forghani, et al, "*Electromagnetic and Thermal Field Modeling and Application in Electrical Engineering*," Science Press (in Chinese), Beijing, 2009.

- [14] A.J.Moses, "Characterisation and performance of electrical steels for power transformers operating under extremes of magnetisation conditions," *International Colloquium Transformer Research and Asset Management*, Cavtat, Croatia, Nov.12-14, 2009.
- [15] M.Enokizono, H.Shimoji, A.Ikariga, et al, "Vector magnetic characteristic analysis of electrical machines," *IEEE Trans. on Magn.*, vol.41, no.5, pp.2032-2035, 2005.
- [16] K.Fujiwara, T.Adachi, and N.Takahashi, "A proposal of finite-element analysis considering two-dimensional magnetic properties," *IEEE Trans. on Magn.*, vol.38, no.2, pp.889-892, 2002.
- [17] H. Nishimoto, M.Nakano. K.Fujiwara, and N.Takahashi, "Effect of frequency on magnetic properties," *Papers of Technical Meeting on Magnetism, IEE Japan*, MAG-98-56, 1998 (in Japanese).
- [18] J.Zhu, J.J.Zhong, Z.W.lin, et al, "Measurement of magnetic properties under 3-D magnetic excitations," *IEEE Trans. on Magn.*, vol.39, no.5, pp. 3429-3431, 2003.
- [19] J.Turowski, M.Turowski, and M.Kopec, "Method of three-dimensional network solution of leakage field of three-phase transformers," *IEEE Trans. On Magn.*, vol. 26, no. 5, pp. 2911-2919, 1990.
- [20] N.Takahashi, S.Nakazaki, and D.Miyagi, "Optimization of electromagnetic and magnetic shielding using ON/OFF method," *IEEE Trans. on Magn.*, vol.46, no.8, pp.3153-3156, 2010.
- [21] M.Horii, N.Takahashi, and J.Takehara, "3-D optimization of design variables in x-, y-, and z-directions of transformer tank shield model," *IEEE Trans. on Magn.*, vol.37, no.5, pp.3631-3634, 2001
- [22] J. Turowski, X.M. Lopez-Fernandez, A. Soto, and D. Souto, "Stray losses control in core- and shell-type transformers," *Advanced Research Workshop on Transformers*, Baiona, Spain, 29-31 Oct., 2007.
- [23] K.V.Namjosji and P.P.Biringer, "Efficiency of eddy current shielding of structural steel surrounding large currents: a circuit approach," *IEEE Trans. on Magn.*, vol.27, no.6, pp.5417-5419, 1991.
- [24] R.Tang, Y.Li, F.Lin, and L.Tian, "Resultant magnetic fields due to both windings and heavy current leads in large power transformers," *IEEE Trans. on Magn.*, vol.32, no.3, pp.1641-1644, 1996.
- [25] R.M.D.Vecchio, "Eddy current losses in a conducting plate due to a collection of bus bars carrying currents of different magnitudes and phases," *IEEE Trans. on Magn.*, vol.39, no.1, pp.549-552, 2003.
- [26] P.Marketos, S.Zurek, and A.Moses, "A method for defining the mean path length of Epstein," *IEEE Trans. on Magn.*, vol.43, no.6, pp.2755-2757, 2007.
- [27] A.De Rochebrune, J.M.Dedulle, and J.C.Sabonnadiere, "A technique of homogenization applied to the modeling of transformers," *IEEE Trans. on Magn.*, vol. 26, no.2, pp.520-523, 1990.
- [28] H.Kaimori, A.Kameari, and K.Fujiwara, "FEM computation of magnetic field and iron loss using homogenization method," *IEEE Trans.on Magn.*, vol.43, no.2, pp.1405-1408, 2007.
- [29] H.Kaimori, A.Kameari, and K.Fujiwara, "FEM computation of magnetic field and iron loss in laminated iron core using homogenization method," *IEEE Trans. on Magn.*, vol.43, no.4, pp.1405-1408, 2007.
- [30] K.Preis, O.Biro, and I.Ticar, "FEM analysis of eddy current losses in nonlinear laminated iron cores," *IEEE Trans. on Magn.*, vol.41, no.5, pp.1412-1415, 2005.
- [31] T.Kohsaka, N.Takahashi, S.Nogawa, and M.Kuwata, "Analysis of Magnetic characteristics of three-phase reactor model of grain-oriented silicon steel," *IEEE Trans. on Magn.*, vol.36, no.4, pp.1894-1897, 2000.
- [32] H.Igarashi, K.Watanabe, and A.Kost, "A reduced model for finite element analysis of steel laminations," *IEEE Trans. on Magn.*, vol.42, no.4, pp.739-742, 2006.
- [33] O.Biro and K.Preis, "Finite element analysis of 3-D eddy currents," *IEEE Trans. on Magn.*, vol.26, no.2, pp.418-423, 1990.
- [34] O.Biro, K.Preis, and K.R.Richter, "Various FEM formulation for the calculation of transient 3D eddy currents in nonlinear media," *IEEE Trans. on Magn.*, vol.31, no.3, pp.1307-1312, 1995.
- [35] O.Biro, K.Preis, U.Baumgartner, and G.Leber, "Numerical modeling of transformer losses," presented at *International Colloquium Transformer Research and Asset Management, Cavtat, Croatia*, Nov.12-14, 2009.
- [36] J.P.Webb and B.Forghani, "T-Omega method using hierarchical edge elements," *IEE Proc.-Sci.Meas. Technol.*, vol.142, no.2, 1995, pp.133-141.
- [37] Z.Cheng, S.Gao, and L.Li, "Eddy Current Analysis and Validation in Electrical Engineering," Higher Education Press (in Chinese), Beijing, 2001.

Oszkár Bíró  
Graz University of Technology  
[biro@tugraz.at](mailto:biro@tugraz.at)

Gergely Koczka  
Graz University of Technology  
[gergely.koczka@tugraz.at](mailto:gergely.koczka@tugraz.at)

Bernhard Wagner  
Siemens Transformers Austria  
[bernhard.a.wagner@siemens.com](mailto:bernhard.a.wagner@siemens.com)

Ulrike Baumgartner  
Siemens Transformers Austria  
[ulrike.baumgartner@siemens.com](mailto:ulrike.baumgartner@siemens.com)

Gerald Leber  
Siemens Transformers Austria  
[gerald.leber@siemens.com](mailto:gerald.leber@siemens.com)

## FINITE ELEMENT METHOD FOR NONLINEAR EDDY CURRENT PROBLEMS IN POWER TRANSFORMERS

### SUMMARY

An efficient finite element method to take account of the nonlinearity of the magnetic materials when analyzing three dimensional eddy current problems is presented in this paper. The problem is formulated in terms of vector and scalar potentials approximated by edge and node based finite element basis functions. The application of Galerkin techniques leads to a large, nonlinear system of ordinary differential equations in the time domain.

The excitations are assumed to be time-periodic and the steady state periodic solution is of interest only. This is represented in the frequency domain as a Fourier series for each finite element degree of freedom and a finite number of harmonics is to be determined, i.e. a harmonic balance method is applied. Due to the nonlinearity, all harmonics are coupled to each other, so the size of the equation system is the number of harmonics times the number of degrees of freedom.

The harmonics would be decoupled if the problem were linear, therefore, a special nonlinear iteration technique, the fixed-point method is used to linearize the equations by selecting a time-independent permeability distribution, the so called fixed-point permeability in each nonlinear iteration step. This leads to uncoupled harmonics within these steps resulting in two advantages. One is that each harmonic is obtained by solving a system of algebraic equations with only as many unknowns as there are finite element degrees of freedom. A second benefit is that these systems are independent of each other and can be solved in parallel. The appropriate selection of the fixed point permeability accelerates the convergence of the nonlinear iteration.

The method is applied to the analysis of a large power transformer. The solution of the electromagnetic field allows the computation of various losses like eddy current losses in the massive conducting parts (tank, clamping plates, tie bars, etc.) as well as the specific losses in the laminated parts (core, tank shielding, etc.). The effect of the presence of higher harmonics on these losses is investigated.

**Key words:** Finite element method, fixed point technique, harmonic balance method, nonlinearity, parallel computation

## 1. INTRODUCTION

The saturation of iron parts of transformers gives rise to the presence of higher harmonics in the electromagnetic fields, leading to additional losses. The prediction of these losses is important in the design of large power transformers. A method for the analysis of transformer losses has been presented in [1] with the assumption of sinusoidal time variation, i.e. neglecting higher harmonics. The present paper extends this method for the case of general periodic time variation.

The most straightforward method of solving nonlinear electromagnetic field problems in the time domain by the method of finite elements (FEM) is using time-stepping techniques. This requires the solution of a large nonlinear equation system at each time step and is, therefore, very time consuming, especially if a three-dimensional problem is being treated. If the excitations are non-periodic or if, in case of periodic excitations, the transient solution is required, one cannot avoid time-stepping. In many cases however, the excitations of the problem are periodic, and it is only the steady-state periodic solution which is needed. Then, it is wasteful to step through several periods to achieve this by the "brute force" method [2] of time stepping.

A time domain technique using the fixed-point method to decouple the time steps has been introduced in [3] and applied to two-dimensional eddy current problems described by a single component vector potential. The optimal choice of the fixed point permeability for such problems has been presented in [4] both in the time domain and using harmonic balance principles. The method has been applied to three-dimensional problems in terms of a magnetic vector potential and an electric scalar potential ( $\mathbf{A}, \nu\text{-}\mathbf{A}$  formulation) in [5] and, employing a current vector potential and a magnetic scalar potential ( $\mathbf{T}, \Phi\text{-}\Phi$  formulation), in [6] and [7].

The aim of this work is to show the application of the method to industrial problems arising in the design of large power transformers. In this context, the computation of losses due to higher saturation harmonics is investigated.

The paper is structured as follows: In the following two sub-sections of the Introduction, two FEM potential formulations of eddy current problems are briefly reviewed and the harmonic balance method to obtain their steady state periodic solution is introduced. In section 2, a method is developed to decouple the harmonics from each other and hence to solve for each harmonic separately. This is trivial for linear problems, but a special fixed point iteration technique is introduced to treat nonlinearity with the harmonics decoupled. Section 3 is devoted to a numerical example involving a large power transformer. The losses due to higher harmonics are computed and analyzed here. The results of the paper are concluded in section 4.

### 1.1. Finite element potential formulations

The electromagnetic field problem to be solved in the eddy current domain  $\Omega_c$  (such as the tank, the clamping plates and tie bars as well as some laminates at the core boundary exposed to stray fields) is described by Maxwell's equations in the quasi-static limit:

$$\text{curl}\mathbf{H} = \mathbf{J} + \text{curl}\mathbf{T}_0, \quad (1)$$

$$\text{curl}\mathbf{E} = -\frac{\partial\mathbf{B}}{\partial t}, \quad (2)$$

$$\text{div}\mathbf{B} = 0, \quad (3)$$

$$\text{div}\mathbf{J} = 0 \quad (4)$$

where:  $\mathbf{H}$  is the magnetic field intensity,  $\mathbf{J}$  is the eddy current density,  $\mathbf{T}_0$  is a current vector potential whose curl is the given current density in the windings,  $\mathbf{E}$  is the electric field intensity,  $\mathbf{B}$  is the flux density and  $t$  is time. In the insulating region  $\Omega_n$  (such as oil and air domains, the windings, as well as laminated parts free of eddy currents) it is sufficient to solve (1) with  $\mathbf{J}=\mathbf{0}$  in addition to (3) for the magnetic field quantities. The material relationships are

$$\mathbf{B} = \mu(|\mathbf{H}|)\mathbf{H} \text{ or } \mathbf{H} = \nu(|\mathbf{B}|)\mathbf{B} \quad (5)$$

$$\mathbf{J} = \sigma\mathbf{E} \text{ or } \mathbf{E} = \rho\mathbf{J} \quad (6)$$

where:  $\mu$  is the permeability,  $\nu$  is its reciprocal, the reluctivity and  $\sigma$  is the conductivity with  $\rho$  denoting its reciprocal, the resistivity. In magnetic materials (steel), the relationships (5) are nonlinear, i.e. the permeability and the reluctivity depend on the magnetic field intensity or the magnetic flux density as indicated.

The numerical solution of the problem is carried out by the method of finite elements. The application of FEM is straightforward if potential functions are introduced. Basically, two options are open: the field quantities can either be represented by a magnetic vector potential  $\mathbf{A}$  and an electric scalar potential  $v$  ( $\mathbf{A}, v$ - $\mathbf{A}$  formulation) as

$$\mathbf{B} = \text{curl}\mathbf{A} \text{ in } \Omega_c \cup \Omega_n, \quad \mathbf{E} = -\frac{\partial}{\partial t}(\mathbf{A} + \text{grad}v) \text{ in } \Omega_c, \quad (7)$$

or by a current vector potential  $\mathbf{T}$  and a magnetic scalar potential  $\Phi$  ( $\mathbf{T}, \Phi$ - $\Phi$  formulation) as

$$\mathbf{H} = \mathbf{T}_0 + \mathbf{T} - \text{grad}\Phi \text{ in } \Omega_c \cup \Omega_n, \quad \mathbf{J} = \text{curl}\mathbf{T} \text{ in } \Omega_c \quad (8)$$

with  $\mathbf{T}=\mathbf{0}$  in  $\Omega_n$ . The definitions (7) satisfy (2) and (3), whereas those in (8) ensure that (1) and (4) hold. Therefore, the differential equations (1) and (4) are to be solved in the  $\mathbf{A}, v$ - $\mathbf{A}$  formulation:

$$\text{curl}(v\text{curl}\mathbf{A}) + \frac{\partial}{\partial t}[\sigma(\mathbf{A} + \text{grad}v)] = \text{curl}\mathbf{T}_0, \quad (9)$$

$$-\text{div}\left[\sigma\frac{\partial}{\partial t}(\mathbf{A} + \text{grad}v)\right] = 0, \quad (10)$$

and the Maxwell's equations (2) and (3)

$$\text{curl}(\rho\text{curl}\mathbf{T}) + \frac{\partial}{\partial t}[\mu(\mathbf{T} - \text{grad}\Phi)] = -\frac{\partial}{\partial t}(\mu\mathbf{T}_0), \quad (11)$$

$$\text{div}[\mu(\mathbf{T} - \text{grad}\Phi)] = -\text{div}(\mu\mathbf{T}_0) \quad (12)$$

remain to be solved in the  $\mathbf{T}, \Phi$ - $\Phi$  formulation.

Introducing the edge based vector basis functions  $\mathbf{N}_i(\mathbf{r})$  ( $i = 1, 2, \dots, n_e$ ) and the node based scalar basis functions  $N_i(\mathbf{r})$  ( $i = 1, 2, \dots, n_n$ ) in the finite elements ( $n_e$  is the number of edges and  $n_n$  the number of nodes in the finite element mesh,  $\mathbf{r}$  denotes the space coordinates), the potentials are approximated as

$$\mathbf{A}(\mathbf{r}, t) \approx \mathbf{A}_h(\mathbf{r}, t) = \sum_{k=1}^{n_e} a_k(t) \mathbf{N}_k(\mathbf{r}), \quad \mathbf{T}(\mathbf{r}, t) \approx \mathbf{T}_h(\mathbf{r}, t) = \sum_{k=1}^{n_e} t_k(t) \mathbf{N}_k(\mathbf{r}), \quad (13)$$

$$v(\mathbf{r}, t) \approx v_h(\mathbf{r}, t) = \sum_{k=1}^{n_n} v_k(t) N_k(\mathbf{r}), \quad \Phi(\mathbf{r}, t) \approx \Phi_h(\mathbf{r}, t) = \sum_{k=1}^{n_n} \phi_k(t) N_k(\mathbf{r}). \quad (14)$$

The vector  $\mathbf{T}_0$  is represented by edge basis functions similarly to  $\mathbf{T}$  in (13). The coefficients for  $\mathbf{T}_0$  are easily computed as its line integrals along the edges of the finite element mesh.

Applying Galerkin techniques to (9) and (10) leads to the following ordinary differential equations for the  $\mathbf{A}, v$ - $\mathbf{A}$  formulation:

$$\int_{\Omega_c} \text{curl}\mathbf{N}_i \cdot v\text{curl}\mathbf{A}_h d\Omega + \frac{d}{dt} \int_{\Omega_c} \sigma \mathbf{N}_i \cdot (\mathbf{A}_h + \text{grad}v_h) d\Omega = \int_{\Omega_c} \text{curl}\mathbf{N}_i \cdot \mathbf{T}_0 d\Omega, \quad i=1,2,\dots,n_e, \quad (15)$$

$$\frac{d}{dt} \int_{\Omega_n + \Omega_c} \sigma \text{grad}N_i \cdot (\mathbf{A}_h + \text{grad}v_h) d\Omega = 0, \quad i=1,2,\dots,n_n. \quad (16)$$

Gathering the unknown time functions  $a_k(t)$  ( $k = 1, 2, \dots, n_e$ ) and  $v_k(t)$  ( $i = 1, 2, \dots, n_n$ ) in (13) and (14) in a vector  $\mathbf{x}(t)$ , the matrix form of (15), (16) is the system of ordinary differential equations

$$\mathbf{S}[\nu(\mathbf{x}(t))] \mathbf{x}(t) + \mathbf{M}(\sigma) \frac{d\mathbf{x}(t)}{dt} = \mathbf{f}(t) \quad (17)$$

where: the dependence of the stiffness matrix  $\mathbf{S}$  on  $\nu$  and of the mass matrix  $\mathbf{M}$  on  $\sigma$  is explicitly shown. Since the reluctivity depends on the field,  $\nu$  depends on  $\mathbf{x}$  and hence on  $t$  as indicated. The right hand side vector is denoted by  $\mathbf{f}$ .

In a similar manner, Galerkin's method applied to (11) and (12) results in the ordinary differential equations

$$\int_{\Omega_c} \text{curl} \mathbf{N}_i \cdot \rho \text{curl} \mathbf{T}_h d\Omega + \frac{d}{dt} \int_{\Omega_c} \mu \mathbf{N}_i \cdot (\mathbf{T}_h - \text{grad} \Phi_h) d\Omega = -\frac{d}{dt} \int_{\Omega_c} \mu \mathbf{N}_i \cdot \mathbf{T}_0 d\Omega, \quad i=1,2,\dots,n_e, \quad (18)$$

$$-\frac{d}{dt} \int_{\Omega_n + \Omega_c} \mu \text{grad} N_i \cdot (\mathbf{T}_h - \text{grad} \Phi_h) d\Omega = \frac{d}{dt} \int_{\Omega_n + \Omega_c} \mu \text{grad} N_i \cdot \mathbf{T}_0 d\Omega, \quad i=1,2,\dots,n_n \quad (19)$$

for the  $\mathbf{T}, \Phi$ - $\Phi$  formulation. The vector  $\mathbf{x}(t)$  now consists of the unknown time-dependent coefficients  $t_k(t)$  ( $k = 1, 2, \dots, n_e$ ) and  $\phi_k(t)$  ( $k = 1, 2, \dots, n_n$ ) in (13) and (14). The matrix form of the Galerkin equations is the system of ordinary differential equations

$$\mathbf{S}(\rho) \mathbf{x}(t) + \frac{d}{dt} [\mathbf{M}(\mu(\mathbf{x}(t))) \mathbf{x}(t)] = \frac{d}{dt} \mathbf{g}(\mu(\mathbf{x}(t)), t) \quad (20)$$

where: the stiffness matrix  $\mathbf{S}$  is now independent of  $\mathbf{x}$  and hence of time, but the mass matrix  $\mathbf{M}$  depends on the permeability which is itself field- and time-dependent. The product of the mass matrix and the unknown vector is differentiated with respect to time. The excitation vector  $\mathbf{g}$  depends on  $\mathbf{x}$  and  $t$ , and its time-derivative appears on the right hand side.

## 1.2. Harmonic balance method

The right hand side vectors of the systems of ordinary differential equations (17) and (20) are time periodic, i.e.  $\mathbf{f}(t) = \mathbf{f}(t+T)$  and  $\mathbf{g}(\mu, t) = \mathbf{g}(\mu, t+T)$  where  $T = 1/f$  is the period determined by the frequency  $f$  of the excitation, i.e. of the winding currents of the transformer. Since we are only interested in the steady state periodic solution satisfying the periodicity condition  $\mathbf{x}(t) = \mathbf{x}(t+T)$ , the solution is approximated by a complex Fourier series with  $N$  harmonics as

$$\mathbf{x}(t) \approx \mathbf{x}_N(t) = \text{Re} \left( \sum_{k=1}^N \mathbf{X}_k e^{jk\omega t} \right) \quad (21)$$

where:  $j$  is the imaginary unit,  $\omega = 2\pi f$  is the angular frequency of the excitation and  $\mathbf{X}_k$  is the complex Fourier coefficient of the  $k$ -th harmonic at the angular frequency  $k\omega$ . It can be computed as

$$\mathbf{X}_k = \mathcal{F}_k(\mathbf{x}) = \frac{1}{T} \int_0^T \mathbf{x}(t) e^{-jk\omega t} dt. \quad (22)$$

Setting the approximation (21) into (17) and (20), respectively, and computing the  $N$  Fourier coefficients of both sides, a system of equations with  $N$  times as many unknowns is obtained as there are unknown time-functions, i.e. degrees of freedom, in  $\mathbf{x}(t)$ :

$$\mathcal{F}_m \{ \mathbf{S}[\nu(\mathbf{x}_N)] \mathbf{x}_N \} + jm\omega \mathbf{M}(\sigma) \mathbf{X}_m = \mathcal{F}_m(\mathbf{f}), \quad m = 1, 2, \dots, N, \quad (23)$$

$$\mathbf{S}(\rho) \mathbf{X}_m + \mathcal{F}_m \left\{ \frac{d}{dt} [\mathbf{M}(\mu(\mathbf{x}_N)) \mathbf{x}_N] \right\} = \mathcal{F}_m \left[ \frac{d}{dt} \mathbf{g}(\mu(\mathbf{x}_N), t) \right], \quad m = 1, 2, \dots, N. \quad (24)$$

In the linear terms in (23) and (24), the Fourier coefficients of the  $m$ -th harmonic appear only. The time derivative in (17) corresponds to a multiplication by  $j m \omega$  in (23). The right hand side of (23) can be computed directly from  $\mathbf{f}$  as shown in (22). On the other hand, the nonlinear terms containing the permeability  $\mu(\mathbf{x}_N)$  or the reluctivity  $\nu(\mathbf{x}_N)$  depending on the unknown solution (21) couple all Fourier coefficients to each other. Therefore, due to the nonlinearity, one cannot solve for each harmonic alone, a fact which significantly increases the complexity of the problem.

## 2. DECOUPLING OF HARMONICS

It is highly desirable that the harmonics be decoupled and hence be determined independent of each other. This would lead to  $N$  systems of equations, each with as many unknowns as there are degrees of freedom in the FEM approximation. As shown below, the decoupling is trivial in the linear case but, for nonlinear problems, special techniques are needed.

### 2.1. Linear problems

If the permeability and the reluctivity are independent of the magnetic field, the systems of ordinary differential equations (17) and (20) become linear, since  $\mathbf{S}$  in (17) and  $\mathbf{M}$  in (20) do not depend on  $\mathbf{x}(t)$ . Hence, the Fourier coefficients indicated by  $\mathcal{F}_m$  in (23) and (24) become

$$\mathcal{F}_m \{ \mathbf{S}(\nu) \mathbf{x}_N \} = \mathbf{S}(\nu) \mathbf{X}_m, \quad \mathcal{F}_m \left\{ \frac{d}{dt} [\mathbf{M}(\mu) \mathbf{x}_N] \right\} = jm\omega \mathbf{M}(\mu) \mathbf{X}_m, \quad \mathcal{F}_m \left[ \frac{d}{dt} \mathbf{g}(\mu, t) \right] = jm\omega \mathcal{F}_m(\mathbf{g}) \quad (25)$$

Hence, (23) and (24) indeed become decoupled, each harmonic can be determined independently:

$$[\mathbf{S}(\nu) + jm\omega \mathbf{M}(\sigma)] \mathbf{X}_m = \mathcal{F}_m(\mathbf{f}), \quad m = 1, 2, \dots, N, \quad (26)$$

$$[\mathbf{S}(\rho) + jm\omega \mathbf{M}(\mu)] \mathbf{X}_m = jm\omega \mathcal{F}_m(\mathbf{g}), \quad m = 1, 2, \dots, N. \quad (27)$$

The right hand side vectors in (26) and (27) can be easily computed by traditional Fourier decomposition as in (22).

### 2.2. Fixed point iteration technique for nonlinear problems

The fixed point iteration method for the solution of nonlinear equations reduces the problem to finding the fixed point of a nonlinear function. The fixed point  $\mathbf{x}_{FP}$  of the function  $\mathbf{G}(\mathbf{x})$  is defined as

$$\mathbf{x}_{FP} = \mathbf{G}(\mathbf{x}_{FP}). \quad (28)$$

The fixed point can be determined as the limit of the sequence

$$\mathbf{x}^{(s+1)} = \mathbf{G}(\mathbf{x}^{(s)}), \quad s = 0, 1, 2, \dots, \quad (29)$$

provided  $\mathbf{G}(\mathbf{x})$  is a contraction, i.e. there exists a contraction number  $-1 < q < 1$  so that for any  $\mathbf{x}$  and  $\mathbf{y}$

$$\|\mathbf{G}(\mathbf{x}) - \mathbf{G}(\mathbf{y})\| \leq q \|\mathbf{x} - \mathbf{y}\| \quad (30)$$

where:  $\|\cdot\|$  is a suitable norm. Furthermore, the sequence (29) converges to the same fixed point independent of the choice of the initial guess  $\mathbf{x}^{(0)}$ .

A general nonlinear equation  $\mathbf{F}(\mathbf{x}) = \mathbf{0}$  can be transformed to a fixed point problem by selecting a suitable linear operator  $\mathbf{A}$  and defining  $\mathbf{G}$  as

$$\mathbf{G}(\mathbf{x}) = \mathbf{x} + \mathbf{A}^{-1} \mathbf{F}(\mathbf{x}). \quad (31)$$

The fixed point iterations (29) then become

$$\mathbf{A}^{(s)} \mathbf{x}^{(s+1)} = \mathbf{A}^{(s)} \mathbf{x}^{(s)} + \mathbf{F}(\mathbf{x}^{(s)}), \quad s = 0, 1, 2, \dots \quad (32)$$

where: the superscript  $s$  of  $\mathbf{A}^{(s)}$  indicates that the linear operator  $\mathbf{A}$  can be changed at each iteration step to accelerate convergence.

In case of the ordinary differential equations (17) and (20) obtained by Galerkin FEM techniques, the selection of a linear operator is straightforward: the permeability or reluctivity has to be set to a value independent of the magnetic field. This value,  $\mu_{FP}$  or  $\nu_{FP}$ , is not necessarily independent of the space coordinates  $\mathbf{r}$ , i.e. generally  $\mu_{FP} = \mu_{FP}(\mathbf{r})$  or  $\nu_{FP} = \nu_{FP}(\mathbf{r})$  are permeability or reluctivity distributions varying in the problem domain but independent of the field and hence of time. By the same argument as

the one used for the linear operator  $\mathbf{A}$  above,  $\mu_{FP}$  or  $\nu_{FP}$  can also change at each iteration step. This fixed point permeability or reluctivity function will be denoted by  $\mu_{FP}^{(s)}$  or  $\nu_{FP}^{(s)}$  below.

Once a suitable fixed point permeability or reluctivity has been selected, (17) and (20) can be iteratively solved by obtaining  $\mathbf{x}^{(s+1)}(t)$  from the equations

$$\mathbf{S}(\nu_{FP}^{(s)})\mathbf{x}^{(s+1)}(t) + \mathbf{M}(\sigma)\frac{d\mathbf{x}^{(s+1)}(t)}{dt} = \mathbf{S}(\nu_{FP}^{(s)} - \nu^{(s)})\mathbf{x}^{(s)}(t) + \mathbf{f}(t) \quad s = 0, 1, 2, \dots \quad (33)$$

$$\mathbf{S}(\rho)\mathbf{x}^{(s+1)}(t) + \frac{d}{dt}\left[\mathbf{M}(\mu_{FP}^{(s)})\mathbf{x}^{(s+1)}(t)\right] = \frac{d}{dt}\left[\mathbf{M}(\mu_{FP}^{(s)} - \mu^{(s)})\mathbf{x}^{(s)}(t)\right] + \frac{d}{dt}\mathbf{g}(\mu^{(s)}, t) \quad s = 0, 1, 2, \dots \quad (34)$$

at each step. The permeability or reluctivity distribution  $\mu^{(s)}$  or  $\nu^{(s)}$  are determined from the solution  $\mathbf{x}^{(s)}(t)$  i.e., in contrast to  $\mu_{FP}^{(s)}$  or  $\nu_{FP}^{(s)}$ , they are time dependent. The stiffness matrix  $\mathbf{S}$  on the right hand side of (33) is obtained with  $\nu$  replaced by  $\nu_{FP}^{(s)} - \nu^{(s)}$  and the mass matrix  $\mathbf{M}$  on the right hand side of (34) is computed with  $\mu_{FP}^{(s)} - \mu^{(s)}$  written instead of  $\mu$ . Indeed, these matrices depend linearly on  $\nu$  and  $\mu$ , respectively.

Since (33) and (34) are linear ordinary differential equation systems, they can be solved by the harmonic balance method with decoupled harmonics as in (26) and (27). The corresponding equations to be solved for  $s = 0, 1, 2, \dots$  are:

$$\left[\mathbf{S}(\nu_{FP}^{(s)}) + jm\omega\mathbf{M}(\sigma)\right]\mathbf{X}_m^{(s+1)} = \mathcal{F}_m\left[\mathbf{S}(\nu_{FP}^{(s)} - \nu^{(s)})\mathbf{x}^{(s)}(t) + \mathbf{f}(t)\right], \dots m = 1, 2, \dots, N, \quad (35)$$

$$\left[\mathbf{S}(\rho) + jm\omega\mathbf{M}(\mu_{FP}^{(s)})\right]\mathbf{X}_m^{(s+1)} = jm\omega\mathcal{F}_m\left[\mathbf{M}(\mu_{FP}^{(s)} - \mu^{(s)})\mathbf{x}^{(s)}(t) + \mathbf{g}(\mu^{(s)}, t)\right], \dots m = 1, 2, \dots, N \quad (36)$$

where:  $\mathbf{x}^{(s)}(t)$  is obtained from the harmonics similarly to (21) as

$$\mathbf{x}^{(s)}(t) = \text{Re}\left(\sum_{k=1}^N \mathbf{X}_k^{(s)} e^{jk\omega t}\right). \quad (37)$$

The nonlinear iterations are terminated once the change of  $\mu^{(s)}$  or  $\nu^{(s)}$  between two iteration steps becomes less than a suitable threshold.

The most computational effort is needed for the solution of the  $N$  linear equation systems in (35) and (36), respectively. Since these are independent of each other, they can be solved parallel with each core responsible for the solution for one harmonic  $\mathbf{X}_m^{(s+1)}$ . Once these parallel computations are ready, the right hand side for the next iteration can be determined by first computing the time function of the solution as in (37) and then carrying out the Fourier decompositions indicated in (35) and (36). This is the part of the process when no parallelization is possible, but since the computational effort necessary for it is negligible in comparison to the solution of the large linear algebraic systems, the method is massively parallel.

One of the most important factors influencing the rate of the convergence of the fixed point technique is the choice of the fixed point permeability or reluctivity. As pointed out above, this is not necessarily constant with respect to the space coordinates, i.e. it can be selected to be different at each Gaussian integration point of the finite element mesh. The analysis of the optimal choice has been carried out in [4], the result for  $\mu_{FP}^{(s)}$  below is taken from there:

$$\mu_{FP}^{(s)} = \max\left\{\frac{\int_0^T [\mu^{(s)}]^2 dt}{\int_0^T \mu^{(s)} dt}, \frac{\min_{t \in [0, T]}(\mu^{(s)}) + \max_{t \in [0, T]}(\mu^{(s)})}{2}\right\}. \quad (38)$$

The optimal fixed point reluctivity is obtained in a similar way. The permeability  $\mu^{(s)}$  and the reluctivity  $\nu^{(s)}$  are functions of the space coordinates and also of time since they are determined by the magnetic field distribution, itself space and time-dependent. According to (38), the fixed point permeability depends on the space coordinates but not on time. The computational effort necessary for the evaluation of (38) in each nonlinear iteration step is negligible.

### 3. COMPUTATION OF TRANSFORMER LOSSES

The eddy current losses of a transformer can be obtained by integrating the Joule loss density computed from the current density distribution. The current density can be computed from the potentials as shown in (6) and (7) in case of the  $\mathbf{A}, \nu\text{-}\mathbf{A}$  formulation and as given in (8) for the  $\mathbf{T}, \Phi\text{-}\Phi$  formulation. Since the potentials are provided as Fourier series of the form (21) by the harmonic balance method presented, the current density is obtained as

$$\mathbf{J}(\mathbf{r}, t) \approx \text{Re} \left( \sum_{k=1}^N \mathbf{J}_k(\mathbf{r}) e^{jk\omega t} \right) \quad (39)$$

where:  $\mathbf{J}_k(\mathbf{r})$  is the complex amplitude of the  $k$ -th harmonic of the current density. Hence, the eddy current losses are obtained as

$$P_{\text{eddy}} = \frac{1}{T} \int_0^T \left( \int_{\Omega_c} \frac{|\mathbf{J}(\mathbf{r}, t)|^2}{\sigma} d\Omega \right) dt = \frac{1}{2} \sum_{k=1}^N \int_{\Omega_c} \frac{|\mathbf{J}_k(\mathbf{r})|^2}{\sigma} d\Omega. \quad (40)$$

The iron losses can be computed by integrating the specific losses per unit volume given as a function  $\rho(|\mathbf{B}|)$  of the flux density provided by the manufacturer as described in [1] for the case of sinusoidal time variation. In fact, the specific losses are customarily given for unit weight but multiplying them by the specific weight yields the losses per unit volume. Usually, the specific losses are measured for one single frequency  $f_0$  (e.g.  $f_0=50$  Hz), this is denoted by  $\rho(|\mathbf{B}|, f_0)$ . In order to approximately take account of the dependence of the specific losses on frequency, the following algorithm is adopted. It is assumed that

$$\rho(|\mathbf{B}|, f) = \rho_{cl}(|\mathbf{B}|) f^2 + \rho_{hyst}(|\mathbf{B}|) f \quad (41)$$

where:  $\rho_{cl}(|\mathbf{B}|) = \frac{\sigma \pi^2 d^2}{6} |\mathbf{B}|^2$ , ( $d$  is the thickness of the laminates, see [8]). Hence,  $\rho_{hyst}(|\mathbf{B}|)$  can be obtained as

$$\rho_{hyst}(|\mathbf{B}|) = \frac{1}{f_0} \left[ \rho(|\mathbf{B}|, f_0) - \frac{\sigma \pi^2 d^2}{6} |\mathbf{B}|^2 f_0^2 \right], \quad (42)$$

and, finally,

$$\rho(|\mathbf{B}|, f) = \frac{\sigma \pi^2 d^2}{6} |\mathbf{B}|^2 f^2 + \frac{f}{f_0} \left[ \rho(|\mathbf{B}|, f_0) - \frac{\sigma \pi^2 d^2}{6} |\mathbf{B}|^2 f_0^2 \right]. \quad (43)$$

Similarly to the current density, the magnetic flux density is also obtained in the form of a Fourier series when using the harmonic balance technique:

$$\mathbf{B}(\mathbf{r}, t) \approx \text{Re} \left( \sum_{k=1}^N \mathbf{B}_k(\mathbf{r}) e^{jk\omega t} \right). \quad (44)$$

In lack of any better assumption, the specific losses are simply computed for each harmonic from (43) and then added:

$$P_{iron} = \sum_{k=1}^N \int_{\Omega} \rho(|\mathbf{B}_k|, k\omega/2\pi) d\Omega . \quad (45)$$

As an example, the autotransformer analyzed in [1] is presented here. Its name plate data are given in Table I.

Table I- Name Plate Data of a Single-phase Autotransformer

Rated Power	450/450/85 MVA
System Voltage	500/ $\sqrt{3}$ //230/ $\sqrt{3}$ //13.8 kV
Rated Current	1559/3389/6159 A

The FEM model used has been improved in comparison to [1], it consists of 334,110 finite elements. The problem has been solved using the  $\mathbf{T}, \Phi-\Phi$  formulation, resulting in 2,217,625 degrees of freedom for the potentials. The model is shown in Fig. 1.

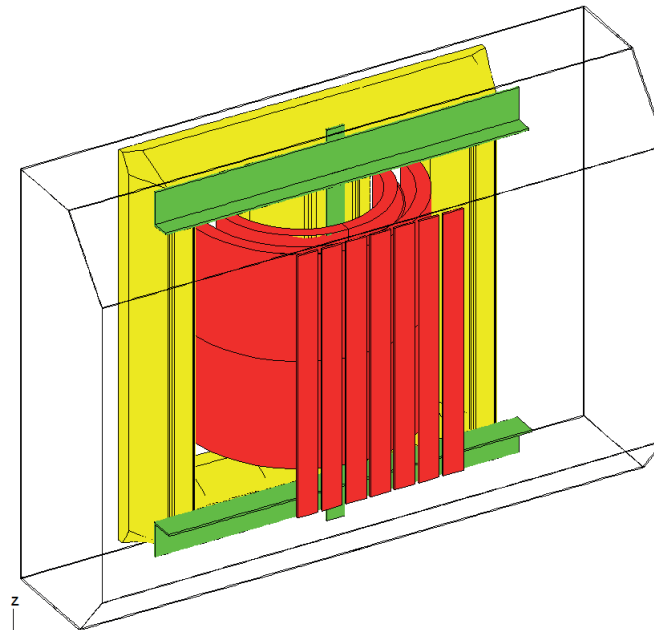


Figure 1 - FEM model of the analyzed single-phase autotransformer. The model comprises one half of the transformer. The tank is shown transparent, the core is yellow, the clamping plates and the tie bars are shown green. The windings and the tank shieldings are red.

Two short circuit computations have been carried out with the winding currents taken to be sinusoidal and the magnetization current neglected. In one of them, the method of [1] assuming sinusoidal time variation for all field quantities has been used and, in the second one, the harmonic balance method of the present paper using  $N=9$  harmonics has been employed (only odd harmonics appear in the field quantities). The losses have been computed as described above. The computed losses in the two cases are summarized in Tables II and III, given as a percentage of the total measured short circuit losses.

Table II - Losses in Percentage of Total Measured Losses of Autotransformer Analyzed. All Quantities are Sinusoidal

DC copper losses (measured)	66.92%
AC copper losses (computed from 2D FEM)	21.75%
Tank (computed from model presented)	3.76%
Clamping plates (computed from model presented)	2.80%
Tie bars (computed from model presented)	0.21%
Tank shielding (computed from model presented)	0.51%
Core (computed from model presented)	2.75%
Total	98.70%

Table III- Losses in Percentage of Total Measured Losses of Autotransformer Analyzed.  
Harmonics up to the 9th are taken into Account

DC copper losses (measured)	66.92%
AC copper losses (computed from 2D FEM)	21.75%
Tank (computed from model presented)	2.55%
Clamping plates (computed from model presented)	2.08%
Tie bars (computed from model presented)	0.18%
Tank shielding (computed from model presented)	0.97%
Core (computed from model presented)	6.05%
Total	100.50%

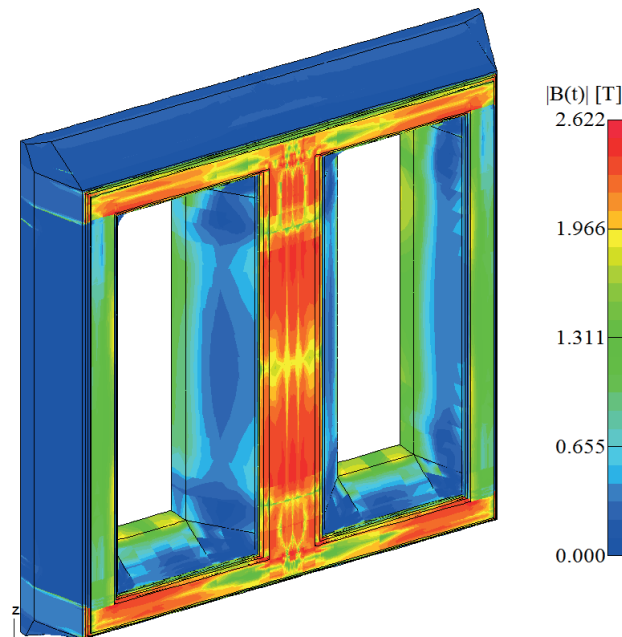


Figure 2 – Magnetic flux density in the core at the time instant of maximal winding current

These results indicate that in parts of the transformer where significant saturation is present, like in the first laminates of the core exposed to stray magnetic fields (see Figure 2), the losses due to the higher harmonics are considerable.

#### 4. CONCLUSION

It has been shown that the use of FEM in conjunction with the harmonic balance method is capable of providing the solution to large, complex real-world problems with higher harmonics due to nonlinearity allowed for, and can hence be incorporated in the design cycle of large transformers. Taking account of the additional losses due to the higher harmonics in strongly saturated parts of the transformer improves the agreement of the computed losses with measurements.

#### REFERENCES

- [1] O. Bíró, U. Baumgartner, K. Preis, G. Leber, “Numerical modeling of transformer losses”, Proceedings of the International Colloquium Transformer Research and Asset Management, Cavtat, Croatia, November 12 – 14, 2009, Session I, Numerical Modeling, 9 pages
- [2] R. Albanese et al., “Periodic solutions of nonlinear eddy current problems in three-dimensional geometries”, IEEE Transactions on Magnetics, 28 (1992), 1118-1121
- [3] O. Bíró and K. Preis, “An efficient time domain method for nonlinear periodic eddy current problems”, IEEE Transactions on Magnetics, 42, (2006), 695–698.

- [4] G. Koczka et al., "Optimal convergence of the fixed-point method for nonlinear eddy current problems", IEEE Transactions on Magnetics, 45 (2009), 948-951.
- [5] G. Koczka et al., "Optimal fixed-point method for solving 3D nonlinear periodic eddy current problems", COMPEL, 28 (2009), 1059-1067.
- [6] G. Koczka and O. Bíró, "Fixed-point method for solving nonlinear periodic eddy current problems with  $T, \Phi-\Phi$  formulation", COMPEL, 29 (2010), 1444-1452.
- [7] O. Bíró et al., "Fast time-domain finite element analysis of 3D nonlinear time-periodic eddy current problems with  $T, \Phi-\Phi$  formulation", IEEE Transactions on Magnetics, 47 (2011), 1170-1173.
- [8] G. Bertotti, "Hysteresis in Magnetism". Academic Press, 1998.

Robert Sitar  
Končar - Electrical Engineering Institute  
rsitar@koncar-institut.hr

Žarko Janić  
Končar - Power Transformers Ltd.  
A Joint Venture of Siemens & Končar  
zarko.janic@siemens.com

## IMPACT OF ELECTROMAGNETIC SHIELDS ON LOCAL OVERHEATING IN TRANSFORMER TANK

### SUMMARY

The paper describes different influences of magnetic and electromagnetic shielding on stray flux distribution in power transformers. The application of electromagnetic shields on the reduction of high temperature spots in transformer tank is studied in detail by using a 3D model for a coupled electromagnetic-thermal calculation.

The analysis of transformer models with various shapes and dimensions of electromagnetic shields show which factors are the most important for reduction of temperature hot spots in the tank. Proposed shielding solution should reduce the total stray loss and maximum temperature value. It is shown that the reduction of these values is not always achieved by shielding most of the area endangered by the stray flux from the high current leads. The choice of the shield must take into account the surrounding component material properties and transformer lead arrangement.

**Keywords:** coupled calculation, electromagnetic shielding, high current leads, stray flux, transformer

### 1. INTRODUCTION

Reduction of stray losses in transformer tanks can be realized with various methods. The goal of every method is to reduce magnetic flux in steel parts. The most common solution is to insert magnetic or electromagnetic shields.

Magnetic shields divert the flux from the transformer tank. By shunting the tank they reduce the amount of flux that goes in the tank, leading to reduction of tank losses. On the other hand, electromagnetic shields use the reacting effect of eddy currents and prevent the stray flux from going into the tank [1]. In both cases, losses arise in the shields. The shielding is considered satisfactory if the total losses in the tank and shields are less than losses in the unshielded tank.

Nevertheless, reduction of losses does not always include reduction of high loss density spots in the tank. If these spots are not appropriately cooled, high temperature rise can occur.

This paper will show how electromagnetic shields can be used for shielding of metal parts endangered by the stray flux from LV leads. The possibility of shaping electromagnetic shields in many ways makes it easy to shield these parts.

## 2. REDUCTION OF TOTAL STRAY LOSSES

In order to demonstrate the efficiency of various shielding methods, a simple 2D model is chosen for the estimation of stray losses in a transformer. This model will be used for the comparison of transformer stray losses when using electromagnetic and magnetic shielding. Program used for the calculation is MagNet (Infolytica software package for electromagnetic calculation). The calculation is performed using finite element method (FEM). Model is shown in figure 1.

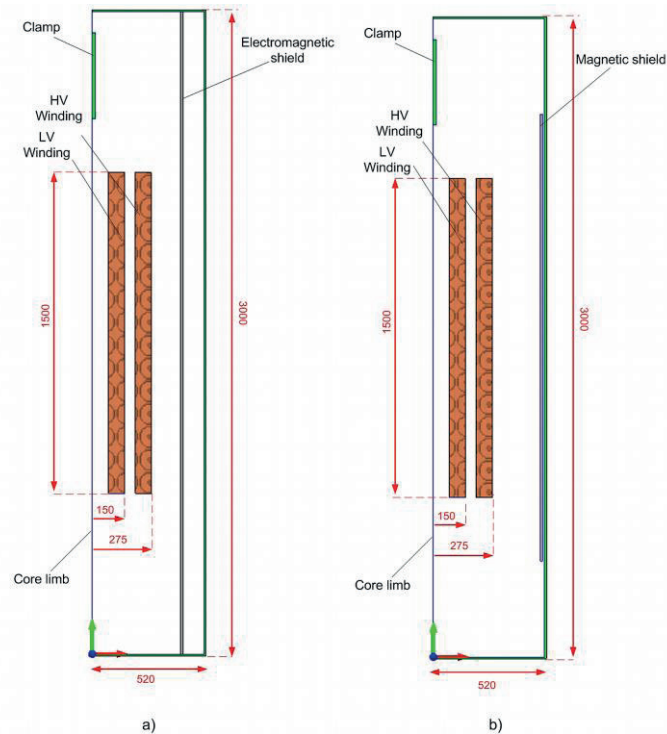


Figure 1 - Model for analysis of winding stray flux losses with a) electromagnetic and b) magnetic shields on the tank

In order to design a simple model for investigation of stray losses in a transformer, some simplifications have been chosen to achieve faster and practical analysis of the problem:

- 2D model is planar
- only one phase is accounted in the analysis while neglecting the effect of other phases
- currents in the windings are equally distributed, while their values are sinusoidal functions of time
- eddy currents in the windings are neglected
- geometry is simplified, various constructional parts are excluded from the model
- material parameters are linear (Table I), transformer core limb is modeled with a normal field boundary condition

Table I - Material properties

Material	Electrical conductivity [MS/m]	Relative magnetic permeability	Thermal conductivity [W/Km]
Magnetic steel	5,6	250	40
Nonmagnetic steel	1,5	1,5	20
Aluminium	37,7	1	200
Electrical steel	0	20000	-

Different stray flux distribution can be observed from the comparison of results for models with electromagnetic (aluminium) shields and magnetic (electrical steel) shields. Results are shown in figure 2.

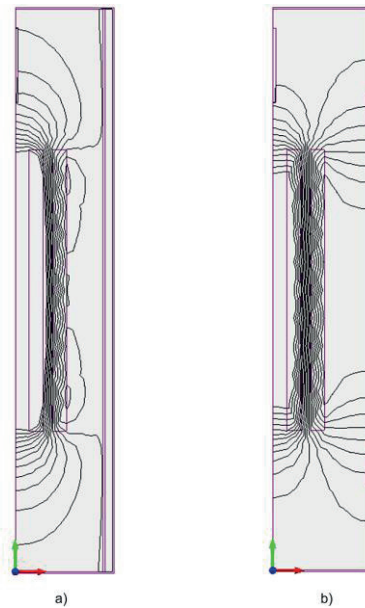


Figure 2 - Winding stray flux distribution with a) electromagnetic and b) magnetic shielding of the tank

When using electromagnetic shielding, flux is diverted from the tank and more flux is present in the winding and other constructional parts of the transformer (for example transformer clamps). On the other hand, when using magnetic shield, most of the winding stray flux goes into the shields. For this reason stray flux does not have to be closed through the other parts of the transformer. Influence of various paths of the stray flux on the losses in the transformer parts are analyzed in [2]. The dependence of stray losses on the thickness of electromagnetic shields is discussed in [3]. It is concluded that the best way to use the electromagnetic shields is to weld them on the tank. When choosing the thickness of the electromagnetic shields, one has to consider the thermal effects of the shields and the effect on the total cost of the transformer.

Taking in consideration the stray losses in the tank, shields, windings and other constructional parts of the transformer, magnetic shields are more efficient in total reduction of winding stray losses [2].

### 3. REDUCTION OF LOCAL OVERHEATING

#### 3.1. Model definition

Reduction of total stray losses does not always lead to the reduction of local temperature rises in the constructional parts. When defining a numerical model, one has to consider the geometry of the transformer in detail. Local overheating can occur in parts that are usually neglected in simplified 2D models used for numerical calculations. So, in this case, all transformer stray flux sources have to be considered. For now, only winding stray flux was taken into account. If a transformer has high LV current value, due to the small clearances between leads and metal parts, high loss density spots can be generated. If these spots are not cooled appropriately, high temperature rise in these spots can occur.

For the purpose of the analysis of generation of hot spots, a 3D transformer model has to be defined. Also, in order to analyze temperature rise in the metal parts, model has to be adapted for the thermal calculation.

The goal of the model is to investigate impact of electromagnetic aluminium shields on local overheating in metal constructional parts. Since magnetic shields are chosen for the shielding from the winding stray flux, only parameters of the model will be dimensions and positions of electromagnetic shields.

For the calculation of losses and temperatures MagNet and ThermNet software packages are used [4]. When making a thermal calculation, heat sources are represented by the losses that are already calculated in MagNet. Although a strong coupling exists between electromagnetic and thermal phenomena, in this paper, weak coupling method is employed. This means that all material parameters

are independent of temperature [5]. Also, values of heat transfer coefficient do not depend on the value of the temperature rise of the component. The basic characteristics of the 3D model are:

- all three phases are accounted in the model
- low voltage leads are modeled in detail
- windings are modeled as cylinders, where the currents are equally distributed while the effect of eddy current is neglected
- metal parts that are included in the model are transformer tank and the clamping system
- core has zero electrical conductivity with linear isotropic relative permeability
- steel parts are linear and are given in Table I

Transformer core, windings and LV leads from the 3D model are shown in figure 3.

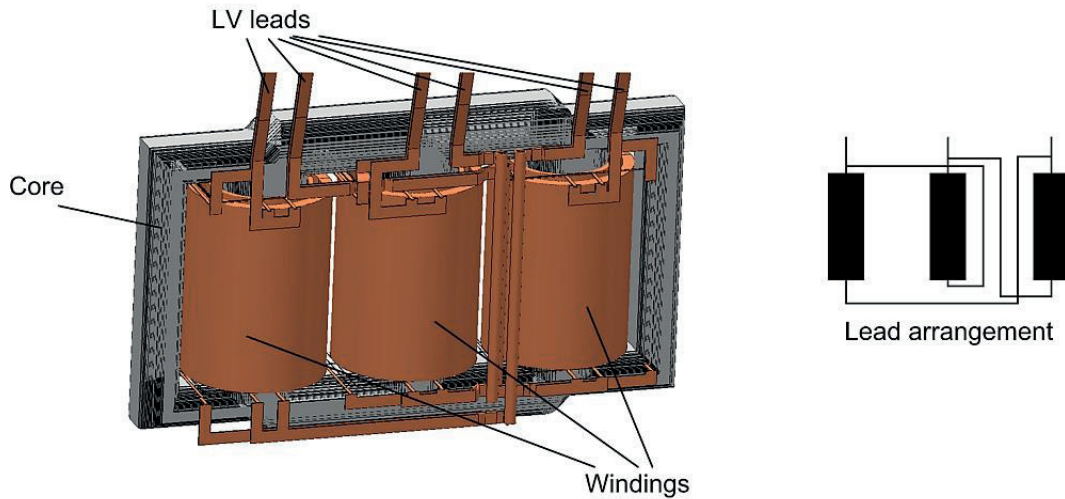


Figure 3 - Transformer with modeled lead arrangement

The main aspect of this paper is local overheating of the tank. Transformer tank is shown in figure 4. Since the current in LV winding is 10 kA, nonmagnetic steel is used for the construction of the part of the tank cover (metal enclosure). Electrical steel is used for the magnetic shielding of vertical tank parts from the winding stray flux. Temperature distribution for the transformer is shown in figure 5.

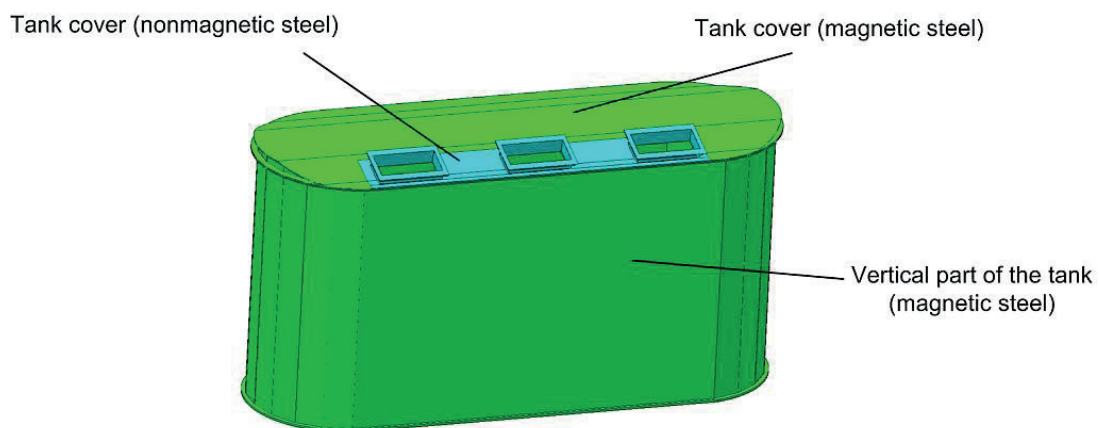


Figure 4 - Transformer tank

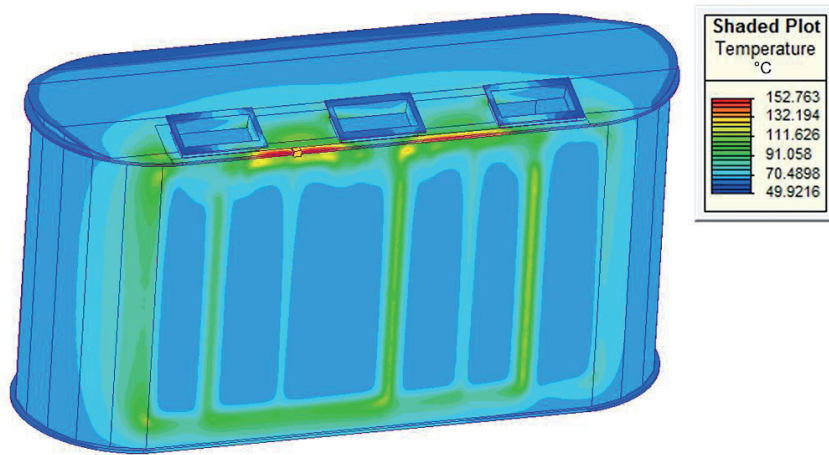


Figure 5 - Temperature distribution on the tank

Because magnetic shields are not designed for the shielding from the flux induced by high current leads, another shielding has to be added. Electromagnetic shields are a better choice than the magnetic shields because they are easier to shape and mount at various positions inside a transformer. Also they are used to direct the flux away from the surfaces that they cover. First type of aluminium shield ("L" shaped) that will be used in the calculation is shown in figure 6. Positions and thicknesses of the shield can be varied in accordance with space left between the leads and the top cover of the transformer (figure 7). By this way the dependence of stray losses and temperature rise on the shielding position and thickness can be shown.

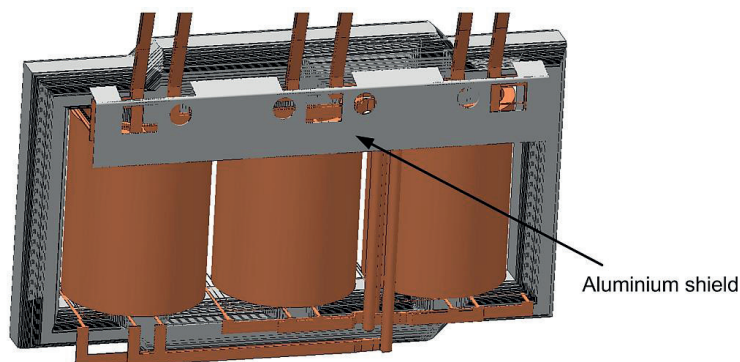


Figure 6 - Aluminium shield used for electromagnetic shielding of the tank of the transformer

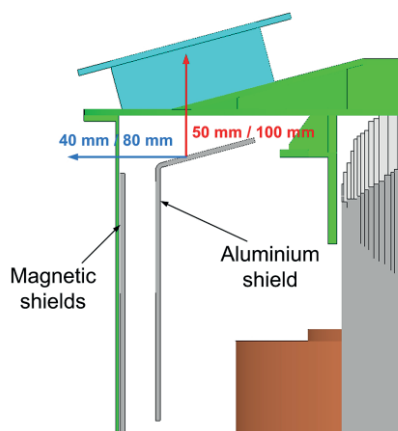


Figure 7 - Positioning of the aluminium shield inside the tank

### 3.2. Local overheating and stray losses with the "L" shaped electromagnetic shield

Temperature distribution on the transformer tank for the thickness of the shield 15 mm is shown in figure 8. From the start, the aluminium shield is positioned 160 mm from the tank cover and 125 mm from the vertical part of the tank. Aluminium shield is also moved in another two positions (table II) with three different thicknesses (table III). First position makes the shield 50 mm closer to the tank cover and 40 mm closer to the vertical part of the tank, while the second position makes the shield 100 mm closer to the tank cover and 80 mm closer to the vertical part of the tank.

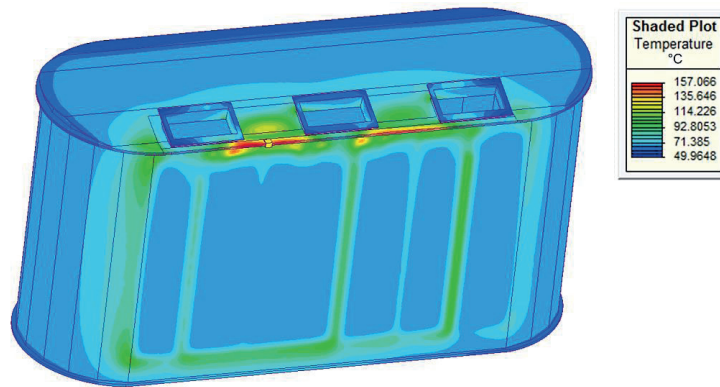


Figure 8 - Temperature distribution with the "L" shaped aluminium shield in the position 1

Table II - Position of the "L" shaped aluminium shield

Position	Distance from the vertical part of the tank	Distance from the tank cover
1	125	160
2	85	110
3	45	60

For a more detailed analysis, change of losses in transformer tank is shown in table III. It can be concluded that all the losses in magnetic steel parts are reduced, while losses in the tank cover part made of nonmagnetic steel have risen.

Table III - Losses and maximum temperatures

	no Al shield	5 mm			15 mm			25 mm		
		1	2	3	1	2	3	1	2	3
Tank cover - nonmagnetic part [kW]	6,9	7,8	8,2	9,0	7,9	8,4	9,2	7,9	8,4	9,4
Tank cover - magnetic part [kW]	5,9	5,8	5,7	5,7	5,8	5,7	5,7	5,8	5,7	5,7
Vertical part of the tank [kW]	31,7	27,5	27,8	28,1	27,7	28,1	28,3	27,5	27,9	28,1
Aluminium shield [kW]	0	14,5	13,1	11,8	6,9	6,1	5,5	6,3	5,5	5,0
Total losses [kW]	44,5	55,6	54,8	54,6	48,3	48,3	48,7	47,5	47,5	48,2
Maximum temperature [°C]	152,7	156,3	160,1	166,6	157,1	161,4	169,1	157,1	161,6	169,5

In order to reduce the local overheating in nonmagnetic steel, main cause of this temperature and loss rise has to be investigated. Further investigation will have to include the analysis of distribution of stray flux induced by high current leads. This will simply be done by introducing 2D models in the analysis.

### 3.3. Research of high current leads stray flux

Aluminium shields can have influence on loss value and temperature rise when the horizontal leads are present close to the top cover of the transformer [6]. For this purpose, a simple 2D model corresponding to the dimensions of the transformer in figure 5 is made. Figure 9 shows the model and figure 10 the resulting flux for various positions and shapes of the aluminium shields.

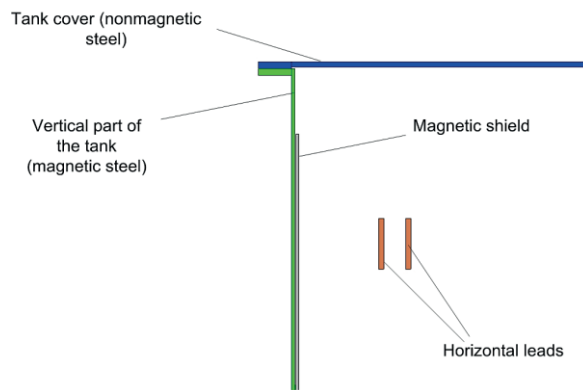


Figure 9 - 2D model

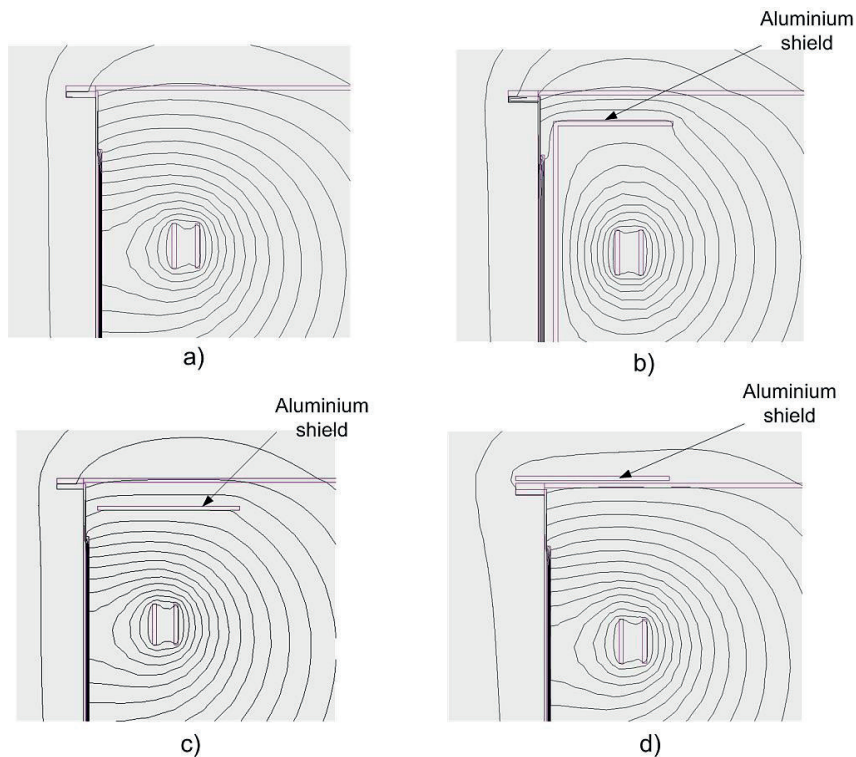


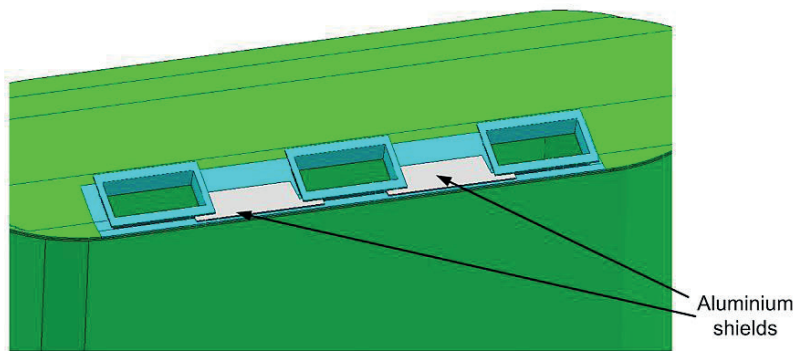
Figure 10 - Flux distribution for 2D model for a) no aluminium shield, b) "L" shaped aluminium shield, c) horizontal aluminium shield below the top cover, d) horizontal aluminium shield above the top cover

From table IV it can be concluded that although “L” shaped aluminium shields cover the biggest surface of the tank and top cover, they result with loss rise in the tank and the cover.

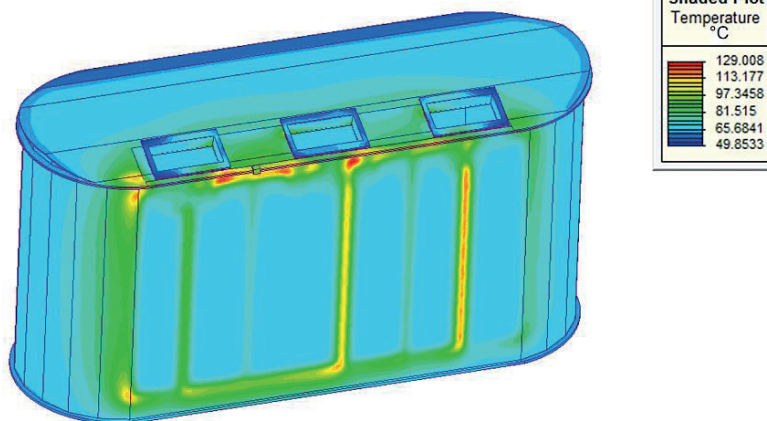
Table IV - Calculated losses and temperatures for the 2D model

	no shield	"L" shaped Al shield			horizontal Al shield inside			horizontal Al shield outside
		Position 1	Position 2	Position 3	Position 1	Position 2	Position 3	
Losses in vertical part of the tank [W/m]	431,9	452,4	506,2	553,1	393,4	408,9	425,3	395,8
Losses in tank cover [W/m]	380,2	495,5	576,9	669,4	344,7	355,9	359,3	219,9
Al shield losses [W/m]	0	269,2	212,6	172,2	73,4	54,3	40,8	37,6

For this reason, another shapes and positions of the shields have to be proposed. Results from the 2D model show that the best way to reduce losses in metal parts is to place aluminium outside the transformer, just over the top cover. This conclusion is adapted to the transformer 3D model (figure 11). Losses and temperatures for the transformer with the aluminium shield above the tank cover are shown in table V.



a)



b)

Figure 11 - a) Model with aluminium shields above the tank cover and b) results of the thermal calculation

Table V - Calculated losses and temperatures for the 3D model with and without aluminium shield above the tank cover

	No Al shield	Al shield outside
Tank cover - nonmagnetic part [kW]	6,9	5,1
Tank cover - magnetic part [kW]	5,9	5,9
Vertical part of the tank [kW]	31,7	31,1
Aluminium shield [kW]	0	0,6
Total losses [kW]	44,5	42,7
Maximum temperature [°C]	152,7	129,0

The use of aluminium shields above the top cover reduces the temperature hot spot value and total losses in the tank. This proves that horizontal leads are the main source of high loss density spots in the tank. The comparison of results in table V with results of the transformer model with the optimal position of the "L" shaped aluminium shield is shown in figure 12.

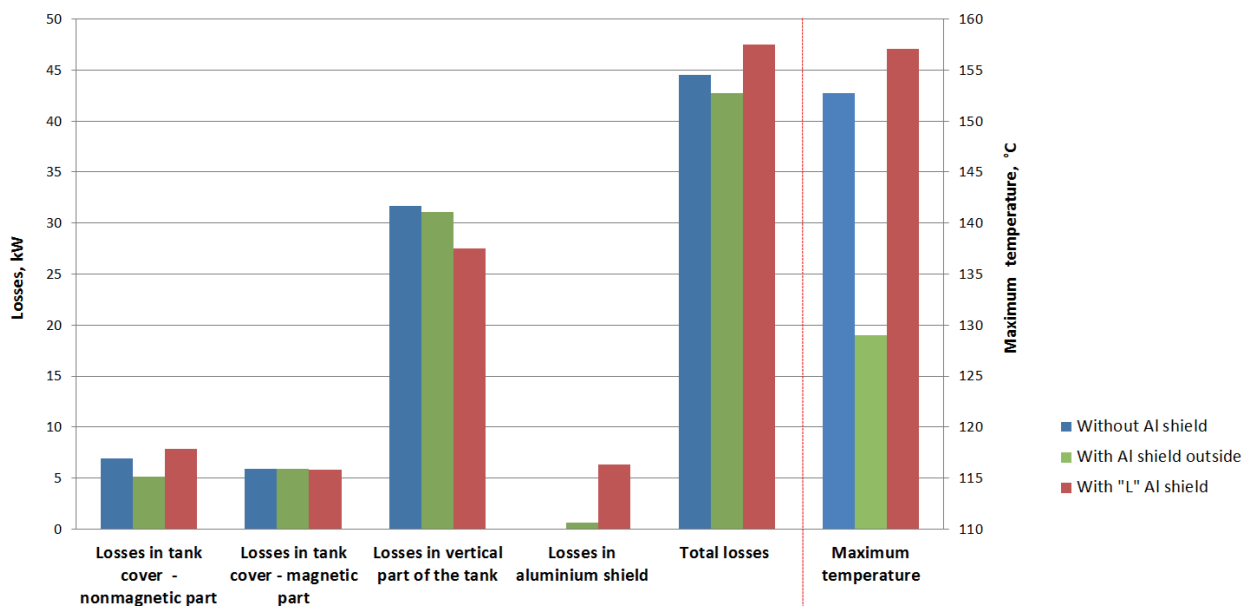


Figure 12 - Losses and maximum temperature in the tank for the 3D transformer model

#### 4. CONCLUSION

When using aluminium shields for reduction of high loss density values in metal parts it is important to analyze the shielding effect on the stray flux redistribution. Using modern FEM tools for coupled electromagnetic - thermal calculation it is possible to quickly study the best position and shape that could be used in practice.

As it is shown in the paper, the best shielding effect is not always achieved by shielding most of the endangered areas. When studying the flux induced by high current leads, it is important to determine which leads have the biggest influence on the temperature hot spots. Usually, this could be the horizontal leads which are common for the delta connected LV leads. Also, nonmagnetic and magnetic steel used in

the tank construction can have an important impact on the position of the hot-spot. In the paper it is shown that for the studied lead arrangement the highest loss density values are generated in the nonmagnetic part of the top cover. The way to be sure that the flux will not go through the nonmagnetic steel is to place aluminium plates above the top cover. Reactions of eddy currents in electromagnetic shields force the flux out of the top cover which reduces its losses and temperature hot-spot value. So, when making a shielding selection, one should always consider the effect of various materials of shields and surrounding constructional components.

The possibility of placing the shields outside the tank has already been mentioned in [7]. Although the suggested position of the aluminium shield is not usually seen in practice, the desired effect of temperature hot-spot value reduction is achieved.

## 5. REFERENCES

- [1] N. Mullineux, J. R. Reed, "Eddy current shielding of transformer tanks", *Proc. IEE*, Vol. 113, No. 5, May 1966, pp. 815 -818
- [2] Z. Valković, "Analysis of stray losses in transformer tank", in Croatian, PhD dissertation, University of Zagreb, Croatia, Zagreb, 1975.
- [3] A. Tugulea, N. Cristea, "L'influence de l'écran électromagnétique sur les pertes dans les cuves des transformateurs", *Rev. Roum. Sci Techn. Électrotechn et Énerg.*, Bucarest, 1971, p. 65-110
- [4] Infolytica MagNet and ThermNet Software, [www.infolytica.com](http://www.infolytica.com)
- [5] B. Cranganu-Cretu, A. Kertesz, J. Smajić: "Coupled Electromagnetic-Thermal Effects of Stray Flux: Ad-hoc Software solution for an Industrial Environment", Proceedings of the 2008 International Conference on Electrical Machines, Vilaumora, Portugal, 6-9 September 2008, Paper ID 1302
- [6] Y. Junyou, T. Renyuan, L. Yan, "Eddy Current Fields and Overheating Problems due to Heavy Current Carrying Conductors", *IEEE Transactions on Magnetics*, September 1994, Vol. 30, No. 5
- [7] B. Cranganu-Cretu, J. Smajić, G. Testin: "Usage of Passive Industrial Frequency Magnetic-Field Shielding for Losses Mitigation: A Simulation Approach", Advanced Research Workshop on transformers, Baiona, Spain, October, 2007, pp. 325-330

Franjo Kelemen  
Končar Power Transformers Ltd.  
[franjo.kelemen@siemens.com](mailto:franjo.kelemen@siemens.com)

Kosjenka Capuder  
Končar Power Transformers Ltd.  
[kosjenka.capuder@siemens.com](mailto:kosjenka.capuder@siemens.com)

Leonardo Štrac  
Končar Power Transformers Ltd.  
[leonardo.strac@siemens.com](mailto:leonardo.strac@siemens.com)

## SKIN – EFFECT LOSSES IN DIFFERENT LOADING CONDITIONS OF A POWER TRANSFORMER

### SUMMARY

The subject of the analysis is a 300 MVA auto-connected power transformer in different loading conditions with regard to the load losses. During the electrical design time, some operating points of the transformer were analyzed in more detail using 2D electromagnetic field finite element method (FEM) software. The models included 2D magnetic stray field calculation and covered a range of transformer loading cases that covered some that are more difficult to solve with traditional analytic methods based on the static magnetic field calculations. This is due to the presence of a phase shift between the currents through the windings. The results of the static magnetic Rabins' method field calculation and the FEM method are compared and the best practice method is defined and determined accordingly.

**Key words:** Finite element method, load losses, phase shift, power transformer, skin – effect.

### 1. INTRODUCTION

Load losses in a power transformer consist of different loss components. In general, these are the ohmic losses due to the winding and lead resistance, the skin-effect and proximity effect losses [1] in windings due to the stray field and additional losses outside of windings in the metal parts of transformer. As all these components add-up together in each case of the transformer load, the calculation of the stray flux density field distribution and, consequently, the losses is the first step to be taken. The usual approach in losses calculation is to use the 2D cylindrical coordinate system and Rabins' method [1] to model the stray field distribution. However, this method relies on static magnetic field distribution and needs to have a balance of ampere-turns on the transformer-leg to be applied correctly within the scope of the method. When there is a phase shift present in the winding currents, although the net sum of ampere turns in each time instance is still zero, the magnitudes of currents can not be directly fed to the mathematical model and used without some modifications. This is why the 2D FEM solver is applied to test the range or feasibility of application of Rabins' method in power transformer design. The inherent drawback of the quasistatic calculation of the losses in conductor strands is in its need of high number of elements to represent the geometry in a correct manner. The number of elements is in direct correlation with execution time of the calculation process and makes the usage of FEM less feasible in comparison with analytic methods.

## 2. MAGNETIC STRAY FIELD DISTRIBUTION IN A POWER TRANSFORMER DURING DIFFERENT LOADING CONDITIONS

The power transformer must be capable of continuous service in all normal operational points. However, different loading conditions change the distribution of the ampere turns in the transformer winding geometry. Hence, the additional losses along with skin-effect and proximity effect losses that are primarily influenced by the distribution of the stray field will also vary. The cooling system must be capable of exchanging the heat between the transformer and the environment, keeping the temperatures of the transformer copper and iron in the acceptable range. Therefore, the relevant loading case has to be found with respect to the load loss and additional losses. The stray field of a transformer, or the magnetic induction distribution in the transformer, is a function of the current excitation through the windings. Traditional methods only use analytic static magnetic field solution [1], [2] inside the core window based on the Rabins' method. The choice of operating points is made with maximum load losses in mind (see Table I). The graphical representation of the spatial 2D distribution of the magnitude of the magnetic induction vector field in cylindrical coordinate system is shown in the Fig. 1 for three normal (operating points without the phase shift between the currents) and one with the phase shift (cases correspond to ones given respectively in Table I).

Table I Load cases considered.

Loading condition	$I_{TV}$ in A	$I_{FR1}$ in A	$I_{FR2}$ in A	$I_p$ in A	$I_s$ in A
HV/LV(+)	0	1120∠0°	1120∠0°	687∠0°	433∠0°
HV/LV (0)	0	1312∠0°	1312∠0°	879∠0°	433∠0°
HV/LV (-)	0	1584∠0°	1584∠0°	1151∠0°	433∠0°
HV/LV/TV	2436∠90°	1121∠-3.31°	1121∠-3.31°	763∠-14.38°	400∠18.18°

The final load case from the table I is illustrated in Fig. 1 d) and is represented graphically with complex magnitude of the vector of magnetic induction, or

$$\max_{t, \varphi} (B(r, \theta, z, \omega t - \varphi)) \text{ for each } \forall r, \theta, z \quad (1)$$

Calculated ohmic losses are given in the table II. The ohmic losses are only one part of the total losses and calculated directly, while the additional losses are estimated through the stray flux in a certain tap position of the power transformer. Due to the fact that stray flux entering the conductive parts of a transformer is directly connected to the stray losses, different estimation formulae are constructed to emulate the behavior of the stray losses with respect to the stray flux level. Usually, the losses are modeled through the portion of the flux entering the conductive materials. While the currents are of the same phase angle, the distribution of the stray field in connection with the additional losses estimation can be done through the results at a single time instant. However, when the phase shift between the load currents is present, the stray flux distribution changes in time (the character of the distribution changes). Consequently, the overall local maxima in stray flux distribution have to be found, the reduced stray flux curves need to be calculated and only then is the estimation of the stray losses possible using the same principles as in the other cases of operation. The illustration of the basic idea of additional (stray) losses estimation is presented in figure 2. The (axial component of) magnetic flux density distribution through the middle of the windings, the stray flux and reduced stray flux integral curves are given as a visual representation of the stray losses in different tap positions and operating points.

Table II Ohmic loss in different loading conditions.

Configuration	T ohmic loss in kW/phase	FR ohmic loss in kW/phase	LV ohmic loss in kW/phase	HV ohmic loss in kW/phase	Total ohmic loss in kW
HV-LV(+)	1.7	13.5	49.8	126.7	575.0
HV-LV(0)	0.3	0.1	70.8	126.7	593.7
HV-LV(-)	0.4	25.9	115.1	126.8	804.8
HV-LV(1)-T	36.6	4.5	56.1	105.0	606.6

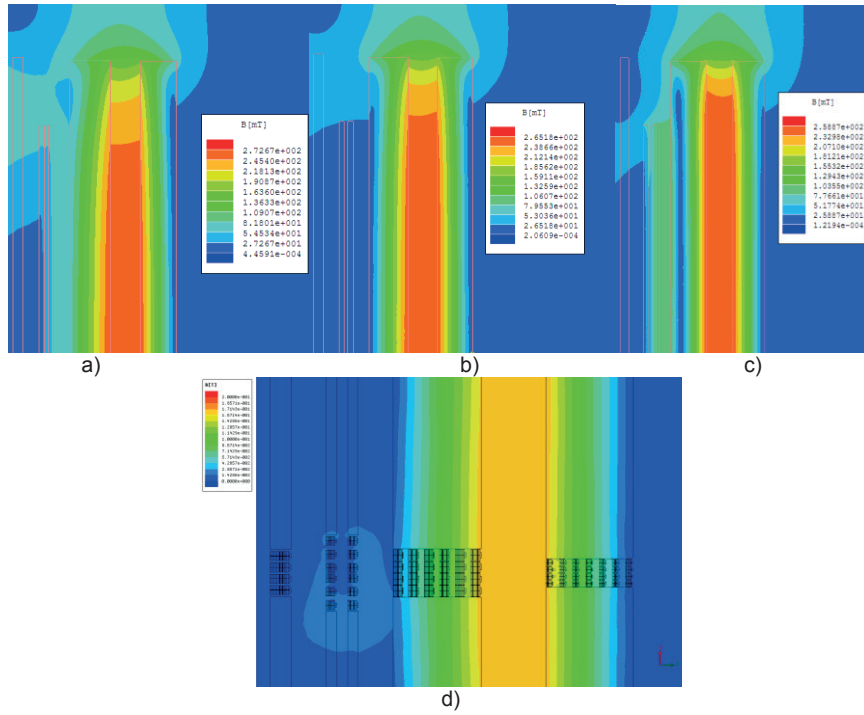


Fig. 1 Distribution of the magnitude of the magnetic induction vector (complex magnitude) on the 2D axisymmetric geometry of a power transformer; a) HV/LV(+); b) HV/LV (0); c) HV/LV (-); d) HV/LV/TV loading condition.

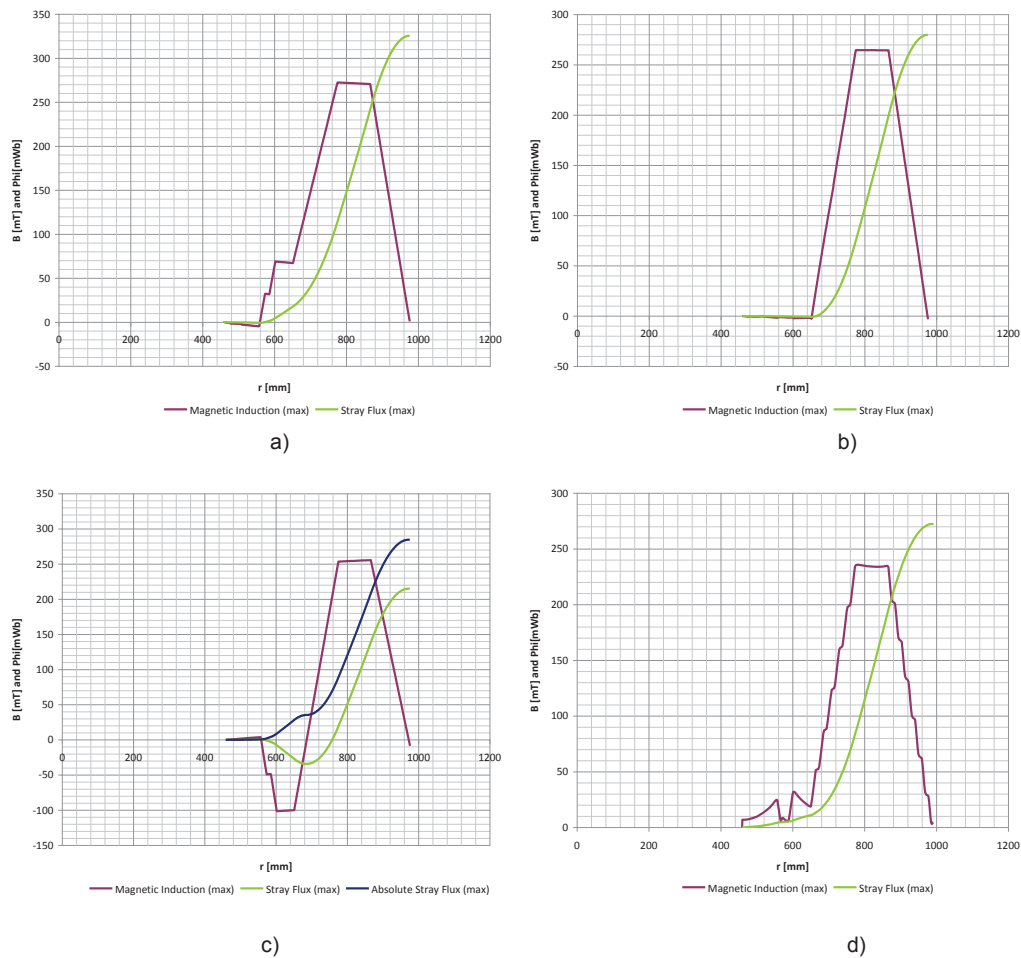


Fig. 2 Axial magnetic induction distribution (complex magnitude) in the radial direction in the plane of the symmetry of the winding heights during different loading conditions; a) HV/LV(+); b) HV/LV (0); c) HV/LV (-); d) HV/LV/TV.

The stray flux lines of the transformer stray field have predominantly axial component (see Fig. 1) in the middle of the winding and for the most of the winding height. At the top and bottom of the winding, the stray flux lines gain the radial component. Therefore, the winding can be effectively subdivided in two regions, one with predominant radial skin-effect and one with the axial skin-effect. The skin-effect calculation requires that each strand of the continuously transposed conductor (CTC) is modeled. As the radial flux density field is strongest at the winding ends, it is enough to model 5-10% of the winding height in more detail. The other part of the winding that needs to be represented in more detail is the middle of the winding, where the axial skin-effect is the strongest. Subdivisions that allow the simplification of geometry are presented in Fig. 3.

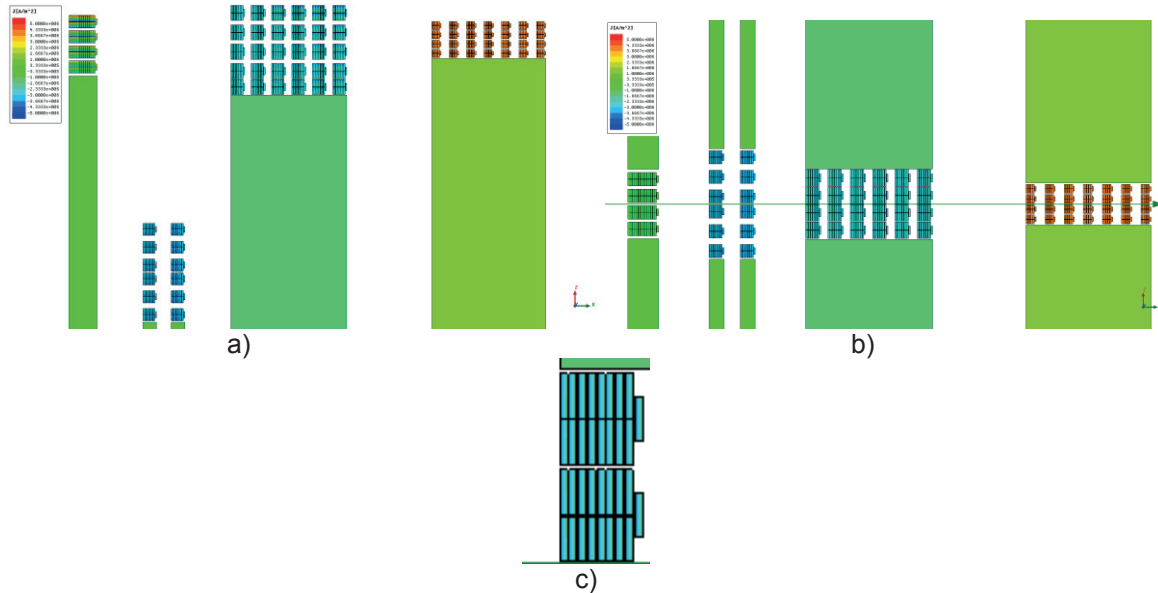


Fig. 3 FEM model of the winding end a), winding middle b) and a detail of CTC conductor array modeled c).

It is fairly easy to recognize that the calculation process with high detailed windings using FEM takes significantly higher amount of time to be completed than using analytic method. Therefore, the previous knowledge of the stray flux behavior is used to simplify the calculations and model only the regions that are notably different with respect to losses calculation. The overall losses are then calculated using the results obtained through the regions.

### 3. ANALYTICAL APPROACH

With some modifications, analytical method can still be applied in the cases of phase shift between the winding load currents. The key is to model two different time instants that differ by 90° degrees electrical. To test the applicability of the approach, elaborate models based on 2D magnetic FEM quasistatic field solution are used first to confirm the overall quality of the skin-effect calculation by traditional methods and then to scrutinize the “new” approach that broadens the spectrum of application of the analytical software currently in use. Based on the magnetic field density vector fields obtained in the calculation, additional losses are estimated and skin-effect losses are calculated.

Total power in the windings is calculated using:

$$P_{tot}(t) = p_1(t) + p_2(t) + \dots + p_n(t) \quad (2)$$

In (2),  $p_{tot}(t)$  is a time function of power, where  $p_1(t), \dots, p_n(t)$  are components of power in respective windings. These components of power are obtained through the set of equations:

$$\begin{aligned} p_1(t) &= u_1(t) \cdot i_1(t) \\ &\vdots \\ p_n(t) &= u_n(t) \cdot i_n(t) \end{aligned} \quad (3)$$

where:  $u_1(t), \dots, u_n(t)$  denote the voltages and  
 $i_1(t), \dots, i_n(t)$  are currents at a time instant  $t$ .

Specifically, in the case of simple harmonic functions of voltage and current the following holds:

$$p_1(t) = U_1 \sin \omega t \cdot I_1 \sin(\omega t - \phi_1) = U_1 I_1 \frac{\cos \phi_1 - \cos(2\omega t - \phi_1)}{2}, \quad (4)$$

Where:  $U_1$  and  $I_1$  are peak values of voltage and current,

$\omega$  is the angular frequency ( $\omega=2\pi f$ ),

$\phi_1$  is the phase shift between voltage and current waveforms,

$f$  is the line frequency.

The mean value of  $p_1$  represents ohmic losses,  $P_{mean1}$ , which can be expressed using relation (5).

$$P_{mean1} = \overline{p_1(t)} = \frac{U_1 I_1 \cos \phi_1}{2} \quad (5)$$

In general, for each argument  $\alpha$ ,  $p_1(\alpha)$  can be expressed as in (6).

$$p_1(\alpha) = U_1 \sin \omega \alpha \cdot I_1 \sin(\omega \alpha - \phi_1) = U_1 I_1 \frac{\cos \phi_1 - \cos(2\omega \alpha - \phi_1)}{2} \quad (6)$$

It is convenient to proceed with calculation for the time instant that differs by  $90^\circ$  degrees electrical, i.e. time instants  $p_1(\alpha)$  and  $p_2(\alpha+\pi/2)$ :

$$\begin{aligned} p_2\left(\alpha + \frac{\pi}{2}\right) &= U_1 \sin\left(\omega \alpha + \frac{\pi}{2}\right) \cdot I_1 \sin\left(\omega \alpha + \frac{\pi}{2} - \phi_1\right) \\ &= U_1 I_1 \frac{\cos \phi_1 - \cos(2\omega \alpha + \pi - \phi_1)}{2} = U_1 I_1 \frac{\cos \phi_1 + \cos(2\omega \alpha - \phi_1)}{2} \end{aligned} \quad (7)$$

Careful inspection of relations (6) and (7) reveals that the arithmetic average of these two respective functions equals to (5). Therefore, their mean value  $P_{mean}$  can be modeled using the respective powers calculated in two different time instances that are  $90^\circ$  electrical degrees apart, regardless of the initial parameter  $\alpha$ . So, without losing the generality, the parameter  $\alpha$  can be chosen arbitrarily and is usually set to zero.

$$P_1(\alpha) + P_2\left(\alpha + \frac{\pi}{2}\right) = U_1 I_1 \cos \phi_1 \quad (8)$$

$$P_{mean1} = \frac{P_1(\alpha) + P_2\left(\alpha + \frac{\pi}{2}\right)}{2} = U_1 I_1 \frac{\cos \phi_1}{2} \quad (9)$$

The important result written in the formula (9) that gives the total mean power (or losses), that is in fact independent of parameter  $\alpha$ , allows the calculation of the losses in all possible cases of current distributions and phase shifts in the windings because the same holds true for  $P_{mean2}, P_{mean3}, \dots, P_{meann}$ . Using the developed approach, the losses in windings for the loading conditions with the phase shift between the currents are calculated. The results are given in the table III for each of the main windings and overall for one phase of a transformer.

Table III Ohmic losses in main windings and overall per phase losses calculated using FEM and Rabins' method for the case 4 in Table I.

	LV ohmic loss in W/phase	HV ohmic loss in W/phase	Total ohmic loss in W/phase
Analytic method	55251	105670	202569
FEM	56067	105013	202185
Difference	-1.48%	0.62%	0.19%

In table IV all the results of the calculated losses are compared using relative and absolute differences with respect to FEM calculation.

Table IV Ohmic loss in different loading conditions calculated using FEM and Rabins' method.

Configuration	Total ohmic loss FEM in kW	Total ohmic loss - analytic in kW	Absolute differences in kW	Relative differences in %
HV-LV(+)	575.0	575.5	0.50	0.09
HV-LV(0)	593.7	594.1	0.40	0.07
HV-LV(-)	804.8	805.8	1.00	0.12
HV-LV(1)-T	606.6	607.7	1.10	0.18

#### 4. CONCLUSION

The comparison of results presented in previous chapter confirms that the simple Rabins' method used in calculation of the stray field and skin-effect losses in the windings can be used in more general scenarios with currents with shifted phase angles. The differences between the FEM method and analytic method in the results in such cases are below 0.2% and can be neglected. The major part of these differences is a byproduct of the numerical inaccuracy of the methods used in respective approaches. The analytic method of calculation is more practical with respect to the execution time of the process and therefore more suitable for usage in different optimization schemes.

#### BIBLIOGRAPHY

- [1] R. M. Del Vecchio, B. Poulin, P.T. Feghali, D. M. Shah, R. Ahuja, "Transformer Design Principles", Gordon and Breach Science Publishers, p. 149-184.
- [2] Z. Haznadar, Ž. Štih, "Electromagnetic Fields, Waves and Numerical Methods", IOS Press, Amsterdam, Berlin, Oxford, Tokyo, Washington, 2000.

Franjo Kelemen  
Končar Power Transformers Ltd.  
[franjo.kelemen@siemens.com](mailto:franjo.kelemen@siemens.com)

Goran Plišić  
Končar Power Transformers Ltd.  
[goran.plisic@siemens.com](mailto:goran.plisic@siemens.com)

Sead Berberović  
Faculty of Electrical Engineering and Computing  
[sead.berberovic@fer.hr](mailto:sead.berberovic@fer.hr)

## ESTIMATION OF STRAY LOSSES IN POWER TRANSFORMERS USING 3D FEM AND STATISTICS

### SUMMARY

Total losses of a power transformer are subdivided in several distinctive parts. The  $I^2R$  losses are easy to calculate and can be precise to a level of measurement repeatability and tolerances of the guaranteed material properties. The additional losses inside the windings can be calculated almost with the same precision using analytic methods. The third part of the load losses that consists of stray losses is the smallest and the most difficult to estimate. However, stray losses estimation is very important in the design phase of a power transformer. Not only because the guaranteed design parameters have to be satisfied, but also the utmost care has to be taken that local losses density across the power transformer does not exceed levels that are permissible in the long term loading conditions of a transformer. The additional losses estimation process presented in this paper models the additional losses level in a transformer as a unit.

**Key words:** eddy losses, finite element method, power transformer, stray field, stray losses

### 1. INTRODUCTION

Estimation of stray losses in the power transformers is a well known topic that is being tackled from different angles continuously through time. Some considerations that make the calculation of the stray losses in power transformers so complicated are given in more recent literature (e.g. [1], [4]), and others are well known for some time, so analytic approaches are developed that make calculation of, for example, excess losses easier in special cases [5], [6]. In addition, studies about behavior of ferromagnetic material used in transformer construction parts are made with calculation of additional losses in mind [4]. Using the available computing power with modern 3D finite element software, coupled with the knowledge of material properties and behavior, a statistical model can be developed that can estimate the additional losses in a power transformer that is both - more accurate and more precise than the 2D estimation process. But, the test results of additional losses measurement on different transformers of the same type show that significant amount of statistical variation is already included in the measurements, i.e. the variation of losses inside this set can not be calculated using the computer model because their origin is of other nature.

## 2. ADDITIONAL OR STRAY LOSSES

The calculation of stray losses on complex geometries is usually done using numerical techniques and different software for field calculation. However, there are results in analytical approaches in eddy losses calculation that can be extended to the more general cases [1], [2] [5], [6], [7]. Different relations estimating the additional losses in the material have the same structure, but due to geometrical variations or different boundary conditions, some parts of the formulae used to calculate the losses change. Usually, the magnetic field is considered through magnetic field intensity variable which is mathematically connected to the losses. The field intensity and magnetic flux density across the transformer geometry varies with respect to time and spatial coordinates. For the statistical modeling to be applied to the transformer geometry, this behavior of the field has to be defined with respect to losses. The amount of losses is modeled to be directly proportional to the some power of the time maximum of the magnetic flux density at one point in space. Losses on the surface area are represented by the integral of the squared magnetic flux density vector across the surface as given in

$$B_{eq} = \sqrt{\frac{\iint_S (\vec{B}\vec{n})^2 dS}{\iint_S dS}}, \quad (1)$$

$$P'_{add} = \xi_j \cdot B_{eq,i,j}^{\eta_j} \cdot S_{i,j} \cdot \delta_{i,j} \cdot c_{i,j}, \quad (2)$$

where:  $B_{eq}$  denotes equivalent magnetic flux density,  $S$  is the surface of the element,  $\mathbf{n}$  is the surface normal vector,  $dS$  the surface differential,  $P'_{add}$  additional losses on an element,  $\xi$  and  $\eta$  are the unknown coefficients that need to be determined through statistics,  $i$  and  $j$  are indices that run through different construction elements and different measurements,  $\delta$  is the skin depth of the material,  $c$  is the number of skin-depths considered. The equivalent magnetic induction defined by (1) is used across the different surfaces (2) in the power transformer to calculate the overall stray losses. There are also stray losses that are result of to the stray magnetic field of the winding leads, which can readily be modeled by the following equation:

$$P'_{add,leads} = k \cdot \Phi_{FR,i}^2, \quad (3)$$

where:  $P'_{add,leads}$  represents the losses due to the stray field of leads,  $k$  is the coefficient of proportionality, while the  $\Phi_{FR}$  is the magnetic flux due to the regulating winding leads,  $i$  is a running index.

## 3. TRANSFORMER GEOMETRY AND FEM MODEL

The overall power transformer geometry can be very different with respect to the type of outer cooling system etc. Fig. 1 shows the geometry of a transformer with separate cooling bank. Although the appearance of the transformer varies, the situation with stray losses on different units is very similar. The active part of the transformer that is shown in Fig. 1b consists of the standard construction parts.

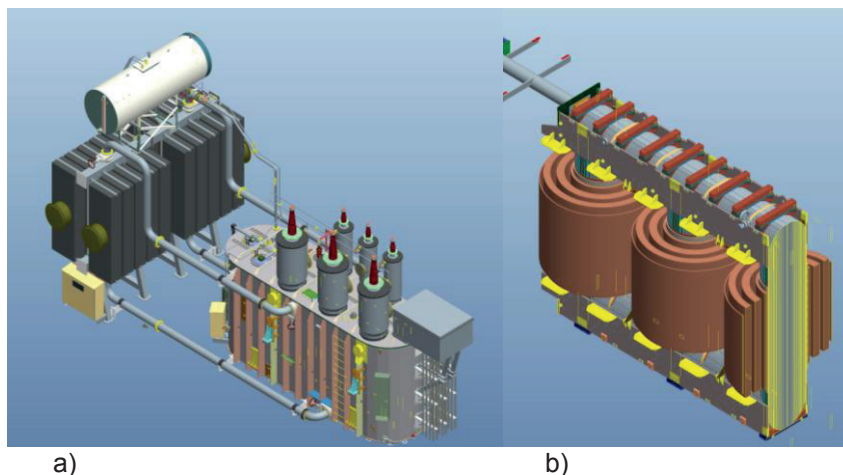


Fig. 1 Transformer geometry

For the purpose of stray-losses and stray field calculation only the inner geometry of the transformer is important. The losses appear in the conductive materials, so these parts of the geometry need to be modeled in more detail. Moreover, the analyzed part of the losses occurs outside of the winding, which ensures that the transformer windings can be modeled by cylinders without modeling each individual conductor or a strand. The sources of the stray field are current carrying conductors in the windings, while the field distribution outside of the windings is determined by the geometry of the core, clamping system and tank. These elements are predominantly made of constructional steel. The first step to modeling is to know the magnetic permeability of the material and its electrical conductivity. The parameters of the material are statistically distributed and, consequently, the losses are different, even on different units of the same type. The other sources of statistical variation are due to the small, but inevitable differences in the transformer production (within tolerances), and, finally, measurement. The constructional steel material used in transformer production, along with the tie-plate material have been studied recently to obtain the values that represent the real material properties the best in the stray losses calculation models [4]. The recommended values are used in the analyses presented here. The simplified power transformer geometry used in 3D FEM calculations is given in Fig. 2. Elements that predominantly influence the stray magnetic field distribution are the core, clamping plates, the tank and tie plates. The sources of the magnetic field are modeled with the overall nominal ampere-turns in different tap positions according to transformer data.

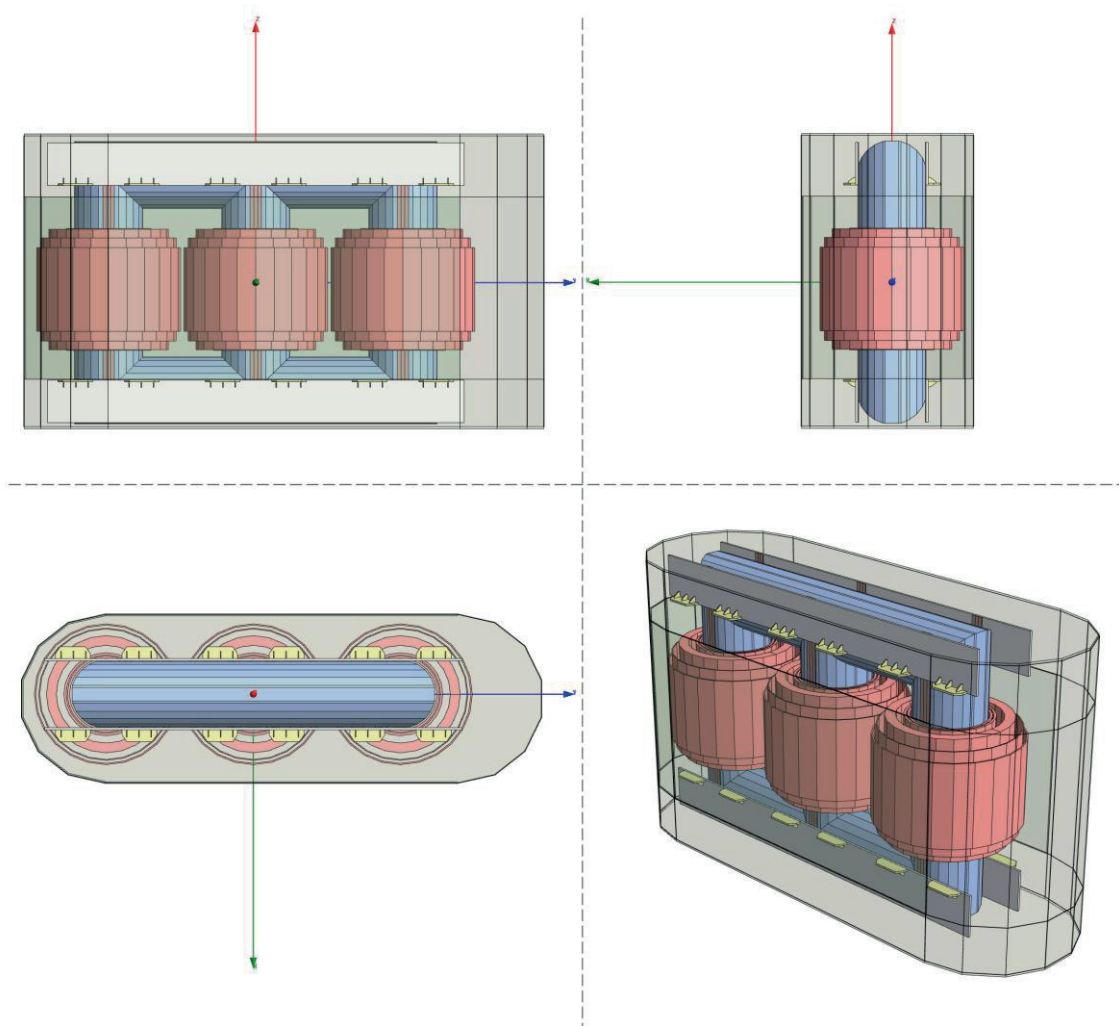


Fig. 2 The simplified 3D FEM model geometry of a typical power transformer in the analysis.

The fundamental element to the analysis is the solution to the magnetic stray field distribution using commercial Ansoft Maxwell v13 software for finite element method (FEM) calculations on a three-dimensional computer model. The approach is a natural extension to the analysis given in [1] with new parameters, and relies on similar statistical principles that govern estimation of stray losses that is currently in use in power transformer electrical design. Here, the connection is established between the

local magnetic field solution on the element, the geometrical properties and local losses on the particular element. Finally, the losses are added together and statistically correlated to the test values. The process of the calculation takes time, and for the time being is not suitable for use in optimization schemes.

#### 4. STRAY FIELD

After the basic elements required for the field calculations are defined (geometry, properties of materials, excitation, boundary conditions), the results obtained on one model of a power transformer are represented graphically in Fig. 3. The distribution of the stray field is the principle component behind the stray losses, so the distribution of the stray magnetic flux density in a way reflects the losses.

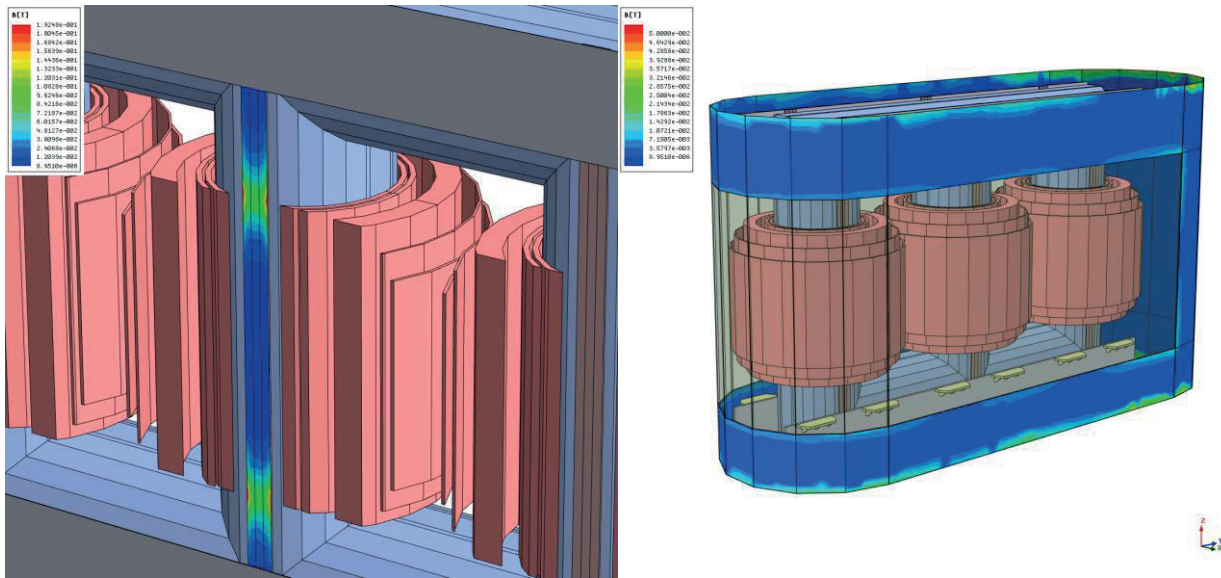


Fig. 3 Details of the power transformer geometry with the magnetic flux density field solution on a) transformer tie plates; b) transformer tank wall (parts not covered by magnetic shunts).

#### 5. STATISTICAL MODEL

The next step is the acquisition of the results and plugging them in the mathematical model of the following form

$$P'_{add,i} = \sum_{j=1}^N \xi_j \cdot B_{eq,i,j}^{\eta_j} \cdot S_{i,j} \cdot \delta_{i,j} \cdot c_{i,j} + k \cdot \Phi_{FR,i}^2, \quad (4)$$

where:  $i$  is index representing a single tap position of a transformer,  $P'_{add}$  are total additional losses outside of windings,  $N$  is the number of elements in the analysis,  $\xi$  is the shape factor of the element,  $B_{eq}$  is the equivalent induction,  $\eta$  is the exponent,  $S$  is the surface area of the element,  $\delta$  is the skin depth of the field,  $c$  is the number of skin depths in the volume,  $k$  is the coefficient modeling the stray losses due to the fine regulating winding current loop and  $\Phi_{FR}$  is the calculated magnetic flux produced by the leads of the fine regulating winding. These losses across elements are finally fed to mathematical minimization process of the objective function (5) that will result in unknown coefficients that model the losses statistically in the best possible way (i.e. the sum of squares of differences between test and calculation results is minimal).

$$F(\xi, \eta, k) = \sum_{i=1}^N (P'_{add,meas,i} - P'_{add,calc,i})^2, \quad (5)$$

where:  $F$  is the objective or cost function,  $N$  is the number of the measurements,  $P'_{add,meas}$  are measured additional losses,  $P'_{add,calc}$  are calculated losses (4), while  $i$  is the running index representing a single measurement. In this manner, the test results are linked through statistical model to the calculation results. Through this connection and the fact that the FEM 3D model is used (instead

of some form of 2D approximating geometry that cannot model structural parts of the transformer accurately) some merits over traditional methods of stray losses estimation are expected. These expectations include lowering statistical dispersion of the calculated vs. test results regarding stray losses outside of windings and ability to predict the stray losses outside of windings with greater statistical confidence.

## 6. RESULTS

The results of the statistical modeling process are given graphically in Fig. 4.

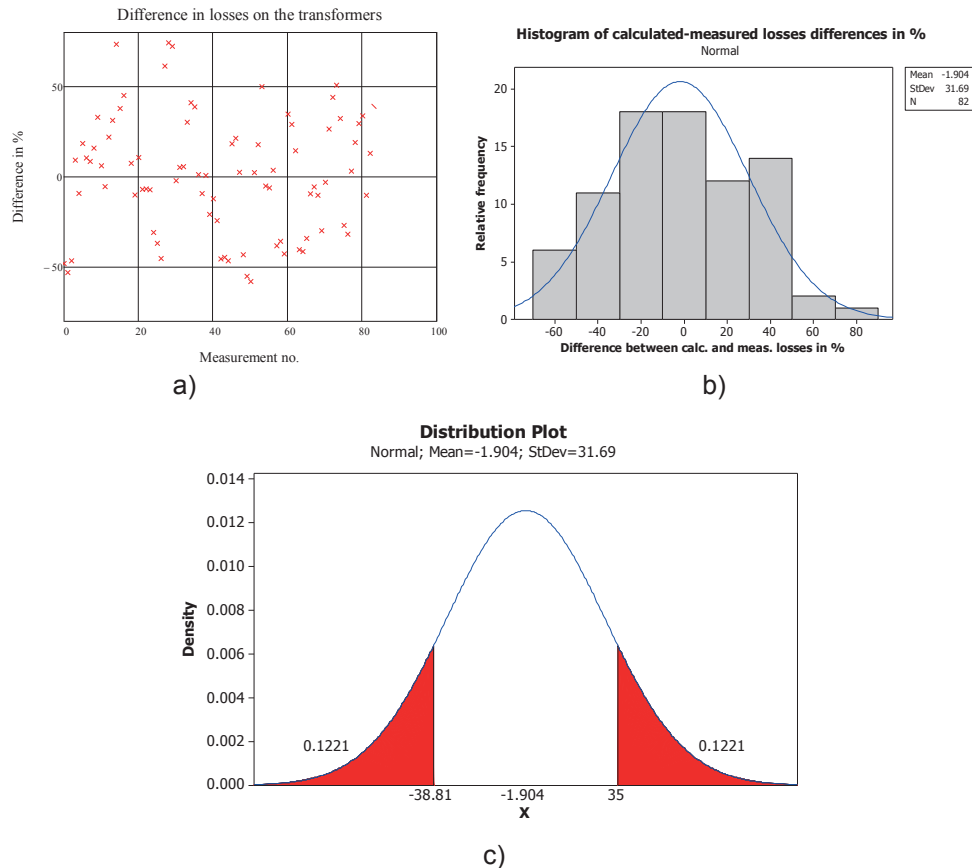


Fig. 4 Relative differences of the calculated and measured losses a); the statistical distribution of the differences b); illustration of the percentage of the results outside the +/-35 % boundary c).

More than 75% of the results fall into the range between +/- 35 % from the measured values. This difference in losses may seem significant, but the fact has to be kept in mind that the measured additional losses do not represent only the statistical variation of the stray losses, but also reflect the statistical distribution of other components of losses that measured additional losses are calculated from. This is why this kind of results dispersion is not considered to be too high. When the results are compared through their relative frequencies, the resulting histogram exhibits the behavior of normal statistical distribution. This is a final confirmation that the minimization process finished correctly and that no strong trend is present in the residual values.

## 7. CONCLUSION

Because of their previously described behavior, the statistical approach to the estimation of additional losses is used. It was already stated that the measurements of additional losses exhibit statistical dispersion as a byproduct of several influences like the manufacturing tolerances, the measurement uncertainty, the range of material properties etc. Due to the stochastic nature of the processes involved, a statistical method of additional losses estimation based on 3D FEM is a natural extension to the widely used 2D methods in the losses calculation. It has its advantages and drawbacks.

The main drawbacks of the presented method are that it requires substantially more time in execution and that the transformer construction geometry should be known at the time of the calculation. The latter makes the application of the method not feasible for the quick and simple estimation during evaluation of the different design solutions. However, the advantage of 3D calculation over the 2D estimation of additional losses is in its inherent capability to model the geometry of the constructional parts of the transformer more accurately. Finally, it is a reasonable assumption that this approach can have more success in the additional losses estimation on new or different power transformer geometry.

## REFERENCES

- [1] F. Kelemen, L. Štrac, and S. Berberović, "Estimation of Stray Losses Outside of Windings in Power Transformers Using Three Dimensional Static Magnetic Field Solution and Statistics", presented at the International Conference on Electrical Machines (ICEM) 2008, Vilamoura, Portugal, 2008.
- [2] Z. Haznadar, Ž. Štih, "Electromagnetic Fields, Waves and Numerical Methods", IOS Press, Amsterdam, Berlin, Oxford, Tokyo, Washington, 2000.
- [3] R. M. Del Vecchio, B. Poulin, P.T. Feghali, D. M. Shah, R. Ahuja, "Transformer Design Principles", Gordon and Breach Science Publishers, p. 149-184.
- [4] L. Štrac, „Modeliranje elektromagnetskih svojstava čelika za proračun dodatnih gubitaka u energetskim transformatorima“, dissertation, Faculty of electrical engineering and computing, Zagreb, Croatia, 2010.
- [5] C. Serpico, C. Visone, I. D. Mayergoyz, V. Basso and G. Miano, "Eddy Current Losses in Ferromagnetic Laminations", Journal of Applied Physics, vol. 87, no. 9, pp. 6923-6925, May 2000.
- [6] I. Mayergoyz and C. Serpico, "Nonlinear Diffusion of Electromagnetic Fields and Excess Eddy Current Losses", Journal of Applied Physics, vol. 85, no. 8, pp. 4910-4912, April 1999.
- [7] I. Mayergoyz, "Nonlinear Diffusion of Electromagnetic Fields-With Applications to Eddy Currents and Superconductivity", Academic Press, San Diego, 1998.

Branimir Ćučić, Ph.D  
Končar - Distribution and Special Transformers Inc.  
branimir.cucic@koncar-dst.hr

## MAGNETIC FIELD COMPUTATION OF A LOADED TRANSFORMER

### SUMMARY

A simple numerical method based on integral approach was described to compute the stray magnetic field in the surrounding region of a loaded distribution transformer. The model for magnetic field computation was made of transformer windings and low voltage conductors. Windings were modeled by rectangular and round blocks with uniform amper-turn distribution throughout the winding cross section. Low voltage conductors were modeled as series of straight current-carrying wire segments. The computed and measured results of magnetic induction are in good agreement.

**Key words:** loaded distribution transformer, stray magnetic field, magnetic induction

### 1. INTRODUCTION

The sensitivity of population regarding the electromagnetic emissions has significantly increased over the last fifteen years, mainly due to intensive use of mobile phones. In this paper extremely low frequency magnetic field of the transformer is to be determined. The term "extremely low frequencies" (ELF) is commonly used to describe any frequency below 300 Hz, in this case 50 Hz.

The magnetic induction reference level at 50 Hz recommended by ICNIRP is 100  $\mu\text{T}$  for the public exposure, and 500  $\mu\text{T}$  for the occupational exposure [1]. ICNIRP guidelines are based on short-term, immediate health effects. Most of the European countries follow these guidelines. However, some countries have decided to take a more precautionary approach by lowering the limits for exposure (Switzerland - 1  $\mu\text{T}$  [2], Italy - 3  $\mu\text{T}$  [3], Slovenia - 10  $\mu\text{T}$  [4], Croatia - 40  $\mu\text{T}$  [5], etc.).

Another issue is electromagnetic compatibility. ELF magnetic field can cause interference with electronic devices even if the field value is below reference level.

Distribution transformer as a part of power system generates 50 Hz magnetic field. The stray magnetic field in the surrounding region of a transformer is usually determined in short circuit test [3], [6] where low voltage windings are shorted and rated currents flow through all windings. However, such determined magnetic field can be significantly different from the field generated by loaded transformer. The reason for that are low voltage conductors, usually cables and busbars, through which transformer is loaded. In many practical cases they are the main source of the magnetic field. In this paper one such case was analyzed. A simple numerical method based on integral approach was described to compute quasistatic magnetic field of a loaded distribution transformer. The field was determined in the area above a 1000 kVA distribution transformer placed in a substation.

## 2. GEOMETRY AND MAIN TECHNICAL DATA

Analyzed configuration is shown in Figure 1. A voltage is applied to the primary side (high voltage side) of the distribution transformer. Load is connected to the secondary. The magnetic field was computed in two planes in the office room above the transformer ( $z=2.48$  m and  $z=3.48$  m). The origin of the coordinate system ( $z=0$ ) was set at the top of the transformer tank.

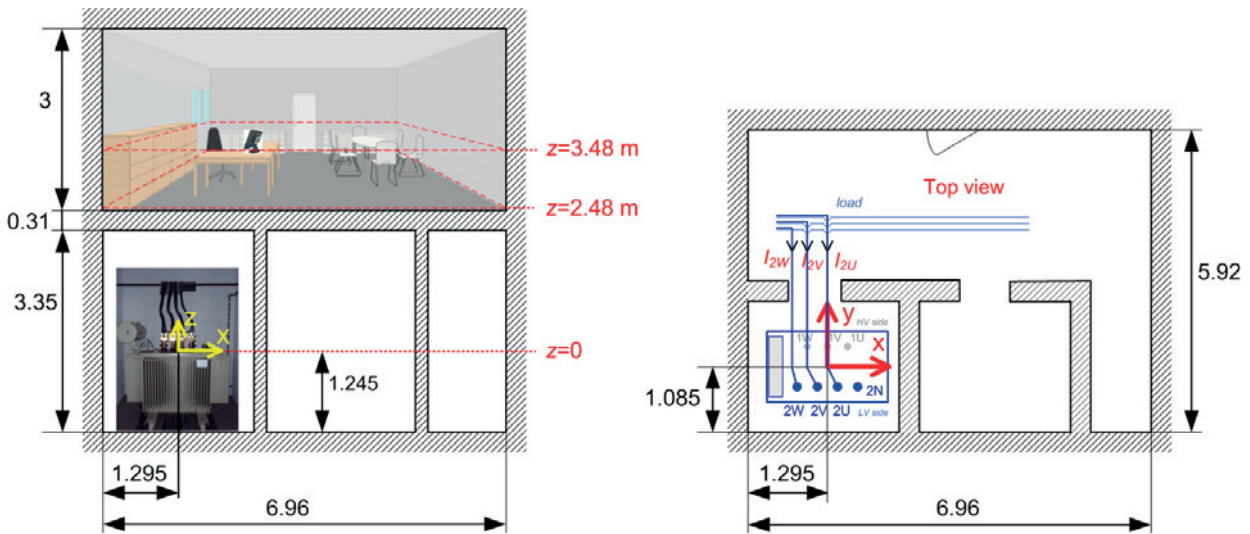


Figure 1 - Geometry of the problem. Dimensions are in meters

Transformer technical data are given in Table I.

Table I. Transformer technical data

Type	Three-phase oil immersed distribution transformer
Rated power	1000 kVA
Rated high voltage	20(10) kV
Rated low voltage	420 V
Vector group	Dyn5
Impedance voltage	6 %
Rated current through HV terminals	28.9 (57.7) A
Rated current through LV terminals	1375 A
Rated current in HV windings	16.7 A
Rated current in LV windings	1375 A
Rated number of turns in HV winding	1568
Rated number of turns in LV winding	19

## 3. MODEL OF THE LOADED TRANSFORMER IN THE SUBSTATION

### 3.1. Model of the loaded transformer

The sources of the magnetic field are all current-carrying elements. According to Figure 2, these sources are low voltage (LV) and high voltage (HV) windings, leads, cables and busbars. In configuration shown in Figure 1, where magnetic field is computed in the planes 2.48 m and 3.48 m far from the transformer tank cover, main source of the magnetic field are LV cables. Magnetic field in these planes is not significantly influenced by the transformer core, tank, clamping system or any other part of transformer substation, the reason why all these parts were ignored. Furthermore, the current in HV side is  $10000/420 \approx 24$  times lower than current in LV side. Because of that, all HV conductors, except windings, were ignored.

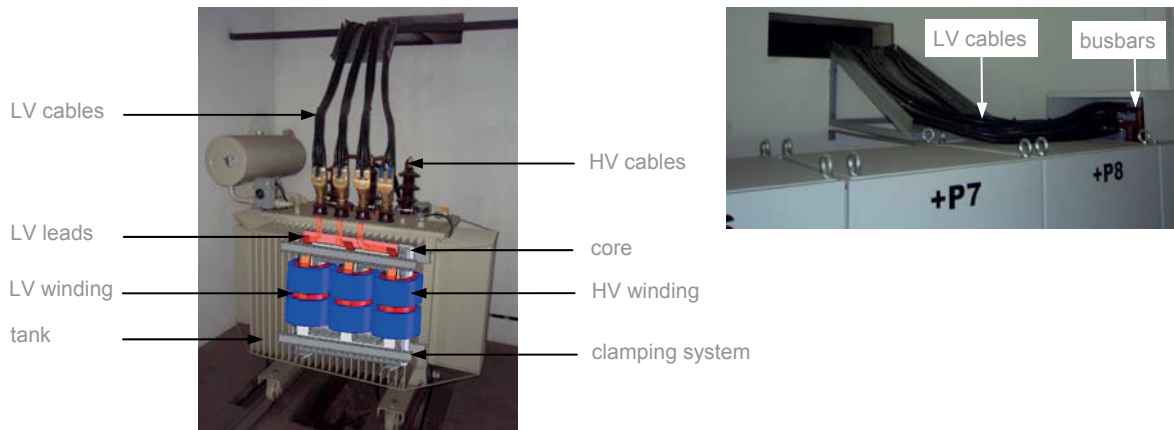


Figure 2 - Main parts of loaded transformer in the substation

The loaded transformer in the transformer substation was modeled by using transformer windings and all LV conductors (leads, cables and busbars) [7]. The model is shown in Figure 3.

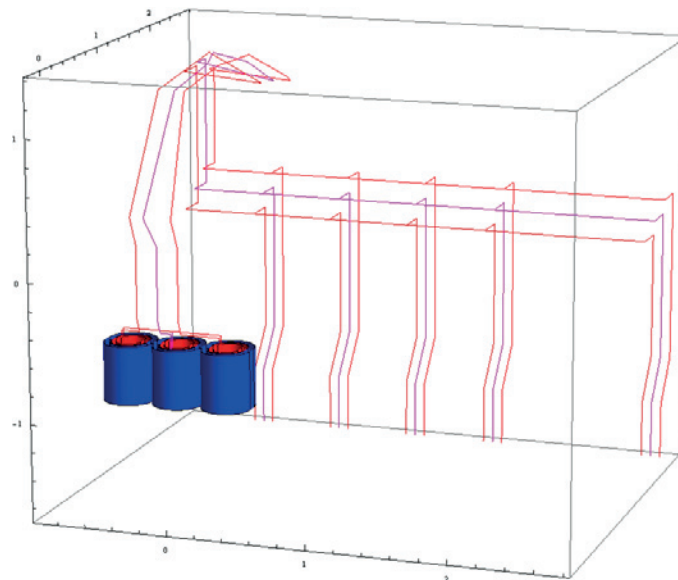
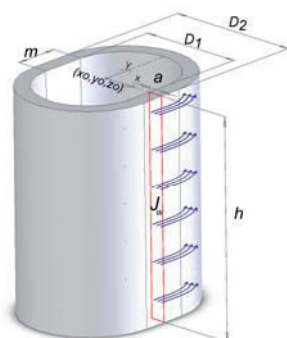


Figure 3 - Model of loaded transformer for the magnetic field computation

### 3.2. Model of the winding

Windings were modeled by rectangular and round blocks with uniform amper-turn distribution throughout the winding cross section as illustrated in Figure 4, where:



$D_1$  – inner diameter of the winding

$D_2$  – outer diameter of the winding

$a$  – winding width

$m$  – length of straight part of oval winding

$(x_0, y_0, z_0)$  – coordinates of the center of the upper part of the winding

$h$  – winding height

$J_w$  – winding current density ( $A/mm^2$ )

$I_{ph} \cdot W$  – amperturns

Figure 4 - Model of oval winding

Input data for all windings are given in Table II.

Table II. Input data for all windings

	LV phases			HV phases		
	a	b	c	A	B	C
$D_1$ (m)	0.179			0.260		
$D_2$ (m)	0.244			0.345		
$m$ (m)	0.079			0.079		
$x_0$ (m)	0.354	0	-0.354	0.354	0	-0.354
$y_0$ (m)	0			0		
$z_0$ (m)	-0.407			-0.415		
$h$ (m)	0.424			0.408		
$\dot{I}_{ph} \cdot W$ (Amperturns)	26118	$26118 \cdot e^{j(-120^\circ)}$	$26118 \cdot e^{j120^\circ}$	-26118	$-26118 \cdot e^{j(-120^\circ)}$	$-26118 \cdot e^{j120^\circ}$

### 3.3. Model of LV conductors

LV conductors were modeled as series of straight current-carrying thin wire segments. According to Figure 5, every straight wire segment carrying current  $I$  is defined by start coordinates  $(x_1, y_1, z_1)$  and end coordinates  $(x_2, y_2, z_2)$ .

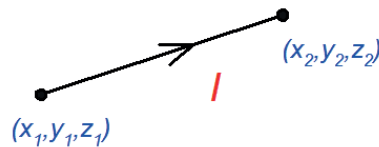


Figure 5 - A straight wire segment carrying current  $I$

Input data for all straight current-carrying wire segments are given in Table III.

The current through each straight wire segment is  $k \cdot 1375$  in "a" phase,  $k \cdot 1375 e^{j(-120^\circ)}$  in "b" phase, and  $k \cdot 1375 e^{j120^\circ}$  in "c" phase.

Table III. Input data for straight current-carrying wire segments

Phase	$x_1$ (m)	$y_1$ (m)	$z_1$ (m)	$x_2$ (m)	$y_2$ (m)	$z_2$ (m)	$k$	$x_1$ (m)	$y_1$ (m)	$z_1$ (m)	$x_2$ (m)	$y_2$ (m)	$z_2$ (m)	$k$
a	0.35	-0.16	-0.41	0.35	-0.16	-0.30	-1	0.37	2.48	0.28	0.37	2.73	0.28	-0.35
	0.35	-0.16	-0.30	0.08	-0.16	-0.30	-1	0.37	2.73	0.28	0.37	2.73	-0.95	-0.35
	0.08	-0.16	-0.30	0.08	-0.20	-0.20	-1	0.37	2.73	-0.95	0.37	2.48	-1.24	-0.35
	0.08	-0.20	-0.20	0.08	-0.20	0.31	-1	0.37	2.48	-1.24	0.37	2.48	-1.64	-0.35
	0.08	-0.20	0.31	-0.05	0.00	0.45	-1	0.37	2.48	0.28	0.97	2.48	0.28	-0.5
	-0.05	0.00	0.45	-0.11	0.43	1.26	-1	0.97	2.48	0.28	0.97	2.73	0.28	-0.15
	-0.11	0.43	1.26	-0.11	1.10	1.33	-1	0.97	2.73	0.28	0.97	2.73	-0.95	-0.15
	-0.11	1.10	1.33	0.00	1.41	1.36	-1	0.97	2.73	-0.95	0.97	2.48	-1.24	-0.15
	0.00	1.41	1.36	0.00	2.21	1.07	-1	0.97	2.48	-1.24	0.97	2.48	-1.64	-0.15
	0.00	2.21	1.07	-0.13	2.63	0.96	-1	0.97	2.48	0.28	1.57	2.48	0.28	-0.35
	-0.13	2.63	0.96	-0.77	2.63	1.01	-1	1.57	2.48	0.28	1.57	2.73	0.28	-0.15
	-0.77	2.63	1.01	-0.77	2.73	1.01	-1	1.57	2.73	0.28	1.57	2.73	-0.95	-0.15
	-0.77	2.73	1.01	-0.77	2.73	0.28	-1	1.57	2.73	-0.95	1.57	2.48	-1.24	-0.15
	-0.77	2.73	0.28	-0.77	2.48	0.28	-1	1.57	2.48	-1.24	1.57	2.48	-1.64	-0.15
	-0.77	2.48	0.28	-0.23	2.48	0.28	-1	1.57	2.48	0.28	2.77	2.48	0.28	-0.2
	-0.23	2.48	0.28	-0.23	2.73	0.28	-0.15	2.77	2.48	0.28	2.77	2.73	0.28	-0.2
	-0.23	2.73	0.28	-0.23	2.73	-0.95	-0.15	2.77	2.73	0.28	2.77	2.73	-0.95	-0.2
	-0.23	2.73	-0.95	-0.23	2.48	-1.24	-0.15	2.77	2.73	-0.95	2.77	2.48	-1.24	-0.2
	-0.23	2.48	-1.24	-0.23	2.48	-1.64	-0.15	2.77	2.48	-1.24	2.77	2.48	-1.64	-0.2
	-0.23	2.48	0.28	0.37	2.48	0.28	-0.85	0.35	-0.13	-0.41	0.35	-0.13	-0.29	1
							0.35	-0.13	-0.29	0.00	-0.13	-0.29	1	

Phase	$x_1$ (m)	$y_1$ (m)	$z_1$ (m)	$x_2$ (m)	$y_2$ (m)	$z_2$ (m)	$k$	$x_1$ (m)	$y_1$ (m)	$z_1$ (m)	$x_2$ (m)	$y_2$ (m)	$z_2$ (m)	$k$
b	0.00	-0.16	-0.41	0.00	-0.16	-0.30	-1	0.30	2.48	0.12	0.30	2.73	0.12	-0.35
	0.00	-0.16	-0.30	-0.08	-0.16	-0.30	-1	0.30	2.73	0.12	0.30	2.73	-0.95	-0.35
	-0.08	-0.16	-0.30	-0.08	-0.20	-0.20	-1	0.30	2.73	-0.95	0.30	2.48	-1.24	-0.35
	-0.08	-0.20	-0.20	-0.08	-0.20	0.31	-1	0.30	2.48	-1.24	0.30	2.48	-1.64	-0.35
	-0.08	-0.20	0.31	-0.25	0.00	0.45	-1	0.30	2.48	0.12	0.90	2.48	0.12	-0.5
	-0.25	0.00	0.45	-0.18	0.43	1.26	-1	0.90	2.48	0.12	0.90	2.73	0.12	-0.15
	-0.18	0.43	1.26	-0.20	1.10	1.33	-1	0.90	2.73	0.12	0.90	2.73	-0.95	-0.15
	-0.20	1.10	1.33	-0.27	1.41	1.36	-1	0.90	2.73	-0.95	0.90	2.48	-1.24	-0.15
	-0.27	1.41	1.36	-0.13	1.71	1.26	-1	0.90	2.48	-1.24	0.90	2.48	-1.64	-0.15
	-0.13	1.71	1.26	-0.24	2.58	0.96	-1	0.90	2.48	0.12	1.50	2.48	0.12	-0.35
	-0.24	2.58	0.96	-0.84	2.58	1.07	-1	1.50	2.48	0.12	1.50	2.73	0.12	-0.15
	-0.84	2.58	1.07	-0.84	2.73	1.07	-1	1.50	2.73	0.12	1.50	2.73	-0.95	-0.15
	-0.84	2.73	1.07	-0.84	2.73	0.12	-1	1.50	2.73	-0.95	1.50	2.48	-1.24	-0.15
	-0.84	2.73	0.12	-0.84	2.48	0.12	-1	1.50	2.48	-1.24	1.50	2.48	-1.64	-0.15
	-0.84	2.48	0.12	-0.30	2.48	0.12	-1	1.50	2.48	0.12	2.70	2.48	0.12	-0.2
	-0.30	2.48	0.12	-0.30	2.73	0.12	-0.15	2.70	2.48	0.12	2.70	2.73	0.12	-0.2
	-0.30	2.73	0.12	-0.30	2.73	-0.95	-0.15	2.70	2.73	0.12	2.70	2.73	-0.95	-0.2
	-0.30	2.73	-0.95	-0.30	2.48	-1.24	-0.15	2.70	2.73	-0.95	2.70	2.48	-1.24	-0.2
	-0.30	2.48	-1.24	-0.30	2.48	-1.64	-0.15	2.70	2.48	-1.24	2.70	2.48	-1.64	-0.2
	-0.30	2.48	0.12	0.30	2.48	0.12	-0.85	0.00	-0.13	-0.41	0.00	-0.13	-0.29	1
Phase	$x_1$ (m)	$y_1$ (m)	$z_1$ (m)	$x_2$ (m)	$y_2$ (m)	$z_2$ (m)	$k$	$x_1$ (m)	$y_1$ (m)	$z_1$ (m)	$x_2$ (m)	$y_2$ (m)	$z_2$ (m)	$k$
c	-0.35	-0.16	-0.41	-0.35	-0.16	-0.30	-1	0.23	2.48	-0.04	0.23	2.73	-0.04	-0.35
	-0.35	-0.16	-0.30	-0.23	-0.16	-0.30	-1	0.23	2.73	-0.04	0.23	2.73	-0.95	-0.35
	-0.23	-0.16	-0.30	-0.23	-0.20	-0.20	-1	0.23	2.73	-0.95	0.23	2.48	-1.24	-0.35
	-0.23	-0.20	-0.20	-0.23	-0.20	0.31	-1	0.23	2.48	-1.24	0.23	2.48	-1.64	-0.35
	-0.23	-0.20	0.31	-0.35	0.00	0.45	-1	0.23	2.48	-0.04	0.83	2.48	-0.04	-0.5
	-0.35	0.00	0.45	-0.30	0.43	1.26	-1	0.83	2.48	-0.04	0.83	2.73	-0.04	-0.15
	-0.30	0.43	1.26	-0.30	1.10	1.33	-1	0.83	2.73	-0.04	0.83	2.73	-0.95	-0.15
	-0.30	1.10	1.33	-0.30	1.41	1.36	-1	0.83	2.73	-0.95	0.83	2.48	-1.24	-0.15
	-0.30	1.41	1.36	-0.30	2.47	0.96	-1	0.83	2.48	-1.24	0.83	2.48	-1.64	-0.15
	-0.30	2.47	0.96	-0.35	2.48	0.96	-1	0.83	2.48	-0.04	1.43	2.48	-0.04	-0.35
	-0.35	2.48	0.96	-0.91	2.48	1.01	-1	1.43	2.48	-0.04	1.43	2.73	-0.04	-0.15
	-0.91	2.48	1.01	-0.91	2.73	1.01	-1	1.43	2.73	-0.04	1.43	2.73	-0.95	-0.15
	-0.91	2.73	1.01	-0.91	2.73	-0.04	-1	1.43	2.73	-0.95	1.43	2.48	-1.24	-0.15
	-0.91	2.73	-0.04	-0.91	2.48	-0.04	-1	1.43	2.48	-1.24	1.43	2.48	-1.64	-0.15
	-0.91	2.48	-0.04	-0.37	2.48	-0.04	-1	1.43	2.48	-0.04	2.63	2.48	-0.04	-0.2
	-0.37	2.48	-0.04	-0.37	2.73	-0.04	-0.15	2.63	2.48	-0.04	2.63	2.73	-0.04	-0.2
	-0.37	2.73	-0.04	-0.37	2.73	-0.95	-0.15	2.63	2.73	-0.04	2.63	2.73	-0.95	-0.2
	-0.37	2.73	-0.95	-0.37	2.48	-1.24	-0.15	2.63	2.73	-0.95	2.63	2.48	-1.24	-0.2
	-0.37	2.48	-1.24	-0.37	2.48	-1.64	-0.15	2.63	2.48	-1.24	2.63	2.48	-1.64	-0.2
	-0.37	2.48	-0.04	0.23	2.48	-0.04	-0.85	-0.35	-0.13	-0.41	-0.35	-0.13	-0.29	1
-0.35	-0.16	-0.41	-0.35	-0.16	-0.30	-1	-0.35	-0.13	-0.29	0.00	-0.13	-0.29	1	

#### 4. MAGNETIC FIELD COMPUTATION

The analysis of the magnetic field was made in phasor domain, meaning that every sinusoidal function of time was represented as a phasor which encodes the magnitude and phase angle of the sinusoid. In this paper phasor is denoted by a point above the letter (eg. current  $\dot{i}$ ), vector by a bold letter (eg. position vector  $\mathbf{R}$ ), and phasor-vector by a point above a bold letter (eg. magnetic induction  $\dot{\mathbf{B}}$ ).

Magnetic induction is computed at a point  $(x,y,z)$ . First, the magnetic induction of each winding ( $\dot{\mathbf{B}}_w$ ) is computed, then the magnetic induction of every straight current-carrying wire segment ( $\dot{\mathbf{B}}_L$ ). After that, the contribution of all windings and all straight wire segments are summarized ( $\dot{\mathbf{B}}$ ). Finally, the magnetic induction is transformed into time-domain ( $B$ ). All magnitudes are assumed to be RMS.

##### 4.1. Magnetic field of a winding

Magnetic induction of a winding  $\dot{\mathbf{B}}_w$  is computed as follows [8]:

$$\dot{\mathbf{B}}_w(\mathbf{r}) = \frac{\mu_0}{4\pi} \int_{V_o} \dot{\mathbf{J}}_w \cdot \mathbf{a}_w(\mathbf{r}') \times \frac{\mathbf{R}}{R^3} dV' \quad (1)$$

where:

- $\dot{j}_w$  – winding current density (A/mm<sup>2</sup>)
- $\mathbf{a}_w(\mathbf{r}')$  – unit vector to specify the direction of the current through the winding
- $dV'$  – differential element of volume  $V_o$  of the winding
- $\mathbf{R}$  – position vector
- $R$  – distance between the observation  $(x,y,z)$  and the integration point  $(x',y',z')$
- $\mu_0$  – permeability of air ( $\mu_0 = 1,256 \cdot 10^{-6}$  H/m)

$$\dot{j}_w = \frac{\dot{i}_{ph} \cdot W}{a \cdot h} \quad (2)$$

$$\mathbf{R} = \mathbf{r} - \mathbf{r}' = (x - x')\mathbf{a}_x + (y - y')\mathbf{a}_y + (z - z')\mathbf{a}_z \quad (3)$$

$$R = \sqrt{(x - x')^2 + (y - y')^2 + (z - z')^2} \quad (4)$$

#### 4.2. Magnetic field of a straight wire segment

Biot-Savart's law was applied to the magnetic field computation of a straight wire segment carrying current  $\dot{i}$  [8]. According to Figure 6,  $d\dot{\mathbf{B}}_L$  is magnetic induction contribution at point  $(x,y,z)$  from the current element  $\dot{i}dL$ :

$$d\dot{\mathbf{B}}_L = \frac{\mu_0 \dot{i} dL \times \mathbf{R}}{4\pi R^3} \quad (5)$$

$\mathbf{R}$  is position vector pointing from the current element  $\dot{i}dL$  towards the point  $(x,y,z)$  at which  $d\dot{\mathbf{B}}_L$  is computed.

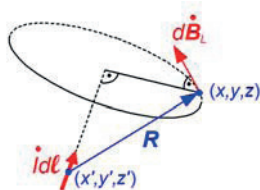


Figure 6 - Magnetic field contribution of a current element

As depicted in Figure 7, the straight current-carrying wire segment is defined by start  $(x_1, y_1, z_1)$  and end coordinates  $(x_2, y_2, z_2)$ . To compute the magnetic induction  $\dot{\mathbf{B}}_L$  of such segment, the origin of new coordinate system  $S''$  is set up at the midpoint  $(x_0, y_0, z_0)$  of the segment in a way that the current  $\dot{i}$  flows in the direction of  $+x''$  axis. Magnetic induction is first computed in the local coordinate system  $S''$  and then transformed into main coordinate system  $S$ .

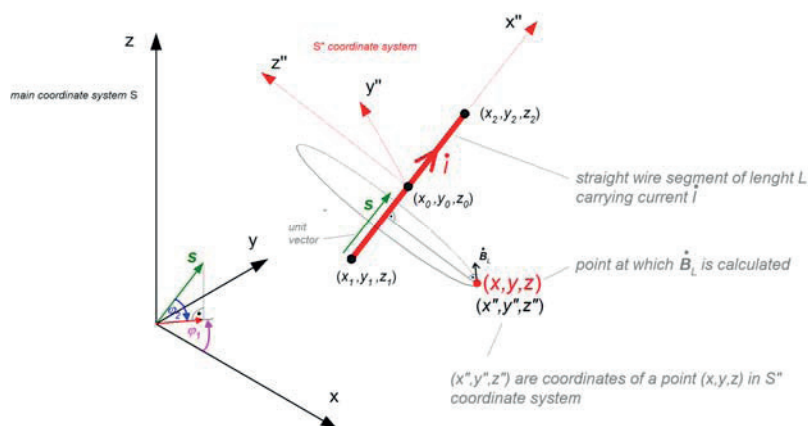


Figure 7 - Magnetic field of a straight current-carrying wire segment

The components of the phasor-vector  $\dot{\mathbf{B}}_L$  are computed at the point  $(x,y,z)$  as follows:

$$x_0 = \frac{x_1 + x_2}{2}; \quad y_0 = \frac{y_1 + y_2}{2}; \quad z_0 = \frac{z_1 + z_2}{2}; \quad (6)$$

$$L = \sqrt{(x_2 - x_1)^2 + (y_2 - y_1)^2 + (z_2 - z_1)^2} \quad (7)$$

$$s_x = \frac{x_2 - x_1}{L}; \quad s_y = \frac{y_2 - y_1}{L}; \quad s_z = \frac{z_2 - z_1}{L} \quad (8)$$

$$k_1 = \cos \varphi_1 = \frac{s_x}{\sqrt{s_x^2 + s_y^2}}; \quad k_2 = \sin \varphi_1 = \frac{s_y}{\sqrt{s_x^2 + s_y^2}} \quad (9)$$

$$k_3 = \cos \varphi_2 = \frac{\sqrt{s_x^2 + s_y^2}}{\sqrt{s_x^2 + s_y^2 + s_z^2}}; \quad k_4 = \sin \varphi_2 = \frac{-s_z}{\sqrt{s_x^2 + s_y^2 + s_z^2}} \quad (10)$$

$$x'' = (x - x_0) \cdot k_1 \cdot k_3 + (y - y_0) \cdot k_2 \cdot k_3 - (z - z_0) \cdot k_4 \quad (11)$$

$$y'' = -(x - x_0) \cdot k_2 \cdot k_3 + (y - y_0) \cdot k_1 \cdot k_3 \quad (12)$$

$$z'' = (x - x_0) \cdot k_1 \cdot k_4 + (y - y_0) \cdot k_2 \cdot k_4 + (z - z_0) \cdot k_3 \quad (13)$$

$$d_1 = x'' + \frac{L}{2}; \quad d_2 = x'' - \frac{L}{2} \quad (14)$$

$$d_3 = \sqrt{y''^2 + z''^2} \quad (15)$$

$$R_1 = \sqrt{d_1^2 + d_3^2}; \quad R_2 = \sqrt{d_2^2 + d_3^2}; \quad (16)$$

$$\dot{B}_{Lx} = \frac{\mu_0 \dot{I}}{4\pi d_3^2} \cdot \left( \frac{d_1}{R_1} - \frac{d_2}{R_2} \right) \cdot (y'' \cdot k_1 \cdot k_4 + z'' \cdot k_2) \quad (17)$$

$$\dot{B}_{Ly} = \frac{\mu_0 \dot{I}}{4\pi d_3^2} \cdot \left( \frac{d_1}{R_1} - \frac{d_2}{R_2} \right) \cdot (y'' \cdot k_2 \cdot k_4 - z'' \cdot k_1) \quad (18)$$

$$\dot{B}_{Lz} = \frac{\mu_0 \dot{I}}{4\pi d_3^2} \cdot \left( \frac{d_1}{R_1} - \frac{d_2}{R_2} \right) \cdot y'' \cdot k_3 \quad (19)$$

Equations (9) – (19) are not valid when a current-carrying segment is parallel to z-axis.

In this special case, components of  $\dot{\mathbf{B}}_L$  are calculated as follows:

$$d_1 = z - z_0 + \frac{L}{2}; \quad d_2 = z - z_0 - \frac{L}{2} \quad (20)$$

$$d_3 = \sqrt{(x - x_0)^2 + (y - y_0)^2} \quad (21)$$

$$R_1 = \sqrt{d_1^2 + d_3^2}; \quad R_2 = \sqrt{d_2^2 + d_3^2}; \quad (22)$$

$$\dot{B}_{Lx} = -\frac{\mu_0 \dot{I}}{4\pi d_3^2} \cdot \left( \frac{d_1}{R_1} - \frac{d_2}{R_2} \right) \cdot (y - y_0) \cdot s_z \quad (23)$$

$$\dot{B}_{Ly} = \frac{\mu_0 \dot{I}}{4\pi d_3^2} \cdot \left( \frac{d_1}{R_1} - \frac{d_2}{R_2} \right) \cdot (x - x_0) \cdot s_z \quad (24)$$

$$\dot{B}_{Lz} = 0 \quad (25)$$

Finally, the magnetic induction of a straight wire segment in phasor domain is given by:

$$\dot{\mathbf{B}}_L = \dot{B}_{Lx} \mathbf{a}_x + \dot{B}_{Ly} \mathbf{a}_y + \dot{B}_{Lz} \mathbf{a}_z \quad (26)$$

### 4.3. Total magnetic field

Summarizing the contribution of all windings and all straight current-carrying wire segments, total magnetic induction is:

$$\dot{\mathbf{B}} = \sum_{i=1}^{N_w} \dot{\mathbf{B}}_{w_i} + \sum_{j=1}^{N_L} \dot{\mathbf{B}}_{L_j} = \dot{B}_x \mathbf{a}_x + \dot{B}_y \mathbf{a}_y + \dot{B}_z \mathbf{a}_z \quad (27)$$

where:

$N_w$  – number of windings ( $N_w = 6$  for above case of a three phase transformer)

$N_L$  – number of straight current-carrying wire segments ( $N_L = 122$  for above case)

RMS value of magnetic induction in time domain is given by [9]:

$$B = \sqrt{|\dot{B}_x|^2 + |\dot{B}_y|^2 + |\dot{B}_z|^2} = \sqrt{B_x^2 + B_y^2 + B_z^2} \quad (28)$$

where  $B_x$ ,  $B_y$  and  $B_z$  are magnitudes of the components  $\dot{B}_x$ ,  $\dot{B}_y$  and  $\dot{B}_z$  of the phasor-vector  $\dot{\mathbf{B}}$ .

## 5. COMPARISON BETWEEN COMPUTATIONS AND MEASUREMENTS

Magnetic field was computed and measured in the rectangular region ABCD (1.365 m x 2.4 m) in two planes ( $z=2.48$  m and  $z=3.48$  m) above the transformer and LV conductors (Figure 8).

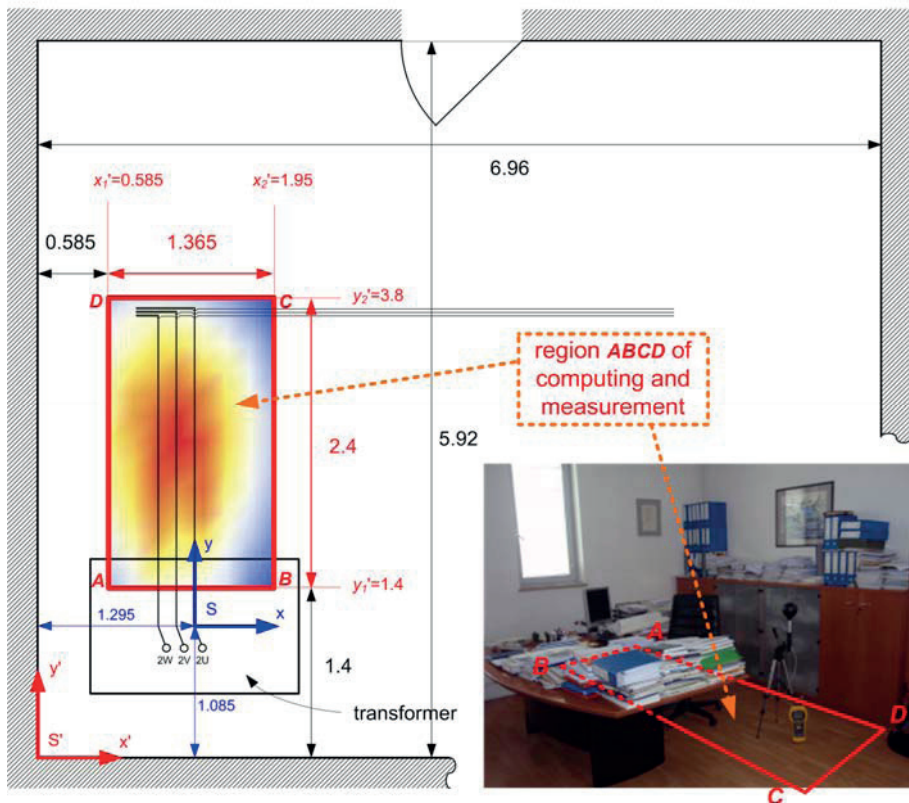


Figure 8 - Region of computing and measurement

Magnetic induction was measured by using CA 42 fieldmeter. The field was measured at average load of 46 % (638 A  $\pm$  15%). Maximum load asymmetry was 10 % and it was ignored in the model. Measured values of magnetic induction were normalized to values corresponding to nominal current by multiplying them by 1375/638. Normalized measured results of magnetic induction were compared with computed results at rated load. The results are shown in Figures 9-12.

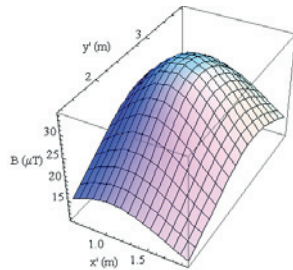
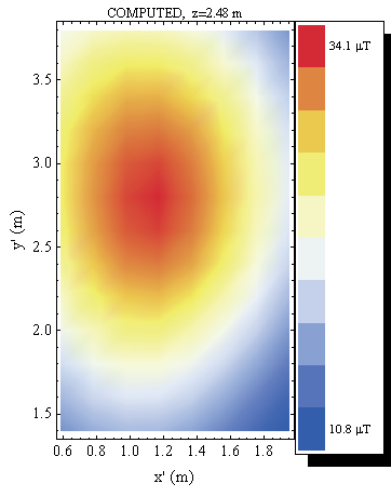


Figure 9 - Computed results for plane  $z=2.48$  m

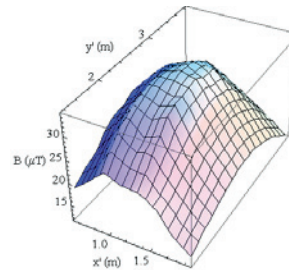
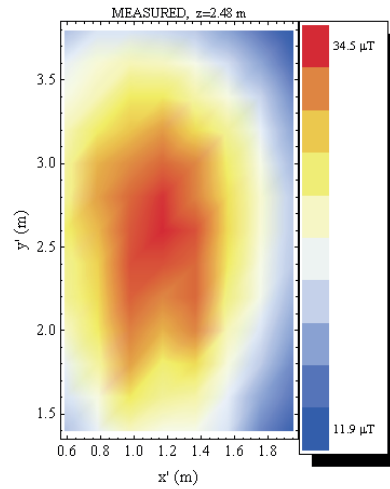


Figure 10 - Measured results for plane  $z=2.48$  m

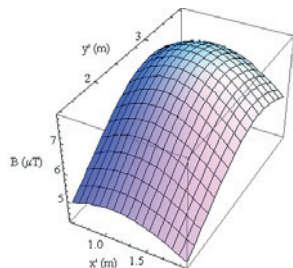
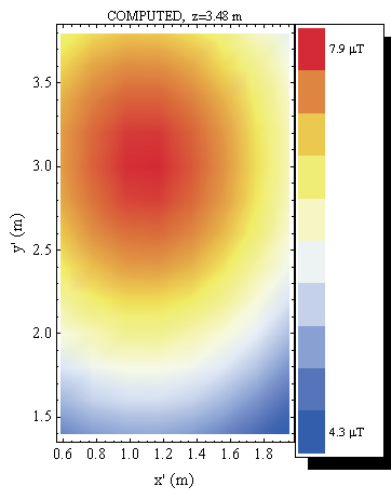


Figure 11 - Computed results for plane  $z=3.48$  m

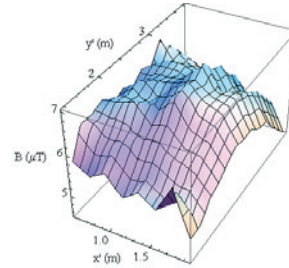
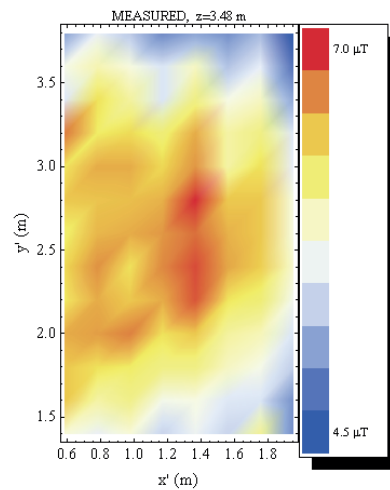


Figure 12 - Measured results for plane  $z=3.48$  m

The results show the highest value of magnetic induction at rated load to be 34.5  $\mu\text{T}$ . That was measured in the plane 6.5 cm above the floor level ( $z=2.48$  m). In the plane 106.5 cm above the floor level ( $z=3.48$  m) the highest computed value is 7.9  $\mu\text{T}$  (measured 7  $\mu\text{T}$ ). Since the field was computed in the area of occupational exposure, all values are far below the limits recommended by ICNIRP (500  $\mu\text{T}$ ) [1] or required by Croatian ordinance (100  $\mu\text{T}$ ) [5]. However, those field values can cause interference with electronic devices. For example, if the computer is in such area, then image movement (jitter) on the CRT monitor screen may be noticed. This problem can be solved by replacing CRT monitor with LCD.

The comparison shows that there is a good agreement between computations and measurements. Deviation between them for the highest values of magnetic induction is 1 %, in plane  $z=2.48$  m, and 13 % in plane  $z=3.48$  m.

Depending on the place where the magnetic field is computed, the model can be simplified by omitting the windings. This can be done if the LV conductors are the most dominating source of the magnetic field, like in this particular case. Computations on a simplified model gave almost the same results as for the model with windings. The difference for the highest value of magnetic induction is not more than 1 %.

## 6. CONCLUSION

The proposed method of evaluating low frequency stray magnetic field in the surrounding region of a loaded distribution transformer appears to be very effective and practical. The method was validated by comparison with measurements. The results of the computations and measurements are in good agreement. Field values are far below the limits recommended by ICNIRP or required by Croatian ordinance. The advantage of proposed method is that no commercial magnetic field software is needed.

## 7. REFERENCES

- [1] "ICNIRP Guidelines for Limiting Exposure to Time-Varying Electric, Magnetic and Electromagnetic Fields (up to 300 GHz)", ICNIRP, 1998.
- [2] "Ordinance relating to Protection from Non-Ionising Radiation (ONIR)", The Swiss Federal Council, 1999.
- [3] M. Breschi, A. Christofolini, "Experimental and numerical analysis of stray field from transformers", IEEE Transactions on Magnetics, Vol. 43, No. 11, November 2007.
- [4] "Uredba o elektromagnetnem sevanju v naravnem in življenjskem okolju", Uradni list št. 70, 1996.
- [5] "Pravilnik o zaščiti od elektromagnetskih polja", Ministarstvo zdravstva RH, 2003.
- [6] B. Čučić, "Magnetic field in the vicinity of distribution transformers", International Colloquium Transformer Research and Asset Management, Cavtat, Croatia, November 12 – 14, 2009.
- [7] I. Kapetanović, V. Madžarević, A. Muharemović, H. Salkić, "Exposure to Low Frequency Magnetic Fields of a Transformer Station", International Journal of Electrical Systems Science and Engineering 1;2, 2008.
- [8] B. Čučić, "Magnetsko polje u okolini distribucijskih transformatora (Magnetic field in the vicinity of distribution transformers)", doktorska disertacija (PhD Thesis in Croatian), FER, Zagreb, 2009.
- [9] B. Čučić, Z. Haznadar, Ž. Štih, "The 3D magnetic field calculation of a dry type transformer by integral equations", The 25th International Review of Progress in Applied Computational Electromagnetics (ACES 2009), Monterey, California, 2009.

Ralf Wittmaack  
Siemens E T TR EU PN EN4  
[Ralf.Wittmaack@Siemens.com](mailto:Ralf.Wittmaack@Siemens.com)

## CFD SIMULATIONS OF OIL IMMersed AND DRY TYPE TRANSFORMERS

### SUMMARY

At Siemens the in-house CFD code UniFlow is employed to investigate fluid flow and heat transfer in oil immersed and dry type transformers as well as transformer components like windings, cores, tank walls, and radiators. We outline its physical models and numerical solution methods.

As an oil transformer application of the method, the simulation of oil flow and heat transfer in 5 windings of a prototype transformer with ONAN/ONAF cooling mode is described. It corresponds to a heat run test with the total losses.

Furthermore, we outline an application to an AFWF cast resin transformer prototype operated at ships in an enclosure. The ventilator driven air flow is cooled by sea water. In addition to the LV and HV windings the core is simulated. Here also the heat radiation makes a significant contribution to the heat transfer.

**Key words:** Thermal design, CFD, physical models, radiant heat transfer, numerical methods

### 1. INTRODUCTION

Thanks to its flexibility and accuracy CFD (Computational Fluid Dynamics) is becoming more and more frequently applied to analyses of transformer thermal design. This follows the trend established in other branches of advanced technology development, like aerospace, automotive, and power generation, where CFD simulations since many years are indispensable parts of the product development cycles.

Employing commercial CFD codes, several detailed studies of disc-type transformer windings were performed, e.g., by Torriano, Chaaban, and Picher [1]. Moreover, extended full geometry CFD analyses coupled to electromagnetic simulation of the load and no-load losses in core and windings were presented, e.g., by Smolka and Nowak [2].

Our intention is to provide a simulation method that may be used for detailed CFD analyses on fine grids as well as for simplified coarse grid studies. The in-house code UniFlow is designed to be easily applicable also by users that have only little experience in CFD. For this reason, e.g., in simple geometries it allows to set-up complex flow and heat transfer calculations without prior grid generation with an auxiliary code and coupling of the fluid and solid regions.

## 2. PHYSICAL MODELS AND NUMERICAL METHODS

### 2.1. Physical models

Our physical model is aimed at investigating flows with several kinds of heat transfer in complex geometry. It simulates the flow of single-component incompressible Newtonian fluids in a three-dimensional geometry. In addition to the fluids, in gaseous or liquid state, several structural materials are considered as hydrodynamic obstacles and thermodynamic heat structures. The hydrodynamics is described by the continuity and the Navier-Stokes equation. For the simulation of turbulence the algebraic Baldwin-Lomax eddy viscosity model is available. To simulate the transition between laminar and turbulent flows the algebraic transition models of Drela and Mayle are employed.

For temperature dependent density or material properties of the viscous stress tensor, the hydrodynamics of the fluid is coupled to the thermodynamics. For this reason, internal heat transfer (by convection and conduction) and heat generation by internal sources as well as heat transfer to the surroundings are modelled via a heat transport equation. To allow for simulation of phase transitions it is provided in enthalpy formulation. At the rigid boundaries heat conduction is considered. For coarse grids convective heat transfer coefficients may be employed at solid-liquid interfaces. Radiant heat transfer is simulated at structural material surfaces. The material properties (density, dynamic viscosity, specific heat, heat conductivity, and convective heat transfer coefficient) depend on the temperature.

#### 2.1.1. Dynamic equations

Our dynamic equations are written in Cartesian coordinates. The continuity equation for incompressible flow is [3]

$$\frac{\partial}{\partial x^m} (\rho v^m) = 0, \quad (1)$$

where:  $\rho$  is density and  $v$  velocity.  $x$  are the space coordinates and we use Einstein's summation convention for the space direction index  $m$ . Introduction of the continuity equation into the Navier-Stokes equation [3] leads to a momentum equation in strong conservation form,

$$\rho \frac{\partial v_i}{\partial t} + \frac{\partial}{\partial x^m} \left[ \rho v_i v^m - \mu \left( \frac{\partial v_i}{\partial x_m} + \frac{\partial v^m}{\partial x^i} \right) \right] = - \frac{\partial p}{\partial x^i} + \rho g_i, \quad (2)$$

where:  $t$  is time,  $p$  pressure, and  $g$  gravitational acceleration. After inclusion of the continuity equation our heat transport equation in strong conservation form reads

$$\rho \frac{\partial h}{\partial t} + \frac{\partial}{\partial x^m} \left( \rho h v^m - \lambda \frac{\partial T}{\partial x_m} \right) = P_d. \quad (3)$$

Here  $h$  is specific enthalpy,  $T$  temperature,  $\lambda$  heat conductivity, and  $P_d$  density of the heat sources or sinks.

#### 2.1.2. Radiant heat transfer model

Radiant heat transfer may be simulated between structural material surfaces adjacent to the fluid. The employed radiation model assumes that the radiating surfaces are boundaries of a hollow space with linear dimension much greater than their distance. It is applicable for, e.g., parallel plates and concentric cylinders. With this simplifying assumption the power received by surface 'a' via the heat transfer from surface 'b' to surface 'a' is [4]

$$P_{ab} = c_{ab} A_{ab} (T_b^4 - T_a^4); \quad c_{ab} := \frac{\sigma}{\frac{1}{\varepsilon_a} + \frac{A_a}{A_b} \left( \frac{1}{\varepsilon_b} - 1 \right)}. \quad (4)$$

Here  $A$  is area of a radiating structural material surface,  $T$  surface temperature,

$\sigma = 5.67051 \cdot 10^{-8} \frac{W}{m^2 K^4}$  the Stefan-Boltzmann constant, and  $\varepsilon$  emissivity of a structural

material surface. Computation domain nodes undergoing radiant heat transfer may have their radiation partner nodes inside the computation domain or at the boundary.

## 2.2. Numerical methods

For the numerical representation of our model we developed a finite volume method and employ boundary fitted, curvilinear, non-orthogonal, block-structured grids. The blocks may be connected via 1-to-1 or patched couplings. The arrangement of the dynamic variables in the control volumes of the grid is collocated at the node centre. The dynamic equations are solved sequentially. For the solution of the momentum, pressure-correction, and heat transport equations we use implicit schemes. The system of continuity and momentum equations is solved by a SIMPLE [5], SIMPLEC [6], or PISO [7] algorithm.

To speed-up the code execution and to ease the estimation of discretisation errors a FAS multi-grid algorithm is employed [8]. It is a geometric approach with standard coarsening applied to the outer iterations, visiting the grid levels in V-cycles. For steady-state problems it operates as full multi-grid algorithm (FMG) while for transient problems the algorithm starts at the finest grid.

For the efficient solution of sparse linear equations several algorithms are available. The parabolic momentum and heat transport equations may be solved with SIP solvers that are modified to handle block couplings via the residual vector [5]. For the elliptic pressure-correction equation an aggregation-based algebraic multi-grid algorithm [9] is available in addition.

## 3. APPLICATIONS

In the following 2 transformer applications of our method are outlined. In these geometrically simple simulations we analyse only the middle of the 3 limbs in 2-dimensional cylindrical coordinate systems with rectangular grids.  $x_1$  designates the radial and  $x_3$  the vertical space direction. Geometrically more complex UniFlow calculations are described, e.g., in [10].

In both of the applications mentioned in this paper we analyse the steady state. Furthermore, load losses are calculated by Maxwell-solvers and subsequently mapped to the CFD grids.

Another common feature of the presented applications is that only the active part is studied with prescribed fluid flow via in- and outlet boundary conditions, i.e., only parts of the entire coolant loops are considered.

### 3.1. Oil transformer prototype

As an oil transformer application we consider the windings of a prototype transformer operated in ONAN or ONAF cooling mode. The rated power is 63 MVA in the HV windings. At this transformer a set of windings at each limb consists of LV, MVR, MV, HV, and HVR windings. Our thermal simulation corresponds to a heat run test with the total losses, i.e., including the no-load losses of the core.



Figure 1 – Prototype transformer with ONAN / ONAF cooling in test field

### 3.1.1. Spatial discretisation and boundary layer thickness

A grid with 4 blocks is used for spatial discretisation. The 4 blocks represent the LV, MVR, MV, and HV / HVR windings respectively. Patched couplings are employed at the interfaces of the grid blocks. The grid is made up of 31023 nodes in the computation domain, where 14862 represent the oil while the remaining 16161 nodes correspond to the winding materials. The node lengths are 2 to 10 mm.

With the height of the windings as characteristic length  $l = 1.684$  m and estimations of the oil velocity and temperature, the Reynolds number is  $R = 10880$  and the Prandtl number is  $Pr = 61$ . This indicates laminar oil flow, where the hydrodynamic and thermal boundary layer thickness may be estimated via [3]

$$\delta_h \propto \frac{l}{\sqrt{R}} ; \quad \delta_t \propto \delta_h Pr^{-\frac{1}{3}} \quad (5)$$

This leads to a hydrodynamic boundary layer thickness of 16.1 mm and a thermal boundary layer thickness of 4.1 mm. As  $\delta_t$  is more than 2 times the node length at the interfaces to the structural materials, the grid provides a reasonable resolution of the boundary layers.

### 3.1.2. Material properties

In the windings we consider material mixtures to account for the influence of the insulation between the Cu wires on the material properties density  $\rho$ , specific heat at constant pressure  $c_p$ , and heat conductivity  $\lambda$ . The mixture properties are calculated via

$$\begin{aligned} \rho_{mix} &:= \sum_{i=1}^{n_{mat}} \alpha_i \rho_i & \alpha_i &:= \frac{V_i}{V} \\ c_{p,mix} &:= \sum_{i=1}^{n_{mat}} x_i c_{pi} & x_i &:= \alpha_i \frac{\rho_i}{\rho_{mix}} \\ \lambda_{mix} &:= \left( \sum_{i=1}^{n_{mat}} \frac{\alpha_i}{\lambda_i} \right)^{-1} \end{aligned} \quad (6)$$

where:  $\alpha$  is volume fraction,  $x$  mass fraction,  $V$  volume, and  $n_{mat}$  no. of material constituents. Compared to pure Cu, the most relevant effect of mixture properties is a significant reduction of the heat conductivity.

### 3.1.3. Power density of load losses

The next figure shows the spatial distribution of the load losses calculated by the Maxwell-solver SAPR and its subsequent mapping to the CFD grid.

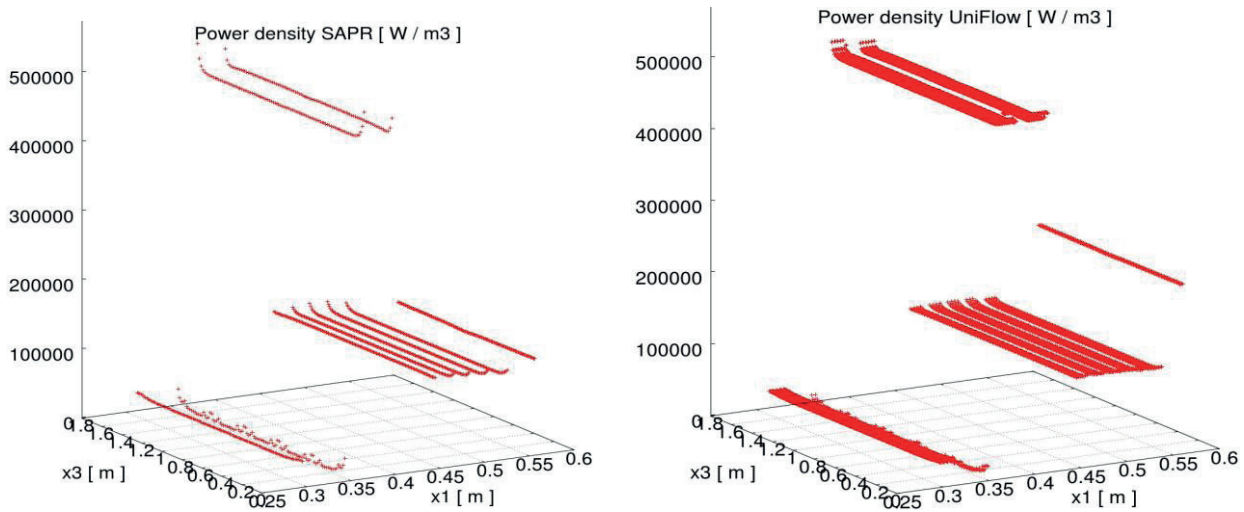


Figure 2 – Power density of load losses in ONAF transformer windings

As the CFD model includes only the inner half of the HVR windings the mapped power density is twice as high here. For this reason, in the UniFlow run in the HVR only half the power density shown in the figure is used.

### 3.1.4. Boundary conditions

As only a part of the oil natural convection loop is simulated, the inlet mass flows and temperatures are taken from integral thermo-hydraulic calculations. Adiabatic conditions are assumed at all computation domain boundaries, except the in- and outlets. For this reason only the inner half of the HVR windings is considered.

### 3.1.5. Simulation results

The next figure shows a vector representation of the velocity and its vertical component in the ONAF run. At the right figure the different colours are related to data of different grid blocks. As a result of its high power density of the load losses, the highest velocities occur in the MV windings. For ONAN cooling the oil velocity is similar but slightly smaller than for ONAF.

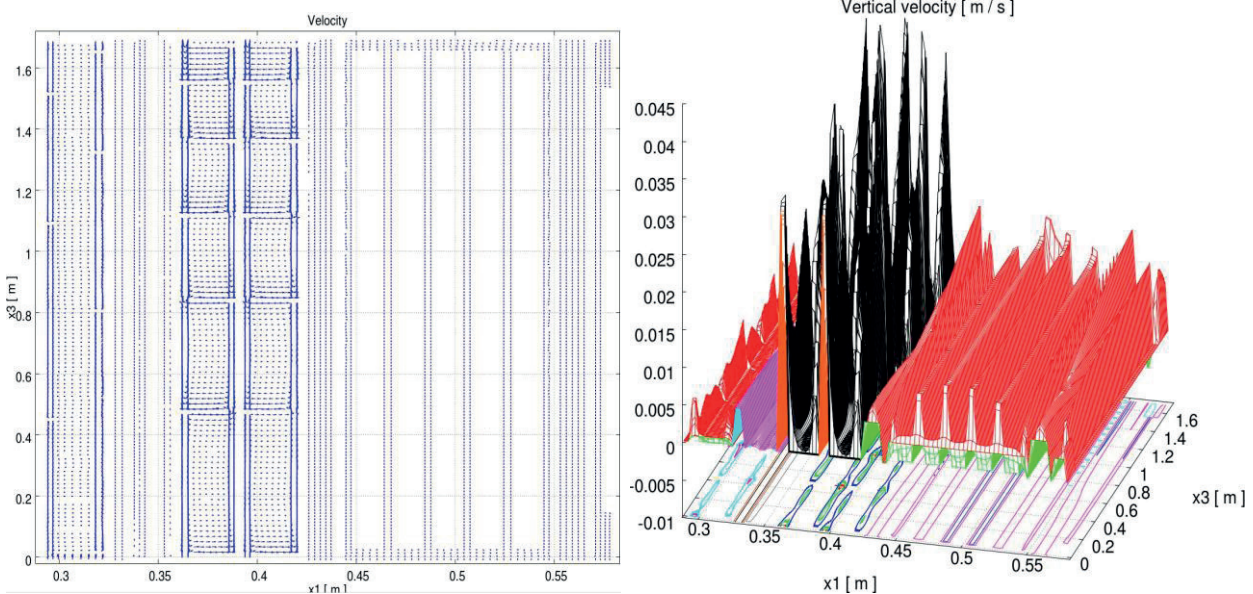


Figure 3 – Oil velocity and vertical velocity component in ONAF simulation

The next figure shows that the temperature distributions of oil and windings in the ONAN and ONAF simulations are similar, but the ONAF values are higher. The winding temperatures are closely related to the local oil velocity and the power density. Due to its high power density of the load losses, the highest temperatures are encountered in the MV windings. The adiabatic boundary condition on top and at the bottom of the MV windings causes enhanced temperatures at these locations.

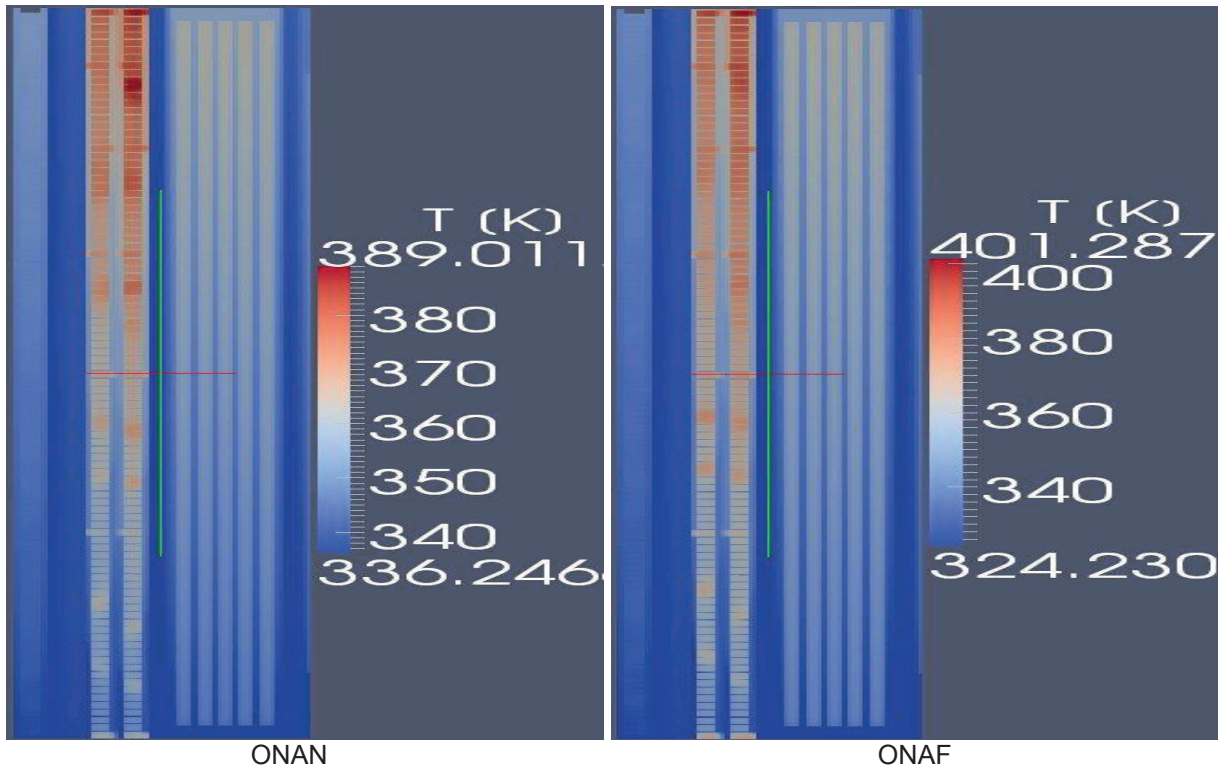


Figure 4 – Temperatures in ONAN and ONAF simulations

The investigated conditions in our analysis do not lead to critical structural material temperatures in the transformer. On the other hand, the maximum oil temperature is close to values where cracking might take place and would be critical for its long-term stability.

### 3.2. Cast resin transformer for ships

As a cast resin transformer application we consider an AFWF transformer operated at ships in an enclosure. The ventilator driven air flow is cooled by sea water. A set of windings at each limb consists of three LV and one HV windings. We analyse the core and the windings with prescribed air flow via in- and outlet boundary conditions imposed by the ventilator.



Figure 5 – Side and top views of cast resin transformer without enclosure

The right side of the figure shows that between the LV and HV windings there is a thin polyester radiation cylinder. This enhances the heat transfer to the air.

### 3.2.1. Spatial discretisation and boundary layer thickness

A single-block grid with 38528 computation domain nodes is used for spatial discretisation. 27633 nodes represent the air while the remaining 10895 nodes correspond to structural materials. The node lengths are 1 to 54 mm.

With the height of the HV windings as characteristic length and estimations of the air velocity and temperature, the Reynolds number is  $R = 270000$  and the Prandtl number  $Pr = 0.71$ . The vertical air flow along the windings resembles flow along a flat plate, where the transition from laminar to turbulent flow occurs between  $R = 3.5 \cdot 10^5$  and  $10^6$  [11]. This indicates that the air flow is laminar, i.e., the hydrodynamic and thermal boundary layer thickness may be estimated via (5). This leads to  $\delta_h = 2$  mm and  $\delta_t = 2.2$  mm at the upper end of the windings, i.e., the grid of our simulation of the cast resin transformer for ships is fine enough to resolve the hydrodynamic and thermal boundary layers.

### 3.2.2. Material properties

The structural materials considered in the simulation are steel of the core, Al of LV and HV windings, cast resin, prepreg, polyester, and Cr-Ni steel of the enclosure. The layers of the aluminium conductor and the prepreg / polyester insulation at the LV and HV windings are too thin to be resolved in the simulation. However, the vertical orientation of the layers leads to a heat conductivity of 237 W/(m K) in the vertical and 2.2 W/(m K) in the radial direction. To take this into account, we use prepreg / polyester insulation at the inner and outer boundaries of the LV and HV windings.

### 3.2.3. Power density of load and no-load losses

The next figure shows the spatial distribution of the load losses calculated by the in-house Maxwell-solver empower and its subsequent mapping to the CFD grid. It indicates a strong increase of the losses at the lower and upper end of the windings related to the radial component of the oscillating magnetic field. The high peak values correspond to the LV windings.

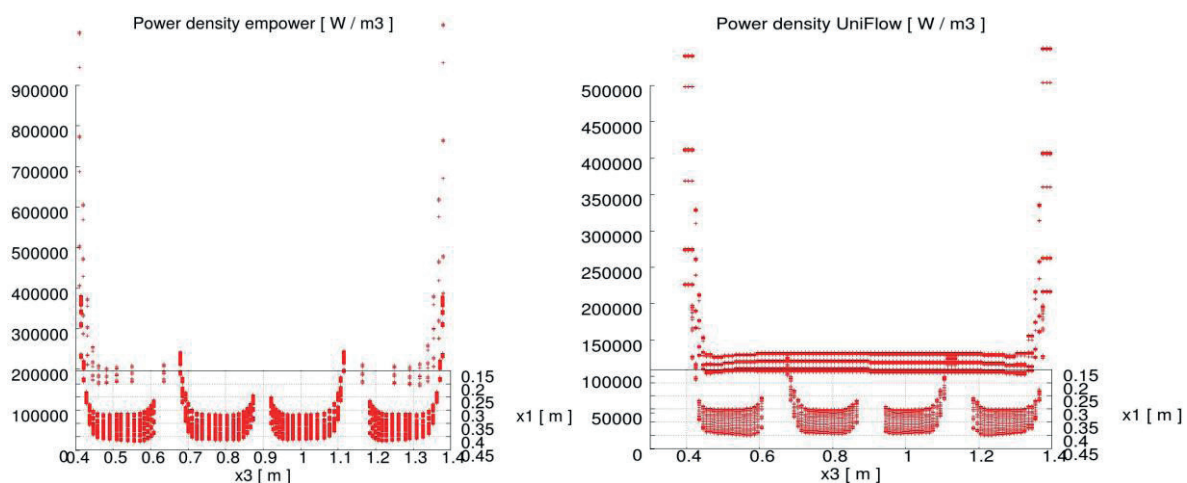


Figure 6 – Power density of load losses in cast resin transformer windings

The spatial distributions of the power density of the Maxwell-solver and CFD simulation are similar. The values mapped to the CFD grid are lower since part of the windings volume in the CFD grid is related to insulators.

The no-load losses of the core are assumed to be spatially constant.

### 3.2.4. Boundary conditions

As only a part of the air cooling loop is simulated we employ in- and outlet boundary conditions. The inlet air flow is estimated via the ventilator characteristics. The inlet velocity is 5 m/s, the inlet temperature 300 K. Adiabatic conditions are assumed at all computation domain boundaries, except the in- and outlets.

Radiant heat transfer is considered at all structural material surfaces.

### 3.2.5. Simulation results

A vector representation of the velocity and a plot of the vertical velocity component are given in the figure below. They show the location of in- and outlet boundaries, core, three LV and one HV windings, radiation cylinder, and horizontal flow barrier. In the windings the vertical velocity component is about 4 m/s. Recirculation regions exist at the side wall of the enclosure and on top of the core.

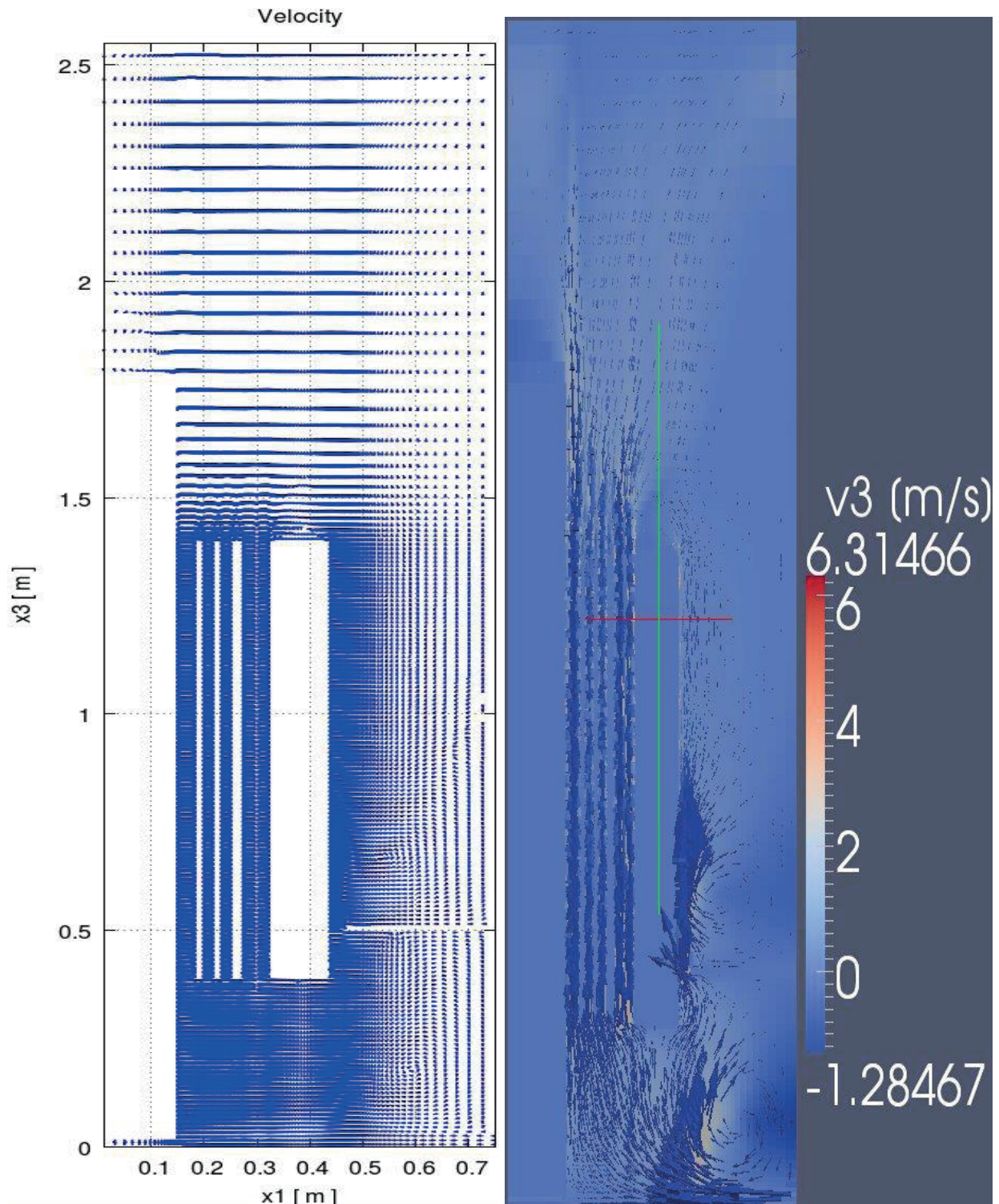


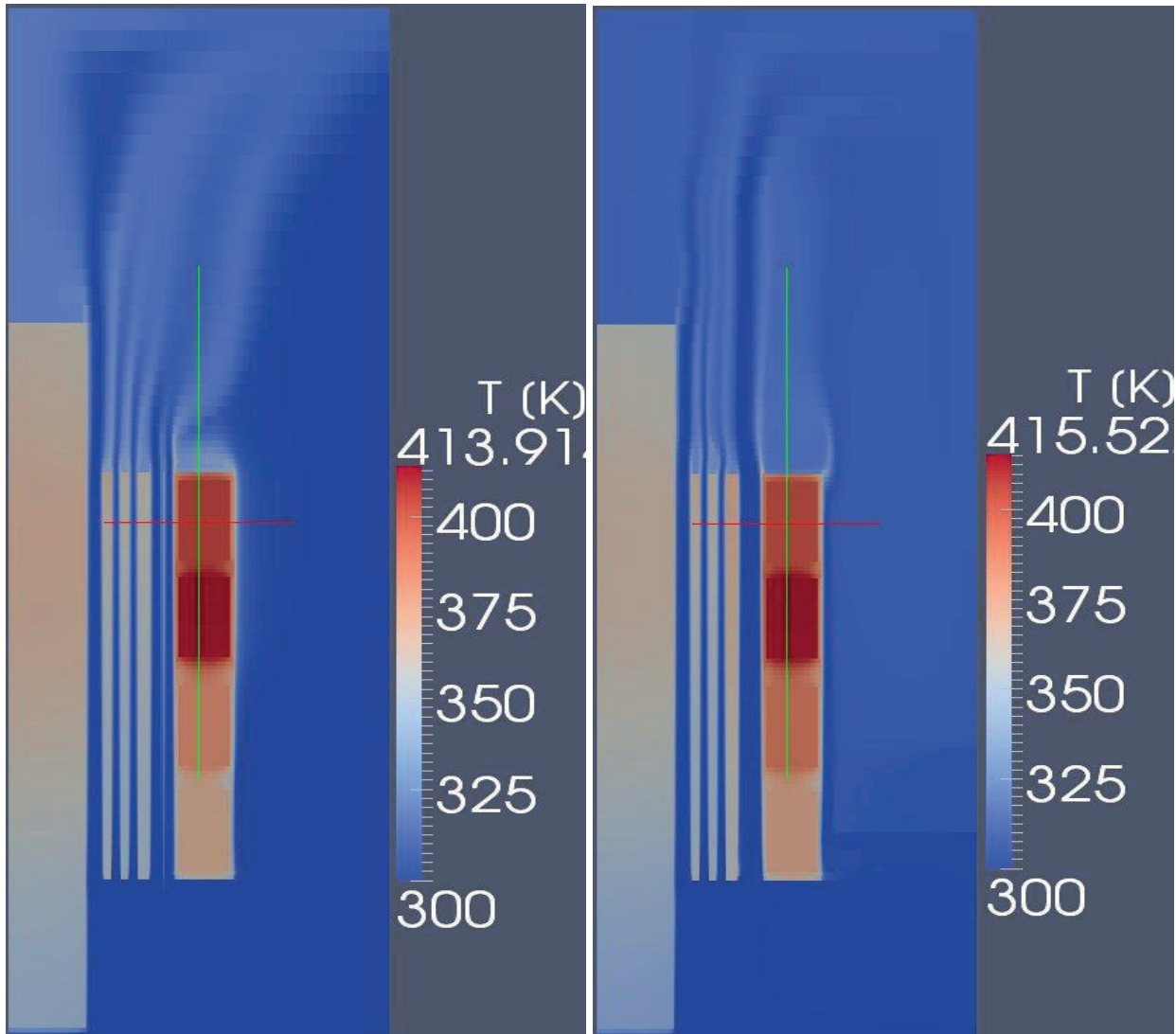
Figure 7 – Air velocity and vertical velocity component in cast resin transformer

A key result of the simulation is the temperature of air and structural materials shown in the figure below. The winding temperatures are related to local air velocity, radiant heat transfer, and spatial

variation of the power of the heat sources. In the HV windings lower temperatures correspond to the cast resin in the surroundings of the aluminium and the polyester. The 4 steps in the HV temperature are related to aluminium / polyester regions separated by cast resin. The figure also shows the upward convection of air heated up at the boundary layers adjacent to core, windings, and radiation cylinder.

As a result of the constant power density, in the radial direction there is a quadratic temperature profile in the core. However, the vertical temperature variation is much more pronounced.

Comparison of the left and right side of the figure shows that the radiation cylinder reduces the winding temperatures. This is most pronounced in the LV windings close to the radiation cylinder.



With radiation cylinder

Without radiation cylinder

Figure 8 – Temperature of air, core, and windings in cast resin transformer

The investigated conditions in our analysis lead to maximum temperatures in the HV windings at the limit of class F material. The calculations can be used as a basis for design optimisation via a set of simulations with modification of various design parameters. For instance, the efficiency of the radiation cylinder between the LV and HV windings as a means of heat removal may be analysed via calculations with and without this cylinder.

#### 4. CONCLUSION

The presented results indicate that UniFlow is a useful code for the thermal design of oil immersed and dry type transformers. It can be used to investigate advantages and shortcomings of design features and to perform design optimisation.

In addition to the results shown in this paper, also the pressure loss encountered in a device as a result of the fluid flow may be a major result of a simulation. This is demonstrated, e.g., in [10]. Other applications are related to detailed analyses on segments of disc windings with respect to, e.g., modelling of material compositions, width of oil channels, etc.. Another field of application are oil flows in cores. Moreover, combined oil and air flows are analysed in the context of fin type distribution transformers. This is aimed at, e.g., optimisation of the thermal efficiency of the fins. Furthermore, combined oil and air flows in radiators are investigated.

The calculated integral results of UniFlow, e.g., temperature differences between mid of windings and mid of oil channel, are similar to those calculated by correlation based methods. However, the spatial detail resolution of the results is superior.

#### REFERENCES

- [1] Torriano, F., Chaaban, M., Picher, P., "Numerical study of parameters affecting the temperature distribution in a disc-type transformer winding", *Applied Thermal Engineering*, 30, pp. 2034-2044, 2010
- [2] Smolka, J., Nowak, A. J., "Experimental validation of the coupled fluid flow, heat transfer and electromagnetic numerical model of the medium power dry-type electrical transformer", *Int. J. Thermal Sciences*, 47, pp. 1393-1410, 2008
- [3] Landau, L. D., Lifshitz, E. M., "Course of theoretical physics, vol. 6 : Fluid mechanics", Pergamon Press, Oxford, UK, 1989
- [4] Baehr, H. D., Stephan, K., "Heat and mass transfer", Springer-Verlag, Berlin, 2006
- [5] Ferziger, J. H., Peric, M., "Computational methods for fluid dynamics", Springer-Verlag, Berlin, 1999
- [6] van Doormal, J. P., Raithby, G. D., "Enhancements of the SIMPLE method for predicting incompressible flows", *Numer. Heat Transfer*, 7, pp. 147-163, 1984
- [7] Issa, R. I., "Solution of implicitly discretized fluid flow equations by operator splitting", *J. Comp. Phys.*, 62, pp. 40-65, 1986
- [8] Trottenberg, U., Oosterlee, C. W., Schüller, A., "Multigrid", Academic Press, New York, ISBN 012701070X, 2001
- [9] Notay, Y., "An aggregation-based algebraic multigrid method", *Electronic Transactions on Numerical Analysis*, 37, pp. 123-146, Kent State University, ISSN 1068-9613, 2010
- [10] Tenbohlen, S., Weinläder, A., Wittmaack, R., "Prediction of the oil flow and temperature distribution in power transformers by CFD", *CIGRE Session 2010, Report A2-301*, Paris, 2010
- [11] Schlichting, H., "Boundary-layer theory", McGraw-Hill, New York, USA, 1979

Wilerson Calil  
ABB Ltda  
wilerson.calil@br.abb.com

Vinicius Rubio  
ABB Ltda  
vinicius.rubio@br.abb.com

Jorge Inhasz  
ABB Ltda  
jorge.inhasz@br.abb.com

## DEVELOPMENT OF A PROGRAM FOR THE DETERMINATION OF THE TEMPERATURE AT TRANSFORMERS COPPER BUS BARS BY CALCULATING THEIR DIMENSIONLESS NUMBERS

### SUMMARY

The present technical study aims to demonstrate how to make the determination of the temperature at Transformers Copper Bus Bars by calculating their dimensionless numbers its will explain about the development of a thermal software that represents a viable and cost-effective to dimensioning the transformers Bus Bars due the temperature rise generate by the current. In this environment, the program is basically a virtual lab where is only necessary the cost of specialized engineering analysis and the critical time analysis.

This program allows to be done a large number of tests with different types of Bus Bars and different positions of this Bus Bars with the main objective of loss and temperature reduction, material and final cost of the equipment it can also be used to avoid a possible re-work, non-acceptance or disapproval in heating tests, improving the overall performance of the equipment.

To find the temperature at the Bus Bar was necessary to calculate the losses at the Bus Bars and the dimensionless numbers of Prandtl which is the ratio of momentum diffusivity (kinematic viscosity) to thermal diffusivity, Grashof which is a dimensionless number in fluid dynamics and heat transfer which approximates the ratio of the buoyancy to viscous force acting on a fluid, Rayleigh which is associated with buoyancy driven flow (also known as free convection or natural convection) and is the product of the Grashof number and the Prandtl number also and finally Nusselt which is the ratio of convective to conductive heat transfer across (normal to) the boundary. The conductive component is measured under the same conditions as the heat convection but with a (hypothetically) stagnant (or motionless) fluid. All dimensionless numbers were considered for natural convection.

To do this calculation an analytical program using Visual Basic at MSEXcel was created. To find this temperature some variables are dependent. In that case, this variables need to be fixed after the first temperature found at copper Bus Bars. Some iterations must be done using the program starting from this first temperature to find the correct final temperature.

After this procedure is possible to determinate the temperature considering the paper layer of the copper Bus Bars when it exists.

The measured results show the reliability of the proposed model by calculating the dimensionless numbers for the determination of the temperature at Transformers copper Bus Bars.

**Key words:** Losses, Prandtl, Nusselt, Rayleigh, Temperature, Program.

## 1. INTRODUCTION

ABB Brazil Transformer Division is performing a technical study about the temperature at High Current Leads in Power Transformers. This Leads are very common in Generate Step-Up Transformers and Industrial Transformers.

This study was done considering the transformer location, the copper bus bar, the winding type, the current density, the temperature rise and top oil temperature.

The main objective of this report is the technical study to find the temperature at the High Current Leads in Power Transformers.

To find the temperature at the Bus Bar was necessary to calculate the dimensionless numbers of Prandtl, Rayleigh, Grashof and Nusselt when the natural convection is being considered.

The Bus Bar dimensions can be seen at the Fig. 1 below as example:

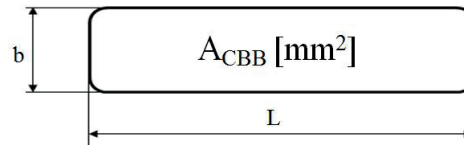


Figure 1 - Bus Bar Section Example

## 2. LOSSES CALCULATION

To calculate the losses, the electrical resistance and the current must be known.

The current of busbar lead is established by the winding. The resistance is calculated across of resistivity of copper. To fix the resistance is possible to fix the resistivity. In that case the fixed resistivity was used. To calculate the resistance was input in the calculation the temperature rise and the electrical factors as skin factor, proximity factor and leakage flux factor.

This factors are calculated from electromagnetic 3D software which use numerical method (Finite Element Method).

$$R_{CuCalc} = \frac{\rho_0 \cdot \{1 + [\alpha_{Cu} \cdot (T_{CuCalc} - T_{20^\circ C})]\}}{\left(\frac{L}{1000} \cdot \frac{X}{1000}\right)} \cdot f_s \cdot f_p \cdot f_d \quad (1)$$

where:

- L = characteristic length [m]
- X = busbar thickness [m]
- T<sub>cu<sub>calc</sub></sub> = Calculated Temperature [°C]
- α<sub>Cu</sub> = correction resistivity coefficient [°C<sup>-1</sup>]
- ρ = copper resistivity at 20°C DC [Ω/m]
- f<sub>s</sub> = skin factor [ ]
- f<sub>p</sub> = proximity busbar factor [ ]
- f<sub>d</sub> = winding leakage flux factor [ ]

The losses are calculated as below.

$$Q = I_{busbar}^2 \cdot R_{AC\theta} \quad (2)$$

where:

- I<sub>busbar</sub> = BusBar Current [A]
- R<sub>ACθ</sub> = Resistance at Calculated Temperature [Ω/m]
- Q = Power Losses [W]

### 3. DEFINITION OF DIMENSIONLESS NUMBERS

#### 3.1. Prandtl Number

The Prandtl number Pr is a dimensionless number; the ratio of momentum diffusivity (kinematic viscosity) to thermal diffusivity.

$$P_r = \frac{\nu}{\alpha} = \frac{\text{ViscousDiffusionRate}}{\text{ThermalDiffusionRate}} = \frac{c_p \cdot \mu}{k} \quad (3)$$

where:

- $\nu$  : kinematic viscosity,  $\nu = \mu / \rho$  [ $\text{m}^2/\text{s}$ ]
- $\alpha$  : thermal diffusivity,  $\alpha = k / (\rho \cdot c_p)$  [ $\text{m}^2/\text{s}$ ]
- $\mu$  : dynamic viscosity [ $(\text{N}\cdot\text{s})/\text{m}^2$ ]
- $k$ : thermal conductivity [ $\text{W}/(\text{m}\cdot\text{K})$ ]
- $c_p$  : specific heat [ $\text{J}/(\text{kg}\cdot\text{K})$ ]
- $\rho$  : density [ $\text{kg}/\text{m}^3$ ]

#### 3.2. Grashof Number

The Grashof number Gr is a dimensionless number in fluid dynamics and heat transfer which approximates the ratio of the buoyancy to viscous force acting on a fluid. It frequently arises in the study of situations involving natural convection.

$$G_{rL} = \frac{g \cdot \beta \cdot (T_s - T_\infty) \cdot L^3}{\nu^2} \quad (4)$$

where:

- $g$  = acceleration due to Earth's gravity [ $\text{m}/\text{s}^2$ ]
- $\beta$  = volumetric thermal expansion coefficient [ $1/^\circ\text{C}$ ]
- $T_s$  = surface temperature
- $T_\infty$  = bulk temperature
- $L$  = length [m]
- $\nu$  = kinematic viscosity [ $\text{m}^2/\text{s}$ ]

#### 3.3. Rayleigh Number

In fluid mechanics, the Rayleigh number for a fluid is a dimensionless number associated with buoyancy driven flow (also known as free convection or natural convection).

The Rayleigh number is the product of the Grashof number and the Prandtl number. Hence the Rayleigh number itself may also be viewed as the ratio of buoyancy forces and (the product of) thermal and momentum diffusivities.

For free convection near a vertical wall, this number is:

$$R_a = G_r \cdot P_r = \frac{g \cdot \beta}{\nu \cdot \alpha} \cdot (T_s - T_\infty) \cdot L^3 \quad (5)$$

where:

- $L$  = Characteristic length [m]
- $G_r$  = Grashof number
- $P_r$  = Prandtl number

- $g$  = acceleration due to Earth's gravity [ $m/s^2$ ]
- $T_s$  = Surface temperature
- $T_\infty$  = Quiescent temperature
- $\nu$  = kinematic viscosity [ $m^2/s$ ]
- $\alpha$  = Thermal diffusivity
- $\beta$  = volumetric thermal expansion coefficient [ $1/^\circ C$ ]

### 3.4. Nusselt Number

The Nusselt number is the ratio of convective to conductive heat transfer across (normal to) the boundary. The conductive component is measured under the same conditions as the heat convection but with a (hypothetically) stagnant (or motionless) fluid.

The convection and conduction heat flows are parallel to each other and to the surface normal of the boundary surface, and are all perpendicular to the mean fluid flow in the simple case.

$$N_u = \frac{h \cdot L}{k} = \frac{\text{ConvectiveHeatTransferCoefficient}}{\text{ConductiveHeatTransferCoefficient}} \quad (6)$$

And considering  $\frac{dI}{dt} = 0$ , the heat transfer is:

$$h = \frac{Q}{A \cdot \Delta T} \quad (7)$$

where:

- $L$  = characteristic length [m]
- $k_f$  = thermal conductivity of the fluid [ $W/(m \cdot K)$ ]
- $h$  = convective heat transfer coefficient [ $W/(m^2 \cdot K)$ ]
- $Q$  = losses [W]
- $\Delta T$  = rise temperature
- $A$  = cooling area,  $A_{cool} = 2 \cdot \left( \frac{b}{1000} + \frac{L}{1000} \right)$  [ $m^2$ ]

The selection of the characteristic length should be in the direction of growth (or thickness) of the boundary layer.

Typically, for free convection, the average Nusselt number is expressed as a function of the Rayleigh number and the Prandtl number, written as:  $Nu = f(Ra, Pr)$ .

$$N_u = 0.68 + \frac{0.67 \cdot R_a^{\frac{1}{4}}}{\left[ 1 + \left( \frac{0.492}{Pr} \right)^{\frac{9}{16}} \right]^{\frac{4}{9}}} \quad (8)$$

$$R_a \leq 10^9$$

where:

- $Ra$  = Rayleigh number
- $Pr$  = Prandtl number

#### 4. TEMPERATURE FUCTIONS VARIABLES

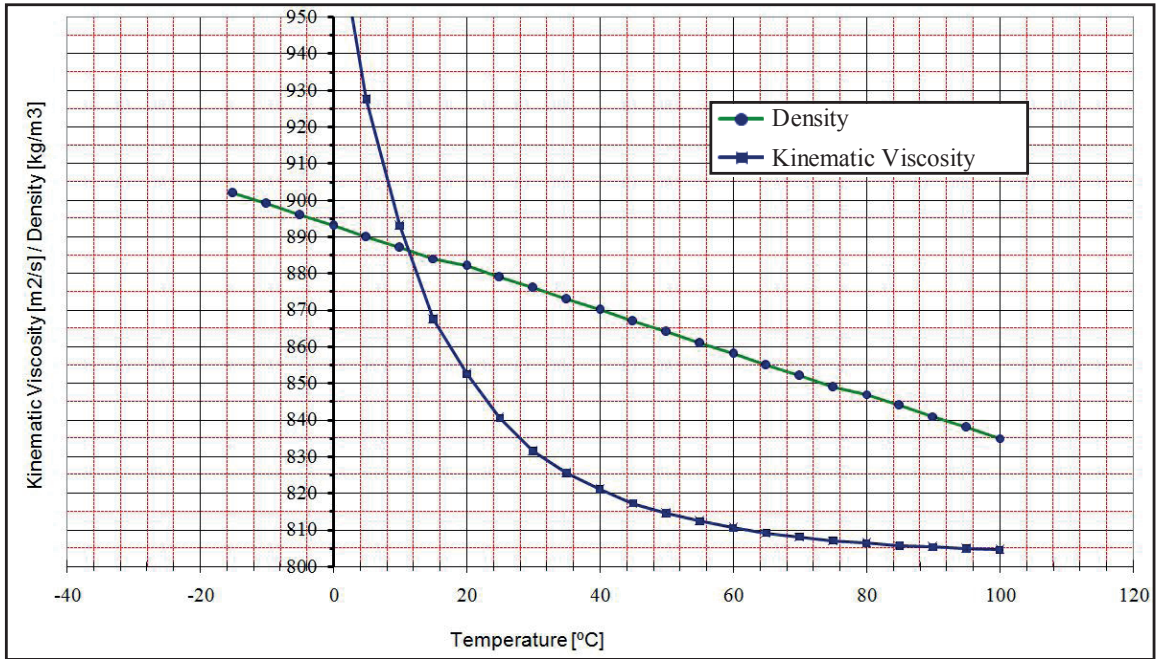


Figure 2 - Density and Kinematic Viscosity Variation

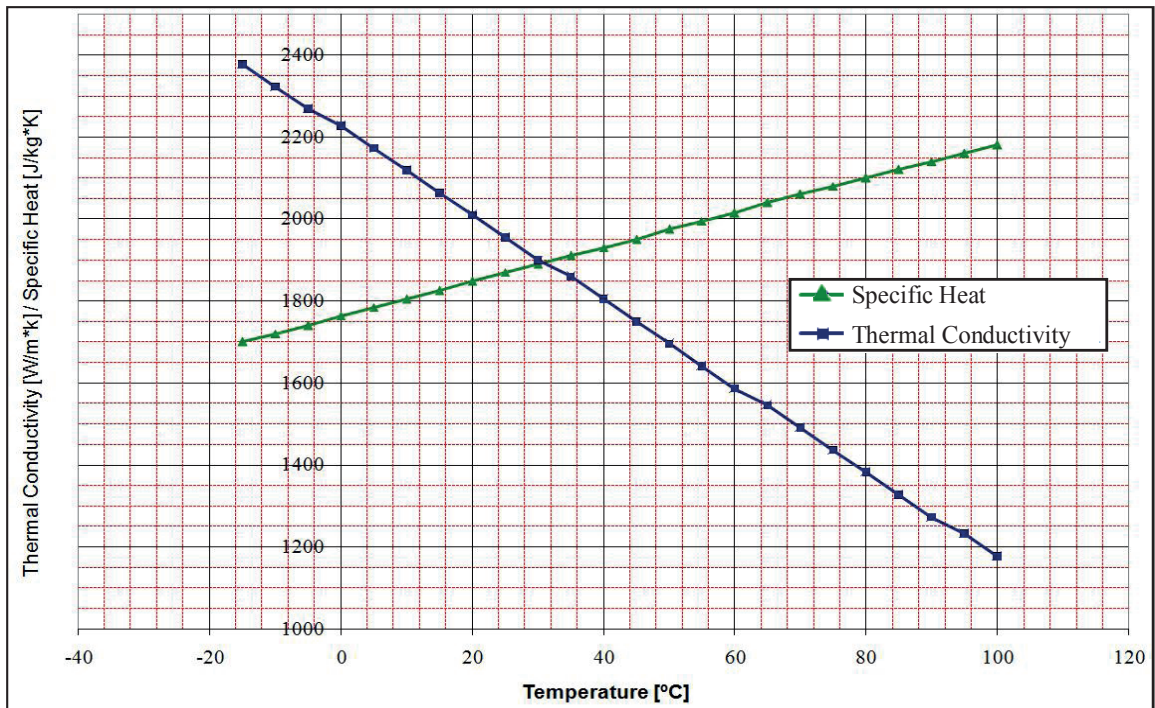


Figure 3 - Thermal Conductivity and Specific Heat Variation

## 5. TEMPERATURE RISE DUE TO PAPER COVERED

To calculate the temperature at the paper layer of the copper bus bar, the following expression must be used:

$$\Delta T_{paper} = \frac{Q}{A} \cdot \left( \frac{1}{h} + \frac{e}{k_p} \right) \quad (9)$$

where:

- Q = losses [W]
- $k_p$  = Paper Thermal Conductivity [W/(m\*K)]
- h = convective heat transfer coefficient [W/(m<sup>2</sup>\*K)]
- e = Paper thickness
- $\Delta T_{paper}$  = rise temperature at the layer of paper
- A = cooling area,  $A_{cool} = 2 \cdot \left( \frac{b}{1000} + \frac{L}{1000} \right) [m^2]$

## 6. PROGRAM FLUXOGRAM

Some variables are temperature dependent. In that case, this variable need to be fixed after the first temperature found at copper busbar. Some iterations must be done starting from this temperature to fix the new temperature found across the formulas written before. See figure below:

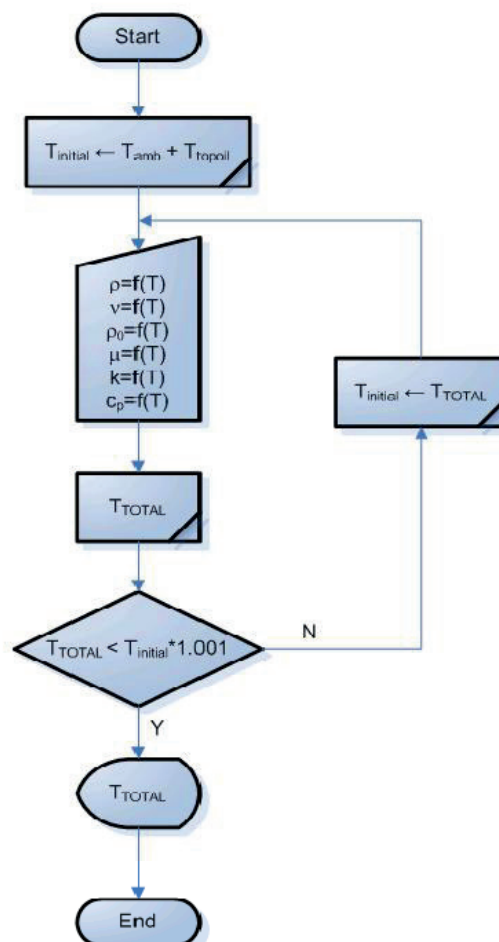


Figure 4 - Program Fluxogram

## 7. PROGRAM LAYOUT

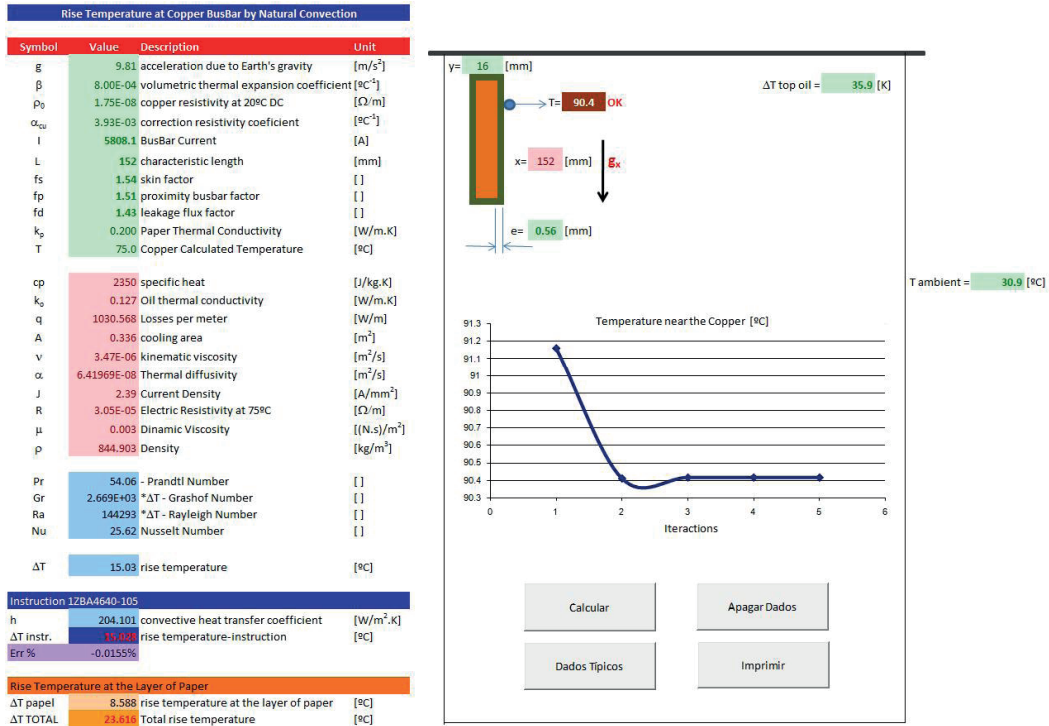


Figure 5 - Software BBT - BusBar Temperature - Visual Basic Application

### 7.1. Input data

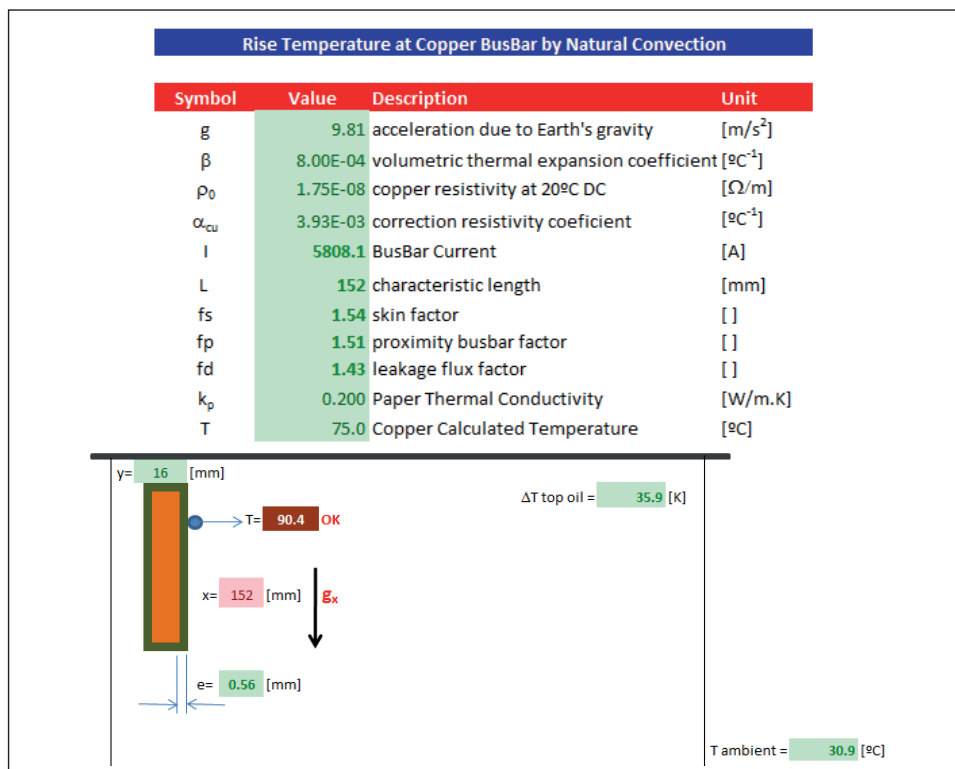


Figure 6 - Input Data - Only Green Square

## 7.2. Output data

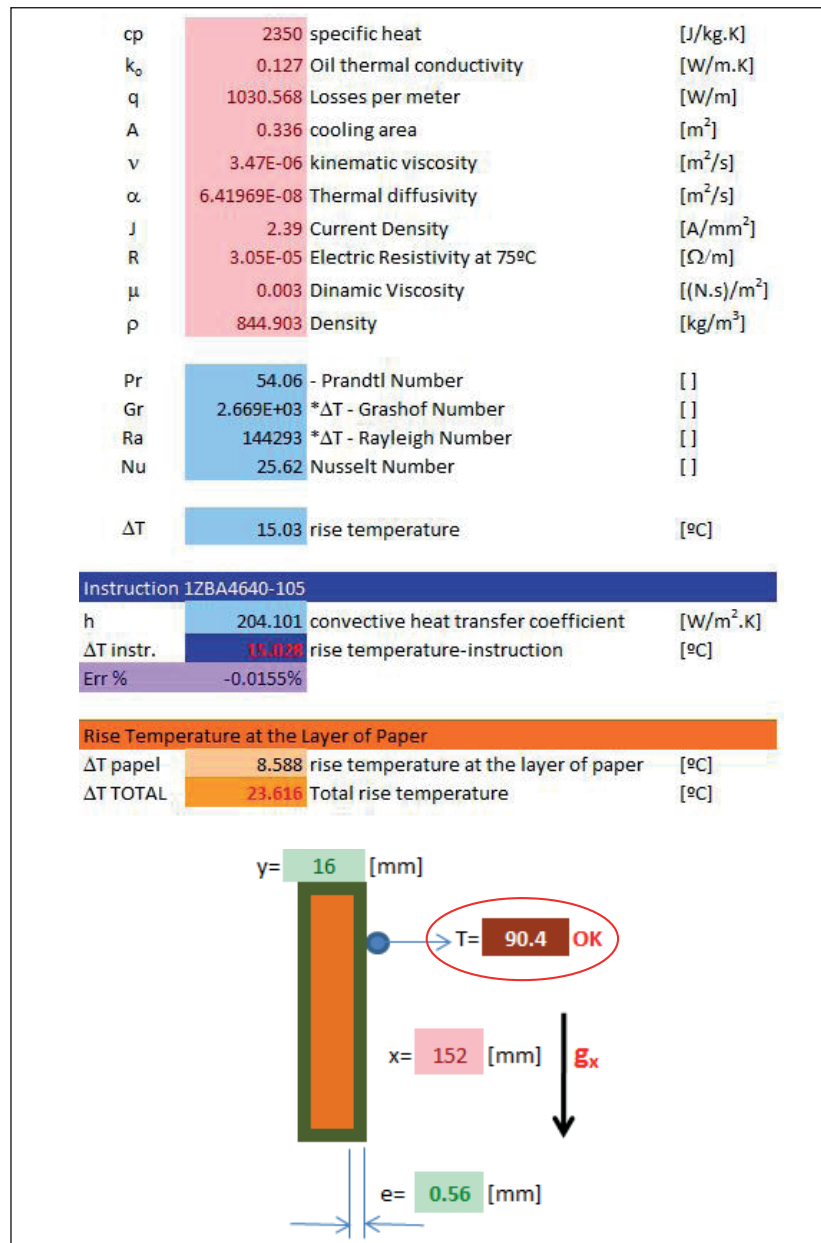


Figure 7 - Output Data - Absolute Temperature at BusBar

## 7. RESULTS FROM REAL CASE

The real case tested was a transformer 460MVA Nominal Power, 13.2kV Low Voltage Busbar , 60Hz frequency, Cooling System ODAF. The heating hest was 100% load during 72 hours and with internal measurements using optical fibers.

The used sensor was the model T2™ Fiber Optic Temperature Sensor from NEOPTIX. The Fig. 8 shows the optical fibers positioning for the measurement of temperature on the busbars.

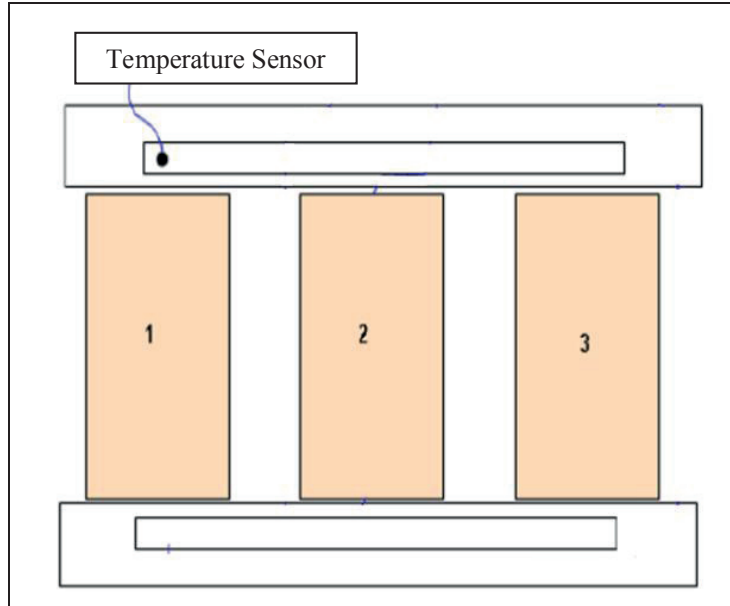


Figure 8 - Optical Fibers Positioning

The calculated value of the temperature on the Copper Bus Bars was 90.4°C, while the average value measured through optical fibers was 89.7°C, resulting in a percentage error of 0.78%.

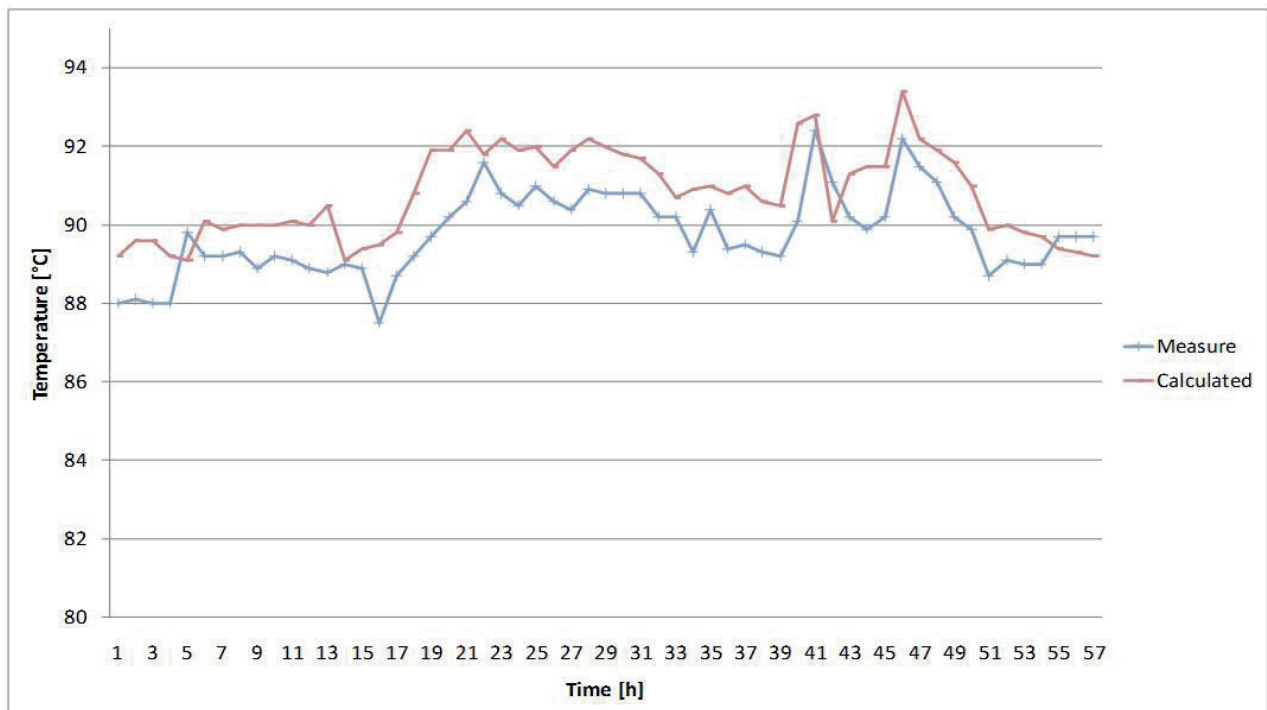


Figure 9 - Measure (test lab) and Calculated Values

The Fig. 9 shows in detail all the measured values and compares the proximity of the calculated value during the heating test.

## 8. ACKNOWLEDGMENTS

The authors would like to thank the test laboratory staff at ABB Guarulhos for their contributions to this work.

## 9. CONCLUSION

Comparing the results from the presented software with the results measured at this real case (test laboratory), it is possible to observe a close proximity of the values.

This analysis validates the developed program and allows a better dimensioning of copper Bus Bars with a great save of material.

Then, it is possible to conclude that the program allows to be done a large number of tests with different types of Bus Bars and different positions of this Bus Bars with the main objective of loss and temperature reduction, material and final cost of the equipment, this calculation can also be used to avoid a possible re-work, non-acceptance or disapproval in heating tests, improving the overall performance of the equipment, as said before.

## 5. REFERENCES

- [1] 1ZBA4640-105 - Low Voltage High Current Leads in Power Transformers.
- [2] Fundamentos de Transferencia de Calor - Frank P. Incropera, David P. DeWitt - Cuarta Edición - School of Mechanical Engineering Purdue University - Prentice Hall, México, 1999.
- [3] Princípios de Transferência de Calor - Bohn, Mark S.; Kreith, Frank - 1ª Edição - Editora Thomson Heinle, 2003.
- [4] Incropera, DeWitt, Bergman e Lavine. Fundamentos de Transferência de calor e massa, 6ª ed., 2006.
- [5] Turcotte, D.; Schubert, G. (2002). Geodynamics (2nd ed.). New York: Cambridge University Press.
- [6] White, F. M. (2006). Viscous Fluid Flow (3rd. ed.). New York: McGraw-Hill.
- [7] Jaluria, Yogesh. Natural Convection Heat and Mass Transfer (New York: Pergamon Press, 1980).
- [8] Cengel, Yunus A. Heat and Mass Transfer: A Practical Approach, 3rd Edition (Boston: McGraw Hill, 2003).
- [9] Eckert, Ernst R. G. and Drake, Robert M. Analysis of Heat and Mass Transfer (New York: McGraw Hill, 1972).
- [10] Welty, James R. Fundamentals of Momentum, Heat, and Mass Transfer (New York: John Wiley & Sons, 1976).

Rajko Gardijan  
Končar - Electrical Engineering Institute  
[rgard@koncar-institut.hr](mailto:rgard@koncar-institut.hr)

Alen Keller  
Končar - Electrical Engineering Institute  
[akeller@koncar-institut.hr](mailto:akeller@koncar-institut.hr)

## TRANSFORMER BUSHING – A PART OF MEASUREMENT SYSTEM

### SUMMARY

Power transformer is one of the most important and most expensive components in the electric power system (EPS) and requires, from its production and throughout lifetime, continuous monitoring and checks of the availability in the power system. All the measurements and tests on the transformer which manufacturers attempt, in order to determine the quality of their products, are carried out through the connection of different types of bushings, and these measurements and tests are conducted in accordance with requirements of applicable standards. Also, the owner of the transformer during the exploitation phase wishes and needs to know the status and availability of transformers for future work. The only available points of the transformer inside are the bushings. The technical practice from the early beginnings of the transformers are periodic off-line measurements. Following that practice and experience, the need arose for continuous supervision of transformer operation (on-line). In the 90's the first simple systems for the transformer on-line monitoring appeared. Today, it is an established fact that the modern systems for on-line monitoring of transformers provide a complete insight in the transformer state including alarms in the case of critical states. It is realistic to expect in the future that these same systems, apart from providing diagnostics and giving alarms, will be authorized to switch off transformers in the case of necessity with high degree of confidence. An important role in on-line monitoring, as a part of measurement system, has a transformer bushing. For the purpose of both off-line and on-line measurements, manufacturers of the bushings are equipping them with the measuring tap. Unfortunately, despite intentions to standardize the components of the power system, this is not the case with the measuring tap, and the intention of this paper is to draw attention to these problems and to try to find a solution.

**Key words:** power transformer, bushing, measuring tap, on-line monitoring, test

### 1. INTRODUCTION

Bushing is an important component of the transformer, and very often their number can be more than ten per transformer. They function as links between transformer windings and the network with the purpose of raising the voltage level suitable for power transmission with minimum losses, and then lowering the voltage to the level appropriate for the consumer. Price of these bushings in the total price of the transformer can even reach up to 10%. Unfortunately, the bushings are the most common cause of transformer failure, often accompanied with disastrous consequences (explosion of the bushings, transformer fire, ...). Depending on the category of failure, according to some statistics, the participation of a bushing fault to the outage of the transformer reaches up to 50%.

Among many divisions of bushings, for indoor or outdoor installation, the basic division is by the type of insulating medium:

- Oil – Air
- Oil – Oil
- Oil - SF<sub>6</sub>

The second division is performed by the internal construction:

- Capacitance graded bushings (for voltages  $\geq 52$  kV) - bushings in which a desired voltage grading is obtained by an arrangement of conducting or semiconducting layers incorporated into the insulating material
- DIN bushings (distribution voltage levels) – bushing in which the major insulation consists of ceramic, glass or analogous inorganic material.

Capacitance bushings, the main subject of this article, according to IEC 60137:2008 [1] are divided into:

- Oil-impregnated paper bushings (OIP)
- Resin-bonded paper bushings (RBP)
- Resin-impregnated bushings (RIP)

When selecting the bushing, it is important to have information about the measuring tap (test tap, voltage tap,  $\tan\delta$  tap) such as the maximum voltage that may occur in normal operation and load that can be connected to the measuring tap. If the measuring tap is not in use, it must be directly grounded. Also, each capacitance graded bushing must have the data of the main capacitance ( $C_1$ ), the capacitance of the measuring tap ( $C_2$ ) and dielectric dissipation factor ( $\tan\delta$ ). Values of the capacitances ( $C_1$  and  $C_2$ ) are dependent on the constructive solutions of the bushing producers, while the value of  $\tan\delta$  is defined in the standard with the criteria according to [1], Table 8 - Maximum values of  $\tan\delta$  and  $\tan\delta$  increase.

## 2. HIGH VOLTAGE MEASUREMENT SYSTEMS

To use a transformer bushing as a component of a HV measurement system, the bushing has to be condenser type and must have a measuring tap, and all its capacitances and transfer characteristic must be known. The whole measuring system (bushing, measuring impedance, cable...) must have resonance frequency exceeding at least 500 kHz. A simple way to check frequency response of the measuring system is to use recurrent surge generator or a sweep generator and compare input and output voltages, as shown in Figure 2 and 3.

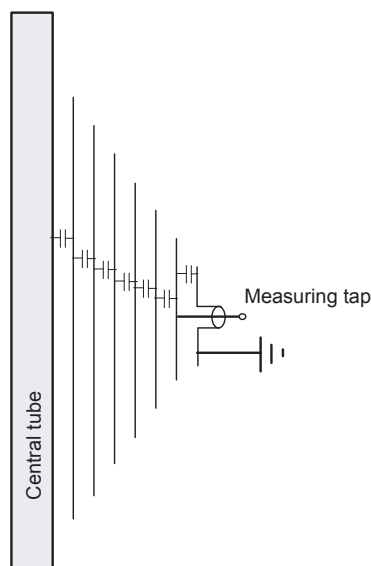


Figure 1 - Capacitance graded bushing

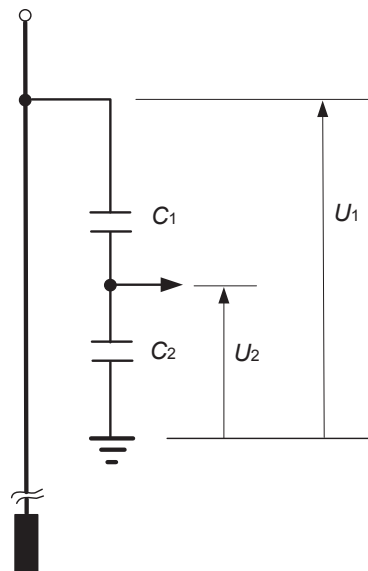


Figure 2 – High voltage divider

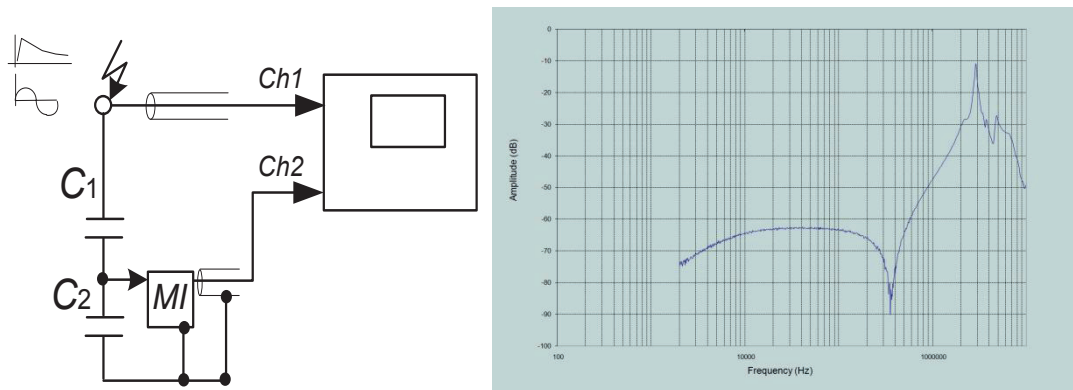


Figure 3 – Principle of checking the transfer characteristics of the measuring system with the bushing and the typical response

Transformer bushing as a component of the measurement system is used for the following tests:

- induced AC voltage tests (ACSD, ACLD), IEC 60076-3: 2000 [2], Clause 12
- lightning impulse voltage test (LI) – IEC 60076-3: 2000, Clause 13
- switching impulse voltage test (SI) – IEC 60076-3: 2000, Clause 15
- on-line monitoring of  $C$ ,  $\tan\delta$
- on-line monitoring of partial discharges
- on-line monitoring of transient overvoltages

## 2.1. Induced AC voltage test

To verify the quality of each manufactured transformer, it must pass routine tests.

One of the most important test is induced AC voltage test.

Depending on the highest voltage for equipment  $U_m$  applicable to a transformer winding and on the rated insulation level for all transformers with  $U_m \geq 72,5$  kV, ACSD test is normally performed with partial discharge measurements to verify partial-discharge-free operation of the transformer in service conditions.

Time sequence for application of test voltage for induced AC voltage test with measurement of partial discharges is shown in figure 4.

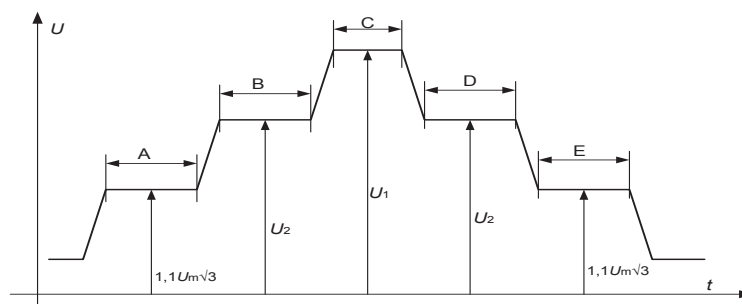


Figure 4 - Time sequence for application of test voltage for induced AC test with measurement of partial discharges.

We can use bushing in two ways:

- as HV capacitive dividers for measurement of applied voltage, and
- coupling capacitor for measurement of partial discharges.

For measurement of AC applied voltage we must know  $C_1$ ,  $C_2$ . Values of capacitances  $C_1$  and  $C_2$  are mostly in pF range, and usually  $C_2$  has a higher value.

All instruments for measurement of peak value  $/\sqrt{2}$  have maximum input voltage up to 150 V, and if we want to measure a higher voltage, we have to modify the HV divider in figure 2.

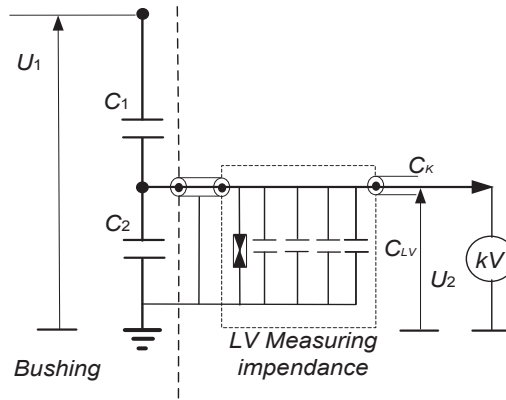


Figure 5 – Measurement configuration according to IEC 60060-2:2010 [3]

$$U_1 = p \times U \quad (1)$$

$$p = \frac{C_2 + C_{LV} + C_K + C_1}{C_1} \quad (2)$$

where:  $p$  – divider ratio (scale factor of kV)  
 $C_2$  – capacitance of measuring tap  
 $C_{LV}$  – capacitance of measuring impedance  
 $C_K$  – capacitance of coax. Cable  
 $U_1$  – test voltage of transformer winding

Alternative method for measurement of test voltage during AC test is shown in figure 5. This method is recommended for on-site testing of power transformers, because in many cases it is not possible to make a test in the same conditions like the one in the test station in the factory.

## 2.2. Measurement of partial discharges

If we use the alternative method for measurement of AC voltage, one way to measure partial discharges is to use transformer bushings as coupling capacitors. Another methods, e.g. using an additional coupling capacitor, are very complicated for connection of the tested transformer, require up to six coupling capacitors and a big area for test arrangement. Regarding sensitivity, the best way to measure is to use bushings.

The method of measurement and test arrangement is shown in figure 6.

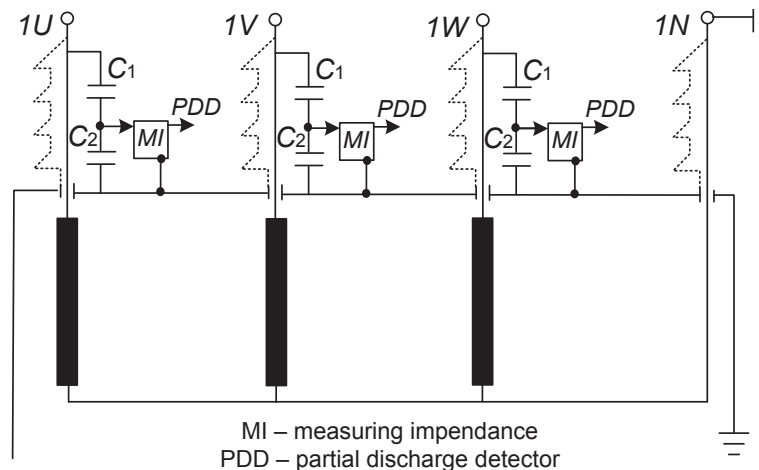


Figure 6 – Principle of measurement of partial discharges on power transformer via bushing

Measuring impedance (MI) has to be placed near the measuring tap of bushing and well earthed. All connections between measuring tap, measuring impedance and partial discharge detector must be with coaxial cable.

The type of measuring impedance depends of its purpose. Today we have integrated solutions that include measurement of partial discharges and measurement of voltage.

Type of measuring impedance is shown on the figure 7.

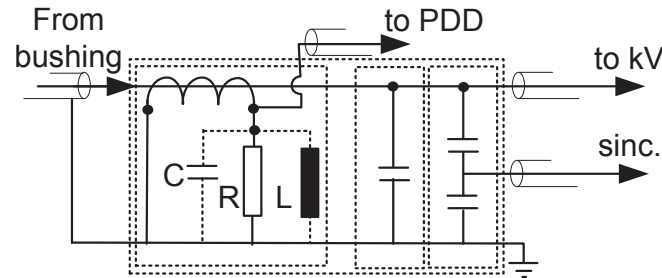


Figure 7 – Measuring impedance for measuring PD and voltage

### 2.3. Impulse test

Impulse test is one of dielectric tests for verification of quality of transformers for different service conditions.

In factory tests all transformer manufacturers use bushings as HV measurement system, especially in switching impulse withstand voltage tests. During the preparation of test circuit the shape of the applied switching impulse has to be in accordance with IEC 60076-3:2000, but the shape also has to give good distribution along tested and untested windings. The difference between tested and untested terminals must be less than  $1,5U_t$ .

The test circuit for the adjusted shape is given in figure 8.

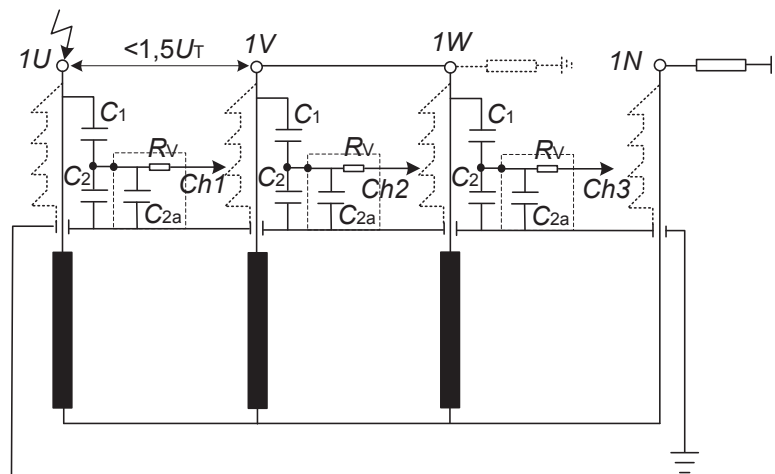


Figure 8 – Test circuit for switching impulse test – adjusted shape of impulse wave

### 2.4. On-line transformer monitoring

In the previous section we analysed the measuring facilities in which we can use transformer bushings for measurements. Also, the bushing can be used for on-line monitoring. During the last ten years we can find different solutions for on-line monitoring systems, which all require connection to the measuring tap of bushing, for example:

- On-line monitoring of the bushing ( $C$ ,  $\tan\delta$ )
- On-line monitoring of the transient over-voltages
- On-line monitoring of the partial discharges

For all those solutions of on-line monitoring systems, the HV measuring circuit has to be prepared. The voltage level on the measuring tap has to be adjusted for measurement and registration. Connection between measuring tap and the measuring impedance must be solidly earthed and waterproof, what is very difficult to achieve.

Another problem is that there are many designs of measuring taps. Each producer of high voltage bushings has their own type of measuring tap and sometimes even the same manufacturer has several designs of measuring taps.

All manufacturers of on-line transformer monitoring systems encounter this problem especially if they have to mount on-line monitoring system on a transformer in service (retro-fitting).

### 3. DESIGN OF THE MEASURING TAPS AND THE ADAPTERS

Measuring tap is placed on the bottom part of bushing, near the bushing flange.

There are lots of designs of measuring taps, but more recently they are of cylindrical design with the thread on the inner or the outer part of the cylinder. Figure 9 shows some of the measuring tap designs of the well known bushing manufacturers.



Figure 9 – Different designs of measuring taps (from left to right: Končar OTF type, ABB Micafil type, Passoni-Villa type)

Measuring tap can be integral part of the bushing (non removable) but it can also be removable as shown on figure 10.

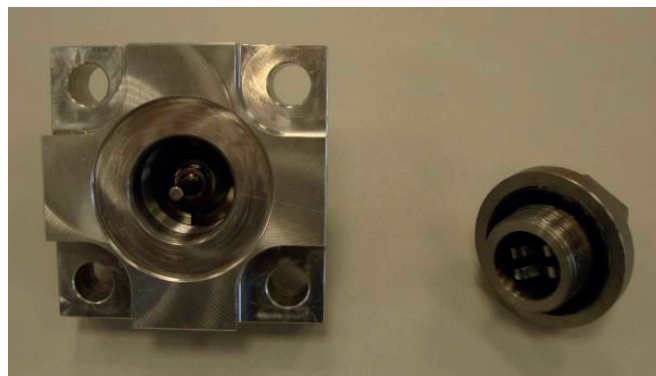


Figure 10 – Measuring tap with the protective cover

Internal connection of the tap depends on the overall construction but it is usually connected to the last capacitive layer of the bushing via spring needle or a wire. The overall capacitance between the power line connection of the bushing and the measuring tap is usually labeled as  $C_1$ , and the capacitance between the measuring tap and the ground is labeled as  $C_2$ . If the measuring tap is not in use, it should be grounded with the protective cover (bypassing the  $C_2$ ). Ungrounded measuring tap during the normal operation of the transformer can result in severe damage.

The use of the measuring tap for periodic off-line measurements is not so demanding like the use for the on-line monitoring systems. Since those systems are supposed to monitor several quantities of the transformers over the longer period of time, the permanent connection to the test tap is required. This is

assured with the specially designed adapters. The adapter connects the tap with the measuring impedance via short patch cable, as shown in the figure 11.

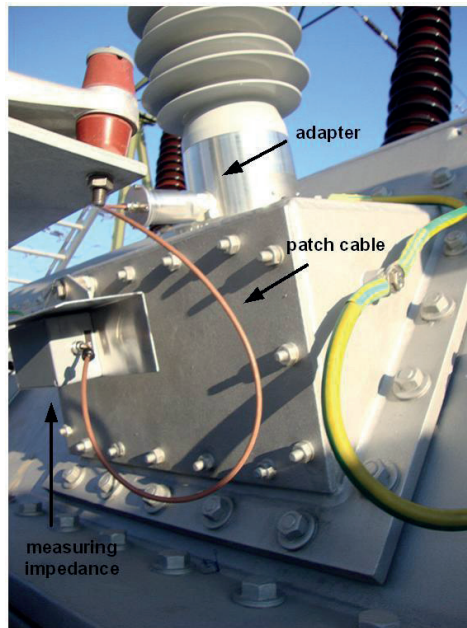


Figure 11 – Adapter and measuring impedance for on-line monitoring purpose

Water penetration is very common problem in this application. Water can create conductive layer between the contacts in the adapter and/or measuring impedance therefore making the measurements non valid. More importantly, water can make severe damage to the contacts of the adapter or the measuring impedance, resulting in an open tap condition. Therefore, the adapter must be waterproof and the special attention should be paid to the connection points of the patch cable. Figure 12 shows how water can easily penetrate into measuring impedance, which is supposed to be completely sealed, and cause severe damage to the components.



Figure 12 – Problem of water penetration

The measuring tap adapter should have protective elements (like GDT's) between the main connection (tap connection) and the ground in case that it loses connection with the measuring impedance, which is the same case as the open (ungrounded) measuring tap. There is also problem of the compatibility of the materials. The measuring taps of older designs are usually made of silumin which is very soft material. Taking into account that all threads are made with some tolerances and that the old measuring tap threads are usually filthy and could already be slightly damaged, the adapter made of the harder material can make permanent damage to the measuring tap thread. This can be manifested in two ways. Either the adapter is stacked to the measuring tap (practically a cold welding point) or the adapter can be removed with some force, but the protective cover could not be inserted anymore, resulting again in an ungrounded tap condition.

Each design of the measuring tap requires differently designed adapter. That fact, as well as the fact that some of measuring tap designs are not suited at all for the continuous on-line measurements, represents big problem for the manufacturers of the on-line monitoring systems.

### 3.1. Proposals for the standardization

The focus of this article will be on the two possible designs types of the measuring tap and the corresponding adapters.

First design is based on the classic cylinder type with the inner thread not smaller than M30, possibly with the fine thread pitch (like M30x1.5). The front surface should be big enough for the gasket of the adapter. The tap itself should be 4 mm in diameter, which is very common value in the current designs. The center line of the measuring tap should be at least 70 mm above the bushing flange, or the earthing screw, for the easy manipulation with the adapter. The tap should not protrude more than 5 mm outside the gasket surface, otherwise the adapter would be too long (figure 13).

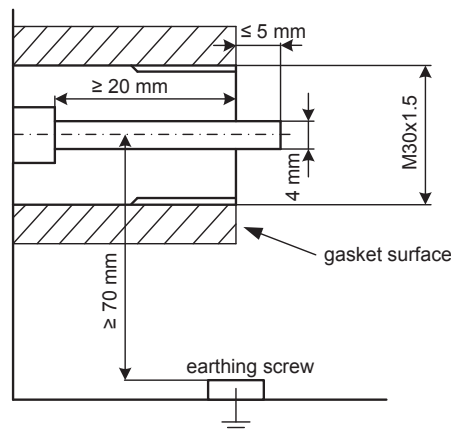


Figure 13 – Proposed dimensions for the measuring tap with inner thread

The adapter and the measuring impedance set for this configuration is shown in figure 14.



Figure 14 – Adapter and the measuring impedance

Due to the problem of the water penetration, the adapter and the measuring impedance should be completely sealed with the water repellent polyurethane compound, as shown in the figure 15.



Figure 15 – Measuring impedance components sealed with water repellent compound

The patch cable should be coaxial type with the high operating temperature (like the RG142) and it should be connected to the adapter and the measuring impedance through a cable gland, so the ends of a cable are also sealed. With this design, the adapter, patch cable and the measuring impedance are forming one unit which is slightly difficult to install, but the experiences so far are showing that even the high quality connectors, that can be mounted at the ends of the patch cable, are not the guarantee that the water will not penetrate. The other end of the measuring impedance, towards on-line monitoring system, should have the connectors with the IP protection as high as possible.

The variation of this design is shown in the figure 16.

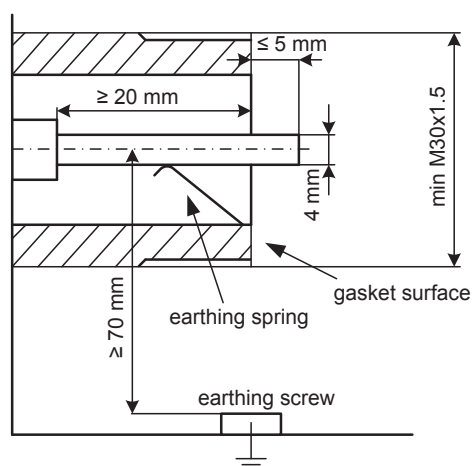


Figure 16 – Proposed dimensions for the measuring tap with outer thread and the corresponding adapter

This design has the outer thread due to the fact that some bushing manufacturers like to use the protective spring that will automatically ground the tap if it is left open. However, all the requirements for the measuring tap and the adapter with the patch cable and the measuring impedance are the same as mentioned above.

The potential problems of this design are the possibility of thread damage and the damage of the patch cable. Due to the potential damage of the patch cable, the adapter must have protective elements (surge arresters), like GDT's, built in.

The figure 17 shows the measuring tap of an old ASEA bushing.



Figure 17 – Measuring tap on ASEA bushing from 1965.

Although this is very old design, it is surprisingly practical for the purpose of the on-line monitoring and it is the base for the second design proposal. The firm connection with the tap is ensured by screwing the wire lug at one end, while the other end of the wire is connected to the measuring impedance. The measuring impedance is integrated in the protective cover, which is mounted to the bushing with the four bolts, and the gasket between the cover and the measuring tap base. The cover should be big enough to easily fit the PCB with the measuring impedance components and the surge arresters. Although the type of the components and their number depend on the measuring impedance purpose (voltage measurement, overvoltage detection, partial discharge measurement,  $\tan\delta$  measurement...), from the past experience, the cover with the inner surface of the 110x100 mm and the depth of 60 mm should be enough. Once the PCB with the components is mounted inside the cover, it should be sealed with the water repellent polyurethane compound. The connector on the outer part of the cover, towards on-line monitoring system, should have IP protection as high as possible (figure 18).

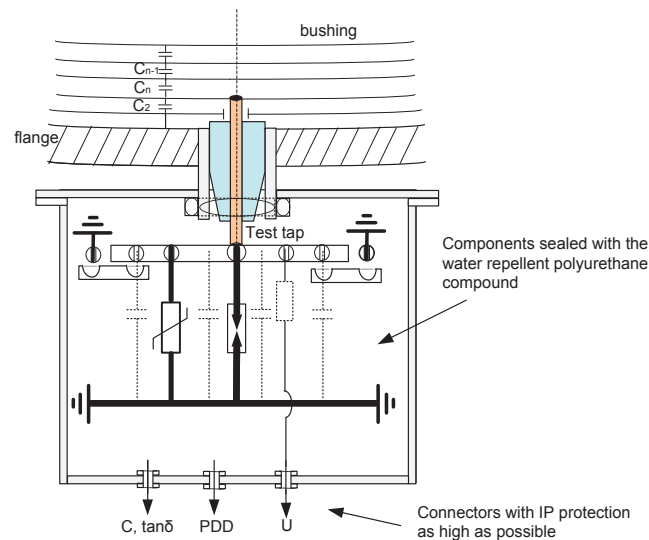


Figure 18 – Design proposal of the measuring tap with integrated measuring impedance

This kind of design has several advantages. The adapter, the patch cable and the measuring impedance from the previous example are all integrated in the cover. Therefore, there are no potential problems of the thread damage or the damage of the patch cable, which makes this design safer for the bushings and the transformer. Also, this solution is much easier to install and is a personal favorite of the authors of this article.

#### 4. CONCLUSION

The importance of on-line monitoring systems has significantly increased in the last few years. Some of the most important measurements on the transformer are taken from the bushing measuring tap, where the bushing is a part of an overall measuring system. The current situation on the market with numerous measuring tap designs is unacceptable from the perspective of on-line monitoring systems manufacturers. The authors of the article have proposed some of the possible designs as a base for the debate and hopefully a new standard. Our goal is to find the solution which will satisfy both, the bushing manufacturers as well as the on-line monitoring manufacturers.

#### REFERENCES

- [1] IEC 600137-2008, Insulated bushings for alternating voltages above 1000 V
- [2] IEC 60076-3:2000, Power transformers- Part 3: Insulation levels, dielectric tests and external clearances in air
- [3] IEC 60060-2:2010, High-voltage test techniques – Part 2: Measuring systems

Subhash Kumar Joshi  
IIT Roorkee, India  
[subhashjoshi2107@gmail.com](mailto:subhashjoshi2107@gmail.com)

Pramod Agarwal  
IIT Roorkee, India  
[pramgfee@gmail.com](mailto:pramgfee@gmail.com)

Hari Om Gupta  
IIT Roorkee, India  
[hariomgupt@gmail.com](mailto:hariomgupt@gmail.com)

Ganesh Kumbhar  
IIT Roorkee, India  
[gkumbfee@iitr.ernet.in](mailto:gkumbfee@iitr.ernet.in)

## FIELD INVESTIGATIONS INTO HARMONICS POLLUTION AFFECTING TRANSFORMERS

### SUMMARY

Field investigations on harmonics caused by loads are essential to have a quantitative visualization and formation of premise of research. Field investigations have been carried out covering spectrum of loads and voltage levels right from generation to consumers, as at present. Investigations have revealed that low tension consumers form cluster of non-linear loads and are major contributors of current harmonics. Traction loads are another major category of harmonic pollutant. Industrial consumers do provide reactive compensation which helps to filter out current harmonics partially. However, in absence of any regulatory measure consumers keep polluting current harmonics into the system and also bear with the consequential disturbances. Voltage harmonics are significant only at leaf ends of distribution distribution system, where source impedence, seen by the harmonics generated by the load, is high. Transformer is the first major equipment in power system to intercept the harmonics. These harmonics caused accelerated ageing of transformers and even objectionable rise of temperature of cover-plate and turrets.

**Key words:** Current Harmonics, Voltage Harmonics, Total Harmonic Distortion, Crest Factor

### 1. INTRODUCTION

Sinusoidal waveform is the most natural waveform and is ideal for generation of electricity through rotating machines. Nevertheless, practical limitation of creating sinusoidal flux distribution has been causing small distortion in the waveform of voltage generated by the rotating machines. Inventions for energy conservation, efficiency and process control have made loads non-linear. Presence of harmonic in power systems is mainly due to non-linearity of loads such as arc load, electronic loads, converter loads, process efficiency and control equipments, non-linear inductances and recurring transients. Various researcher have carried out harmonic survey. It is observed from the reported harmonics [S Jain, Patidar, Waware] that each of them cater to specific needs of the researcher. It was, therefore, considered essential to determine presence of harmonics prevalent across the power system covering various voltage levels right from generation upto distribution.

## 2. HARMONICS IN POWER SYSTEM

Transformer is a nodal element in the power network and an interface between loads and power supply system. Moreover, harmonics generated by load are intercepted by the transformers. Accordingly, measurement of harmonics across the power system were carried out and are classified as under –

- i. Harmonics at generation,
- ii. Harmonics at transmission level,
- iii. Harmonics on traction feeder,
- iv. Harmonics in Industrial area,
- v. Harmonics in commercial area,
- vi. Harmonics in residential area

### 2.1. Harmonics at Generator Terminals

Sanjay Gandhi Thermal Power Station (SGTPS), Birsinghpur, Madhya Pradesh, has total capacity of 1340 MW (2\*2\*210+1\*500 MW units) and is the largest generating station in the state of Madhya Pradesh Power Generating Company Ltd. (MPPGCL) India, having total installed capacity of 3847.5 MW out of which thermal generation capacity is 2932 MW. In a power deficit utility it is difficult to schedule harmonic measurement on unloaded generator. Generating voltage of 500 MW unit and 210 MW units are 21 kV and 15.75 kV, respectively, which are stepped up through generation transformer to 400 kV and 220 kV, respectively. These units are inter connected at the station bus through 315 MVA 400/220 kV Inter-Connecting Transformers (ICTs). The presence of harmonics at generating point, shown in Fig. 1, though small and within permissible limits, is attributed to construction of alternator, having discrete slots to place windings. Amongst these low order harmonics, predominance of the third harmonics is due to non-linearity of magnetic material. Short Circuit Level (SCL) of the generating station is 5803 MVA and is quite high, while current harmonics are quite feeble, and thus voltage harmonics would be close to its no-load values. Neutral current of fundamental frequency is practically negligible, as compared to the line current, since currents of three-phases cancel out. However, the definition of THD and harmonics content is with respect to the magnitude of the fundamental and, therefore, THD and harmonic current in the neutral is high and shall be seen in practically all harmonic recordings presented in this chapter.

HARMONICS TABLE				
Volt	L1	L2	L3	N
THD%f	1.7	1.7	1.9	32.0
H3%f	1.7	1.6	1.8	31.9
H5%f	0.3	0.3	0.4	1.2
H7%f	0.1	0.2	0.1	0.6
H9%f	0.1	0.0	0.1	0.9
H11%f	0.0	0.1	0.1	0.1
H13%f	0.1	0.1	0.1	0.1
H15%f	0.0	0.0	0.0	0.2

20/10/10 05:33:07 230V 50Hz 3Ø WYE EN50160

A - Voltage Harmonics of 500 MW Unit

HARMONICS TABLE				
Volt	L1	L2	L3	N
THD%f	1.2	1.0	0.9	10.3
H3%f	0.4	0.3	0.2	2.1
H5%f	1.1	0.7	0.4	1.3
H7%f	0.2	0.4	0.6	0.9
H9%f	0.1	0.3	0.3	1.3
H11%f	0.2	0.4	0.4	1.2
H13%f	0.1	0.1	0.1	0.9
H15%f	0.1	0.1	0.0	0.9

20/10/10 07:05:03 230V 50Hz 3Ø WYE EN50160

B - Harmonic Voltages on 400 kV side of 400/220 kV ICT

HARMONICS TABLE				
Volt	L1	L2	L3	N
THD%f	1.0	1.1	0.8	30.9
H3%f	0.9	1.0	0.7	30.1
H5%f	0.4	0.2	0.2	1.8
H7%f	0.2	0.1	0.2	0.6
H9%f	0.0	0.1	0.1	2.7
H11%f	0.0	0.1	0.1	2.0
H13%f	0.1	0.1	0.1	1.2
H15%f	0.1	0.1	0.1	1.4

20/10/10 08:05:55 230V 50Hz 3Ø WYE EN50160

C - Voltage Harmonics on 210 MW Unit 1

HARMONICS TABLE				
Amp	L1	L2	L3	N
THD%f	0.8	1.0	0.5	25.3
H3%f	0.3	0.5	0.2	3.7
H5%f	0.7	0.8	0.4	4.0
H7%f	0.2	0.2	0.1	2.8
H9%f	0.1	0.0	0.0	2.6
H11%f	0.1	0.1	0.1	2.6
H13%f	0.0	0.0	0.0	2.9
H15%f	0.0	0.0	0.0	2.7

20/10/10 08:06:27 230V 50Hz 3Ø WYE EN50160

D - Current harmonics in 220 kV generator

Figure 1: Measurement of Harmonics at SGTPS, Birsinghpur, MPPGCL, India

## 2.2. Harmonics at Transmission Level

Transmission lines are the medium for propagation of harmonics into the system, and they converge and diverge at substations. Accordingly, an EHV substation having three voltage levels 132, 33 and 11 kV was taken up for measurement of harmonics. Chattisgarh State Electricity Board (CSEB), India, has a large concentration of industrial loads predominantly metal processing. This is attributed to the existence of one of the largest plant of Steel Authority of India Limited (SAIL) at Bhilai. A 132/33/11 kV Gudiyari substation at Raipur, CSEB was chosen for measurement of harmonics since it is close to Bhilai. The substation has 2x40 MVA, 33/11 kV, YNyn0 Connection, transformers. They are operating on Normal Tap (i.e. tap number 5), percentage impedance at Normal Tap equal to 10.04%. One of the two transformers, having a mix of industrial and town feeders, was taken up for harmonic measurements. Short circuit levels (SCL) of the PCC, which have an impact on voltage harmonics, are also shown in Table 1. There is a consistent increase the short circuit level at the substation. This increase and is attributed to increase in generation and transmission infrastructure, to cater to the increasing load. The increase in short circuit level gives a respite in voltage harmonics (below 1%) and is substantiated in voltage harmonic recordings, despite the presence of current harmonics (about 4%), and below the permissible limit of 5% as per IEEE Std. 519.

Table 1: Trend of Short Circuit Levels (MVA) at 132/33 kV Substation, Gudiyari

S. No	Bus KV	07-08		08-09		09-10		10-11		11-12	
		3 $\phi$	1 $\phi$								
1	132	2812	1780	3196	1948	3215	1958	3386	2059	4157	-
2	33	835	712	866	738	867	739	879	753	922	82

The order of harmonics is comparable on primary and secondary side of 40 MVA transformer and is attributed to its Y-Y connection. Moreover, mutual coupling between the harmonics transfers the harmonics from one side to the other. The Crest Factor (CF) in the recorded current waveform parameters, is as high as 1.75, and is indicative of predominance of 5<sup>th</sup>, 9<sup>th</sup>, and 11<sup>th</sup> harmonic, with a difference of degree. The substation has two separate feeders, one is Industrial Feeder and the other is Town Feeder and its field observations are brought out in the foregoing paras. In the same substation a separate 10 MVA 33/11 kV transformer is on Town Feeder for supply to township and its harmonic recordings are also found to be below 5%.

## 2.3. Harmonics in Traction Feeders

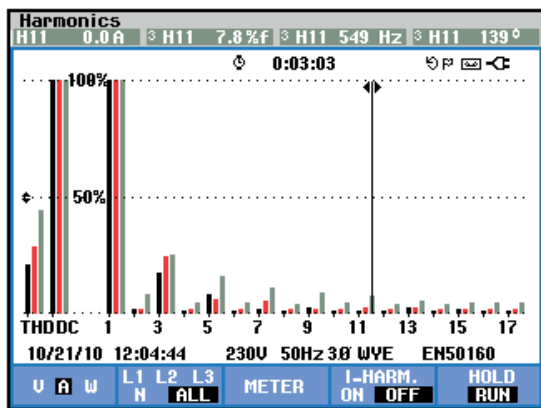
- a) **220 kV Three Phase Traction Feeder** : Madhya Pradesh Power Transmission Company Limited, India (MPPTCL) has a dedicated 220 kV feeder emanating from 315 MVA transformer in 400/220 kV YNyn0D1 substation at Katni. At down end the railways convert it into single phase feeders for use in traction. This substation is receiving supply from 400 kV switchyard of Power Grid Corporation of India Limited (PGCIL) at Satna, which in-turn is closely connected to power hub of NTPC at Vindhyachal Thermal Power station. Fault level at the feeding substation at Satna 400 kV Bus is 10116 MVA, while at 400 kV Katni bus is 4096 MVA. Harmonic measurements have been made at control panel. The harmonic recordings are shown in Fig. 2. It was seen that Phase A, B and C had 21.7%, 38.3% and 43.8% current harmonics, respectively, while voltage harmonics were 2.1%, 2.9%, and 3.1%, respectively. Despite, severe current harmonics, which is characteristic to traction loads the order of voltage harmonics is reasonably subdued. This is attributed to strong linkage of the substation to the power system.

Traction loads are Two Phase loads and they cause unbalanced loading on the transformer at the substation. Moreover, the K-Factor corresponding to the recorded harmonics varies from 1.3 to 2.11. Thus winding carrying highest current THD would age faster. This creates a need of review of ageing criteria based on the philosophy that "strength of the chain is that of its weakest link". The *THD<sub>n</sub>* in neutral current was observed to be above 500%, with individual harmonic components above 75%, and is obvious due to its definition and EHV circuit neutral current is only due to capacitive coupling with the ground.

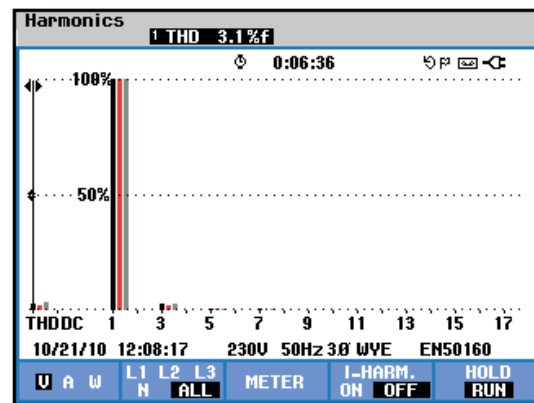
- b) **66 kV Three Phase Traction Feeder** : The 66 kV Ridge Valley substation, national capital Delhi, has a dedicated traction feeder. Railways have, however, at their end shifted load from this feeder on to another supply from Delhi Transco. In view of this, at the time of measurement, only allied loads were catered by railways from supply available on this feeder. Despite, the harmonic patterns on the feeder is shown in Fig. 3 presence of current

harmonics is beyond permissible limits. Presence of 3<sup>rd</sup>, 5<sup>th</sup> and 7<sup>th</sup> harmonic is predominant. Dispersion of  $THD_i$  across phases is within 10% and is considered to be acceptable.

- c) **25 kV Two Phase Metro Rail Feeder** : Measurements were taken at 66 kV substation, at Indira Gandhi International Air Port, Delhi. This substation receives supply from adjoining 132 kV substation of Delhi Transco. At the substation there are 2\*30 MVA 66/33 kV transformers for airport supply. Supply to metro rail is made from this substation through 2\*30 MVA 66/27.5 kV Two-phase to Single phase transformers. Observations on one of the traction feeder are brought out in Fig. 4. It is seen from the current waveforms that electrical system of metro rail is designed for harmonic correction. This is evident from 9.7% THD of current harmonics in Fig. 4-C. Though the  $THD_i$  is above permissible limit of 5%, it is quite low as compared to observations on 220 kV and 66 kV traction feeders.  $THD_i$ , during unloaded condition current 72.8%, Fig. 4.B, and on the face of it is enough to cause panic. However, the associated K-factors, at 98.6 is indicative of negligible fundamental component and accordingly the high  $THD_i$  is attributed to noise, which is quite high in air-port zone. Power transformer neither handle these spurious signals nor do they affect it, and hence it is ignored. Similar observations are made in lightly loaded conditions shown in Fig. 4.D, where current THD is 45.9%. The power factor ( $PF$ ) is seen to be 0.9 while the  $\cos\phi$  is 0.95 as seen in Fig. 4.E and waveforms shown in Fig. 4.A. This further substantiates corrective measures that have been put in place in the electrical systems of the Metro Rail. Voltage harmonics in Fig. 4.F are within acceptable limits due to vicinity of feeding substation.



A - Current Harmonics at Control Panel

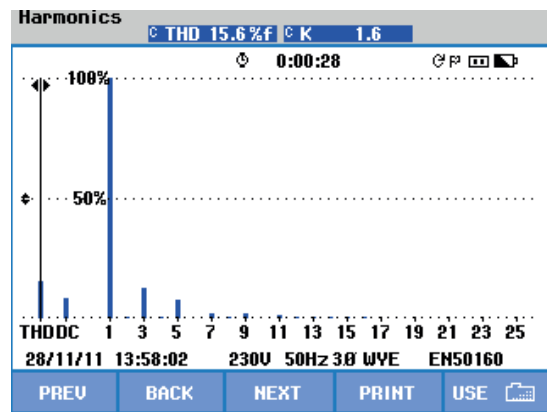


B - Voltage Harmonics at Control Panel

Figure 2: Harmonics in 220 kV Traction Feeder at 400/220 kV Substation

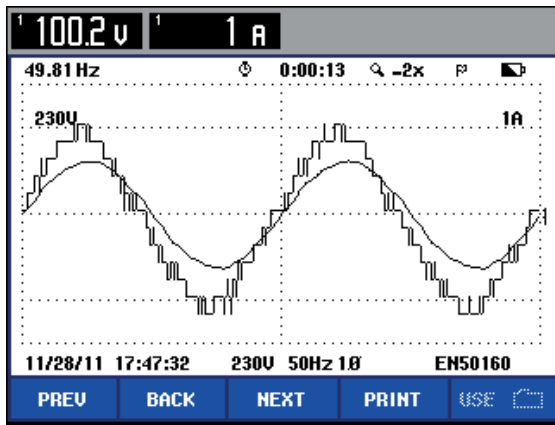
HARMONICS TABLE				
Amp	A	B	C	N
THD% <sub>f</sub>	11.3	10.6	11.7	11.1
H3% <sub>f</sub>	9.0	6.3	8.4	8.4
H5% <sub>f</sub>	5.8	5.2	7.3	6.3
H7% <sub>f</sub>	2.0	3.3	1.6	2.1
H9% <sub>f</sub>	1.7	1.5	1.1	0.9
H11% <sub>f</sub>	1.5	1.8	1.3	1.1
H13% <sub>f</sub>	0.9	1.3	0.7	0.7
H15% <sub>f</sub>	0.2	0.6	0.3	0.4

A. Current Harmonics in the Feeder

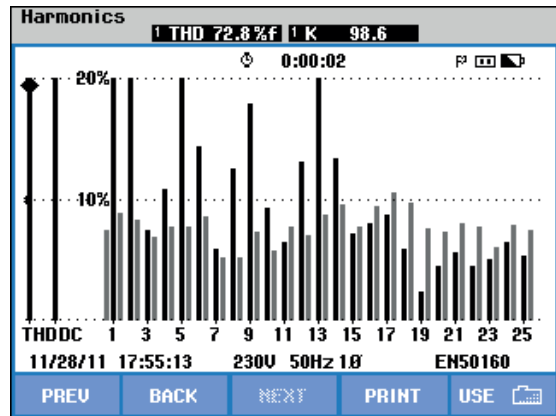


B. Harmonic Spectrum of Current Harmonics in B Phase.

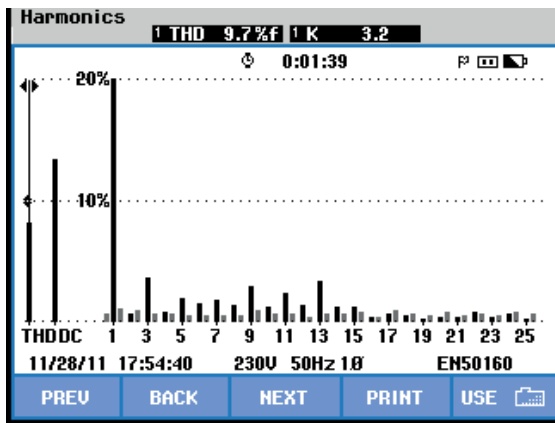
Figure 3: Current Harmonics measured on 66 kV Feeder from Ridge Valley Substation



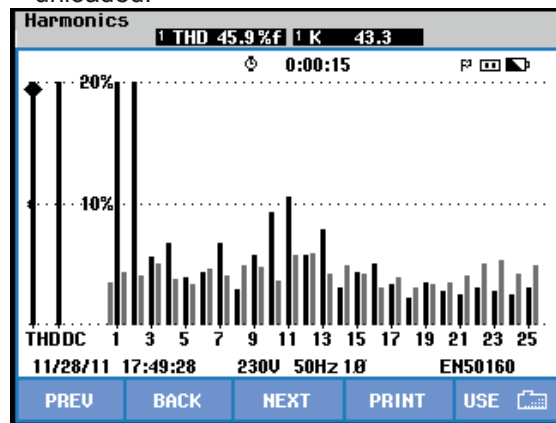
A. Voltage and Current Harmonics Waveform



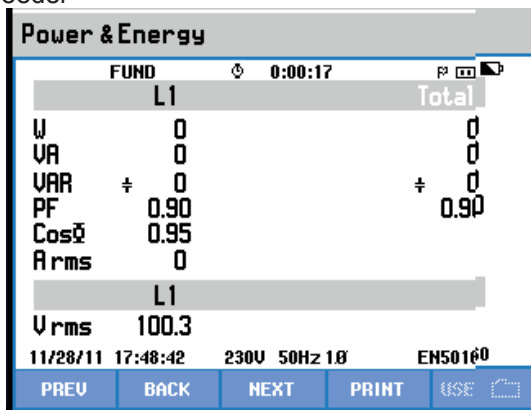
B. Spectrum of Current Harmonic –Feeder unloaded.



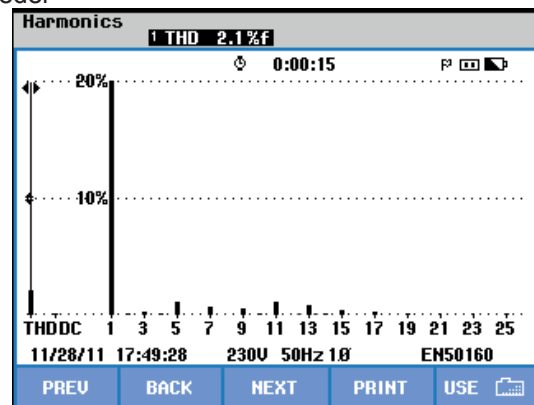
C. Spectrum of Current Harmonic –Loaded Feeder



D. Spectrum of Current Harmonic – Lightly Loaded Feeder



E. Power Measurements



B. Voltage Harmonics

Figure4: Observations on 27.5 kV Feeder of Metro Rail

## 2.4. Harmonics in Industries

A mix of harmonic pollutant industries were taken up for measurement.

- Metal Processing Industry – Arc Furnace** : M/s 3D Innovations is a sponge iron plant where iron scraps are converted into ingots in arc furnace. It has contract demand of 1000 kVA having 2\*500 kVA, 33/0.04 kV, YD connected, 6.9% Z, arc furnace transformers. feeding two independent arc furnaces It receives power supply from Kabeer Nagar Feeder, emanating from 220/132/33 kV Urla S/stn. Frequent failures of 5/5 Amp CTs have been experienced at this location. Since, up-gradation of CT to 10/5 Amp, in Aug'11, failures have

not been experienced. However, the harmonics at the time of recording were about 2% and well within IEEE limits. This was also validated with CF which was about 1.46.

- b) **Metal Processing Industry – Induction Furnace** : M/S Goyal Pipes, Manufacturer of MS Ingots out of Pig Iron and Steel Scrap, Major load Induction Furnace. It uses 2\*3900 kVA 33/0.9 kV three winding transformer with secondary and tertiary winding of equal ratings but Dd0 and Dy11 with 4.12% Z for each of LV winding and 7.81% Z for primary. It has one The unit has contract demand of 6.4 MVA. It has another 1\*950 KVA 33/0.4 kV transformer which caters to auxiliary loads and 2\*350 Capacitor Bank for overall power factor correction. Despite this current harmonics, with predominance of 11th and 13th, was observed to be 10% Power factor at the industry was seen to be 0.99. This indicates that the industry has taken care of only reactive power compensation, to avert low power factor penalties, while harmonic compensation has been ignored in absence of any regulatory measures.
- c) **Rolling Mill** : M/s Chattisgarh Steel Products, Urla, is a rolling mill, which manufacturer of steel sections using MS ingots. It receives supply from nearby 220 kV/132/33 kV substation, Urla, CSEB. Current harmonics have diversity across phase in the range of 13% to 17% with CF as high as 1.9. The industry is operating at PF=0.94 due to use of passive filters to compensate for reactive power absorption and thus to avail the benefit of tariff for evading low power factor penalty. But, the industry has not used active filters for harmonic compensation. This is evident from crest factor also. The necessity of active filter can be realized from load fluctuations observed in Fig.5.

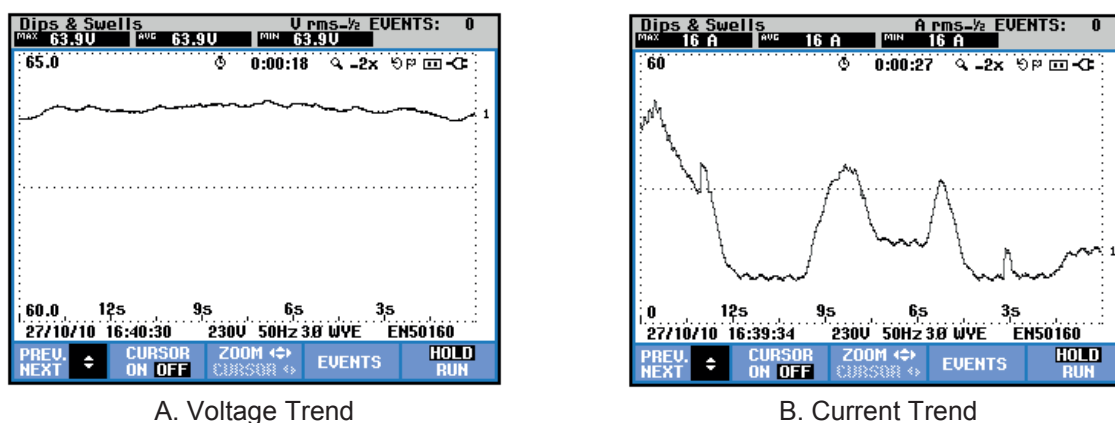
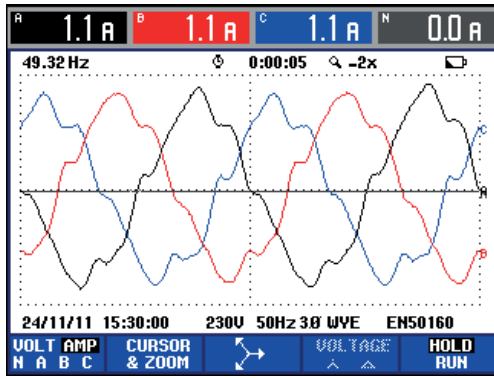


Figure 5: Dynamic Current and Voltages at M/s Chattisgarh Steel Products, Urla, Rolling Mill

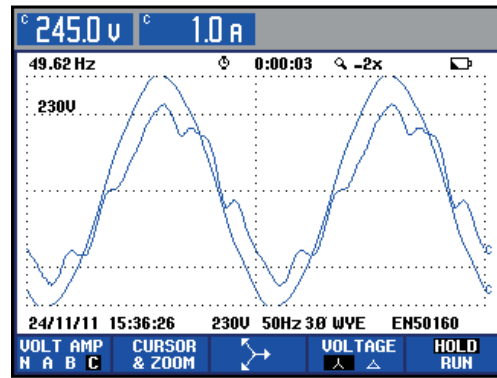
- d) **Industrial Area** : An industrial area catering to small industries from a substation with 3\*1000 kVA 11/0.4 kV transformer was also taken up for measurement of harmonics. Transformers have 5% impedance and accordingly maximum current THD should be 5% as against significant harmonics upto 11<sup>th</sup> order are recorded as shown in Fig.-6-C. Further, presence of even current harmonics, seen in Fig 6-C is substantiated by loss of quarter symmetry in current waveforms in Fig. 6-A and Fig. 6-B.

## 2.5. Harmonics in Commercial Complex

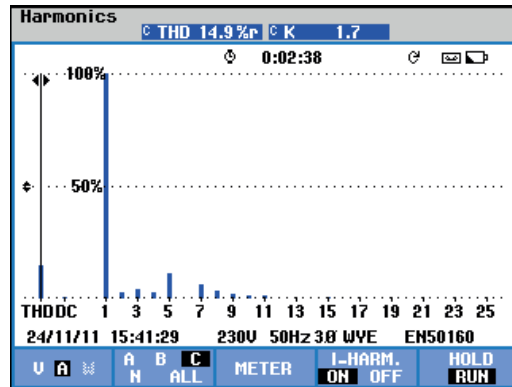
- a) **Shopping Mall**: Select City Walk, biggest mall in Saket, South Delhi has connected load of 8 MVA having 4\*2MVA, 33/0.415 kV transformers, with percentage impedance of 6%. The complex has generator back of equivalent capacity. They have installed 4\*700 kVA detuned switched capacitor bank for reactive power compensation one with each of the transformers. Power factor, which attracts penalty, was seen to be exceptionally good at 0.997. Harmonic recordings at the complex are shown in Fig. 7. Each of the transformers operates in radial mode with changeover facility during contingency. It is seen that harmonic recordings are as high as 11%. Inadequacy of harmonic mitigation, as against reactive power control, even at this organized complex, is attributed to absence of provision in the tariff to penalize for harmonic injection; it is unlike the penalty for low power factor. Only 3<sup>rd</sup>, 5<sup>th</sup> and 7<sup>th</sup> harmonics are found to be predominant.



A. Waveform of Three Phase Currents

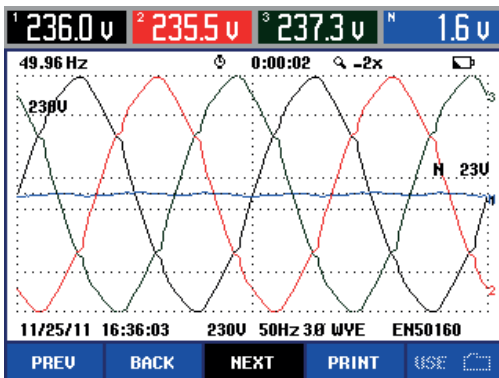


B. Current and Voltage Waveform of R-Phase

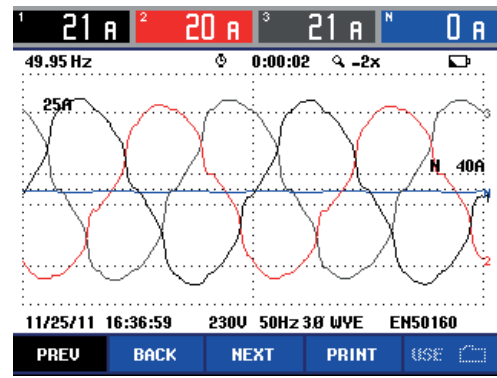


C. Current Harmonic Spectrum in R-Phase

Figure 6: Harmonic Measurements on LT side of Transformer Feeding Cluster of Industries



A. Voltage Waveform of Three Phases

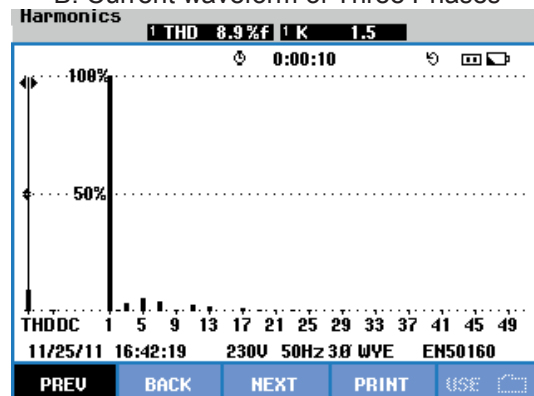


B. Current waveform of Three Phases

**HARMONICS TABLE**

Amp	L1	L2	L3	N
THD%f	9.6	11.1	9.8	455.9
H3%f	4.1	5.1	1.8	342.1
H5%f	6.4	7.5	7.5	11.4
H7%f	4.1	4.4	3.9	20.7
H9%f	0.6	0.2	0.2	30.8
H11%f	2.8	3.1	3.0	10.4
H13%f	2.4	2.5	2.7	18.4
H15%f	0.4	0.2	0.2	19.8

C. Harmonic Content in Current in Three Phases



D. Harmonic Spectrum in A-Phase

Figure 7: Harmonics Recording at Shopping Mall, Delhi

- b) **Commercial-cum-Office Complex** : This shopping-cum-office complex is in a high rise building #96 at Nehru Place, Delhi. #96. Ground floor accommodates assorted shops, while all upper floors are offices with computers and A/Cs. The complex is supplied from 1\*1000 kVA and 1\*630 kVA transformers on ground floor. The observations were made on LT side of 1 MVA transformer and in Figure 2.14. The A phase had highest harmonic content predominant third, fifth, second seventh and ninth in descending order. Significant DC component was seen and is attributed to the nature of loads.

Volts/Amps/Hertz				
	L1	L2	L3	N
Urms	248.5	251.4	247.9	1.6
Upk	344.6	348.5	343.1	2.7
CF	1.39	1.39	1.38	OL
Hz	49.67			
	L1	L2	L3	N
Arms	9	9	13	0.0
Apk	14	16	24	0.1
CF	1.67	1.81	1.80	OL

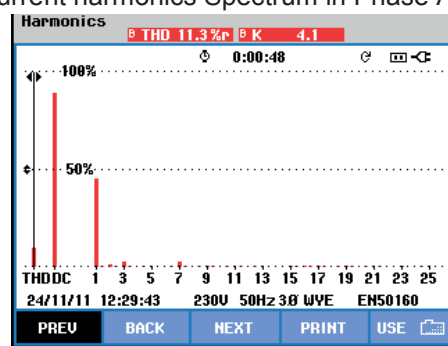
15/12/10 11:53:58 230V 50Hz 3Ø WYE EN50160

HARMONICS TABLE				
Amp	L1	L2	L3	N
THD%f	15.0	9.8	22.9	156.4
H3%f	10.0	6.8	13.9	81.2
H5%f	9.2	5.1	12.6	58.2
H7%f	5.3	2.5	10.5	18.5
H9%f	0.6	1.1	3.9	27.2
H11%f	0.9	2.0	2.1	13.7
H13%f	0.8	1.9	0.9	17.7
H15%f	0.7	0.9	1.4	14.3

15/12/10 12:10:04 230V 50Hz 3Ø WYE EN50160

A. Current Harmonics in Three Phases

B. Current harmonics Spectrum in Phase A



C. Current harmonics Spectrum in Phase B

D. Current harmonics Spectrum in Phase C

Figure 8: Recording of Harmonics at Commercial-cum-Office Complex

## 2.6. Harmonics in Residential Area

- a) **Residential Area** : Indian Institute of Technology Roorkee, is the residential institute with extensive infrastructure to support academics, research and on the campus boarding. The non-linear loads in the institute include main computer center, laboratories of different departments, air conditioning, and compact fluorescent lamps (CFLs) alongwith high power LT machines with a total maximum load of 6 MVA. Though, all loads are of low voltage, but power supply to these low voltage loads is met through 10 number substations, which are connected in a grid on 11 kV. The grid receives supply from the state power utility on two feeders emanating from 33/11 kV substation, located on outskirts of the institute. Saraswati Kunj substation is the major load center of the institute, having a mix of residential and institute loads, was preferred, amongst other sub-stations, for harmonic measurements. It has 2\*800+1\*630 kVA, 11/0.4 kv DY11 transformers feeding separate set of feeders. Rerecording of harmonics on secondary side of one of the 800 kVA transformer are shown in Fig. 9. The effect of non-linear loads is visible in harmonic recordings in Fig 8. Almost all the loads are single phase and are responsible for predominance of 3<sup>rd</sup>, 5<sup>th</sup> and 7<sup>th</sup> order harmonics (Fig 9.B), Voltage waveform, is almost unaffected and is seen from the CF of voltage (Fig 9.A) and is attributed to the vicinity of power source. In continuation to this, reference to observations of harmonic and reactive power presence in various field observations, discussed above is relevant. Residential uses of electricity suffer from severe harmonic disorder and high reactive power, and this can be attributed to lack of awareness amongst consumer which have a high diversity. As regards regulatory measures, through tariff it is seen to be a distant future, in wake of the fact that there are no penalty on harmonic violations even for bulk and organized power consumers.

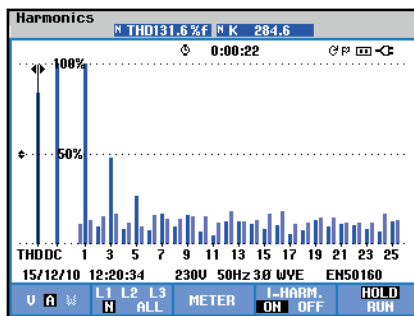
- b) **High-Rise Residential Complex** : A high-rise (tweve storied) residential complex was taken up for harmonic measurement. It has 100% disel gereator backup. Though the voltage harmonics both of the diesel generator on no-load and utility supply were seen to be within limits, however current harmonics were seen to vary from 8% to 15% across the threwe phases. Thepower factor of the load was about 0.6%. The observations are brought out in Fig 10.

Volts/Amps/Hertz				
	L1	L2	L3	N
Vrms	248.5	251.4	247.9	1.6
Vpk	344.6	348.5	343.1	2.7
CF	1.39	1.39	1.38	0L
Hz	49.67			
	L1	L2	L3	N
Arms	9	9	13	0.0
Apk	14	16	24	0.1
CF	1.67	1.81	1.80	0L

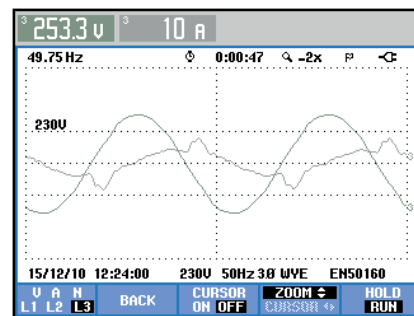
A. Waveform Parameters

HARMONICS TABLE				
Amp	L1	L2	L3	N
THD%f	15.0	9.8	22.9	156.4
H3%f	10.0	6.8	13.9	81.2
H5%f	9.2	5.1	12.6	58.2
H7%f	5.3	2.5	10.5	18.5
H9%f	0.6	1.1	3.9	27.2
H11%f	0.9	2.0	2.1	13.7
H13%f	0.8	1.9	0.9	17.7
H15%f	0.7	0.9	1.4	14.3

B. Current Harmonics on LT Side

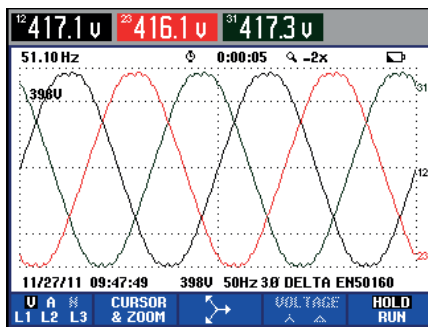


C. Harmonics in Neutral Current

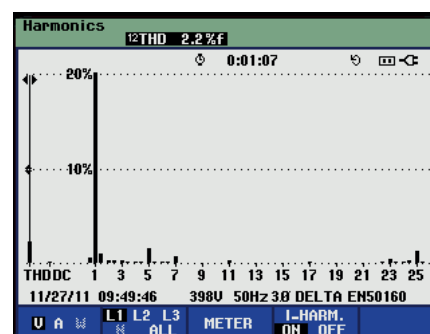


D. Current and Voltage Waveform

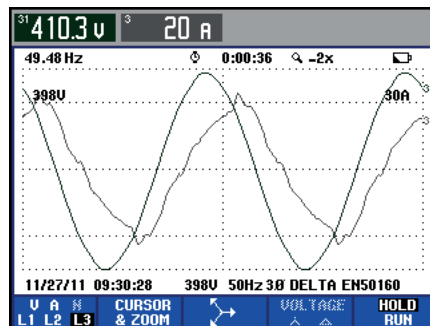
Figure 9: Harmonics at 11/0.4 kV Transformer at Sarswati Kunj



A. Voltage Waveforms



B. Harmonic Spectrum



C. Current and Voltage Waveforms of C-Phase

Figure 10: Harmonics Recorded on Captive power Generator of Residential Complex

### 3. CONCLUSIONS

Investigation into causes of harmonics is not the objective of this research work. However, harmonic survey across the power system is carried out to determine state of the harmonics prevalent in the system. Alternators, despite technological developments have constraints of placing armature coils in discrete slots and thus causing inception of voltage harmonics, though in small magnitude, right at the point of generation. Presence of current harmonics is predominant at distribution level with an exception of traction feeders which are either on HV or EHV. Consumers which exercise proper management of reactive power and harmonics have shown comparatively lower presence of harmonics. But, this is not true for all the industries. L.T consumers, commercial and residential loads, are individually small but their combined effect becomes quite severe. This is evident from the observations on harmonics in commercial and residential area. The future trend in this regard is of large and high rise complexes and is seen as an opportunity of effective harmonic management. Harmonics generated at consumer end are intercepted by the transformers and there is lot of diversity across phases in respect of harmonics. This diversity of harmonics cause heating of transformer windings, and the effect of heating of windings is in the order of harmonic content and causes accelerated ageing. Thus a criterion of ageing of transformer based on highest harmonic loading is important. It is seen that some of organized consumers have taken suitable measures for power factor correction, however, measures of harmonic mitigation are found to be insufficient and current harmonics are seen to be beyond permissible limits, with a difference of degree, practically in all cases.

Further, heating of cover plate and turrets for bushing, specially in high current current transformers has been been a matter of concern. Use of non-magnetic inserts, and even non-magnetic cover-plate of transformer has been suggested by various reserachers to control the heating of cover-plate. This problem becomes more vulnerable in presence of harmonics. Separately this aspect has been investigated by the authors and they have proposed a remedy using aluminum shield around the low voltage leads of transformer, specially feeding either non-linear loads or cluster of such loads.

Investigation into presence of has created a data set covering the spectrum of power system right from generation till distribution, spanning over various voltage levels and category of loads. Some of the load centers covered in the investigations are generally inaccessible. This papers, due to space limitations contains salient data. However, in case the dataset is a reasonable pointer to the state of harmonics that would inflence transformer.

Antun Mikulecky  
Končar - Electrical Engineering Institute  
[amikul@koncar-institut.hr](mailto:amikul@koncar-institut.hr)

## TRANSFORMER BUSHINGS – FAILURE CASE STUDIES

### SUMMARY

Relationship between bushing failure and transformer failure is discussed and, in regard of that, two bushing failure types are recognized: incipient bushing failure that does not result in transformer damage and terminal bushing failure having transformer failure as a consequence. It can be seen, that without applying the diagnostics, all bushing failures are terminal. Thirteen bushing failures have been analyzed regarding their cause, failure mechanism and consequences. In that sense, the ability and limitation of off line and on line diagnostics are discussed and some improvements are proposed. Some switchyard properties in the aspect of fire protection are indicated and, especially, the possible influence of rigid tubular connections on bushing failures. Beside mentioned design, service, condition diagnostics and other properties of all three condenser types of bushings are described in the paper.

**Key words:** bushing, failure, power transformer, diagnostics, tubular connection, fire protection

### 1. INTRODUCTION

Transformer bushing is a device through which the connection between the switchyard and the transformer winding is achieved, [1]. It conducts current and provides insulation to the tank. Bushing is positioned on the border of insulation media, usually oil on the lower side, and air, SF<sub>6</sub> or oil on the upper side, and it separates them from each other. This feature defines, to a great extent, certain fire protection characteristics of oil transformers. There are two main types of bushings used most frequently in the transformer technology: ceramic (porcelain) bushings, which are dominant at distribution voltages, and condenser type bushings, used for the past 50 years as the only choice for higher voltages. This paper deals with condenser type bushings. They are produced in three types of technology: RBP (resin bonded paper), OIP (oil impregnated paper), and RIP (resin impregnated paper), by wrapping on a central tube or conductor, with electrodes being inserted at certain diameters that grade radial and axial voltage stresses. A drawing of the oil – air OIP type condenser bushing is shown in Figure 1, and a schematic drawing of the bushing condenser body is shown in Figure 2. Condenser bodies, Figures 1 and 2 are schematically almost identical for all three bushing technologies, but their physical features differ. Condenser bodies of RBP and RIP represent solid products which are processed by turning. They mechanically adhere firmly and tightly to the flange (position 9 in Figure 1), so in this manner and with their integrity, they separate transformer oil from the surrounding medium. Therefore, the lower envelope (position 8 in Figure 1) is not necessary, because the body itself fulfills its task. In the case of condenser body breakdown (position 1), the integrity of the body and its sealing effect on the flange is usually preserved well enough to prevent the oil from leaking from the transformer, but, nevertheless, in a certain percentage of failures, leakage does occur. This, then, causes transformer fires because the oil leaks right onto the glowing hot bushing parts, heated due to the breakdown. In the case of OIP bushing, the situation is essentially different. There is no sealing effect of the condenser body to the flange, so in the

case of a fracture of both lower and upper envelopes, oil leaks from the transformer, often leading to fires. In the case of the upper envelope fracture, oil will not leak from the transformer because the lower envelope is fixed to the flange and the sealing effect is preserved. (In some older versions of OIP bushings, the sealing effect was assured by the axial force, so the fracture of at least one envelope would cause oil leakage from the transformer; therefore, this version is significantly worse than the OIP bushing case in Figure 1).

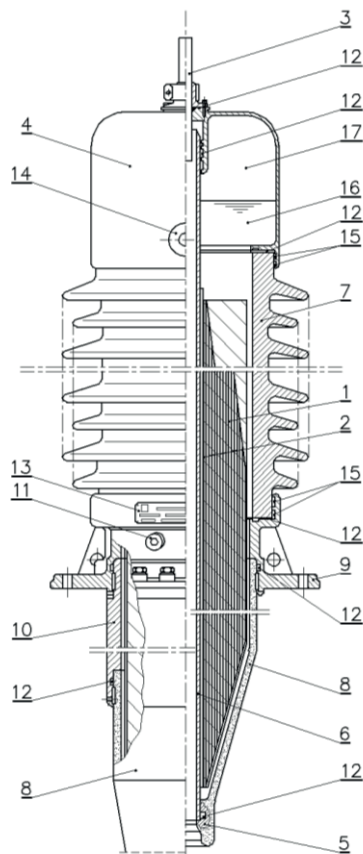


Figure 1: Drawing of the oil – air OIP type bushing

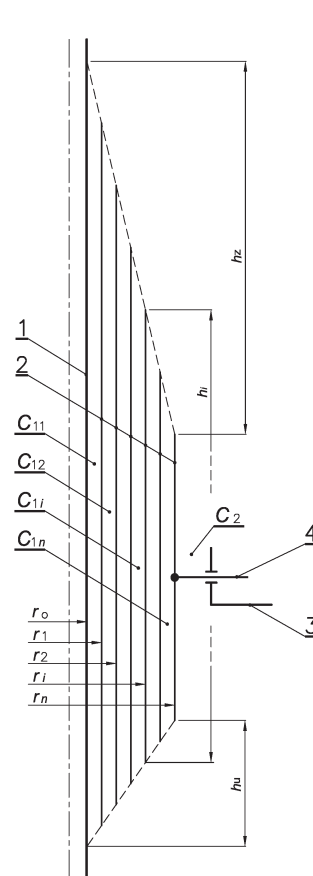


Figure 2: Bushing condenser body (schematically)

Designations, Figure 1:

- 1 – Condenser body
- 2 – Electrodes
- 3 – HV connection
- 4 – Head
- 5 – Electrostatic screen
- 6 – Central tube
- 7 – Upper anvelope
- 8 – Lower anvelope
- 9 – Flange
- 10 – Flange extension
- 11 – Test tap
- 12 – Sealing
- 13 – Marking plate
- 14 – oil gauge
- 15 – Binding cement
- 16 – insulating oil
- 17 – Expansion space

Designations, Figure 2:

- 1 – Central tube
- 2 – Electrodes
- 3 – Flange
- 4 – Test tap
- $C_{1i}$  – Capacitor,  $i^{\text{th}}$  in line
- $r_i$  – Radius of the  $i^{\text{th}}$  electrode
- $h_i$  – Height of the  $i^{\text{th}}$  electrode
- $h_z$  – Slope of the aerial part
- $h_u$  – Slope of the oil part
- $C_1$  – Condenser body capacitance  
( $1/C_1 = 1/C_{11} + \dots + 1/C_{1i} + \dots + 1/C_{1n}$ )
- $C_2$  – Test tap capacitance

It is interesting to note that the shut-of valve, which serves the purpose of preventing oil leakage from the conservator in case of tank rupture, often does not fulfill its role, due to low oil flow when bushing failure occurs. Adjusting the shut-of valve to a lower flow may lead to transformer trip because its false activation is caused by the sudden cooling of the transformer. False shut-of valve activation leads to Buchholz relay activation without the action of any other protection relays. Upper oil – air bushing envelopes (position 7 in Fig. 1) contain sheds to ensure satisfactory creepage distance and are made of porcelain or composite materials, with silicone sheds, or, most recently, silicone sheds are applied directly on the RIP body. In OIP bushings, the space between the condenser body and the upper envelope is filled with oil, and in RBP bushings, it is filled with insulation liquid. In RIP bushings, this space is filled with oil or with insulation foam for the completely dry construction, or the space does not exist if silicone sheds are applied directly onto the body. The porcelain upper envelopes are durable but breakable. They usually burst during bushing breakdown and are sensitive to vandalism. Their hydrophobicity is reduced in the polluted atmosphere. Composite upper envelopes, on the other hand, are mechanically tougher, more resistant to vandalism, they do not burst and their hydrophobicity is better, but they are less durable than the porcelain ones. RBP and, especially, RIP bushings can operate for some time even if the upper envelope breaks. Due to greater toughness of the condenser bodies, RBP and, especially, RIP bushings have better seismic characteristics than OIP bushings, [2, 3]. RBP and RIP bushings can withstand temperatures up to 120 °C, whereas OIP bushings are resistant up to 105 °C. OIP and RIP bushings have a very low partial discharge (PD), regularly several pC at test voltages. RIP bushings are

sensitive to the presence of PD because they have no possibility of regeneration that OIP ones have. Concerning this matter, RBP bushings have essentially poorer characteristics. Their PD reaches several hundred pC at test voltages and it can be even a hundred at operating voltage. The reason is that they always contain some air, so this technology is nowadays considered obsolete. Capacitance and  $\tan\delta$  for OIP and RIP bushings are permanent parameters until a disturbance occurs, making them very favorable for diagnostics. RBP bushings gradually increase capacitance during operation (even by ten or more %) due to oil impregnation and this can mask their defects.

## 2. BUSHING FAILURE DEFINITION

In the physical sense, failure occurs when service strength exceeds withstand strength of the material. Based on this, the definition widely accepted in engineering states that failure of a machine/device comprises the loss of functional properties resulting in termination of service. Repair or replacement is necessary before restarting. [4]. Partial loss of properties is referred to as defect. This definition of failure is based on the assumption that the device possesses bipolar functional features (functional properties exist – no failure and vice versa). The definition is clear, but more suitable for the device manufacturers than for the users. The users are more interested in the operational availability of the device. Namely, there are situations when a device is not operationally available, but there is no loss of functional properties. Characteristic situations of this kind are outages due to planned or unplanned condition diagnostics or for maintenance. In the sense of availability, every unplanned outage tends to be considered a failure. In this sense, a very interesting definition [5] states that failure presents any situation resulting in an unplanned outage for the purpose of investigation, repair or replacement. It takes into account the fact that condition monitoring by means of off line and on line diagnostics gives good results and has become the common practice of power utilities throughout the world. On the other hand, transformers can have more than ten bushings and failure of any one of them results in transformer failure. The second above mentioned definition is more appropriate for devices, whose condition is regularly diagnostically monitored, although it can, due to legal consequences, lead to intensive discussions between users and manufacturers. Defining the decision criteria when failure has been diagnosed by measurement but the device can still be in service, is a very delicate problem. This kind of decision criteria will not be well and impartially defined soon. It is interesting to note that decision criteria depend on whether diagnostics is periodical or continuous. An additional problem is that, according to this definition, very similar events may or may not be considered as bushing failure meaning that it is not unambiguous. The latter definition has another consequence: two types of bushing failures have to be recognized with respect to the failure impact on the transformer (or the power system). They can be named terminal and incipient failure. In the first case, complete loss of operational properties occurs while in the latter case, there is an initial defect that can evolve into a complete loss of service features during operation. Therefore, two types of bushing failures can be distinguished:

- **Terminal bushing failure** presents a complete loss of bushing service ability. This is usually a bushing explosion that causes great damages and transformer pollution as well as fires resulting in great collateral damage. Therefore, these are unplanned, forced outages [4] with large direct and indirect costs. The cause of an explosion is always breakdown: condenser body, upper or lower envelope.
- **Incipient bushing failure** occurs when a defect that can evolve into a terminal failure is detected by a diagnostic method. This type of failure can usually be fixed without serious consequences for the transformer and in a relatively short down-time; therefore, with low direct and indirect costs.

Considering the complete situation, bushing failures cannot be prevented by condition diagnostics (they are defined by bushing quality and service conditions), but the proportion of terminal to incipient bushing failures can be reduced, resulting in better service reliability and considerable cost reduction.

## 3. FAILURE CASE STUDIES

In this section, terminal and incipient bushing failures in the past twenty two years, in which author was involved, are described. Their ratio in this paper is not realistic because initial failures are often not even registered, especially if they are less severe and do not result in transformer down-time lasting more than a few days. Incipient failures occur, in fact, several times more often than terminal ones. Failure descriptions are methodized based on relevant data: about the transformer (type, voltage and

power), voltage and type of bushing, age, mode of failure (incipient, terminal, fire outbreaks), type of connection, service specificities, weather conditions at the time of failure, previous diagnostic data, estimated cause, and the failure scenario.

### 3.1. 123 kV Bushing Failures

#### 3.1.1. Case 1:

The lower envelope of an OIP type 123 kV bushing on a 150 MVA, 220/110 kV autotransformer, voltage, about 40 years old, exploded in the spring of 2006, during heavy rain, Figure 3. The hydrodynamic shock caused by bushing breakdown was very intense. The transformer tank was ruptured in several places so oil was leaking out. Most of the remaining bushings on the transformer were damaged (upper porcelain envelope damage and dislocation in relation to the head or flange occurred, followed by oil leakage from the bushing). The active part of the transformer was damaged to a great extent (the OLTC was destroyed, tap winding leads were damaged, etc.) and polluted so it had to be scrapped. The bushing was connected to the switchyard by rope.

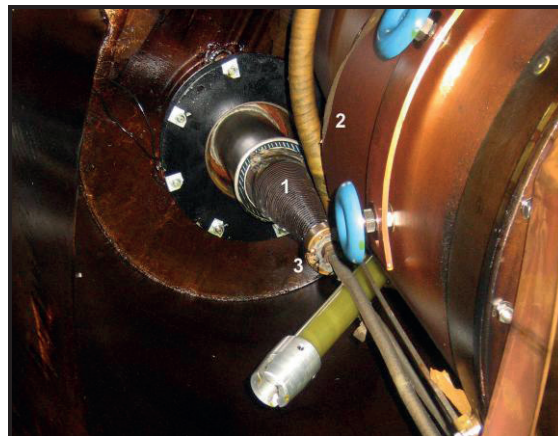


Figure 3: Exploded 123 kV bushing  
(1 – lower part of the bushing without the exploded lower envelope,  
2 – damaged diverter switch cylinder,  
3 – electric arch traces on the lower electrostatic screen)

The transformer was regularly diagnostically tested in approximately four-year intervals. In the period between the last two measurements in the years 2002 and 2005, there was a relatively large increase of the bushing  $\tan\delta$  amounting to 41 %, but its value was still relatively low (0,52 %). The bushing was treated as suspicious and more frequent testing was recommended. A detailed inspection of the bushing debris was performed several months after the failure. The condenser body was unwounded but no traces pointing to the cause of failure were found. The lower part of the condenser body was clean, with no traces of an electric arch. Traces of an electric arch were found only on the lower porcelain envelope fragments that were collected from the transformer tank, flange and lower electrostatic screen.

The following failure scenario can be presumed. Weakening of the sealing system leads to a gradual moistening of the bushing insulation system resulting in an increase of  $\tan\delta$ . Due to heavy rain and rapid cooling of the bushing, water can be sucked into it and this directly causes the lower envelope crepe breakdown (position 8 in Figure 1). Such a hydrodynamic shock breaks the OLTC diverter switch cylinder thus causing the loss of its axial support. Hence, the OLTC drops and moves to the side, deforming 123 kV line lead and on the tap winding leads in the process. Based on this case, it can be concluded that a forty percent increase of  $\tan\delta$  is very significant, despite its relatively low value. The recommendation for more frequent measurement was not good enough. The failure could have been avoided by replacing the bushing or adding an intervention monitoring system.

### 3.1.2. Case 2:

In the spring of 2005, the upper envelope of the 123 kV OIP type bushing on a 40 MVA, 110/10.5 kV transformer, 20 years old, exploded. The shock caused damage to the other bushings and equipment in the switchyard as well as a small fire. The failure occurred during a thunderstorm. Previous diagnostic investigation of the bushing had been undertaken in the years 1996 and 2000, approximately nine and five years previous to the failure, respectively. In that period,  $\tan\delta$  increased by almost 50 % (from 0,17 % to 0,25 %), but the values were very low, even for new bushings. The bushing was connected by rope. All 123 kV bushing were replaced in a few days. Visual inspection of the bushing debris showed a longitudinal breakdown in the space between the condenser body and the upper envelope (space between positions 1 and 7 in Figure 1). This is implicated by the hole on the central tube caused by the electric arch during the breakdown, Figure 4. However, because of the great damage of the condenser body, most part of which was burnt, a possible cause of breakdown could also have been the condenser body breakdown, although in this case it is less likely. The lower envelope was not damaged; preventing oil leakage onto the fault site and thus it was not accompanied by a major fire or transformer active part pollution by bushing fragments. An inspection of the bushing head showed cracks that could have occurred prior to the failure and this fact could be considered as an initial sealing system defect.

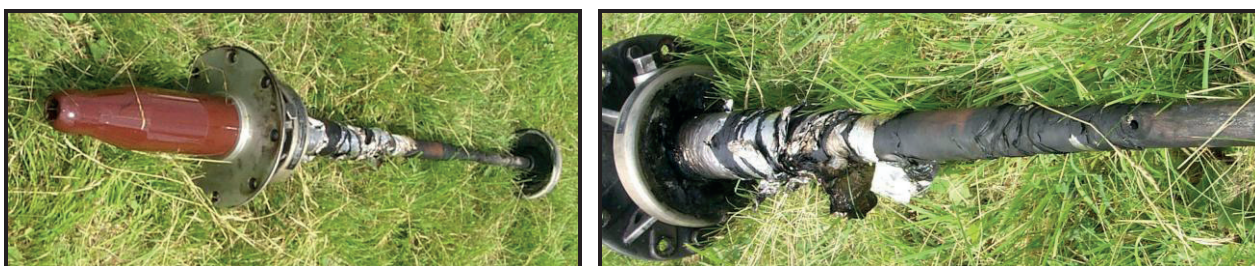


Figure 4: Disassembled failed bushing; Figure left – the whole bushing; Figure right – upper part of the bushing (the hole on the right-hand side of the tube was caused by the electric arch)

The cause of this bushing failure is not completely clear. Possibly, it was caused by a defect in the sealing system or a defect of the bushing condenser body. This case also points out the importance of  $\tan\delta$  change during service despite very small actual values.

### 3.1.3. Cases 3, 4, and 5:

In the period of 1991 to 1998, three 123 kV OIP bushing explosions occurred on three GSU transformers 43 MVA, 115 kV in one hydro-power plant. Frequent on and off switching, just as service at full load is characteristic for this power plant (peak load power plant). In all three cases, the failure appearance was practically identical: HV bushing explosion, thus damaging the other HV and LV bushings, causing a fire that further damaged the entire transformer exterior. Each time, repairs lasted for several months and had to be conducted in the factory. The bushings were connected to the switchyard by tubes, as shown in Figure 5. The first failure occurred in 1991 on a transformer produced in 1981. No data on previous diagnostic investigations were available. According to the visual inspection, the burst progressed radially from the central bushing tube (pos. 6 in Fig. 1) to the flange in the test tap area (positions 9 and 11 in Figure 1). The second failure occurred in 1993 on a transformer also produced in 1981. The inspected breakdown traces were visually identical to the first case. Previous diagnostic investigation had been conducted 14 months prior to the failure, but the results did not show any problems. The third failure occurred in 1998 on a transformer produced in 1988. Breakdown traces progressed axially, from the upper endpoint of the bushing, through interspace between bushing condenser body (pos.1, Fig. 1) and porcelain (pos. 7, Fig. 1), to the flange in the test tap area (positions 9 and 11 in Figure 1). Previous measurement of  $\tan\delta$ , approximately 13 month before the failure, had shown a value of 1,52 %, but, unfortunately, despite this drastic increase in value, the bushing had not been replaced. The three exploded bushings were not produced by the same manufacturer. Traces of all the three breakdowns were in a way associated with the test tap.



Figure 5: Tubular connections between the switchyard and 123 kV bushings

Obviously, these three cases show that something causes bushing properties degradation. The assumption has been made that it is caused by the too rigid tubular connection between the bushing and the switchyard. In addition, the incorrect orientation of the bus dilatation compensator contributes to the degradation (see Fig. 5). It can compensate vertical but not horizontal dilatation, whereas the latter should be dominant. A replacement of the bushing – switchyard connection was recommended. Instead, a part of a tubular connection flexible cable (rope) was used. Switchyard reconstruction was performed approximately twelve years ago and since then there have not been any malfunctions of this type.

### 3.2. 245 kV Bushing Failures

#### 3.2.1. Case 6:

Thermal image scanning of the 250 MVA, 220 kV, 16 years old, GSU transformer in 2002 showed increased heating of the 245 kV bushing head and connection (positions 3 and 4, Figure 1) relative to a healthy bushing, approximately by 60 K. Measurement of the HV Winding resistance showed an increase of 0,87 % in the respective phase therefore indicating the cause of poor contact on the tulip contacts (pos. 3, Figure 1) between the connection and the bolt at the end of the copper cable, Figure 6. Inspection of the HV connection showed traces of metal melting on the tulip contacts and copper transfer from the bolt to the aluminum connection. This incipient failure was eliminated by replacing the tulip contacts spring part, since its weakening is the most probable cause of increased heating, and by cleaning contact surfaces. Owing to the availability of spare parts as well as to detection of the malfunction in the initial stage, repairs took only two days.

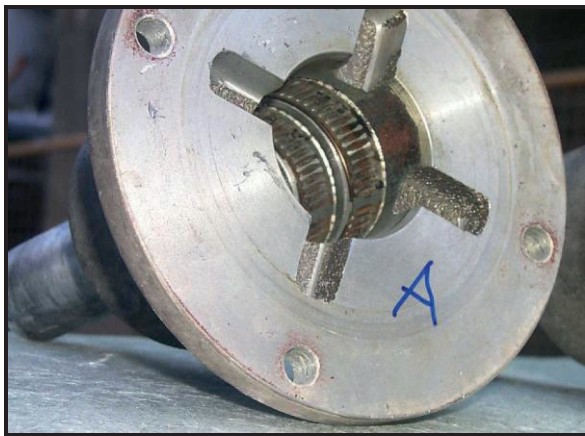


Figure 6: Left: Overheating traces on the HV connection and the tulip contact spring part; Right: Traces of overheating on the bolt

### 3.2.2. Case 7:

A very interesting 245 kV RBP bushing failure in the form of upper envelope and lower bushing part explosion occurred in 2005 on a 400 MVA, 400/220/30 kV, approximately 25 years old transformer. It was accompanied by a small scale fire on the transformer and pollution of the active part by the bushing fragments and other carbonized residues. Upper envelope fragments destroyed the neutral point bushing and one 420 kV bushing sustained damage, Figure 7. No information on diagnostic tests in the period of 5 years prior to the failure was available. Visual inspection of the bushing indicated a radial condenser body breakdown. Based on a detailed inspection of the bushing, the following probable failure scenario was established. Poor contact on the screw of the upper connection and the connector body (pos. 3, Figure 1) caused overheating which, enhanced during service, resulted in melting of the brazing by which copper cables were fixed to the connector body (Figure 7, in the middle top and bottom). Physical separation of the connector body and the cables occurred. Conduction of the current from the connector body was taken over by the central bushing tube. Electricity flowed from the tube onto the copper cables through several undefined locations, this being the only possible way to close the electric circle between the switchyard and the winding. Losses on undefined contacts heated the central tube (Figure 7, right) and bushing insulation, leading to condenser body thermal breakdown as a final consequence. Observed overheating traces suggested that the process took a relatively long time to develop and it is not clear why overheating was not detected by the thermal image scanning (generally performed once a year), which could have resulted in prevention of the bushing terminal failure, as it had been done in the previous case. Both failures were physically identical, but in the former case overheating was detected by thermal image scanning and fixed on time, with minimal costs and minimum down-time.

These two cases clearly show how incipient failure develop into terminal failure and how the absence of bushing condition diagnostics leads to terminal bushing failure, accompanied by great costs and long down-time.

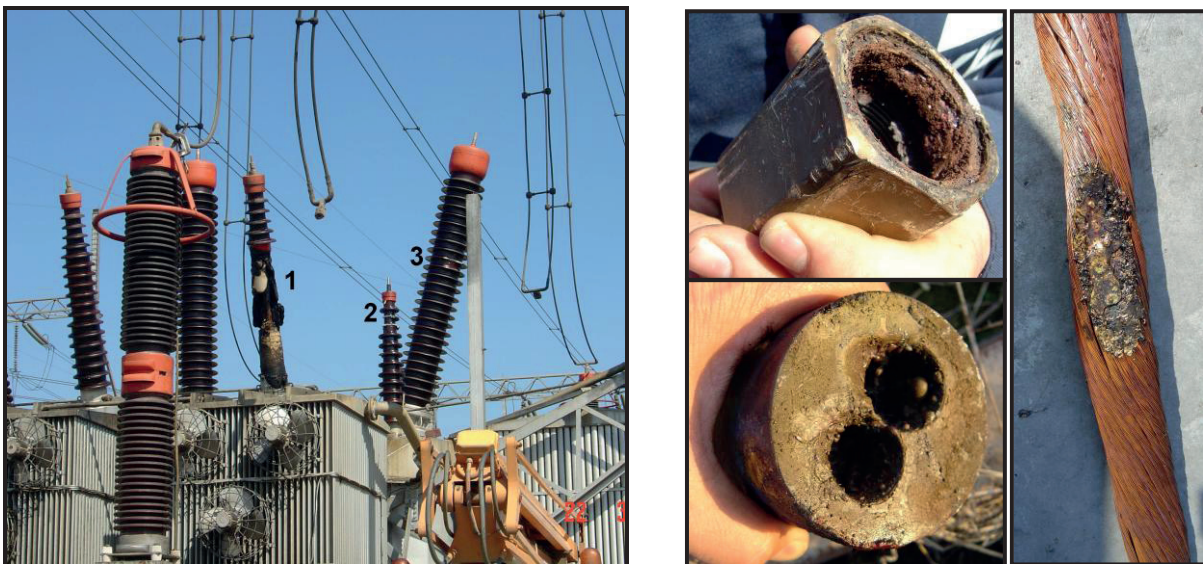


Figure 7: A 400 MVA, 400 kV transformer failure;

Figure left: 1 - burst 245 kV bushing, 2 - destroyed 170 kV neutral point bushing, 3 – damaged 420 kV bushing;

Figure middle top: traces of overheating on the top connection;

Figure middle bottom: connecting bolt body torn off cables;

Figure right: melting trace of brass central bushing tube on the copper rope

### 3.2.3. Case 8:

A failure of a 150 MVA autotransformer, approximately 30 years old, occurred in the spring of 2003. No special indications pointing to the failure mode were visible on the outside. Inspection of the disassembled RBP type bushing showed a burst of the bushing condenser body lower part (pos. 1 in Fig.1), approximately 0,5 m long, Figure 8. The transformer and, especially, the area around the 220 kV winding lead was intensely polluted by the bushing fragments, carbonized insulation and electrodes. Diagnostic tests of the bushing had been undertaken almost eighteen years prior to the failure but there had been no indication of the problem. The connection to the switchyard was flexible, by rope. The cause

of this breakdown is not known. However, breakdown traces indicate thermal breakdown with a wear out being a possible cause. According to the author's information, the transformer was scrapped.



Figure 8 Burst of a 245 kV, RBP type, bushing, the upper porcelain envelope remained intact (left), detail of the burst lower part (right)

### 3.3. 420 kV Bushing Failures

#### 3.3.1. Cases 9 and 10:

Two 400 kV bushing failures occurred on a 300 MVA, 400/110 kV autotransformer, one in 1994, the other in 2003, therefore after approximately 8 and 17 years of service, respectively. The bushings were of OIP type, connected to the switchyard by tubular connections, Figure 9. The first failure was of the incipient type – diagnostic tests showed a  $\tan\delta$  of 2,2 % indicating a high degree of service unreliability. Visual inspection and DGA of oil confirmed the findings. Traces of carbonized oil and considerable concentration of gases resulting from the electric arch (or very strong PD) were detected. Previous diagnostic tests had been performed in 1989, when similar  $\tan\delta$  of approximately 0,22 % had been found on all three bushings. The bushing was replaced with a spare one with down-time lasting a few days.

The second failure was terminal – an explosion followed by a fire, Figure 9, that could not be put out by the fire protection equipment (water spray system) because bushings are, because of large size, outside its action perimeter. Bushing fragments considerably polluted the transformer, but mostly remained inside the bushing turret. The dynamic shock damaged the 400 kV winding lead. The damages were, with a certain risk, fixed on site, with down-time lasting a few weeks. Traces of breakdown on the bushing condenser body indicated radial breakdown, most probably on the flange level. Diagnostic investigation had been conducted approximately three years prior to the burst, but did not indicate any defects ( $\tan\delta$  was 0,23 %).



Figure 9: Bushing terminal failure in 2003 and traces of fire on the 300 MVA, 400 kV autotransformer; The right-hand bushing in the figure was replaced after an incipient failure in 1994. Detail shows the bushing debris and the tubular connection dilatation compensator

It can be presumed that the cause of accelerated bushing degradation could be the tubular connection, even with the applied dilatation compensator (in this case correctly oriented). Service experiences point to the possibility that the compensator can become blocked (seized) after long-term exposure to atmospheric influences, temperature variations etc, after years of service.

### 3.3.2. Case 11:

In 1990 a 420 kV, OIP type bushing exploded on a 725 MVA, approximately five years old GSU transformer. The failure occurred at 658 MVA and caused a fire that had to be put out by the fire brigade. Fire protection equipment (water spray system) had been activated but could not put out the fire because it was located above its action radius. The 420 kV line was pulled out of the coil and bushing fragments considerably polluted the transformer. On the bushing condenser body (pos.1, Fig.1), on flange level, a hole, approximately 4 cm in diameter, with burnt edges can be seen, reaching in depth all the way to the central aluminum tube (pos. 6, Fig.1). Significant electric arch traces can be seen near the test tap. Measurement of the HV bushing capacitance and  $\tan\delta$  was undertaken in 1989, and the results were satisfactory and similar for all three bushings. The HV connection to the switchyard was double Al/steel rope. Repairs were made in the factory and down-time lasted approximately 7 months.

### 3.3.3. Cases 12 and 13:

On the 350 MVA, 400/110 kV autotransformer, two almost identical incipient failures of the RIP type bushing occurred approximately one after another, the second one after three years service. The monitoring system registered a change of approximately 3 % in the 420 kV bushing capacitance, indicating a breakdown between neighboring condenser electrodes. It was confirmed by measurements on the site and on the dismantled bushing in a high-voltage laboratory. The  $\tan\delta$  measured before and after the increase of capacitance, practically had not changed. The bushing was replaced with the down-time lasting several days. After dismantling, the bushings were examined in order to locate the breakdown. Results showed that it had occurred between the last condenser electrode (connected to the test tap) and adjacent electrode to it (breakdown across  $C_{1n}$  on Fig. 2), Figure 10. The exact puncture location was finally determined by microscope. Visually, the breakdown trace was a hole, around half a millimeter in diameter, stretching from the last electrode to the one before last, designated by the arrow.

In these two cases, the monitoring system proved reliable for fast detection of bushing capacitance changes. The observed traces matched with the measured capacitance values.

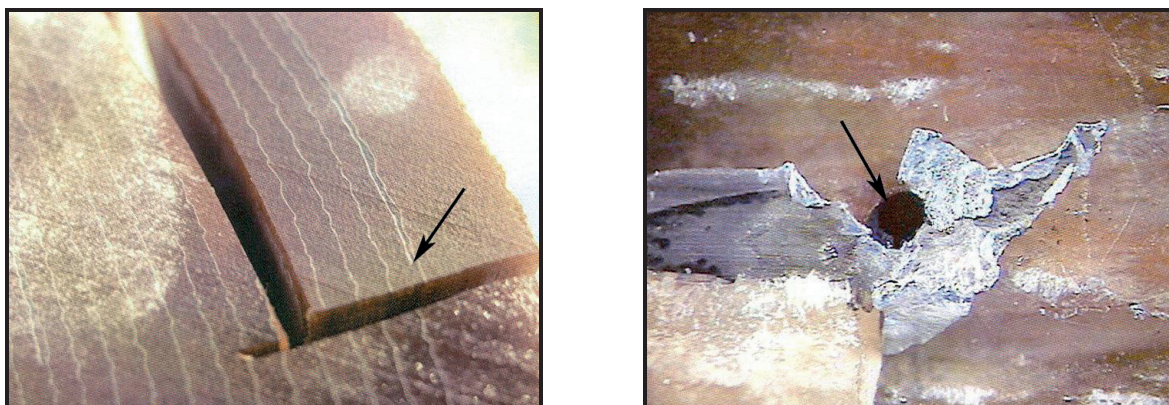


Figure 10: Breakdown position site; Figure left - the puncture is in the material at the depth about 1 cm from the point marked by the arrow; Figure right – the arrow designates the puncture between two electrodes (photo under microscope at magnification  $\times 15$ )

#### 4. CONCLUSION

All transformer bushing failures start with a defect that represents incipient failure of the bushing and end with terminal failure – explosion. Such a course of events can be changed by condition diagnostics. In this way, a defect can be reliably detected in the initial stage, considered the incipient failure, before it develops into terminal failure. Based on considerably lower direct and indirect costs of incipient bushing failure as compared to terminal failure, periodic and continuous condition diagnostics has great economic significance.

Bushing failure analysis shows that condition diagnostics efficiency can be enhanced in several ways:

The first improvement presents regular and planned periodical condition diagnostics.

The second improvement presents periodical condition diagnostics enhancement through the application of relative decision criteria for  $\tan\delta$ . Namely, some bushings show considerable  $\tan\delta$  changes in the period prior to malfunction at relatively low absolute values, even lower than those defined by standard for new bushings [1]. That means establishing and application of the procedure for  $\tan\delta$  conversion to reference temperature values. It consists of two parts: knowledge about temperature dependence of  $\tan\delta$ , [6], and measurement of the bushing insulation system temperature, which might be a special problem when performed on site.

The third improvement presents the application of continuous (on-line) diagnostics. This relatively new technology is effective in preventing terminal failure. By monitoring the capacitance, it is possible to detect a condenser body defect at a very early phase, while it is so small that it needs to be detected by microscope during visual inspection. In cases of ambiguous diagnostic results, or when a suspicious bushing cannot be replaced (no spares, long term of delivery), installation of a bushing monitoring system is advisable, which, if necessary, could even be of mobile type.

In addition to diagnostics enhancement, service conditions improvement can considerably reduce bushing failure rate. It has been shown that tubular connections degrade bushing properties in a still unexplained manner [7], probably due to their mechanical rigidity. This effect is also reported in [8], where most of the bushings with an on-site measured increase of  $\tan\delta$  had rigid tubular connections to the switchyard. It seems that the application of bus dilatation compensators is not satisfactory since they can often become blocked during long-term service. A flexible cable connection is a good solution for the problem.

An interesting aspect in failure analysis is that fire protection equipment (water spray system) is often not able to put out a fire caused by a high voltage bushing explosion because the source of fire, due to the bushing size, is outside the perimeter of its efficient action.

## REFERENCES

- [1] IEC 600137-2008, Insulated bushings for alternating voltages above 1000 V
- [2] R. Krump, H Frielingsdorf: Dry type bushings for operation under difficult conditions, Transform 2001, Munich 23-26. 04.2001. Convention report, 61-74.
- [3] H. Frielingsdorf, J. Frost, N. Koch: Future design for transformer bushings, Transform 1998, Munich 20-22. 04.1998. Convention report, 17-26.
- [4] An international survey on failures in large power transformers in service, Electra 88, May 1983, 21-48.
- [5] CIGRE WG 12.18: Life Management of Transformers, Guidelines for Life Management techniques for Power Transformers, Final report, Draft for comments, 2001.
- [6] Mikulecky, A.: Capacitance and dielectric dissipation factor of transformers bushings, Ph.D thesis, University of Zagreb, FER, Zagreb, 2006, (in Croatian).
- [7] P.V. Goosen: Transformer accessories, CIGRE 1996, Paris, Ref. 12-104.
- [8] Mikulecky, A.: Diagnostics of transformers condenser type bushings, M.Sc. thesis, University of Zagreb, FER, Zagreb, 2003, (in Croatian).

Journal  
of Energy

ENERGY